2013

Development and exploration of potential routes of discovery of new superconductors

Xiao Lin
Iowa State University

Development and exploration of potential routes of discovery of new superconductors

by

Xiao Lin

A dissertation submitted to the graduate faculty

in partial fulfillment of the requirements for the degree of

DOCTOR OF PHILOSOPHY

Major: Condensed Matter Physics

Program of Study Committee:

Paul C. Canfield, Major Professor

Sergey L. Bud'ko

Bruce N. Harmon

Steven D. Kawaler

R. William McCallum

Iowa State University

Ames, Iowa

2013

TABLE OF CONTENTS

LIST OF TABLES

LIST OF FIGURES

ACKNOWLEDGEMENTS

I would like to take this opportunity to express my sincere thanks to those who have helped and supported me during the period of my graduate study.

First and foremost, I would like to thank my advisor Professor Paul C. Canfield for his tremendous guidance and support in both research and life throughout my entire Ph.D. period. I deeply appreciate the opportunities and freedom he gives me to let me explore, learn and grow. His advices, help, understanding and patience are invaluable for me.

I would also like to thank Dr. Sergey L. Bud'ko for his great help on experiments. He is always there and "rescuing me out of the troubles". I am also grateful for his discussions on physics which inspire critical thinking. In addition, I also thank him for his understanding and support in life.

My thanks also go to the members of my committee who have guided me on my research and bring their expertise to bear on my research projects.

Special thanks go to Dr. Milton Torikachvili, Dr. Makariy A. Tanatar and Dr. Vladimir G. Kogan for the nice discussions, encouragement and patience.

I would like to thank my past and present colleagues Shuang Jia, Ni Ni, Eundeok Mun, Rongwei Hu, Estelle Colombier, Andreas Kreyssig, Alex Thaler, Sheng Ran, Stella Kim, Emily Hellerich, Halyna Hodovanets, Tai Kong, Udhara Kaluarachchi, Min Gyu Kim, Anton Jesche and Valentin Taufour for the suggestions, discussions and collaborations. Each of them has given me advice and supports in their own way, from which I will benefit for the rest of my life.

I am deeply appreciative of the support and encouragement I received from my hus-

band, Rui Liu, and my parents. Without their patience and understanding, this work would not have been accomplished.

Lastly, the friendships and experiences I have made in the Department of Physics and Astronomy, Iowa State University are immeasurable, and I thank the faculty, staff, and fellow graduate students for creating a supportive and enthusiastic learning environment.

This work was carried out at the Iowa State University and Ames Laboratory space and supported by the AFOSR-MURI grant No. FA9550-09-1-0603.

ABSTRACT

This thesis summarizes our efforts to develop and explore potential routes for the discovery of new superconductors. The development of viable solutions for sulfur-bearing compounds is presented. It also provides the details of searching for quantum critical points (QCPs) and possible superconductors by suppressing ferromagnetic states via chemical substitution and the application of pressure. By pressure, the ferromagnetism in $La(V_xCr_{1-x})Ge_3$ was successfully suppressed, and, in addition, a potential QCP at ambient pressure was discovered for $x = 0.16$. On the other hand, the $La(V_xCr_{1-x})Sb_3$ series is likely to evolve into new magnetic state with V-substitution with the Cr-based magnetism appearing to be more local-moment like than for the case of $LaCrGe_3$. We also performed detailed characterization on $BaSn_5$ superconductor, giving further understanding of its superconducting state, and on $R_3Ni_{2-x}Sn_7$ and $RNi_{1-x}Bi_{2\pm y}$ series putting to rest spurious claims of superconductivity.

CHAPTER 1. INTRODUCTION

Over a century ago, superconductivity was discovered by the observation of a sudden transition to zero resistance in high-purity mercury [Onnes, 1911]. Since then, superconducting has been one of the most actively studied states in condensed matter physics as well as a source of many industrial applications. It has attracted immense experimental and theoretical efforts. Although the first few superconductors were found in simple elements and alloys, during the last 100 years, more and more superconductors appear in the compounds that once were considered improbable, if not impossible, such as: organic compounds, oxides, magnetic compounds, and most recently whole families of FeAs- and FeSe-based compounds. The discovery of superconductivity is often tightly coupled to the design, discovery, and growth of novel materials. Where to look for and how to find superconductors are the key questions associated with searching for new superconductors. Given that we (as a community) can not yet accurately predict the occurrence of superconductivity, it is of great importance to develop and explore new, potential routes for the discovery of new superconductors. In addition, since superconductivity often occurs in proximity to, and competition with, other novel phases, the exploration of these routes can lead to a plethora of interesting compounds.

Recently, with the discovery of high temperature superconductivity in FeAs-based materials [Hosono, 2008; Rotter et al., 2010], chalcogen (S, Se, Te, etc.) and pnictogen (N, P, As, etc.) based compounds have attracted people's attention. It is believed that compounds with these less-explored N, P, As and S, Se, Te elements as constituents will have electronic density of states that can be tuned and bandwidths that can be

adjusted. However, unlike Nb_3Sn, MgB_2, etc., which shows robust superconductivity for well-ordered, stoichiometric, line compounds, the superconductivity in FeAs- and FeSe-based materials manifests in such a way that the parent compounds have to be doped/modified in the correct way. For example, superconductivity can only appear in $BaFe_2As_2$ when Co or Ni are substituted for Fe [Ni et al., 2008c], but not when Mn or Cr are substituted [Thaler et al., 2011]. Therefore, it is very difficult to discover superconductivity by accident, as a minority phase of a multi-phase sample. Instead specific samples, with systematically controlled compositions, need to be studied. Hence, the growth of new materials, particularly in bulk crystalline form, is an important part of improving the chances of finding new superconductors.

High-temperature solution growth is viewed as one of he most powerful synthetic tools for growing single crystalline samples [Canfield and Fisk, 1992; Canfield, 2010] for basic as well as applied physics. For each specific growth, it is crucial to have a readily accessible and well understood solution. Sometimes growths can be complicated due to the specific properties of the constituent elements, such as high-vapor pressure, high melting point, etc. Arsenic for example, has a very high vapor pressure and is also toxic in both its elemental and oxide forms. Thus, to grow FeAs-based superconductors out of solution, a large effort has been made to develop versatile and safe methods. As we start to examine chalcogen and pnictogen based compounds and search for new superconductors, it becomes an urgent need to develop a wide range of chalcogen and pnictogen based solutions. Whereas some viable solutions have been developed for the use of P and As [Canfield and Fisk, 1992; Ni et al., 2008a], and Se and Te can be used as solvents by themselves, in this thesis, I will mostly focus on the development of S-based solutions that can be utilized for growths of S-bearing compounds.

Another possible route is to search for new superconductors in the vicinity of a quantum critical point (QCP). A QCP is thought to be a singularity in the ground state. At a QCP, the system goes through a quantum phase transition (QPT) which is driven by

non-thermal parameters at zero temperature [Sachdev, 2001]. Superconductivity is often discovered in the vicinity of a QCP and accompanied with non-Fermi liquid behavior. The discoveries of QCP and superconductivity in the ferromagnetic UGe_2 [Taufour et al., 2010; Saxena et al., 2000] and UCoGe [Huy et al., 2007] are considered as providing a better understanding of magnetically mediated superconductivity and non-Fermi liquid behavior. UGe_2 was reported to show coexistence of superconductivity and magnetism in high quality single crystals at pressures from 10 to 16 kbar with its maximum superconducting transition temperature at about 0.7 K [Saxena et al., 2000]. Theoretically, on the boundary of a ferromagnetic state at low temperatures, the superconducting state is due to the strong longitudinal magnetic susceptibility and magnetic interaction [Saxena et al., 2000]. Therefore, suppressing ferromagnetism to drive the criticality offers a potential route for the discovery of new superconductors. Chemical doping, pressure and magnetic field can be used to suppress the magnetic order. For example, by chemical substitution, a QCP is discovered in $CePd_{1-x}Ni_x$ when the doping level is 0.95 [Stewart, 2001]. By applying magnetic field, QCPs were successfully introduced in YbAgGe [Bud'ko et al., 2004], YbBiPt [Mun et al., 2013] and $YbRh_2Si_2$ [Trovarelli et al., 2000]. In the case of MnSi [Stewart, 2001], itinerant-electron magnetism disappears at a first order transition and a QPT appears as pressure is applied. In this thesis, two stoichiometrically similar sets of compounds $La(V_xCr_{1-x})Ge_3$ and $La(V_xCr_{1-x})Sb_3$ were studied. Both $LaCrGe_3$ and $LaCrSb_3$ are ferromagnetic, and with V-substitution and the application of pressure, we were aiming to suppress the ferromagnetism, search for possible QCPs and hopefully superconductivity.

In addition, re-examination of known or reported superconductors that were poorly studied can also offer opportunities to understand the mechanism of superconductivity and discovery of new physics. With careful thermodynamic and transport measurements, $BaSn_5$ has been characterized in detail, and evolution of superconductivity under the application of pressure has also been studied. Growth and study of $R_3Ni_{2-x}Sn_7$ and

$R\mathrm{Ni}_{1-x}\mathrm{Bi}_{2\pm y}$ series, on the other had, revealed that reports of superconductivity associated with these compounds are very probably spurious and associated with second phase impurities.

This thesis is organized as following: Chapter 2 provides some background about materials growth and a description of some of the theoretical physics associated with the states and effects found in the materials studied in this thesis, covering superconductivity, magnetism, spin glass, quantum phase transition and de Haas-van Alphen effect. Chapter 3 covers details about the specific growth methods and techniques I used and provides a brief review of the measurement techniques. In Chapter 4, the development of viable solutions for the synthesis of sulfur bearing single crystals is presented in the form of the published paper. Chapter 5 gives the physical properties of single crystalline BaSn_5 (presented in the form of the published paper). In Chapters 6 and 7 efforts to clarify claims of superconductivity in rare earth based systems are presented. In Chapter 6, the published form of my paper "Anisotropic magnetization, resistivity and heat capacity of single crystalline $R\mathrm{Ni}_{2-x}\mathrm{Sn}_7$ (R = La, Ce, Pr and Nd)" is presented. Chapter 7 presents the published form of my paper "Anisotropic magnetization and resistivity of single crystalline $R\mathrm{Ni}_{1-x}\mathrm{Bi}_{2\pm y}$ (R = La – Nd, Sm, Gd – Dy)". Chapter 8 presents the suppression of ferromagnetism in the $\mathrm{La}(\mathrm{V}_x\mathrm{Cr}_{1-x})\mathrm{Ge}_3$ system. This manuscript has been accepted for publication to Phys. Rev. B. Finally, the data, results and discussion on the suppression of ferromagnetism in the $\mathrm{La}(\mathrm{V}_x\mathrm{Cr}_{1-x})\mathrm{Sb}_3$ system is presented in Chapter 9. In the final chapter, I briefly summarize and discuss future directions for ongoing work.

CHAPTER 2. OVERVIEW

2.1 Crystal Growth

The availability of high quality samples is crucial for many classes of experimental measurements. Although the discovery and preliminary characterization of novel materials are often managed with polycrystalline samples, high purity single crystals are vital for more detailed and sophisticated characterization of the intrinsic properties. First, single crystals with well defined orientation are the basis for anisotropic studies. Secondly, single crystalline samples do not possess grain boundaries, and (at least for solution grown crystals) often have less internal strain and stress as compared with the polycrystalline samples. Also solution grown single crystals can have fewer impurities, resulting in very low residual resistivity. This is critical for many experiments, such as the the observation of quantum oscillations, which can provide information about the topology of the Fermi surface. In addition, as opposed to polycrystalline samples, single crystals have larger crystalline and atomically ordered surfaces, which are vital for many surface sensitive measurements, such as scanning tunnelling microscopy (STM), angle resolved photon emission spectroscopy (ARPES), etc. Finally, single crystal growth from high temperature solutions can, sometimes, be used as a method of new materials discovery. The model Fe-based superconductor parent compound, $CaFe_2As_2$ [Ni et al., 2008b], as well as the binary quasicrystals Sc-Zn [Canfield et al., 2010] and i-*R*-Cd [Goldman et al., 2013] were discovered as the result of single crystal growth out of non-stoichiometric melts.

Many techniques have been developed to growth single crystalline samples, and can be roughly classified into three groups: growth from the melt, growth from a vapor phase and growth from solution [Brice, 1973, 1986; Pamplin, 1975]. Growth from the melt, including Czochralski, Bridgman and skull-melting methods, can be used to grow large single crystals, such as sapphire and silicon used for computer chips. These techniques allow for crystal growth to be monitored and controlled by computer, and these techniques have been widely accepted and optimized by industrial. However, growth from the melt method requires the composition of the melt to be the same, or very similar, to that of the expected product. For the Czochralski method, given that crystals may be grown only at a single, extremely high temperature, the melt can, sometimes become inhomogeneous, and any significant vapor pressure can lead to poorly controlled stoichiometry. A disadvantage of Bridgman method is that a layer of impurities grows at the interface between melt and the solid as this surface moves up the melt, and the impurities become concentrated in the higher part of the crystal. In addition, the crucible can often strain or simply crack the grown crystal upon cooling. On the other hand, growth via vapor transport can provide very high purity crystals with relatively few defects, but this growth method is often very slow (diffusion limited) and requires volatile phases of all the components as well as a transport agent (if self transport is not possible).

High temperature solution growth is perhaps the most common industrial crystal growth technique (e.g. hydrothermal growth of SiO_2 crystals) and is also the method most widely used for exploratory growth of samples for basic characterization and is recognized as a powerful technique for obtaining single crystals of complex materials. It can be used to grow a large variety of congruently and incongruently melting materials with ease, with relatively simple equipment and over relatively short time scales [Canfield and Fisk, 1992; Canfield, 2010]. Take $CeSb_2$ as an example, as the compound does not melt congruently, it can not be synthesized by growth from the melt method. However, via high temperature solution method, single crystals of $CeSb_2$ can be grown out of excess

Sb below 1200 °C [Canfield and Fisk, 1992; Canfield, 2010] in as little as 12 hours. The high temperature solution method can also help reduce the growth temperature, as in the case of CeSb, although it is a congruently melting compound, its melting temperature is about 1400 °C. The high temperature needed for growing CeSb from a stoichiometric melt puts extra requirement on the experiment equipment and conditions. In this case, by using Sn as a solvent, the growth temperature can reduced to below 1150 °C [Canfield and Fisk, 1992; Wiener and Canfield, 2000; Canfield, 2010]. Another advantage of high temperature solution growth is the ability to incorporate volatile elements into solutions and as a result, reduce their vapor pressure. Elemental As, for instance, sublimes at 615 °C. As a consequence, growing the As-based compounds via direct melting can cause explosions of the growth ampoule due to As's high vapor pressure. A safer technique for growing As-based compounds is strongly desired. Given the essentially full solubility of As in Sn solvent, this issue has been successfully solved by introducing Sn as a solvent for some As-based compounds in the high temperature solution growth of $A\mathrm{Fe_2As_2}$ (A = Ca, Sr, and Ba) [Ni et al., 2008a,b; Yan et al., 2008].

A significant part of this thesis work focused on the development of S-based melts that could serve as the high temperature solution for the growth of S-based compounds.

2.2 Superconductivity

2.2.1 Zero resistance and Meissner effect

The discovery of superconductivity was made in 1911 during Onnes' investigation of the electrical resistance of pure metals at low temperatures [Onnes, 1911]. When the specimen was cooled to 4.2 K, the electrical resistance of mercury was found to drop suddenly to 10^{-5} Ω or less, that is to about one ten-thousandth of the value which it had at 4.3 K. DC electrical currents have been observed to flow without attenuation in superconducting rings, also indicating zero resistivity. This phenomena – zero resistivity,

is known as one of the basic characteristics of superconductivity. At a critical temperature T_c, the material undergoes a phase transition from a state of normal resistivity to a superconducting state, seen in Fig. 2.1 [Onnes, 1911].

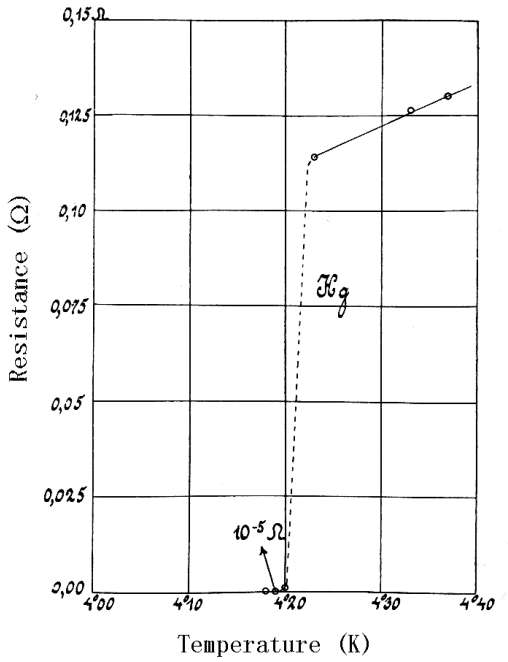

Figure 2.1 Resistance as a function of temperature of mercury. This plot was obtained by Kamerlingh Onnes when he discovered superconductivity in Leiden in 1911 [Onnes, 1911].

The infinite conductivity, i.e. zero resistivity, by itself does not adequately describe the magnetization of a superconductor. In 1933, Meissner and Ochsenfeld [Meissner and Ochsenfeld, 1933] found that if a superconductor is cooled in a magnetic field to below the transition temperature, it will expel the induction $\mathbf{B}$ at the phase transition rather than trapping it (as would be expected for a simple, perfect conductor). This second characteristic of superconductivity, the Meissner effect, is shown in Fig. 2.2. Zero induction implies perfect diamagnetism, as (in CGS unit)

$$\mathbf{B} = \mathbf{H} + 4\pi\mathbf{M}.$$

This suggests that the magnetization $\mathbf{M}$ inside the sample is directly opposite to the

applied field **H**, i.e. $\mathbf{H} = -4\pi\mathbf{M}$. There are two manifestations of this perfect diamagnetism in superconductors. The first aspect is flux expulsion, as mentioned earlier. The field cooled (FC) sample expels the magnetic field, and show Meissner effect. The second is flux exclusion: if the same sample in the normal state is zero field cooled (ZFC), that is cooled below T_c to the superconducting state without any magnetic field present, and is then placed in an external magnetic field (less than the critical field – see below), the field will be excluded from the superconductor as well.

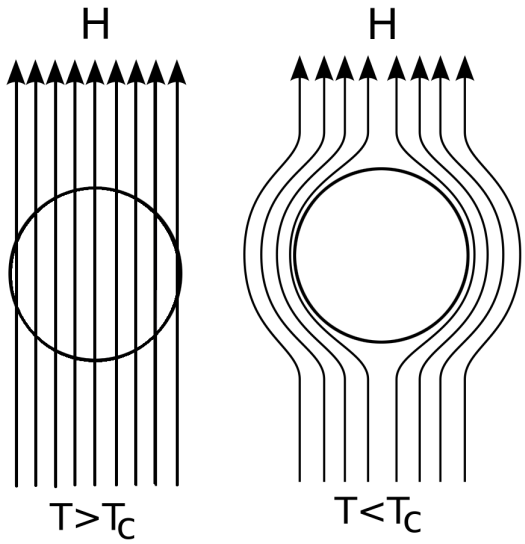

Figure 2.2 Diagram of the Meissner effect in a superconducting sphere cooled in a constant applied magnetic field; on passing below the transition temperature the induction B is repelled from the sphere.

Considering an infinite sample with negligible penetration depth (see below), the work done by the external magnetic field $\mathbf{H}_0$ can be written as:

$$-\int_0^{H_0} \mathbf{M} dH = \frac{1}{4\pi}\int_0^{H_0} H dH = \frac{H_0^2}{8\pi}.$$

Subsequently, the Helmholtz free energy is:

$$F_s(H) = F_s(0) + \frac{H_0^2}{8\pi},$$

where $F_s(0)$ is the free energy of a superconductor in superconducting state in zero magnetic field. When

$$F_s(H_c) = F_n(0) = F_s(0) + \frac{H_c^2}{8\pi},$$

here $F_n(0)$ is the free energy of the material in normal state in zero magnetic field, the normal state is energetically favored, and the superconducting state can be destroyed. This external field H_c, is called thermodynamic critical field.

2.2.2 Type I and type II superconductivity

Experiments show that even when the magnetic induction is expelled from the whole sample, there is some penetration in a small surface layer, the thickness of which is the so-called penetration depth λ. The magnetic field exponentially decays over this length scale as we go in from the surface.

One of the other key characteristic length scales for a superconductor is called coherence length ξ. It was first introduced in the Ginzburg-Landau theory, in which the wave function of the superconducting electrons is given as [Ginzburg and Landau, 1950]:

$$\psi(\mathbf{r}) = |\psi(\mathbf{r})|e^{i\phi}.$$

The coherence length is a measure of the range over which the wavefunction of superconducting condensate cannot change drastically in a spatially-varying magnetic field, and is also a measure of the minimum spatial extent of a transition layer between normal and superconducting state.

The coherence length and the penetration depth depend on the mean free path of the electrons measured in the normal state. It should be noted that the electron mean free path, l, is a third important length scale. The ratio λ/ξ is denoted by κ, which subsequently is used to classify type I and type II superconductors [Abrikosov, 1957; Tinkham, 2004].

$$\kappa < \frac{1}{\sqrt{2}} \qquad \text{for Type I}$$

$$\kappa > \frac{1}{\sqrt{2}} \qquad \text{for Type II}$$

For the type I superconductor, the superconducting phase and the normal state only exist as spatially separated regions. Most elemental superconductors are type I superconductors. In the case of type II superconductor, when $H < H_{c1}$, the magnetic induction $\mathbf{B}$ inside the sample is zero, manifesting the Meissner effect. When $H_{c1} < H < H_{c2}$, the sample can only exclude the magnetic field partially, the magnetic vortices, called fluxoids, penetrate the sample. The sample remains electrically superconducting, but the vortex cores are in a normal state. The density of the vortices increases with increasing external field. When $H > H_{c2}$ (the upper critical field), the sample transits to the normal state (seen in Fig. 2.3).

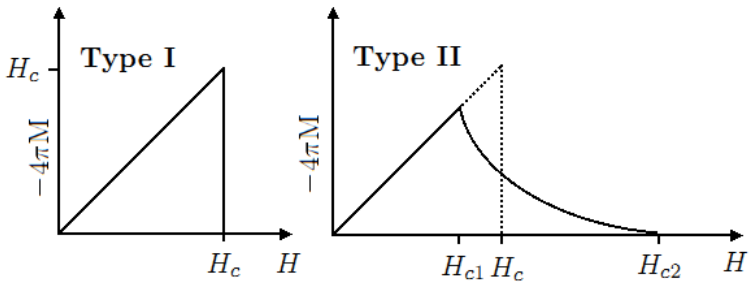

Figure 2.3 Diamagnetic responses to the external field for type I and type II superconductors.

2.2.3 BCS Theory

The theory of Bardeen, Cooper and Schieffer (BCS) [Bardeen et al., 1957] gave the foundation of our present understanding of basic superconductivity. This theory has a wide range of applicability, and can be used to explain diverse superconducting phenomena, such as the Meissner effect, zero resistance, vortex formation, quantum interference, etc. It consists of three fundamental ingredients: the effective attractive electron-electron

interaction as a consequence of interaction with the positively charged ions; the Cooper pair with $\mathbf{k}\uparrow$ and $-\mathbf{k}\downarrow$ forming a bound state, and the pair-pair correlations which give rise to the long range coherence and all the characteristic properties of superconductors [Finnemore, 1992]. A fair amount of assumptions have been made in the derivation of the BCS theory, such as assuming the Fermi surface is spherical, the electron-phonon interaction potential is a constant over a range of energy about the Fermi surface, etc. Hence, it is not appropriate to use it to predict the existence of a superconducting state, nor can it be a first principle calculation of a physical property, such as T_c. However, the BCS theory does provide at least a model that explains the fundamental facts related with superconductivity fairly well.

In 1950, Cooper showed that any net attraction between two electrons near the Fermi surface can lower the total energy of the electron system. This attractive interaction, could lead to an instability in the electron gas leading to bound pairs [Cooper, 1956]. The electron pair with momenta $(k,\ -k)$ and antiparallel spins is called Cooper pair, $(\mathbf{k}\uparrow,\ -\mathbf{k}\downarrow)$, which was supposed to form the singlet coupling to lower energy ($L = 0$ and $S = 0$). By solving the two particle Schrödinger's equation, Cooper found the existence of a bound state with negative energy. Regardless of how small the attractive potential is, it can lead to binding, as the negative contribution to the energy of this attractive potential is bigger than the increased kinetic energy associated with the Cooper pair [Cooper, 1956].

The electron-phonon interaction was first proposed by Fröhlich in 1950 [Fröhlich, 1954] to be the origin of such an attractive interaction. A simple semiclassical picture can be used to illustrate this interaction. As an electron (Electron 1 in Fig. 2.4 (a)) moves through the lattice, the lattice moves towards its path as a consequence of Coulomb interaction. Assuming the motion of the lattice and electrons have sufficient amplitude, then the region of the electron can actually acquire a net positive charge. This overscreening by the lattice, therefore, provides the source of attraction for the other moving electrons.

Thus, another electron (Electron 2 in Fig. 2.4 (b)) passing in the opposite direction then is attracted to this displacement of the lattice. In a quantum mechanical view, the motion of the lattice can be understood as the emission and absorption of phonons. Hence, the indirect coupling of electrons through the phonons arises by the emission of a phonon by one electron and its absorption by another. Given that the deformations of the lattice – phonon is characterized by its frequencies, the cutoff energy $\hbar\omega_c$ is expected to be of the order of the Debye energy $\hbar\omega_D = k_B\Theta_D$ [Tinkham, 2004].

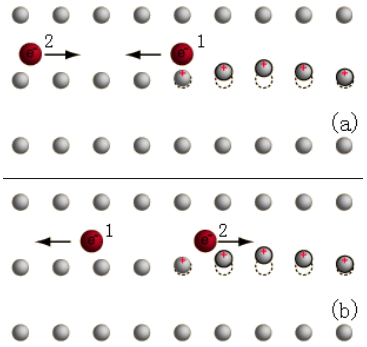

Figure 2.4 Diagram of electron-phonon interaction in superconductors.

On the basis of Cooper pair formation and the electron-phonon interaction, Bardeen, Cooper and Schieffer developed a microscopic theory, the so-called BCS theory [Bardeen et al., 1957]. Several assumptions have been made to simplify the theoretical calculation. The Fermi surface is assumed to be a sphere, i.e. isotropic in k-space. The electron-phonon interaction potential $-V$, is assumed to be a constant over a range around $\hbar\omega_D$ about the Fermi energy E_F. The excitation energy E_k of a quasi-particle (an electron participating in the pairing) of momentum $\hbar\mathbf{k}$ can be express as [Tinkham, 2004]:

$$E_k = (\Delta_{\mathbf{k}}^2 + \xi_{\mathbf{k}}^2)^{1/2},$$

where $\xi_{\mathbf{k}} = \epsilon_{\mathbf{k}} - E_F$, the single-particle energy relative to the Fermi energy; and $\Delta_{\mathbf{k}}$ is the energy gap, and hence is the minimum excitation energy and essentially $\mathbf{k}$-independent.

The BCS theory also gives:

$$\Delta \approx 2\hbar\omega_{\mathrm{D}} e^{-1/VD(E_{\mathrm{F}})},$$

here $D(E_{\mathrm{F}})$ is the density of states per spin at the Fermi level. This approximation is under the condition that $\hbar\omega_{\mathrm{D}} \gg k_{\mathrm{B}}T_{\mathrm{c}}$, which is called the weak-coupling limit.

The gap Δ is associated with the energy needed for Cooper pair breaking. As temperature increases, more and more pairs break, and the gap becomes smaller. At the critical temperature T_{c}, the gap Δ drops to zero. At a finite temperature, one can get the following expression [Tinkham, 2004]:

$$\frac{1}{VD(E_{\mathrm{F}})} = \int_0^{\hbar\omega_{\mathrm{D}}} \frac{\tanh[(\Delta_{\mathbf{k}}^2 + \xi_{\mathbf{k}}^2)^{1/2}/(2k_{\mathrm{B}}T)]}{(\Delta_{\mathbf{k}}^2 + \xi_{\mathbf{k}}^2)^{1/2}} d\xi.$$

This gives:

$$k_{\mathrm{B}}T_{\mathrm{c}} \approx 1.13\hbar\omega_{\mathrm{D}} e^{-1/VD(E_{\mathrm{F}}),}$$

and

$$\Delta(0) \approx 1.764 k_{\mathrm{B}}T_{\mathrm{c}}.$$

The specific heat jump at the critical temperature,

$$\frac{C_s - C_n}{\gamma T_{\mathrm{c}}} \approx 1.43,$$

where $\gamma = \frac{2\pi^2}{3} D(E_{\mathrm{F}}) k_{\mathrm{B}}^2 T$;

at very low temperature, the specific heat can be approximated as

$$C \propto \frac{\Delta(0)^{2.5}}{T^{1.5}} \exp(-\frac{\Delta(0)}{k_{\mathrm{B}}T}).$$

2.3 Magnetism

2.3.1 Larmor diamagnetic susceptibility and Curie law

In the presence of a uniform magnetic field, the contribution of an isolated moment to the Hamiltonian of an ion (atom) is [Ashcroft and Mermin, 1976]

$$\triangle H = \mu_{\rm B}(\mathbf{L} + g_0\mathbf{S}) \cdot \mathbf{H} + \frac{e^2}{8mc^2}H^2 \sum_i (x_i^2 + y_i^2).$$

Here $\mathbf{L}$ and $\mathbf{S}$ represent the total electronic orbital and spin angular momenta of the unfilled shell(s) of the atom respectively; $\mu_{\rm B}$, the Bohr magneton, is given by

$$\mu_{\rm B} = \frac{e\hbar}{2mc} = 0.579 \times 10^{-8}{\rm eV/Oe}$$

and g_0, the electronic g-factor, is given by

$$g_0 = 2[1 + \frac{\alpha}{2\pi} + O(\alpha^2) + ...] = 2.0023,$$

$$\alpha = \frac{e^2}{\hbar c} \approx 1/137$$

and $\sum_i (x_i^2 + y_i^2)$ is the perpendicular distance of the electron from the field axis through the nucleus and is summed over all the electrons in the atom.

It is clear that the first term in the Hamiltonian is the contribution from the angular momenta. For simplicity, we start with examining an ion with zero spin and orbital angular momentum in its ground state $|0>$, i.e., an ion with all electronic shells filled. In this case, we have $\mathbf{J}|0> = \mathbf{L}|0> = \mathbf{S}|0>= 0$. Consequently only the second term in the Hamiltonian contributes to the field-induced shift in the ground-state energy:

$$\triangle E_0 = \frac{e^2}{8mc^2}H^2 \sum_i (x_i^2 + y_i^2) = \frac{e^2}{12mc^2}H^2 <0| \sum_i r_i^2 |0>,$$

where r_i is the the distance between the electron and the nucleus and is summed over all the electrons in the atom.

Accordingly the susceptibility of a solid with a volume of V, composed of N such ions is given by

$$\chi = -\frac{N}{V}\frac{\partial^2 \triangle E_0}{\partial H^2} = -\frac{e^2}{6mc^2}\frac{N}{V} < 0|\sum_i r_i^2|0> .$$

This negative susceptibility is known as the Lamor diamagnetic susceptibility, and also frequently referred to as the Langevin susceptibility. It is used to describe the magnetic response of the core electrons, i.e. electrons in filled shells, and can be rewritten in the form of molar susceptibility [Ashcroft and Mermin, 1976]:

$$\chi^{\text{molar}} = -Z_i N_{\text{A}}\frac{e^2}{6mc^2} < r^2 >= -Z_i\frac{e^2}{\hbar c}\frac{N_{\text{A}}a_0^3}{6} < (r/a_0)^2 >,$$

here Z_i is the total number of electrons in the ion. Given $a_0 = 0.529\ \mathring{A}$, $\frac{e^2}{\hbar c} = 1/137$, and $N_{\text{A}} = 0.6022\ \times 10^{24}$, we can get

$$\chi^{\text{molar}} = -0.79 Z_i \times 10^{-6} < (r/a_0)^2 > \text{cm}^3/\text{mole}.$$

The quantity $< (r/a_0)^2 >$ is of order unity, hence, χ^{molar} is typically of order 10^{-5}, which is very small compared with the angular momentum contribution to the magnetic susceptibility (see discussion below). It also should be noted that the Larmor diamagnetic susceptibility is solely determined by the ion, i.e., Z_i and r, and has no temperature dependence. The noble gas atoms He, Ne, Ar, etc. have full filled shells, thus, their magnetic susceptibility can be best described by the the Lamor diamagnetic susceptibility.

If the shell does not have $J = 0$, the first term in the Hamiltonian will almost always become dominant, and other contributions to the Hamiltonian can often be ignored. With $g_{\text{J}}\mathbf{J} = \mathbf{L} + g_0\mathbf{S}$, by using the Wigner-Eckart theorem [Gottfried, 1966], the ground state energy can be written as [Ashcroft and Mermin, 1976]:

$$< JLSJ_z|\mathbf{L} + g_0\mathbf{S}|JLSJ_z^{'} >= g_{\text{J}}(JLS) < JLSJ_z|\mathbf{J}|JLSJ_z^{'} >,$$

where g_{J} is the Landé g-factor, which can be computed as:

$$g_{\text{J}}(JLS) = \frac{3}{2} + \frac{1}{2}[\frac{S(S+1) - L(L+1)}{J(J+1)}].$$

If only the lowest $2J + 1$ states are thermally excited with appreciable probability, the the free energy is given by:

$$e^{-\beta F} = \sum_{J_z=-J}^{J} (e^{-\beta\gamma H J_z}),$$

where $\beta = \frac{1}{k_{\rm B}T}$, $\gamma = g_{\rm J}(JLS)\mu_{\rm B}$, and $\mu_{\rm B} = \frac{e\hbar}{2mc}$, is the so-called Bohr magneton.

This gives the magnetization as the following:

$$M = -\frac{N}{V} g_{\rm J}\mu_{\rm B} J B_{\rm J}(\beta g_{\rm J}\mu_{\rm B} J H),$$

where $B_{\rm J}(x)$ is the known Brillouin function.

In the low temperature limit ($k_{\rm B}T \ll g_{\rm J}\mu_{\rm B}H$), the magnetization becomes saturated, i.e., each moment is perfectly aligned with the applied field and $|J_z| = J$, and we can define the saturated moment as:

$$M_{\rm sat} = g_{\rm J} J \mu_{\rm B}.$$

In the high temperature (or low field) limit ($k_{\rm B}T \gg g_{\rm J}\mu_{\rm B}H$), the Brillouin function can be expanded in power series, and the magnetic susceptibility can be approximated as:

$$\chi = \frac{\partial M}{\partial H} \simeq \frac{N_{\rm A} J(J+1) g_{\rm J}^2 \mu_{\rm B}^2}{3k_{\rm B}T} = \frac{N_{\rm A} p_{\rm eff}^2 \mu_{\rm B}^2}{3k_{\rm B}T} = \frac{C}{T}.$$

This variation of the susceptibility with respect to the inverse of temperature is known as the Curie law [Ashcroft and Mermin, 1976]. Here $p_{\rm eff}$ is the effective number of Bohr magnetons, defined as

$$p_{\rm eff} = [J(J+1)]^{1/2} g_{\rm J},$$

and the effective moment $\mu_{\rm eff} = p_{\rm eff}\mu_{\rm B}$. The Curie constant C can be written as a function of $\mu_{\rm eff}$:

$$C = \frac{N_{\rm A} J(J+1) g_{\rm J}^2 \mu_{\rm B}^2}{3k_{\rm B}} = \frac{N_{\rm A}\mu_{\rm eff}^2}{3k_{\rm B}}.$$

Comparisons of the experimental values of the effective moment and the saturated moment with the theoretical calculations for trivalent rare earth ions (summarized in

Table 2.1 Components of the orbital angular momentum L; the spin angular momentum S; the total angular momentum J; the calculated values of the Landé g-factor g_J, saturated moment $\mu_{sat} = g_J J \mu_B$; effective moment $\mu_{eff} = [J(J+1)]^{1/2} g_J \mu_B$; and de Gennes factor dG for the trivalent rare earth ions.

$4f$	R^{3+}	L	S	J	g_J	μ_{sat}/μ_B	μ_{eff}/μ_B	dG
0	La	0	0	0	-	-	-	-
1	Ce	3	1/2	5/2	6/7	2.14	2.54	0.18
2	Pr	5	1	4	4/5	3.20	3.58	0.80
3	Nd	6	3/2	9/2	8/11	3.27	3.62	1.84
4	Pm	6	2	4	3/5	2.40	2.68	3.20
5	Sm	5	5/2	5/2	2/7	0.71	0.84	4.46
6	Eu	3	3	0	-	-	-	-
7	Gd	0	7/2	7/2	2	7.00	7.94	15.75
8	Tb	3	3	6	3/2	9.00	9.72	10.50
9	Dy	5	5/2	15/2	4/3	10.00	10.64	7.08
10	Ho	6	2	8	5/4	10.00	10.61	4.50
11	Er	6	3/2	15/2	6/5	9.00	9.58	2.55
12	Tm	5	1	6	7/6	7.00	7.56	1.17
13	Yb	3	1/2	7/2	8/7	4.00	4.54	0.32
14	Lu	0	0	0	-	-	-	-

Table 2.1) are useful in the experimental analysis of rare earth based compounds, such as in the case of determining the concentration of rare earth elements, distribution of moments in materials exhibiting metamagnetic transitions, etc.

2.3.2 Hund's Rules

The total spin **S**, total orbital momentum **L** and total angular momentum **J** quantum numbers are crucial for the theoretical determination of the magnetic properties of a local moment material. The Russel-Saunders rule results in the total angular momentum **J** with a quantum number $|\, L+S \,|$, $|\, L+S-1 \,|$,..., $|\, L-S \,|$. For each J value, there is $2J + 1$ degeneracy with $J_z = J$, J-1,..., -J. Without considering the interactions between the electrons, the ionic ground state would be degenerate, i.e., there would be plenty of

ways of putting the electrons into the $2J + 1$ levels. Nevertheless, this degeneracy is considerably lifted by electron-electron, Coulomb interactions, as well as by the electron spin-orbital interaction. The three Hunds rules as applied to electrons in a given shell of an atom outline how electrons will occupy orbitals in such a way that the ground state is characterized by the following [Ashcroft and Mermin, 1976; Kittel, 2005]:

• The ground state has the largest value of total spin S that is consistent with the exclusion principle.

• For the maximum possible S value, the electrons are distributed between all possible states in accordance with the exclusion principle, and such that the resulting L value is maximum.

• For shells that are less than half-filled, the total angular momentum is given by $J = \mid L - S \mid$. For shells that are more than half-filled, $J = \mid L + S \mid$. For the half-full shell, the application of the first rule gives $L = 0$, and $J = S$.

The first Hund's rule reflects the exclusion principle and the Coulomb repulsion between electrons. The exclusion principle prevents two electrons of the same spin from occupying the same state at the same time. Therefore, the electrons with the same spins are kept apart. Also being "kept" apart results in lowering the Coulomb potential energy for parallel spin electrons. The second rule can be best approached by model calculations, whereas the third rule is a consequence of the sign of the spin-orbital interaction [Kittel, 2005]. The third rule deals with reducing the repulsion between electrons. It can be understood from the classical picture that if all electrons are orbiting in the same direction (higher orbital angular momentum) they meet less often than if some of them orbit in opposite directions.

Using these rules, the ground state of the electronic configuration for the rare earth ions can be determined. The calculated magnetic properties for the free, trivalent ions are shown in Table 2.1.

2.3.3 Mean Field Theory and Curie-Weiss Law

The Curie law has been derived to describe the paramagnetic behavior for the isolated magnetic moments, i.e., moments without interactions. For materials having non-negligible magnetic interactions, the mean field theory (also called Weiss' molecular theory) takes the interactions into account by postulating an effective internal field — exchange field H_{eff} — in addition to the external field H. This H_{eff} is assumed to arise from the thermal average of the surrounding moments and acts on each local moment. Also, H_{eff} is supposed to be proportional to the magnetization of the local moment which it is acting on, and gives the following relation:

$$H_{\text{eff}} = \alpha M,$$

where α is a constant, independent of temperature.

Accordingly, the total magnetic field acting on each moment is $H + H_{\text{eff}}$, and one can substitute this into the Curie law and get:

$$M = \frac{C}{T}(H + H_{\text{eff}}) = \frac{C}{T}(H + \alpha M).$$

Solving for M and the susceptibility, one can get the Curie-Weiss law [Ashcroft and Mermin, 1976] (seen in Fig. 2.5):

$$\chi = \frac{C}{T - \alpha C} = \frac{C}{T - \theta},$$

where $\theta = \alpha C$, representing the Curie-Weiss temperature. The sign of θ can be either positive or negative, depending on the sign of α – the type of the interaction. $\alpha > 0$ implies the internal interaction tending to line up the magnetic moments parallel to each other, i.e., a ferromagnetic interaction, whereas $\alpha < 0$ is the case that the magnetic moments prefer to be antiparallel to each other, manifesting an antiferromagnetic interaction. The ordering temperature of an antiferromagnetic transition is called the Néel temperature T_{N} and is often identified by a well defined kink in the curve of $\chi(T)$. The

ratio of $\theta/T_{\rm N}$ can vary over a fairly large range around 1.0 especially when next-nearest-neighbor interactions are provided for, and when possible sublattice arrangements are considered is determined by the interactions between the magnetic moments [Kittel, 2005].

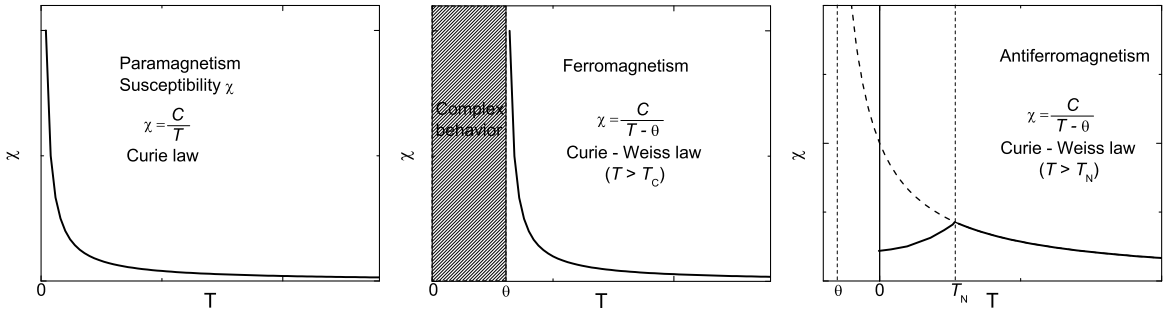

Figure 2.5 Schematic diagrams of the temperature dependent magnetic susceptibility of paramagnetic, ferromagnetic and antiferromagnetic systems. Note: $T_{\rm N}$ is the Néel temperature, the ordering temperature of an antiferromagnetic transition [Kittel, 2005].

The Curie-Weiss law can be rewritten as:

$$1/\chi = \frac{1}{C}(T - \theta).$$

Thus, by plotting $1/\chi(T)$ (as shown in Fig. 2.6), one can obtain the effective moment $\mu_{\rm eff}$ from the slope and the Curie-Weiss temperature θ via extrapolating $1/\chi$ to zero. Consequently, the type and strength of the internal interaction in the paramagnetic state can be evaluated via θ. It should be mentioned that although the Curie-Weiss law is derived based on local moments system, it can be widely used for many itinerant magnetic system as well, such as $ZrZn_2$ [Seeger et al., 1995], MnSi [Wernick, 1972], etc.

2.3.4 de Gennes Scaling

The interaction of two spins can be written as

$$J_{ij}\mathbf{S}_i \cdot \mathbf{S}_j.$$

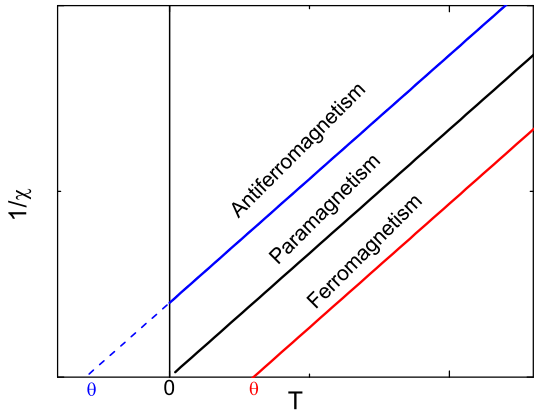

Figure 2.6 Schematic diagrams of the inverse magnetic susceptibility as a function of temperature of paramagnetic, ferromagnetic and antiferromagnetic systems.

For isotropic interaction, the spin momentum may be written in terms of the total momentum $\mathbf{J}$ by combining $\mathbf{J} = \mathbf{L} + \mathbf{S}$ with $\mathbf{L} + 2\mathbf{S} = g_{\mathrm{J}}\mathbf{J}$, so that

$$\mathbf{S} = (g_J - 1)\mathbf{J}.$$

Consequently, one can get:

$$< |\mathbf{S} \cdot \mathbf{S}| >= S(S+1) = (g_J - 1)^2 J(J+1).$$

Here we can define $dG = (g_J - 1)^2 J(J+1)$, which is the well-known de Gennes factor. Within the mean field approximation, $\theta = \alpha C \propto S(S+1)$, thus, one can find that the Curie-Weiss temperature θ scales as the following:

$$\theta \propto (g_J - 1)^2 J(J+1).$$

Therefore, the Curie-Weiss temperature can be simply viewed as directly proportional to the de Gennes factor, which is determined by the quantum numbers, S, L and J. The values of the de Gennes factor for each trivalent rare earth ion are listed in Table. 2.1. Within the same framework of the mean field theory, if the crystal electric field (CEF) is neglected, the Curie temperature T_{C} (for ferromagnetic ordering) or Néel temperature

T_N (for antiferromagnetic ordering), can also be proportional to the de Gennes factor. As shown in Table.2.1, Gd has the highest de Gennes factor, thus, compounds containing Gd can be expected to have the highest ordering temperature in the series. It should be mentioned that deviations from this scaling may occur when a strong CEF splitting constrains the moments to be either along an axis or within a plane.

2.3.5 Pauli paramagnetism and Landau diamagnetism

The previous discussions of magnetism were developed to explain the magnetic properties of spatially localized moments. They are appropriate to understand the magnetism of the insulators and semiconductors associated with $4f$ electrons. However, they do not bear on the problem of the contribution of conduction electrons to the magnetic properties of metallic compounds. The $3d$ electrons in the transition metals often become part of the conduction band, propagating in the materials, thus, their magnetic moments can be remarkably different from those carried by the isolated atoms with partially filled shells.

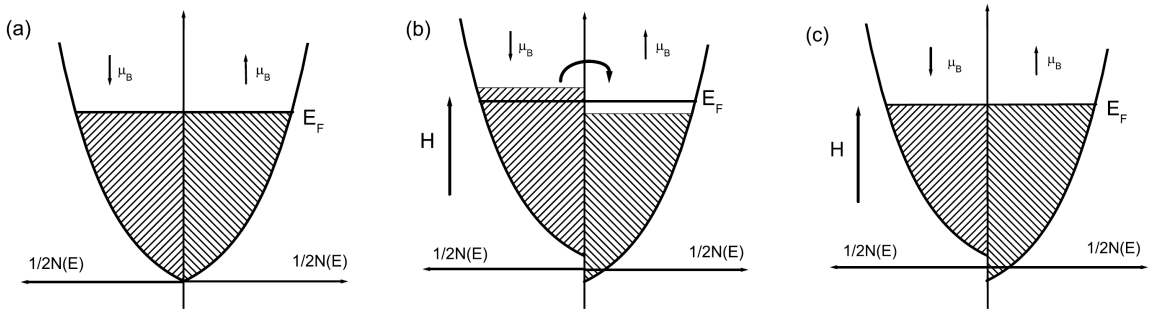

Figure 2.7 Diagram of Pauli paramagnetism. (a) No field applied; (b) Non-equilibrium state in an applied field **H**; (c) Equilibrium state in **H**.

Within the independent electron approximation, the conduction electron system can be viewed as a Fermi sea, which follows the Fermi-Dirac distribution $f(\varepsilon) = \frac{1}{exp[(\varepsilon-\mu)/k_B T]+1}$ (μ is the chemical potential), and obeys the Pauli exclusion principle. If the orbital response can be neglected, the magnetic contribution from the conduction electrons can be

considered as only coming from the spins. We can define n_+ as the number of conduction electrons with spin moment parallel to the applied field **H**, and n_- as the number of conduction electrons with spin moment antiparallel to the applied field **H**. Then the total magnetic moment of the system is:

$$M = \mu_B(n_+ - n_-),$$

here we take $g_0 = 2$. At $T = 0$, without applied field, n_+ should equal to n_-, as shown in Fig. 2.7 (a). The total density of states ($D(\varepsilon)$) is equally distributed into spin up and spin down parts, i.e., $D_+ = D_- = \frac{1}{2}D(\varepsilon)$. Hence, the total magnetization is zero. For $H \neq 0$, if the electrons interact with field only through their magnetic moments, then the only effect of the field is to shift the energy of each electronic level by $\pm\mu_B H$, according to whether the spin moment is parallel (+) or antiparalle (−) to H. Thus, the density of state in the presence of H can be modified as:

$$D_+(\varepsilon) = \frac{1}{2}D(\varepsilon - \mu_B H),$$

and

$$D_-(\varepsilon) = \frac{1}{2}D(\varepsilon + \mu_B H).$$

The number of electrons of each spin moment species is given by:

$$n_\pm = \int d\varepsilon D_\pm(\varepsilon) f(\varepsilon).$$

The electrons with higher energy (+) will flow to the lower energy state (−) (Fig. 2.7 (b)), and reach the equilibrium state (Fig. 2.7 (c)). Most conduction electrons in a metal have no possibility of flipping with the applied field, because most orbitals in the Fermi sea with parallel moments are already occupied. Only the electrons within a range $k_B T$ of the the top of the Fermi distribution have a chance to turn over in the field. Since $\mu_B H$ is only of order 10^{-4} E_F at 10^4 Oe, and E_F is about $10^{-4} k_B T$, the density of state can be expanded as:

$$D_\pm(\varepsilon) = \frac{1}{2}D(\varepsilon \pm \mu_B H) = \frac{1}{2}D(\varepsilon) \pm \frac{1}{2}\mu_B H D'(\varepsilon).$$

Consequently, this gives

$$n_{\pm} = \frac{1}{2}\int_0^{E_{\mathrm{F}}} d\varepsilon D(\varepsilon) \pm \frac{1}{2}\mu_{\mathrm{B}} H D(E_{\mathrm{F}}).$$

Therefore, at zero temperature the one can get the magnetization:

$$M = \mu_{\mathrm{B}}^2 H D(E_{\mathrm{F}}) = \frac{3N\mu_{\mathrm{B}}^2}{2k_{\mathrm{B}}T_{\mathrm{F}}} H,$$

with $D(E_{\mathrm{F}}) = \frac{3N}{2k_{\mathrm{B}}T_{\mathrm{F}}}$, and $k_{\mathrm{B}}T_{\mathrm{F}} = E_{\mathrm{F}}$. Correspondingly, the magnetic susceptibility is given by:

$$\chi = \frac{3N\mu_{\mathrm{B}}^2}{2k_{\mathrm{B}}T_{\mathrm{F}}}.$$

This is called the Pauli paramagnetic susceptibility. In contrast to the paramagnetic susceptibility derived from the Curie law, it is essentially independent of temperature and proportional to the density of state at the Fermi level. The Pauli paramagnetic susceptibility can also be rewritten as:

$$\chi_{\mathrm{Pauli}} = (\frac{2.59}{r/a_0}) \times 10^{-6}.$$

As r/a_0 is of order unity, χ_{Pauli} has the minute size characteristic of Larmor diamagnetic susceptibility, which is remarkably smaller than the paramagnetic susceptibility of the magnetic ions. For $T \neq 0$, a contribution from the thermal excitation can be added:

$$\chi_{\mathrm{Pauli}} = \mu_{\mathrm{B}}^2 D(E_{\mathrm{F}})[1 - \frac{\pi^2}{12}(\frac{k_{\mathrm{B}}T}{E_{\mathrm{F}}})^2].$$

Since $k_{\mathrm{B}}T \ll E_{\mathrm{F}}$, the second term can usually be ignored. However, temperature dependence of χ_{Pauli} can be observed for the case that sharp features of density of states exists near the Fermi level E_{F}.

The above discussion on the magnetism of conduction electrons mainly focuses on the coupling of the spin moments and the magnetic field. In fact, there are also diamagnetic effects arising from the coupling of the field to the orbital motion of the electrons. The wavefunctions of the electrons can be modified by the magnetic field, which leads to a net

non-vanishing magnetization antiparallel to **H**. Landau showed that for free electrons, this diamagnetic susceptibility is:

$$\chi_{\text{Landau}} = -\frac{1}{3}\chi_{\text{Pauli}}.$$

Therefore, the total contribution of the conduction electrons to the magnetic susceptibility is a combination of the Pauli paramagnetism and Landau diamagnetism. In a real solid, the diamagnetic response for conduction electrons can be more complicated.

2.3.6 The RKKY interaction

The various types of mechanisms developed to describe the magnetic interactions between the local moments can be roughly classified into two groups, depending on whether the interaction is direct or indirect. The direct exchange interaction originates from the direct Coulomb interaction among electrons from the two ions. However, for rare earth interametallic compounds, the $4f$ electrons are very strongly bound, and the $4f$ orbitals are relatively compact. Consequently, the possibility of direct exchange interaction between the $4f$ orbitals on different sites is very small. Rather the primary interaction of the magnetic moments in metallic compounds is via the polarization of the conduction electrons, one type of the indirect exchange interaction. According to Pauli paramagnetism, the magnetic susceptibility of conduction electrons arises from the coupling of spins with the magnetic field. When a conduction electron is in the vicinity of a rare earth ion, its spin interacts with the spins of the rare ions. An electron interacting with one rare earth ion site will become polarized and in turn carry this information to other 4f sites; all in a self-consistent manner. This coupling between conduction electrons and the localized magnetic moments is generally known as the Ruderman-Kittel-Kasuya-Yoshida (RKKY) interaction [Kittel, 2005].

In this model, the exchange interaction energy between a conduction electron with

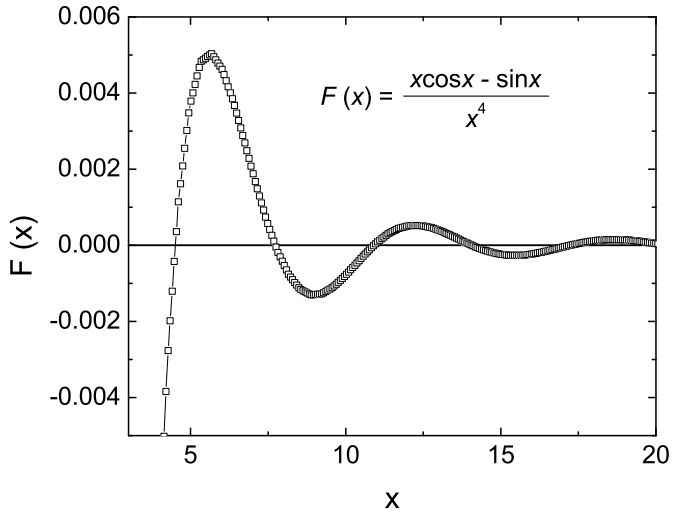

Figure 2.8 The polarization of the conduction electrons via the RKKY interaction (where $x = 2k_{\mathrm{F}}|\mathbf{R}_I - \mathbf{R}_J|$.

spin $\boldsymbol{s}$ and a local moments with spin $\boldsymbol{S}$ is:

$$\triangle E = 2J_{sf}\mathbf{s}\cdot\mathbf{S},$$

where J_{sf} is the exchange parameter, which depends on the positions of the magnetic moments $\mathbf{R}_I$ and $\mathbf{R}_J$. The magnitude of J_{sf} is between 10^{-1} and 10^{-2} eV. Assuming a free electron like dispersion of the conduction electrons, one can get the following relation:

$$J_{sf}(\mathbf{R}_I - \mathbf{R}_J) \sim F(2k_{\mathrm{F}}|\mathbf{R}_I - \mathbf{R}_J|),$$

where k_{F} is the Fermi wavevector, and $F(x)$ is given by:

$$F(x) = \frac{x\cos x - \sin x}{x^4}.$$

As J_{sf} oscillates from positive to negative, as the distance between the two local moments changes, the interaction varies from ferromagnetic to antiferromagnetic accordingly [Elliott, 1972] (see in Fig. 2.8). The total exchange energy of the RKKY interaction is given by:

$$E = \frac{9\pi n^2\Gamma^2}{2E_{\mathrm{F}}}\sum_{I\neq J}\mathbf{S}_I\cdot\mathbf{S}_J F(2k_{\mathrm{F}}|\mathbf{R}_I - \mathbf{R}_J|),$$

where n is the average density of conduction electrons, Γ represents the interaction coefficient and E_{F} is the Fermi energy. Again, this damped oscillatory behavior of the exchange energy with respect to the values of $2k_{\mathrm{F}}|\mathbf{R}_I - \mathbf{R}_J|$, indicates that the magnetic ordering can be ferromagnetic or antiferromagnetic, and the ordering temperature also can increase or decrease with changing $R - R$ spacing.

2.3.7 Stoner theory

The discussion on the Pauli paramagnetism (section 2.3.5) did not take into account the Coulomb repulsion and exchange interactions between electrons. For the transition metals with their relatively large exchange interaction, the band can spontaneously split for spin-up and spin-down electrons, which can lead to ferromagnetic ordering. Although it is very complicated to solve the problem of electrons moving in the potential created by all the other electrons, the Stoner theory was developed to explain this band ferromagnetism by proposing an exchange energy I between the d-band electrons which is independent with their wave vectors. Based on the Pauli exclusion principle, the overall wavefunctions of all the electrons must be antisymmetric. Consequently, two electrons with the same spin can never be in the same place at the same time, whereas two electrons with opposite spins can. Therefore, the electrons with opposite spins can be spatially closer to each other, and hence on average will have a larger exchange energy I than two electrons with the same spin. The total exchange energy of the system with N electrons and magnetization M is given by

$$E_{\mathrm{ex}} = IN_{\uparrow}N_{\downarrow} = \frac{1}{4}IN^2 - \frac{1}{4}IM^2,$$

$$N = N_{\uparrow} + N_{\downarrow}, M = (N_{\uparrow} - N_{\downarrow})\mu_{\mathrm{B}},$$

where $N_{\uparrow}$ is the number of electrons with up-spins, and $N_{\downarrow}$ is the number of electrons with down-spins.

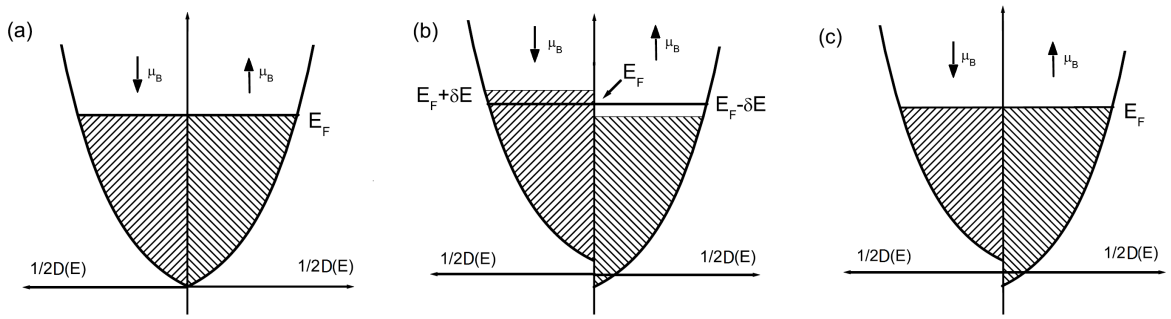

Figure 2.9 Diagram of Stoner theory. (a) Spin-up spin-down balance state with an exchange interaction; (b) Non-equilibrium state; (c) Ferromagnetic equilibrium state.

As shown in Fig. 2.9 (a), with the same number of spin-up and spin-down electrons, the total magnetization M is zero, the total exchange energy has the maximum value $\frac{1}{4}IN^2$. However, the interaction often can cause instability of the Fermi surface (Fig. 2.9 (b)), In this case, energy is minimized when electrons are transferred from one spin state to the other. If a slice of thickness δE, i.e. the amount of $D(E_{\rm F})\delta E$ electrons are transferred, the kinetic energy of the electrons will increase by:

$$\triangle E_{\rm k} = \frac{1}{2}D(E_{\rm F})(\delta E)^2,$$

and the total exchange energy will decrease by:

$$\triangle E_{\rm ex} = \frac{1}{4}IM^2 = \frac{1}{4}ID^2(E_{\rm F})(\delta E)^2.$$

Accordingly, the total energy difference will be:

$$\triangle E = \triangle E_{\rm k} - \triangle E_{\rm ex} = \frac{1}{2}D(E_{\rm F})[1 - \frac{ID(E_{\rm F})}{2}](\delta E)^2.$$

As the spin-down electrons within the range of δE of the Fermi level are moved to the spin-up band, the energy difference is proportional to $(\delta E)^2$.

When $\frac{ID(E_{\rm F})}{2} > 1$, the so-called Stoner's criterion, $\triangle E < 0$. This is the criterion for instability with respect to ferromagnetism; if $\frac{ID(E_{\rm F})}{2} > 1$, then the system will exhibit spontaneous magnetization, i.e. order ferromagnetically (Fig. 2.9 (c)). The saturated

moment of the system in a ferromagnetic ground state may assume non-integral values, corresponding to the band filling. The exchange energy I in this model is very difficult to evaluate, and in practice it is adjusted to fit experiment data.

When $\frac{ID(E_{\mathrm{F}})}{2} < 1$, $\triangle E > 0$, the non-magnetic state is stable, and the system will manifest paramagnetic behavior. With the applied field H, the change of the energy will be:

$$2\delta E = IN_{\uparrow} + \mu_{\mathrm{B}}H - (IN_{\downarrow} - \mu_{\mathrm{B}}H) = I(N_{\uparrow} - N_{\downarrow}) + 2\mu_{\mathrm{B}}H = ID(E_{\mathrm{F}})\delta E\mu_{\mathrm{B}}H.$$

One can obtain the susceptibility as the following:

$$\chi = \mu_{\mathrm{B}}^2 \frac{D(E_{\mathrm{F}})}{1 - \frac{ID(E_{\mathrm{F}})}{2}}.$$

Therefore, the Pauli paramagnetic susceptibility is enhanced by the factor $\frac{1}{1-\frac{ID(E_{\mathrm{F}})}{2}}$. And the factor :

$$Z = \frac{ID(E_{\mathrm{F}})}{2}.$$

is known as the Stoner enhancement factor. By adjusting Z, the magnetism can be tuned systematically, as in the case of $Y(Fe_xCo_{1-x})_2Zn_{20}$ and $Gd(Fe_xCo_{1-x})_2Zn_{20}$ [Jia et al., 2007]. The increase of Fe-concentration leads to the increases of Z value, which consequently gives rise to a monotonic increase of the enhanced magnetic susceptibility of the Y-based series and the magnetic ordering temperature and the saturated magnetization of the Gd-based series.

The Stoner theory successfully explains the observed, non-integral, saturated moments for $3d$ transition metal elements (Fe, Co and Ni). Interesting magnetic behavior may be observed for systems (Pd and Pt) close to the Stoner criterion, where $Z \lesssim 1$). The Stoner theory is useful for describing the ground state of correlated, itinerant electrons systems. However this theory is not able to explain the observed magnetic behavior of these itinerant electron systems at finite temperature, specifically for $T > T_{\mathrm{C}}$.

2.3.8 Arrott Plot

By definition, a ferromagnetic material possesses spontaneous magnetization within a single domain below its Curie temperature T_{C}. The magnetic susceptibility is given by $\chi = \frac{M}{H_i} = \frac{M}{H_0 - 4\pi DM}$, and should go to infinity for $T \leqslant T_{\mathrm{C}}$; here H_i is the internal field in the sample, H_0 is the intensity of the applied field, and D is the demagnetization factor. However, the determination of the Curie temperature via observing spontaneous magnetization in $M(H)$ measurements or tracking the divergent point of $\chi(T)$ experimentally is not without ambiguity. First, the true Curie temperature is found only in the limit of $H_0 = 0$, whereas H_0 is always finite experimentally, resulting a higher transition temperature than the true T_{C}. Secondly, the presence of ferromagnetic impurities with a higher T_{C} or inhomogeneities in the case of alloys and compounds can also set obstacles for approaching the $H_0 = 0$ limit. To tackle these problems, a method was proposed to determine the onset temperature of ferromagnetism, T_{C}, by analysis of the isothermal magnetization data, which is the so-called Arrott plot [Arrott, 1957].

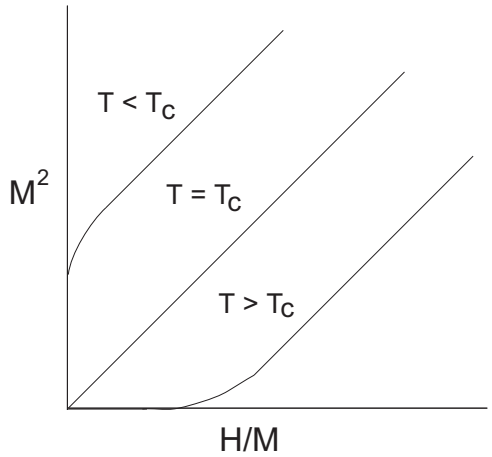

Figure 2.10 Schematic diagram of the Arrott plot in the vicinity of T_{C}.

For simplicity, we first examine a local moment with spin 1/2 system. In the paramagnetic state, according to the Weiss's molecular field theory, the magnetization is given

by:

$$M = M_0 \tanh(\frac{M_0(H+\alpha M)}{N_A k_B T}),$$

where $M_0 = N_A g_J \mu_B J$ is the spontaneous magnetization at zero temperature. This equation can be rewritten as:

$$\frac{M_0(H+\alpha M)}{N_A k_B T} = \tanh^{-1}(\frac{M}{M_0}).$$

The right-hand side can be expanded in a power series for values of $M \ll M_0$, giving:

$$\frac{M_0(H+\alpha M)}{N_A k_B T} = \frac{M}{M_0} + \frac{1}{3}(\frac{M}{M_0})^3 + \frac{1}{5}(\frac{M}{M_0})^5 + ...,$$

for which the inverse susceptibility, $1/\chi$, in the limit of zero field is given by: $1/\chi = \frac{N_A k_B T}{M_0^2} - \alpha$. As $1/\chi = 0$ at the Curie point, we can have $T_C = \frac{\alpha M_0^2}{N_A k_B}$. Hence at $T = T_C$,

$$\frac{M_0 H}{N_A k_B T_C} = \frac{1}{3}(\frac{M}{M_0})^3 + \frac{1}{5}(\frac{M}{M_0})^5 + ...$$

This equation shows the cubic relation between the field and magnetization where the condition $M \ll M_0$ is satisfied. Accordingly, this relation can be rewritten as: $H/M \propto M^2$ at T_C. Figure 2.10 shows a schematic diagram of the isothermal magnetization in the vicinity of T_C for the data plotted as M^2 versus H/M. Thus, the ferromagnetic ordering temperature T_C can be inferred from the magnetization data by noting the temperature at which the low-field data pass though the origin.

In fact, the above relation is not only valid for a local moment system. Based on the Landau theory of second order phase transitions, as long as the magnetization reverses without change in magnitude when the effective field H_{eff} is reversed, the magnetization is an odd function of H_{eff} and vice versa. Hence, for small values of M, we can have the following expansion:

$$H_{\text{eff}} = 1/\chi + \beta(\frac{M}{M_0})^3 + \gamma(\frac{M}{M_0})^5 + ...$$

Again, at T_C, $1/\chi = 0$, and the relation $H/M \propto M^2$ is valid for small values of M in both local and itinerant magnetic systems. In addition, the coefficient of the M^3 term β can

also give information as to what models of magnetization are most suitable for describing the results. It should be noted that deviations from linearity in the $M^2(H/M)$ data are often observed experimentally. The curvatures in the Arrott plot may be associated with the CEF effect, domain wall pinning, the coupling of magnetic impurity clusters with the homogeneous maxtrix or other complex magnetic phenomena which can not be simply defined as Landau type second order phase transition. Nevertheless, the isothermal magnetization data crossing the origin is a criteria of the FM ordering based on the mean field theory.

2.4 The de Haas-van Alphen effect

The de Hass-van Alphen (dHvA) effect is the oscillation of the magnetic moment of a metal as a function of the static magnetic field intensity. The effect can only be observed in high purity samples at low temperatures and high fields. The observation of this phenomena is one of the powerful experimental methods that has been developed for the determination of Fermi surface dimensions

Onsager and Lifshiz made a semiclassical approach in explaining the quantum oscillation phenomena. It is assumed the orbits of a electron in the magnetic field are quantized by the Bohr-Sommerfeld relation [Kittel, 2005]

$$\oint \mathbf{p} \cdot d\mathbf{r} = (n + \gamma)2\pi\hbar,$$

here $\mathbf{p}$ is the momentum of the particle; n is an integer; and γ is a phase correction that for free electrons has value 1/2. As the momentum of an electron in the magnetic field can be expressed as:

$$\mathbf{p} = \hbar\mathbf{k} + e\mathbf{A}/c,$$

here $\mathbf{A}$ is the vector potential, the above momentum path integral can be rewritten as

$$\oint \mathbf{p} \cdot d\mathbf{r} = \oint \hbar\mathbf{k} \cdot d\mathbf{r} + \oint e\mathbf{A}/c \cdot d\mathbf{r} = (n + \gamma)2\pi\hbar = -\frac{e}{c}\Phi,$$

where Φ is the magnetic flux contained within the orbit in real space. Based on the above relation, one can find the orbit of an electron is quantized, and the magnetic flux can be written as:

$$\Phi_n = (n + \gamma)2\pi\hbar c/e.$$

The flux unit $2\pi\hbar c/e = 4.14 \times 10^{-7}$ G cm^2. By converting the orbit into wavevector space, one can obtain the famous Onsager relation [Onsager, 1952]

$$\triangle(\frac{1}{H}) = \frac{2\pi\hbar e}{c}\frac{1}{A_e(E_{\rm F})},$$

where A_e is any extremal cross-sectional area of the Fermi surface in a plane normal to the magnetic field. From measurements of $1/H$, we can deduce the corresponding extremal cross-sectional areas. This periodicity in $1/H$ gives rise to striking oscillatory effects, as what can be observed in the dHvA effect. The population of orbits on or near the Fermi surface oscillates as **H** is varies, therefore, via the observation of the oscillatory effects, one can reconstruct the Fermi surface.

As the temperature increases, the addition of extra scattering can attenuate the dHvA feature, by causing the electrons to be scattered out of their orbits. As a consequence, the Fermi surface is smeared. The Lifshitz-Kosevich (LK) equation has been developed to tackle the effects of finite temperature and impurity scattering on the dHvA effect [Shoenberg, 1984]:

$$M = -2.602 \times 10^{-6}(\frac{2\pi}{HA''})^{1/2} \times \frac{GFT\exp(-\alpha px/H)}{p^{3/2}\sinh(-\alpha pT/H)} \times \sin[(\frac{2\pi pF}{H}) - 1/2 \pm \frac{\pi}{4}]$$

where $\alpha = 1.47(m/m_0)\times 10^5$ G/K, A'' is the second derivative of the cross sectional area of the Fermi surface with respect to wave vector along the direction of the applied field, G is the reduction factor arising from electron spin, ρ is the number of harmonic of the oscillation, and x is the Dingle temperature which is used to characterize the effect of the smearing of Fermi surface due to the increase of temperature. From the slope of $\ln(A/T)$ plotted as a function of temperature, the effective masses can be calculated.

2.5 Spin Glass

2.5.1 Definition

A spin glass can be defined as "a random, mixed-interacting, magnetic system characterized by a random, yet co-operative, freezing of spins at a well-defined temperature T_f below which a highly irreversible, metastable frozen state occurs without the usual long-range spatial magnetic order" [Mydosh, 1993]. There are three important factors of a spin glass system: randomness, mixed interactions and frustration. Randomness can be either site randomness with a distribution of distances between the magnetic spins, or bond randomness where the signs of the neighbouring couplings vary between ferro and antiferromagnetic interactions. Randomness is needed to create disorder, and without disorder, the magnetic ordering will lead to the standard ferromagnetic, ferrimagnetic or antiferromagnetic type of long range order rather than spin glass. For a crystalline system, site randomness can be introduced by substituting local moment bearing impurities onto the sites of a non-magnetic host. For example, substitution of Tb for Y in $(Y_{1-x}Tb_x)Ni_2Ge_2$ gives rise to spin glass states for $x < 0.30$ [Wiener et al., 2000]. The mixed interactions are needed to give rise to the competition between ferro and antiferromagnetic interactions. Frustration is the consequence of the disorder and mixed interactions, which creates a multdegenerate, metastable and frozen ground state for the spin glass.

It is clear that the concentration of the magnetic moments is of great importance in determining the magnetic state. As seen in Fig. 2.11, the schematic graph presents the various concentration regimes for a canonical spin glass, which shows the different types of magnetic behavior that exist as the concentration changes. At the very dilute magnetic concentration (ppm), the magnetic impurities are isolated, and only couple with the conduction electrons, which for hybridizing moments, can result in the Kondo effect. Below the Kondo temperature, the moment disappears and the impurity appears

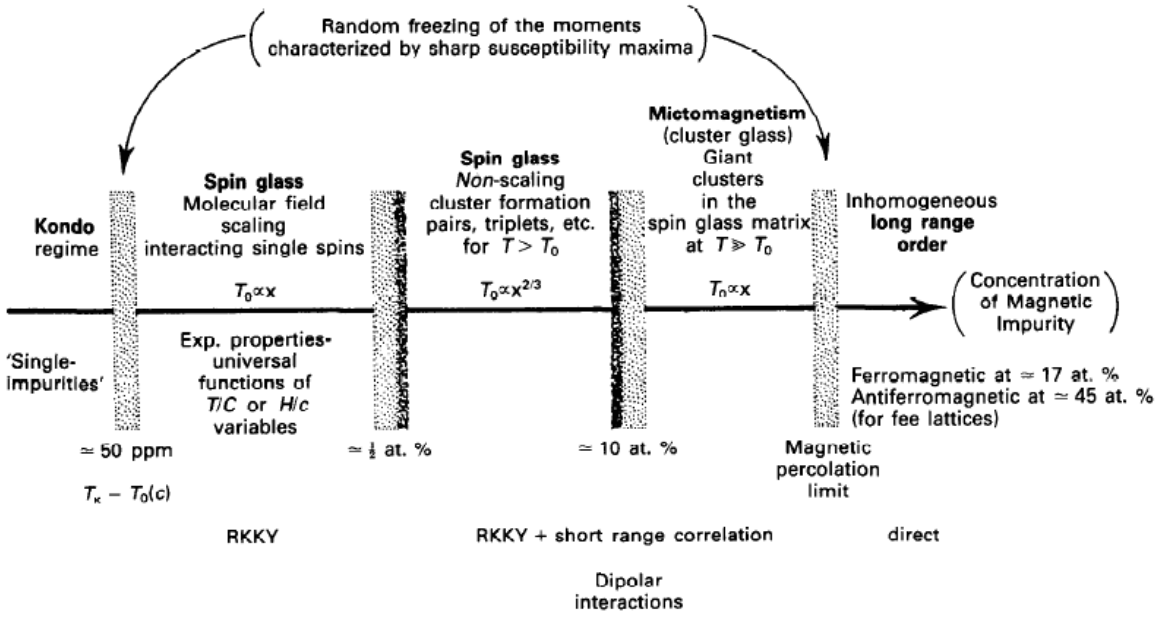

Figure 2.11 Various concentration regimes for a canonical spin glass illustrating the different types of magnetic behavior that exist. [Mydosh, 1993]

non-magnetic. Thus, for hybridizing impurities, the Kondo effect can prevent the formation of spin glass (It should be noted, though, that for local moment impurities such as Gd, this hypothetical Kondo temperature is probably indistinguishable from absolute zero). As the concentration increases up to a few thousand ppm ($\simeq 0.5$ at. %), the system enters a new magnetic state, where the magnetic spins start interacting with each other without any clustering. At this stage, the measurable properties (magnetization, susceptibility, specific heat, and remanences) are universal functions of the concentration scaled parameters T/x and $H_{\rm ext}/x$, and in addition $T_{\rm f} \propto x$. With more and more magnetic impurities, clusters of pairs and triplets (and higher) of spins are formed and begin to influence the system. Around 1/2 at % , theses scaling laws can break down; a non-scaling spin-glass regime occurs with $T_{\rm f} \propto x^{2/3}$. As the concentration reaches 10 – 15 at. %, the magnetic state is dominated by these clusters, and is called mictomagnetism. Finally, the percolation limit is reached, and system can form long-range ferro-

or antiferromagnetic order with a well-defined $T_{\rm C}$ or $T_{\rm N}$. The term "spin glass" can cover the low-temperature state of the system from the dilute limit almost up to the percolation limit for long-range order. It also should be noted that the transformation from one regime to the next is gradual and smooth, without a sharp separation, i.e, critical concentration.

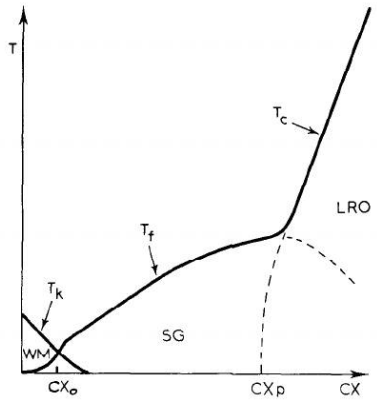

Figure 2.12 Generic $T-x$ phase diagram for a dilute magnetic alloy. [Mydosh, 1993].

A generic $T-x$ phase diagram (ordering temperature versus the concentration of the magnetic impurities) is presented in Fig. 2.12. $T_{\rm k}$ is the 'average' Kondo temperature, and decreases as the concentration x increases. For $T_{\rm k} > T_{\rm f}$, it is called the weak moment concentration regime. For $x > x_0$, the spin-glass regime appears with first linear, followed by a less than linear $T_{\rm f}$ dependence on x. As x is higher than $x_{\rm p}$, the percolation limit is reached, and the system forms long-range magnetic ordering. The transition temperature $T_{\rm C}$ or $T_{\rm N}$ increases as the concentration increases. Therefore, the magnetic state can be tuned systematically via controlling the concentration of the magnetic impurities x. As in the case of the $Y_xTb_{1-x}Ni_2Ge_2$ compounds [Wiener et al., 2000], four regions of magnetic states evolute successively as the Y-concentration increases. For $x < 0.375$, the system has no long-range antiferromagnetic order and possess a magnetic spin-glass state. In the region of $0.375 < x < 0.45$, the antiferromagnetic transition and the irreversibility temperature coincide. As x increase to the 0.45 – 0.75 region, both

antiferromagnetic transition and irreversibility in $\chi(T)$ can be observed, but not at the same temperature. Finally, as x is above 0.75, two antiferromagnetic transitions exist, along with an irreversibility temperature.

2.5.2 DC magnetic properties

Given the combination of the randomness, the competing interactions, and the multidegenerate and metastable ground state, a spin glass system exhibits many interesting properties related to its co-operative but frustrated nature. In the following, we will examine the DC magnetic properties of a spin glass system.

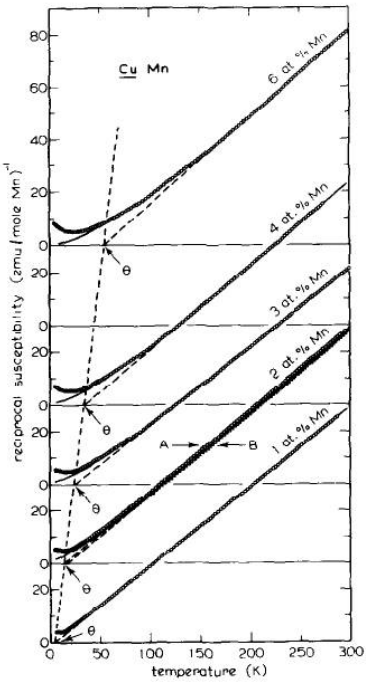

Figure 2.13 The reciprocal susceptibility as a function of temperature of CuMn: the dashed lines are a linear extrapolation to determine θ and the solid line represents the fit to the model calculations [Mydosh, 1993].

At high temperatures, the magnetic moments can be viewed as isolated moments, showing standard paramagnetic behavior. In the paramagnetic state, the temperature dependence of the magnetic susceptibility ($\chi = M/H$) should follow the Curie-Weiss law. Figure 2.13 shows $1/\chi$ as a function of temperature of dilute Mn in a Cu host

(CuMn) as an example. As temperature decreases, χ starts to deviate from the linear behavior, indicating that the ferromagnetic clusters are beginning to develop out of the paramagnetic background. The spin glass state can be considered as being built from these clusters and short range correlations with in the random system. The starting point of deviation moves to higher temperature as the concentration of Mn increases. Given that the Curie-Weiss temperature represents a sum of all exchange interactions in the paramagnetic state, the enhancement of the ferromagnetic interactions by Mn substitution is also manifested by the increasing θ, as shown in Fig. 2.14. On the other hand, the effective Bohr magneton number p_0 stays relatively the same with various concentrations, probably indicating a degree of local ferromagentism.

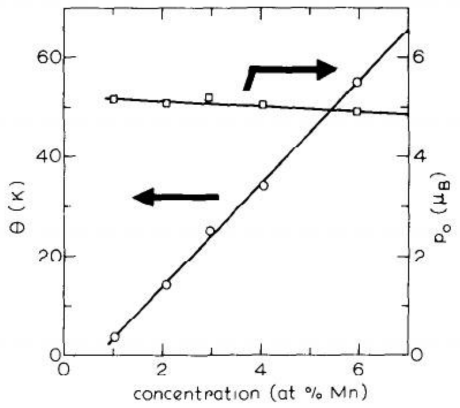

Figure 2.14 Effective Bohr-magneton number p_0 and the Curie-Weiss temperature θ as a function of concentration in CuMn: p_0 and θ are determined from least-squares fitting of the susceptibility at high temperatures [Mydosh, 1993].

Characteristic features of a spin glass transition can also be observed in the zero-field cooled (ZFC) and small field cooled (FC) dc magnetization measured at temperatures spanning T_f. As shown in Fig. 2.15, the magnetization of two concentrations of CuMn were measured in an applied field of 6 Oe. Below T_f, the FC data ((a) and (c)) show a tendency to saturation, and are fully reversible as temperature varies, whereas the ZFC magnetization ((b) and (d)) decreases upon cooling, and is highly sensitive to the rate

of temperature increase, dT/dt [Mydosh, 1993]. The temperature at which the FC and ZFC magnetization data deviate from each other is used as the determination of the freezing temperature $T_{\rm f}$. And it is clearly shown that the $T_{\rm f}$ increases as Mn concentration increases, again implying strong interactions with more magnetic impurities. The magnetization irreversibility at $T_{\rm f}$ and its field-history dependence clearly demonstrates the existence of a multidegenerate groundstate in the spin glass system. In Fig. 2.16, the dc susceptibility is shown for $Y_xTb_{1-x}Ni_2Ge_2$ with (a) $x = 0.25$ and (b) $x = 0.30$ in an applied field of 50 Oe for both ZFC and FC histories for $\mathbf{H} \parallel c$ [Wiener et al., 2000]. As is shown, the ZFC and FC susceptibility data deviate from each other at the low temperatures. Below $T_{\rm f}$, the ZFC susceptibility decreases with temperature whereas the FC susceptibility is nearly temperature independent — a clear manifestation of spin glass state. The freezing temperature $T_{\rm f}$ is defined as the peak in the ZFC magnetization data, and it increases as x increases: for $x = 0.25$, $T_{\rm f} = 2.5 \pm 0.1$ K and for $x = 0.30$, $T_{\rm f} = 3.0 \pm 0.1$ K.

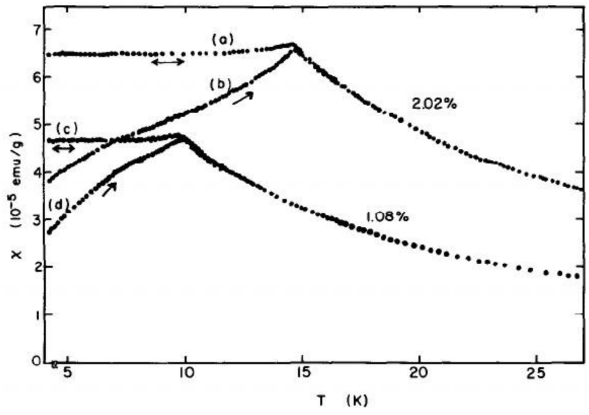

Figure 2.15 Field cooled ((a) and (c)) and zero-field cooled ((b) and (d)) magnetizations ($\chi \equiv M/6$ Oe) for CuMn (1 and 2 at. % as a function of temperature [Mydosh, 1993].

A generic sketch on the ZFC magnetization isotherms of a spin glass at $T \ll T_{\rm f}$ is presented in Fig. 2.17. The small initial slope near the origin is claimed to be comparable with the ac-susceptibility. The virgin $M(H)$ curve shows a S-shaped form, and hysteresis

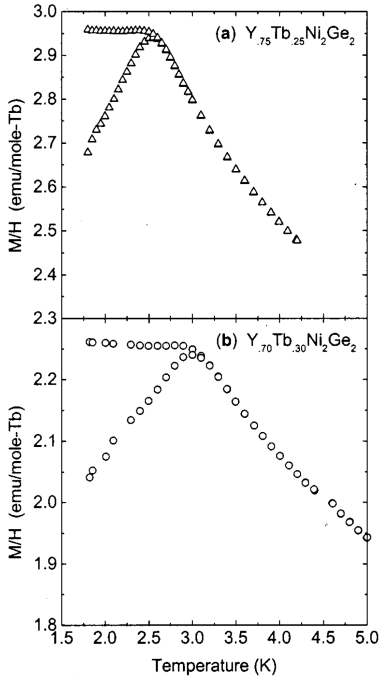

Figure 2.16 The low-temperature dc susceptibility of $Y_xTb_{1-x}Ni_2Ge_2$ with (a) $x = 0.25$ and (b) $x = 0.30$ in an applied field of 50 Oe for both zero-field-cooled (ZFC) and field-cooled (FC) histories for $\mathbf{H} \parallel c$ [Wiener et al., 2000].

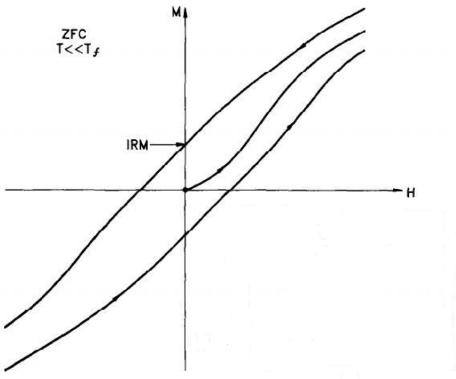

Figure 2.17 Schematic of zero-field cooled hysteresis loop for $T \ll T_{\rm f}$ illustrating the S-shape, the lack of saturation, and the isothermal remanent magnetization (IRM) [Mydosh, 1993].

with the isothermal remanent magnetization (IRM) can be observed for both increasing and decreasing field. The magnetization exhibits a tendency towards saturation as the magnetic field increases. However, a full saturation $M_{\rm sat} = g\mu_{\rm B}S$ can be hardly attained for a spin glass system even at the lowest temperatures and concentrations. As $T \ll T_{\rm f}$, the moments 'freeze', and the external fields are required to rotate and re-orient the spins.

2.6 Quantum phase transition

A phase transition occurs when the equilibrium state of a system changes qualitatively, and the thermodynamic system transforms from one phase or state of matter to another. A phase transition can be driven by many parameters – temperature, pressure, chemical composition, magnetic or electric field etc. Based on Paul Ehrenfest, a phase transition can be classified based on the behavior of the thermodynamic free energy as a function of other thermodynamic variables. The lowest derivative of the free energy that is discontinuous at the transition is used to identify the order of the phase transition.

A first-order phase transition exhibits a discontinuity in the first derivative of the free energy with respect to some thermodynamic variable. The most common example of this type of transition is boiling or freezing water. In this case, the phase transition is accompanied by absorbing or releasing heat (latent heat), whereas the temperature of the system will stay constant. All the other thermodynamic quantities (internal energy, entropy, enthalpy, volume etc.) are discontinuous as well.

On the other hand, a second-order phase transition is continuous in the first derivative whereas exhibiting discontinuity in a second derivative of the free energy. In particular, the specific heat has a pronounced anomaly at the transition, such as superconducting transition. The system having a second order phase transition should be either one state or the other, i.e. the two states can not coexist in the same system with the same

transition parameter. Landau gave a phenomenological theory of second order phase transitions. An order parameter is introduced and the thermodynamic energy can be expanded in power series in terms of this order parameter. The order parameter is a function of temperature, defined as zero in the higher symmetry phase, and non-zero in the lower symmetry ordered phase. A ferromagnetic transition can be a good example, and the spontaneous magnetization can be identified as the order parameter, which vanishes for temperatures above T_{C}.

In a classical system, as the temperature approaches zero, the thermal fluctuations will die out, and the system will be in its ground state. On the other hand, in a quantum system, quantum fluctuations due to the Heisenberg uncertainty principle will always be present, even at $T = 0$. Therefore, as the system gets close to zero temperature, quantum fluctuations will dominate the system's behavior, and possibly drive changes in the ground state. A quantum phase transition (QPT) occurs at $T = 0$, when a non-thermal parameter such as pressure, chemical composition, magnetic or electric field drives the system through a phase change from one state to another state. For a system having a second order QPT, its Hamiltonian $H(g)$ considered as a function of a dimensionless coupling g [Sachdev, 2001]. At a critical g_c, there can be a level-crossing where an excited level becomes the ground state, creating a point of non-analyticity of the ground state energy. These non-analytical points in the ground state energy ($g = g_c$) are defined as the quantum critical points (QCP). Although the definition of a QPT is strictly valid only for $T = 0$, the system's behavior can still be determined by the QCP, as long as the temperature is sufficiently close zero.

In the vicinity of a QCP, non-Fermi-liquid (nFL) behaviors can often be observed, and the scaling analysis was developed as a theoretical model to describe these unusual low-temperature phenomena. The scaling analysis is said to be an extension of the scaling formalism in the Landau model, which describes critical behavior near a second order phase transition at T_c [Stewart, 2001]. In the scaling analysis, at the QCP, the correlation

Table 2.2 Critical exponents for magnetically ordered systems. The order parameter as stated before is the magnetization, m, with the magnetic field H as the conjugate field. t is the proximity to the quantum critical point and d is the spatial dimensionality of the system [Vojta, 2003].

	Exponent	Definition	Conditions
Specific heat	α	$C \propto \lvert t\rvert^{-\alpha}$	$t \to 0, H = 0$
Order parameter	β	$m \propto (-t)^{-\beta}$	$t \to 0$ from below, $H = 0$
Susceptibility	γ	$\chi \propto \lvert t\rvert^{-\gamma}$	$t \to 0, H = 0$
Critical isotherm	δ	$H \propto \lvert m\rvert^{\delta}\mathrm{sign}(m)$	$B \to, t = 0$
Correlation length	ν	$\xi \propto \lvert t\rvert^{-\nu}$	$t \to 0, H = 0$
Correlation function	η	$G(r) \propto \lvert r\rvert^{-d+2-\eta}$	$t = 0, H = 0$
Dynamic	z	$\tau_c \propto \xi^z$	$t \to 0, H = 0$

length, ξ, diverges as $\xi \propto t^{-\nu}$, where ν is the critical exponent, and t is a dimensionless measure of the proximity to the QCP and defined as $t = |g - g_c|/g_c$ [Sachdev, 2001; Vojta, 2003]. The correlation time (time needed for the fluctuations to decay) at the QCP is found as: $\tau_c \propto \xi^z$, here z is the dynamic critical exponent. As a consequence, many other physical properties show power law dependencies on the parameter t. The set of the corresponding exponents, α, β, γ, etc., the so-called critical exponents are summarized in Table. 2.2. These critical exponents are not independent on each other, and they are connected by scaling relations: $2 - \alpha = 2\beta + \gamma$, and $2 - \alpha = \beta(\delta + 1)$; and the hyperscaling relations: $2 - \alpha = d\nu$ as well as $\gamma = (2 - \eta)\nu$ [Vojta, 2003].

The renormalization-group theory has been used to describe the quantum critical phenomena, particularly in a ferromagnetically or antiferromagnetically ordered system [Stewart, 2001]. The results of the model proposed by Hertz and Millis (seen in Table. 2.3), depend on the dimension d, the critical exponent z, the reduced temperature t, and a control parameter g [Hertz, 1976; Millis, 1993]. For the itinerant magnetic systems, a self-consistent renormalization study of the spin fluctuation near magnetic transition was performed by Moriya and Takimoto [Moriya and Takimoto, 1995]. It is used to explain the critical behavior in itinerant magnetic systems, and the application of this model

Table 2.3 Temperature dependence of non-Fermi liquid behavior according to spin fluctuation theories by Hertz, Millis, and Moriya [Hertz, 1976; Millis, 1993; Moriya and Takimoto, 1995; Stewart, 2001].

	Hertz-Millis			
	AFM $z=2$ $d=3$	AFM $z=2$ $d=2$	FM $z=3$ $d=3$	FM $z=3$ $d=2$
C/T	$\gamma - a\sqrt{T}$	$c\log(T_0/T)$	$c\log(T_0/T)$	$T^{-1/3}$
$\Delta\chi$	$T^{3/2}$	$\chi_0 - dT$		
$\Delta\rho$	$T^{3/2}$	T	T	
$T_{N/C}$	$(g_c-g)^{2/3}$	(g_c-g)	$(g_c-g)^{3/4}$	(g_c-g)
	Moriya			
	AFM $d=3$	AFM $d=2$	FM $d=3$	FM $d=2$
C_m/T	$\gamma_0 - a\sqrt{T}$	$-\log T$	$-\log T$	$T^{-1/3}$
$\Delta\chi_Q$	$T^{-3/2}$	$-(\log T)/T$	$T^{-4/3}$	$-T^{-1}\log T$
$\Delta\rho$	$T^{3/2}$	T	$T^{5/3}$	$T^{4/3}$

in a local moment system has limited satisfactory description of the low temperature properties. It gives a more systematic treatment of couplings among different modes of spin fluctuations. The critical exponents predicted by the self-consistent renormalization model is also presented in Table. 2.3.

The itinerant ferromagnetic systems showing QPTs have attracted tremendous attention, as a QCP in itinerant electron system is believed to be associated with enigmatic quantum phases like magnetically mediated superconductivity and nFL behavior. Chemical doping (e.g. Ni_xPd_{1-x} [Stewart, 2001] and $U_xTh_{1-x}Cu_2Si_2$ [Stewart, 2001]), pressure (e.g. MnSi [Thessieu et al., 1995] and UGe_2 [Taufour et al., 2010]) are often used to tune the magnetic orderings to zero and expose the non-Fermi liquid behavior. Take CePd as an example [Stewart, 2001], it orders ferromagnetically at 6.5 K. By substituting Ni for Pd, the Curie temperature is suppressed to zero for 95% Ni substitution. C/T varies as $-\log T$ for $CePd_{0.05}Ni_{0.95}$ between 0.9 and 0.4 K. Pressure, another powerful method of driving criticality, has an advantage of introducing clean (without disorder) pertur-

bations into the system. $ZrZn_2$, for instance, is a ferromagnet below 17 K at ambient pressure. The Curie temperature can be driven to 0 K with applying pressure: $p_c \approx$ 7.5 kbars [Stewart, 2001]. At the critical pressure, nFL behavior is manifested: ρ is $\sim \rho_0 + AT^\alpha$ for 1 K $< T <$ 20 K. The critical component is temperature dependent: $\alpha \approx$ 1.6 for 10 K $< T <$ 20 K and α becomes smaller as $T <$ 10 K.

CHAPTER 3. EXPERIMENTAL METHODS

3.1 High temperature solution growth method

The growth of single crystals of interest via the high-temperature solution method depends on several important factors: solvent, initial concentrations and the temperature profile [Canfield and Fisk, 1992; Canfield, 2010]. Solvent, also called flux in the high temperature solution method, should have a relatively low melting temperature and offer good solubility for the other components in the growth. A good solvent can decrease the growth temperature, hold the volatile components to reduce the vapor pressure, and incorporate all the constituent elements to create a homogeneous solution for the synthesis. Choosing or developing a good solvent is vital for successful single crystal synthesis via high temperature solution method, and more discussion on developing solutions for sulfur-based compounds will be presented in Chapter 4 [Lin et al., 2012b].

Binary and ternary phase diagrams (if available or in existence) provide a map of the initial concentrations and temperature profile for the high temperature solution growths. For simplicity we can examine the Ba – Sn binary phase diagram shown in Fig. 3.1 as an example [Massalski, 1990]. If the compound $BaSn_5$ is to be grown, then, given that it is a peritectically melting compound, methods that use cooling of stoichiometric (or near stoichiometric) melt of $BaSn_5$ will not give single phase $BaSn_5$. With high temperature solution method, $BaSn_5$ can be readily grown in a solution rich in Sn without introducing extra phases such as $BaSn_3$. As long as the initial composition is more Sn-rich than that of the composition of the liquidius line at the peritectic temperature (indicated by the

star on diagram), then the primary solidification (on cooling) will be $BaSn_5$. The starting materials can be slowly heated up to high temperatures, for example 700 °C, and kept at 700 °C for a few hours to obtain a homogeneous solution. Then the growth can be quickly cooled to about 425 °C, during which the liquid stoichiometry does not change. Once the temperature drops below 425 °C, crystalline $BaSn_5$ starts to form and the remaining solution becomes increasingly Sn-rich. The cooling should be stopped at a temperature above the eutectic temperature so that the excess solution can be decanted off. Also since rapid cooling can cause multiple nucleation and dendritic growth, which will result in small and distorted single crystals, slow cooling should begin at a temperature clearly above the temperature at which the crystals start to nucleate. In the case of $BaSn_5$, the slow cooling begins at about 425 °C, and the material was cooled to 270 °C over a period of 40 hours, at which temperature the excess flux was decanted. Long rod-shaped $BaSn_5$ single crystals can be obtained from the growth [Lin et al., 2012c].

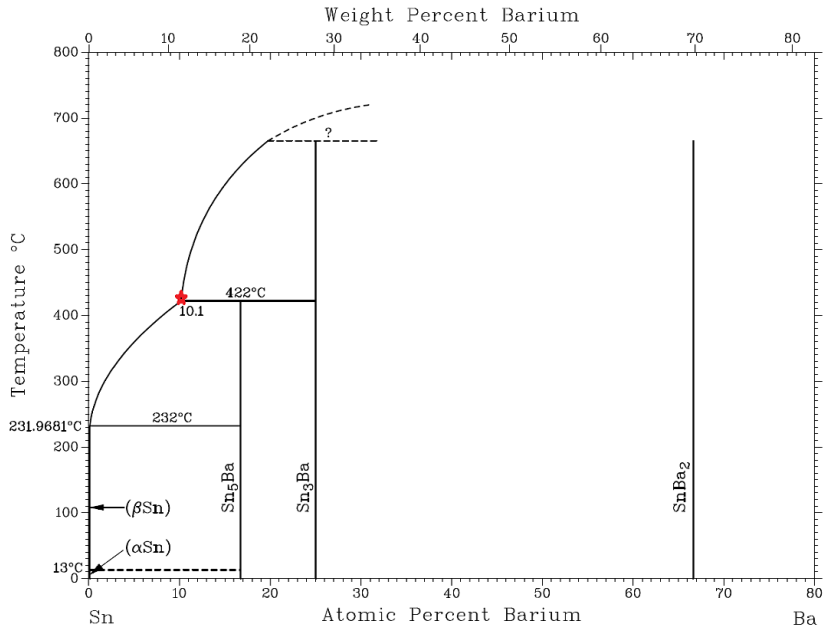

Figure 3.1 Binary phase diagram of Ba – Sn [Massalski, 1990].

In the above case, an excess of one of the constituent elements of the desired compound was used as the solvent, this is sometimes referred to as the self-flux method. However, self-flux is not always a viable choice. In many cases, the the temperature range associated with the primary solidification (between the peritectic temperature and the eutectic temperature) can be limited, either too high, too narrow or non-existent. It should be noted that the maximum temperature that can be used with growths in fused silica tubes is very close to 1200 °C (at which point the fused silica starts to soften and loose its structural integrity, and leads to collapse or explosion of the growth ampoules). In other cases, a solvent with better solubility of the volatile elements is desired to reduce the possible high vapor pressure. Therefore, an extra element (or combination of elements) is needed to act as a flux. A schematic, pseudo-binary phase diagram is presented in Fig. 3.2 [Canfield, 2010]. To grow compound AB, C is used as a third element flux. By growing AB out of C, the starting materials can be heated upto T_1, quickly cooled to certain temperature above T_2, then followed by a slow cooling to T_3, at which point the crystals AB can be separated from the remaining liquid. For example C can be Sn and AB can be CeSb as outlined in ref. [Canfield and Fisk, 1992].

Due to the lack about many information of phase diagrams, the specific nature of each compound and the experimental conditions, growing single crystals via high temperature solution method can be a process of trial and error. The growth profile can usually be modified and optimized based on the previous growths.

3.1.1 Experimental Technique for Flux Growth

Generally, the starting materials were placed inside a 2 ml or 5 ml alumina crucible, called the “growth crucible” (Fig. 3.3). Another crucible, called the ”catch crucible”, is filled with quartz wool and placed, inverted on top of the growth crucible. The crucibles were subsequently sealed in a quartz ampoule, under partial argon (high purity) pressure. The materials were heated up to the desired maximum temperature, at which

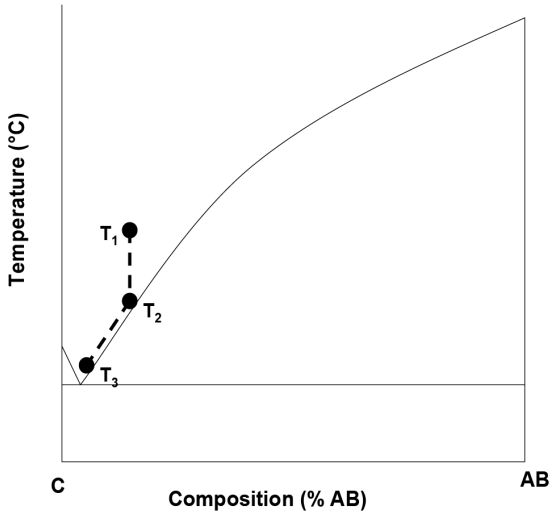

Figure 3.2 Schematic pseudo-binary phase diagram for the C – AB system. The dotted curve represents a possible cooling curve and the associated composition of the solution [Canfield, 2010].

the liquid solution homogenizes for a couple of hours. Then the ampoule is slowly cooled to the decanting temperature, at which point the flux must be removed from the growth crucible. This is done by quickly removing the ampoule from the furnace and inserting it, inverted, into a centrifuge. During the spin, the quartz wool in the catch crucible acts as a strainer which allows the excess flux to flow to the bottom where it solidifies, and holds any crystals that may have detached from the growth crucible. In the following, the experimental details of $LaCrGe_3$ are presented as examples of growing single crystalline ternary compounds by high temperature solution method.

A relatively deep eutectic point exists at 895 °C with a ratio of Cr : Ge = 15: 85 in the Cr-Ge binary (indicated by the red star) [Massalski, 1990]. $Cr_{15}Ge_{85}$ can be used as a flux, and by dissolving La in this flux, it is possible to grow La-Cr-Ge ternary compounds via high-temperature solution method. Thus, the target compound $LaCrGe_3$ (shown as a red square in Fig. 3.5) was synthesized with an initial stoichiometry of La : Cr : Ge = 13 : 13 : 74. High purity (> 3N) elements La, Cr and Ge were pre-mixed by

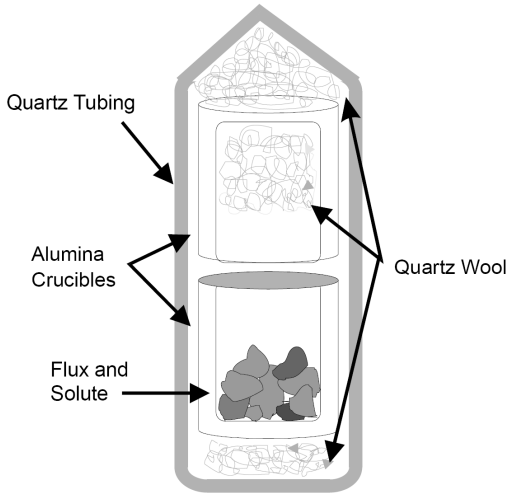

Figure 3.3 Diagram of the ampoule used for crystal growth

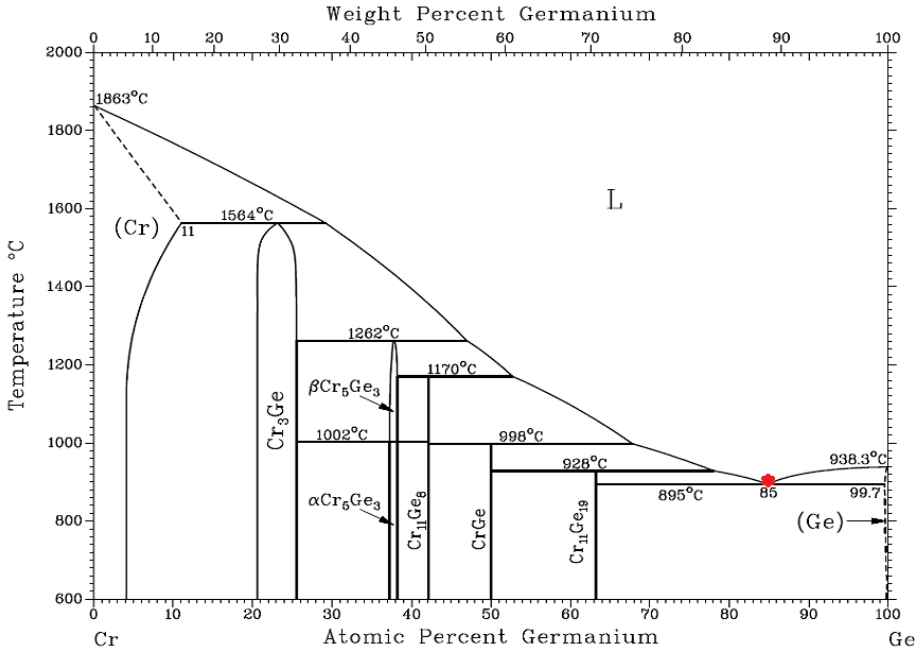

Figure 3.4 Binary phase diagram of Cr – Ge [Massalski, 1990].

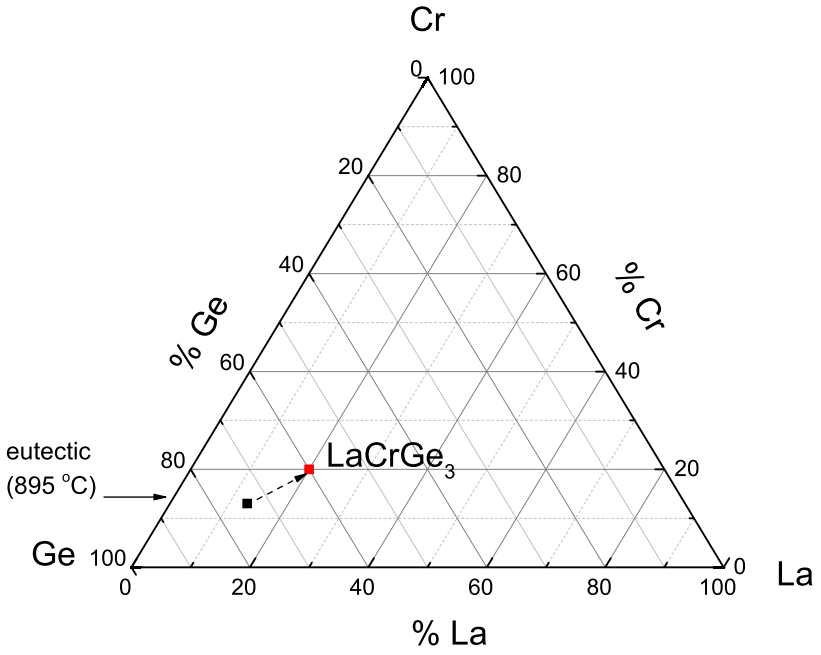

Figure 3.5 Ternary phase diagram of the La-Cr-Ge system.

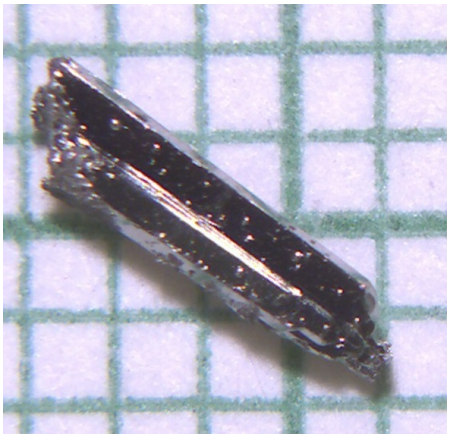

Figure 3.6 Photo of a single crystalline $LaCrGe_3$ sample on a millimeter grid.

arc-melting to ensure the homogeneity. The ingot was then loaded into a 2 ml alumina crucible and sealed in a fused silica tube under a partial pressure of high purity argon gas. The ampoule containing the growth materials was heated up to 1100 °C over 3 h and held at 1100 °C for another 3 h. The growth was then cooled to 825 °C over 65 h at which temperature the excess liquid was removed. Single crystals of $LaCrGe_3$ grew as hexagonal rods with typical size of $\sim 0.7 \times 0.7 \times 5$ mm^3 (shown in Fig. 3.6). A considerable amount of second phase material was grown as the result of secondary solidification, which was identified to be Cr-Ge binaries by powder x-ray diffraction.

3.2 Measurement Methods

3.2.1 Powder x-ray diffraction measurements

Powder x-ray diffraction data were collected on a Rigaku MiniFlex II diffractometer with Cu Kα radiation at room temperature. Samples with clean surface were selected for the measurement and ground into powder for the diffraction. In general, data collection was performed with a counting time of 2 s for every 0.02 degree. refinement of the data was conducted using the program Rietica [Howard and Hunter, 1998]. Error bars associated with the values of the lattice parameters were determined by statistical errors, and Si powder standard ($a = 5.4301$ $\mathring{A}$) was used as an internal reference. For air-sensitive samples, powder x-ray diffraction data on both non-oxidized and oxidized sample were collected. Using $BaSn_5$ as an example, the diffraction pattern of the non-oxidized $BaSn_5$ was taken from the powder of single crystals which was ground in the glovebox. The sample powder was sealed by Kapton film during the measurement to protect it from oxidization, as shown in Fig. 3.7. To study the oxidation effect, a second x-ray diffraction was performed on the same powder after removal of a Kapton film and a seven-hour exposure to the air. By comparing the diffraction patterns of both non-oxidized and oxidized samples, we found that the diffraction pattern associated with

$BaSn_5$ phase completely disappeared, whereas the diffraction peaks associate with Sn seemed unchanged. It is likely that the oxidized phase became the nanocrystalline small or too disordered to diffract (see Chapter 5 for more details).

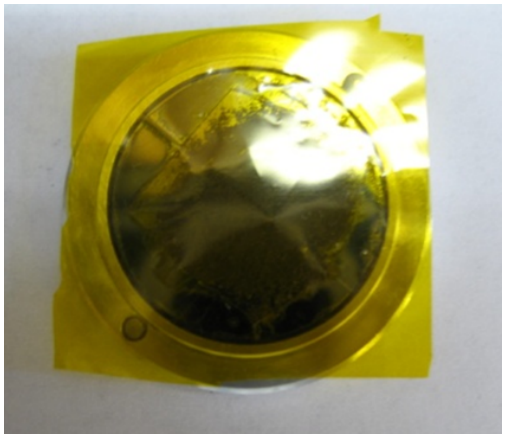

Figure 3.7 Air-sensitive sample for powder X-ray diffraction sealed by Kapton film.

3.2.2 Resistivity measurements

Measurements of the electrical resistivity were made by using a standard ac, four-probe technique. For the non-air-sensitive compounds, the samples were usually polished or cleaved into the desired bar shape. Platinum wires were attached to the bars with Epotek H20E silver epoxy, and cured at 120°C for $\sim$ 40 minutes. For the air-sensitive compounds, to avoid oxidization, samples were usually not polished. Dupont 4929 silver paint was used to attach the platinum wires, and generally $\sim$ 10 min drying in the air is enough to create the electrical and mechanical connection. For the extremely air-sensitive samples, glovebox is needed for whole process of sample preparation. Efforts were made to reduce the contact resistance. With about 100 mA current flowed though the contacts, the typical contact resistances can drop to less than 2 Ω. Temperature and field dependent resistivity was measured using a Quantum Design, Physical Property Measurement System (PPMS) and with LR700 AC resistance bridge in a Quantum

Design, Magnetic Property Measurement System (MPMS). For measurements in PPMS, the AC transport option was used with a frequency of 17 Hz and a current of 1 mA. The temperature ranges from 1.85 K to 300 K, and the applied magnetic field can be up to 50 kOe, 70 kOe, 90 kOe and 140 kOe depending on the equipment used. The absolute values of resistivity are commonly accurate to $\pm$ 20% due to the irregularity of the sample geometry and accuracy of measurements of electrical contacts' position. The residual resistivity ratio (RRR) is usually determined as ρ(300 K)/ρ(1.8 K). However, in the presence of minority phase superconductivity, such as in the case of $R\mathrm{Ni}_{1x}\mathrm{Bi}_{2\pm y}$, RRR is chosen as ρ(300 K)/ρ(5 K) so as to avoid any contamination from the minority phase superconductivity.

3.2.3 Magnetization measurements

Measurements of field and temperature dependent magnetization were performed in a Quantum Design MPMS in applied field $\leqslant$ 55 kOe or 70 kOe and in the temperature range from 1.85 K to 300 K. For the superconducting and ferromagnetic materials, to avoid the errors associated with demagnetization effects, rod-like samples were measured with the magnetic field applied along the long edge. This minimized the demagnetization factor and thereby the demagnetizing field.

3.2.4 Specific heat measurements

Temperature dependent specific heat measurements were performed in a Quantum Design PPMS using the heat capacity option. The samples were attached to the heat capacity platform with Aiezon N grease. To minimize the sample's thermal contact with the environment, the sample chamber was evacuated to $\sim$ 0.01 mTorr. A relaxation technique was used for the specific heat measurements. For the measurement cycle, a known amount of heat is applied at a constant power for a fixed time (heating process); and then the sample is cooled for the same amount of time (cooling process). After

each cycle, the heat capacity value can be obtained by fitting the entire temperature response of the sample platform to a model which includes both thermal relaxation of the sample platform to the bath temperature and the thermal relaxation between the platform and the sample itself. To subtract the contribution of the sample platform and grease from the final measurements, their thermal responses were measured separately for the appropriate temperature ranges.

3.3 Experimental techniques in collaboration

Besides the experimental methods mentioned above, work in this thesis is based on collaborations with researchers using other experimental techniques.

3.3.1 Wavelength dispersive spectroscopy

Given the nature of solution growth, the nominal concentration of the chemical substitution does not have to be the actual concentration in a grown crystal. Therefore, elemental analysis was performed to determine the stoichiometry of the samples by using wavelength-dispersive x-ray spectroscopy (WDS) in a JEOL JXA-8200 electron probe microanalyzer. The measurement was conducted with an accelerating voltage of 20 kV, a probe current of 25 nA and a spot size of 5 μm. The integration time on peak, low background and high background is 10 s, 5 s and 5 s, respectively. Only clear and shiny surface regions were selected for determination of the sample stoichiometry, i.e., regions with residual flux were avoided. For each compound, the WDS data were collected from multiple points on the same sample. Counting statistics suggest there should be 1% or less relative error due to counting. For the calculation of physical quantities, such as the magnetization and specific heat, the actual stoichiometry x_{WDS} was used in this thesis as x rather than x_{nominal}.

3.3.2 Single crystal x-ray diffraction

Single crystal x-ray diffraction data were collected by Bruker APEX diffractometer equipped with a CCD detector, using monochromated Mo Kα radiation ($\lambda = 0.71073$ $\mathring{A}$). Reflections were gathered by taking three sets of 606 frames with 0.3° scans in ω and with an exposure time of 10 s per frame at room temperature. The range of 2θ extended from $\sim$ 4 to 57°. The reflection intensities were integrated with the *SAINT* program. The measured intensities were corrected for Lorentz and polarization effects and were further corrected for absorption using the *SADABS* program as implemented in the *SAINT* [SMART, 2005] program package. Intensity statistics and space group determination were carried out using *XPREP*, a subprogram in the *SHELXTL* software package. The structural models were obtained from direct methods using *SHELXS*-97 and refined by fullmatrix, leastsquares procedures on F^2 as implemented in the *SHELXTL* [SHELXTLPlus, 2003] package.

3.3.3 Magnetization under pressure

To study the pressure effect, low field magnetization under pressures can be measured in MPMS. In the case of $BaSn_5$ [Lin et al., 2012c], magnetization under pressures up to $\sim$ 10 kbar was measured using a commercial, HMD, Be-Cu pistion cylinder pressure cell [QuantumDesign, 2012] with Daphne oil 7373 as a pressure medium and superconducting Pb as a low temperature manometer [Eiling and Schilling, 1981]. With a moissanite anvil cell [Alireza et al., 2007], pressures of up to 5.3 GPa can be achieved. The body of the cell is made of Cu-Ti alloy and the gasket is made of Cu-Be. Daphne 7474 was used as a pressure transmitting medium, and the pressure was determined at 77 K by the ruby fluorescence technique. It should be noted that the data analysis of measurements with high applied magnetic field are limited to the large background of the pressure cell (This is the most likely source of apparent diamagnetic shifts in higher pressure data).

CHAPTER 4. DEVELOPMENT OF VIABLE SOLUTIONS FOR THE SYNTHESIS OF SULFUR BEARING SINGLE CRYSTALS[1]

4.1 Abstract

The discovery of high temperature superconductivity in FeAs and FeSe based compounds has once again focused the condensed matter community on the need to systematically explore compounds containing chalcogens and pnictogens. Whereas some solution growth techniques have been developed to handle P and As, and Sb and Bi are versatile solvents in their own right, S has remained a problematic element to incorporate into conventional solution growth. To a large extent its low boiling point, combined with its polymeric nature in a molten state have made S an uninviting solvent. In this paper we present our development of a range of binary sulfur bearing solutions (some even sulfur rich) and demonstrate how we have been able to use these as useful starting points for growth of wide range of transition metal – sulfur – X ternary compounds. We present growth details and basic characterization data for $Ni_3Bi_2S_2$, $Co_3Sn_2S_2$, Fe_2GeS_4, CoSSb, and $CePd_3S_4$. In addition we present a remarkably simple method for growth of single crystalline Co with crystallization taking place *below* the Curie temperature.

[1]This chapter is a version of the published article: Lin, X., Bud'ko, S. L., and Canfield, P. C., "Development of viable solutions for the synthesis of sulfur bearing single crystals", *Philos. Mag.*, 92 (2012): 2436-2447.

4.2 Introduction

Solution growth of single crystalline samples [Fisk and Remeika, 1989; Canfield and Fisk, 1992; Canfield and Fisher, 2001; Canfield, 2010] for basic as well as applied physics continues to be one of the most powerful synthetic tools in the field of superconductivity, or more broadly, in the field of correlated electron materials. As implied in the name of the technique, the need for a readily accessible and well understood solution to grow the materials out of is a key, first step. Some compounds naturally lend themselves to growth out of certain solutions; RSb_2 or $RAgSb_2$ out of Sb [Bud'ko et al., 1998; Myers et al., 1999], $YbAl_3$ out of Al [Canfield and Fisk, 1992; Hiess et al., 1995], RT_2Zn_{20} out of Zn [Jia et al., 2007], (R = rare earth, T = Fe and Co columns). In other cases the choice of solution is not as obvious, at least not to the novice: e.g. the growth of CeSb or $Yb_{14}MnSb_{11}$ out of Sn [Canfield and Fisk, 1992; Fisher et al., 1999]. Sometimes growths can be complicated by the special requirements imposed by one or more of the constituent elements. For example the refractory nature of boron, combined with limited, low temperature solubility, often restricts the choice of possible solutions; this being said, the growths of RB_6 out of Al [Canfield and Fisk, 1992] or RNi_2B_2C out of the NiB eutectic [Canfield and Fisher, 2001] show that this can be overcome in many cases.

Recently, with the discovery of high temperature superconductivity in FeAs based materials [Hosono, 2008; Rotter et al., 2008], there has been a large effort to develop versatile and safe methods for growing As bearing compounds out of solution. Arsenic presents an unpleasant pairing of high vapor pressure with toxicity in both its elemental and oxide forms. The first solution grown single crystals of FeAs based superconductors were synthesized using Sn as a solvent [Ni et al., 2008b], allowing for greatly reduced vapor pressure as well as relatively dilute As solutions. A second, now commonly used, solution was binary FeAs which, despite its high melting point, can be used between 1200 °C and 1050 °C, although care does need to be taken in the preparation of the FeAs phase

to minimize any free As that could cause unwanted partial pressure Ni-PRB08.

Given the precedent of FeAs-based superconductivity, combined with lessons learned from earlier discoveries of high temperature and novel superconductivity in the cuprates, MgB_2 and the RNi_2B_2C compounds [Canfield, 2011], both the chalcogen and pnictogen elements are being viewed as useful components in materials, specifically to tune the band width. Whereas some viable solutions have been developed for the use of P and As [Canfield and Fisk, 1992; Ni et al., 2008b,c], and whereas Sb and Bi are powerful solvents in their own right [Canfield and Fisk, 1992; Canfield and Fisher, 2001; Canfield, 2010; Bud'ko et al., 1998; Myers et al., 1999], there is a growing need to develop a wide range of S-based solutions that can be utilized for growth of S-bearing materials, specifically, transition metal – sulfur based binaries and ternaries. Although there is also a need to try to develop Se- and Te- based solutions, these elements can be used as solvents, at least over carefully monitored temperature and composition ranges [Sacchetti et al., 2006].

In this paper we outline the use of S-X (X = non-transition metal) as well as S-TM (TM = transition metal) solutions for the growth of S-bearing compounds. The samples we have been able to grow: Bi_2S_3, Pd_4S, $Ni_3Bi_2S_2$, $Co_3Sn_2S_2$, Fe_2GeS_4, CoSSb, and $CePd_3S_4$ should be viewed as proof of principle compounds rather than defining any significant subset of what can (and hopefully will) be grown from these and other, related solutions.

4.3 Experimental Details

Powder x-ray diffraction data on all samples were collected by a Rigaku Miniflex diffractometer with Cu $K\alpha$ radiation at room temperature. The error bars were determined by systematic errors which had been characterized by Si standard. Magnetic field and temperature dependent DC magnetization measurements were performed in a

Quantum Design MPMS-5 SQUID magnetometer. Measurements of the electrical resistivity were made by using the standard ac four-probe method with Pt wires attached by Epotek H20E silver epoxy. Both Quantum Design MPMS-5 SQUID magnetometer with LR-700 resistance bridge and Quantum Design PPMS instrument with the ACT option were used in the resistivity measurement.

4.4 Results

4.4.1 Sulfur – non-transition metal binaries

A survey of binary phase diagrams [Massalski, 1990] reveals that several metal / metalloid elements have limited to moderately accessible liquidus lines (temperature below 1200 °C, relatively low vapor pressure and broad range in concentration) on the metal / metalloid rich side. Of these Bi is the most promising (see Fig 4.1) with a wide range of solubility on the Bi-rich side of Bi_2S_3. Given our initial concern about possibly high partial pressure of sulfur vapor above this melt, we performed several trial growths (using furnaces in vented containment boxes) with increasing amounts of sulfur relative to bismuth. We have found that we can safely bring a mixture of $S_{40}Bi_{60}$ up to 1000 °C without any detectable condensation of S outside of the growth crucible and also without any indication of high vapor pressures. Upon cooling such mixtures to 400 °C over 36 hours we grew single crystals of Bi_2S_3 that could be separated from the remaining liquid via our standard centrifugal decanting method [Canfield and Fisk, 1992; Canfield and Fisher, 2001; Canfield, 2010]. The inset to Fig 4.1 shows the blade-like rod-shaped single crystals with mirrored surfaces.

Having established that a Bi-S melt can be heated to at least 1000 °C we proceeded to grow a transition metal – bismuth – sulfur ternary compound: Parkerite, $Ni_3Bi_2S_2$, out of a Bi-rich melt. Whereas this is a known mineral it has primarily been synthesized in polycrystalline form, or in very small single crystalline form via chemical vapor

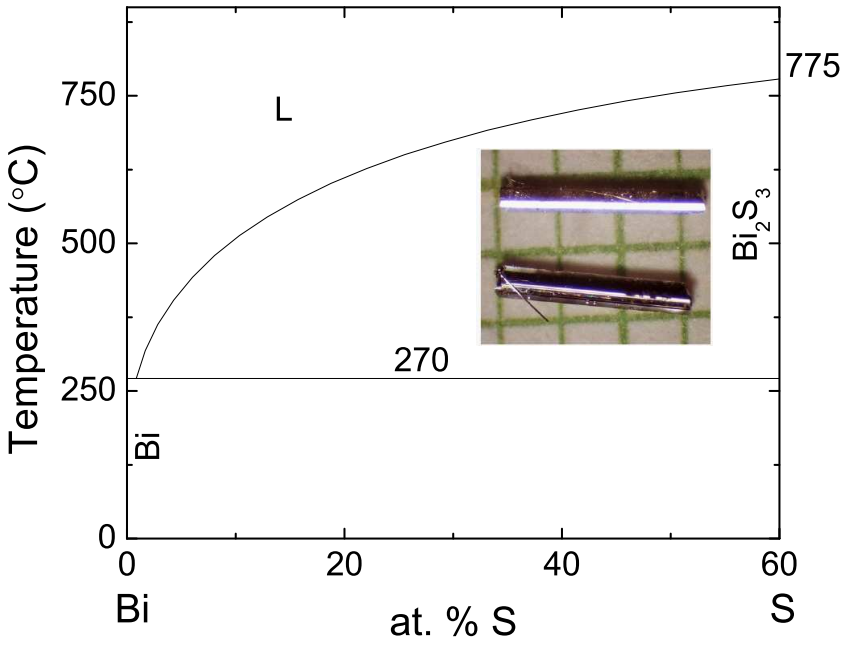

Figure 4.1 The Bi – S binary phase diagram (based on ref. [Massalski, 1990]). Inset: picture of single crystalline Bi_2S_3 on a millimeter grid.[Lin et al., 2012b]

transport [Sakamoto et al., 2006; Baranov et al., 2001]. Elemental Bi, Ni and S can be combined in a 2 ml Al_2O_3 crucible with an initial stoichiometry ranging from $Bi_{88}Ni_6S_6$ to $Bi_{70}Ni_{17}S_{13}$, sealed in an amorphous silica ampoule, and heated to 1050 °C over 2-6 hours, followed by a slow cooling to 550 °C and a decanting. The resultant single crystals have typical dimensions of $\sim 1 \times 4 \times 0.5$ mm^3, but can have much bigger surface areas (see inset to Fig 4.3, below). The powder x-ray diffraction data refines to a monoclinic cell with a = 11.051(2) $\AA$, b = 8.075(1) $\AA$, c = 7.931(1) $\AA$, and β = 133.9(1) °, consistent with the reported unit cell [Sakamoto et al., 2006; Baranov et al., 2001]. The temperature dependent electrical resistivity data are shown in Fig 4.2, manifesting a residual resistivity ratio (RRR) = ρ(300 K) / ρ(2.0 K) of greater than 17. The inset to Fig 4.2 shows the low temperature resistivity and clearly shows a sharp transition to the superconducting state near 0.80 K, a value consistent with earlier reports on polycrystalline samples [Sakamoto et al., 2006]. Figure 4.3 presents anisotropic $H_{c2}(T)$ data for the applied field parallel to the a axis and for the field applied within the bc plane. There is relatively little anisotropy, approximately 1.3, with the $H_{c2}(0)$ curves based on the offset criterion extrapolating to values between 200 and 300 Oe. The onset and offset criteria used for determining transition temperatures are shown in the inset to Fig 4.2.

Although the Sn-S binary phase diagram (shown schematically in Fig 4.4) offers a much smaller region of solubility on the Sn-rich side, this solution can still be used to grow S-based compounds; for example $Co_3Sn_2S_2$, a Shandite structural variant [Zabel et al., 1979; Natarajan et al., 1988] can be readily grown (inset to Fig 4.5b). These single crystals were grown from a ternary melt with an initial composition of $Sn_{86}Co_8S_6$ that was heated to 1050 °C and then slowly cooled to 700 °C over 60 hours. Once the excess liquid was decanted, the resulting, large, thin, hexagonal plates were readily removed from the growth crucible. Powder x-ray diffraction data refines to a hexagonal cell with a = 5.373(1) $\AA$ and c = 13.178(2) $\AA$, consistent with the reported unit cell [Natarajan et al., 1988; Weihrich and Anusca, 2006]. Anisotropic, temperature dependent magnetization

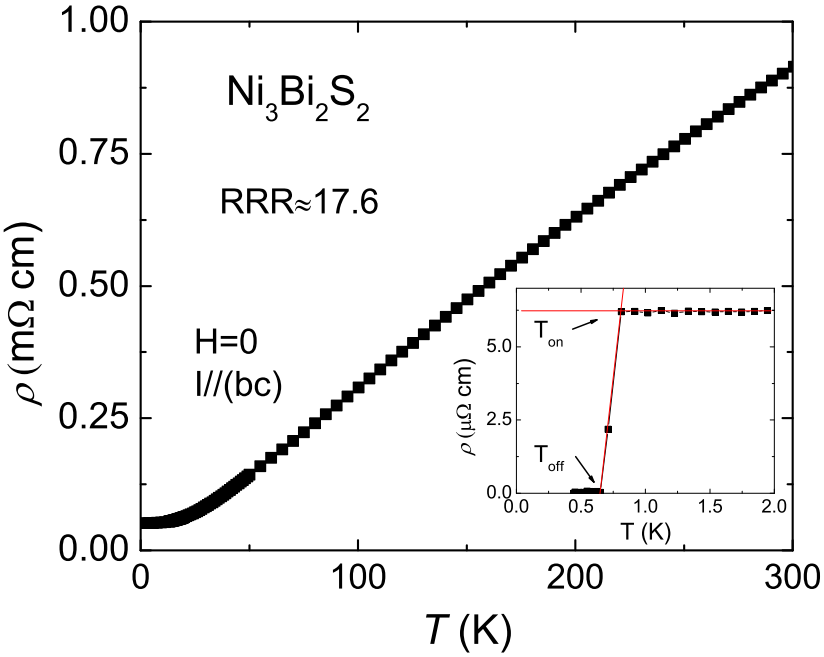

Figure 4.2 Zero-field in plane resistivity of $Ni_3Bi_2S_2$. Inset: enlarged low-temperature part of resistivity with onset and offset criteria shown.[Lin et al., 2012b]

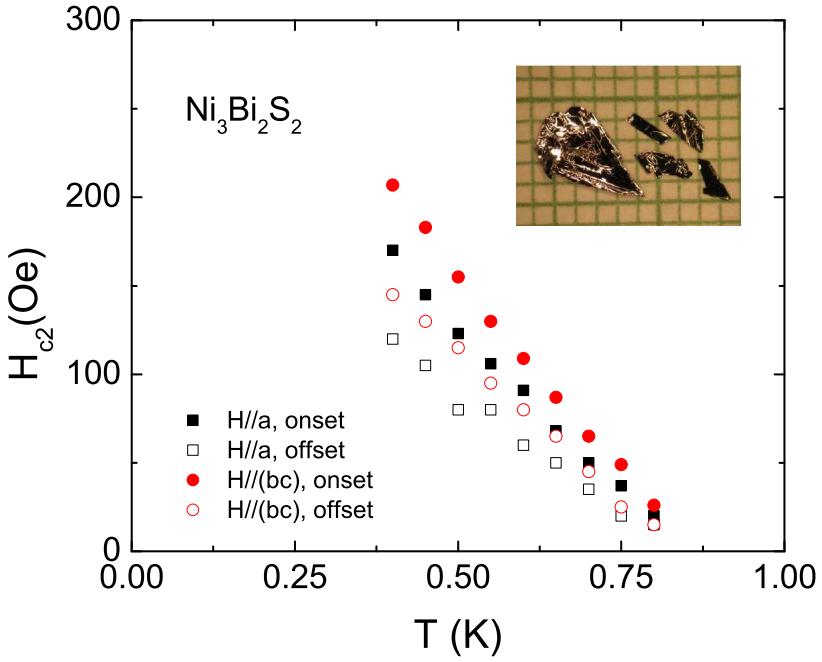

Figure 4.3 Anisotropic upper critical field of $Ni_3Bi_2S_2$ from magnetotransport measurement. Inset: picture of single crystalline $Ni_3Bi_2S_2$ on a millimeter grid.[Lin et al., 2012b]

data (Fig 4.5a) reveal a ferromagnetic phase transition. The $T > T_C$ data, plotted as $H/M(T)$ data in Fig 4.5b, reveal a clear Curie-Weiss behavior with an effective moment of $\sim 0.96\ \mu_B$ per Co for the field along the c axis. Temperature dependent resistivity (in zero applied magnetic field) data (Fig 4.6) reveal a clear loss of spin disorder scattering below 175 K.

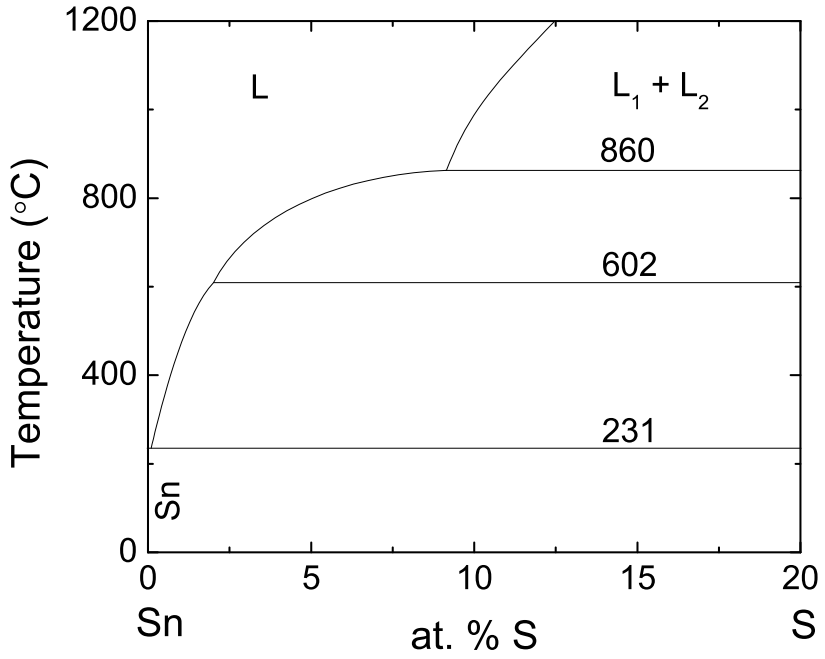

Figure 4.4 The Sn – S binary phase diagram (based on ref. [Massalski, 1990]) [Lin et al., 2012b]

The S-Sb binary phase diagram (shown schematically in Fig 4.7) also offers a range of S-solubility, especially for Sb-rich solutions, albeit at higher temperatures (due to the higher melting temperature of Sb relative to Bi and Sn). We have been able to grow CoSSb (paracostibite) as well as the non-Sb-bearing Fe_2GeS_4 using Sb-rich melts. Whereas previous synthesis CoSSb has been in polycrystalline form, often utilizing high pressure solid state reactions [Carlini et al., 2011; Henry et al., 1975], we were able to

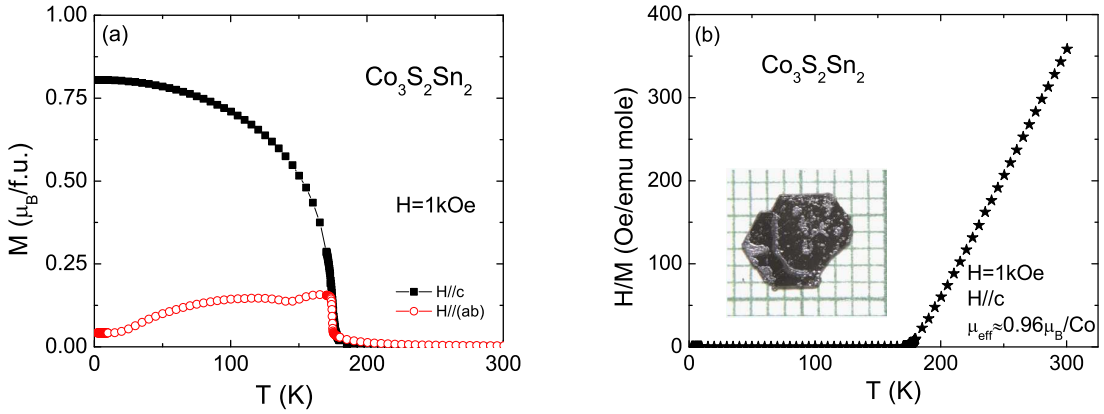

Figure 4.5 (a) Anisotropic temperature-dependent magnetic susceptibility of $Co_3Sn_2S_2$. (b) Temperature dependent inverse magnetic susceptibility of $Co_3Sn_2S_2$, $\boldsymbol{H} \parallel c$. Inset: picture of single crystalline $Co_3Sn_2S_2$ on a millimeter grid. [Lin et al., 2012b]

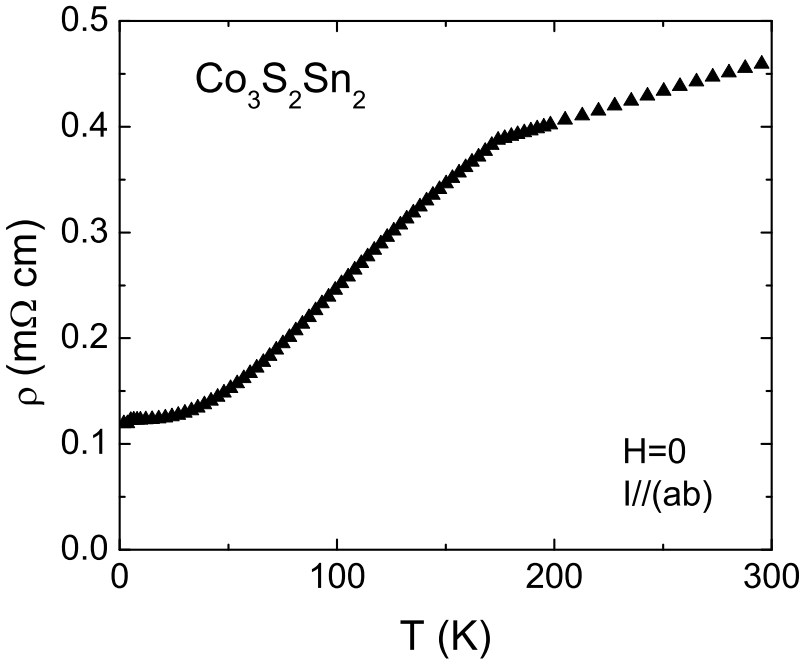

Figure 4.6 Zero-field in plane resistivity of $Co_3Sn_2S_2$. [Lin et al., 2012b]

grow CoSSb by cooling a $Sb_{60}Co_{20}S_{20}$ melt from 1000 °C to 650 °C over 18 hours. Even with this relatively high cooling rate, large single crystals could be removed from the excess liquid via decanting (see inset to Fig 4.8). Powder x-ray diffraction data refines to an orthorhombic cell with a = 5.835(1) $\AA$, b = 5.950(1) $\AA$, and c = 11.661(2) $\AA$, consistent with the reported unit cell [Carlini et al., 2011; Henry et al., 1975]. Temperature dependent magnetization measurements were made on these semiconducting samples in an applied field of 50 kOe (Fig 4.8) showing that CoSbS is essentially non-magnetic (showing a slight Curie tail at low temperatures, most likely attributable to residual flux / impurities).

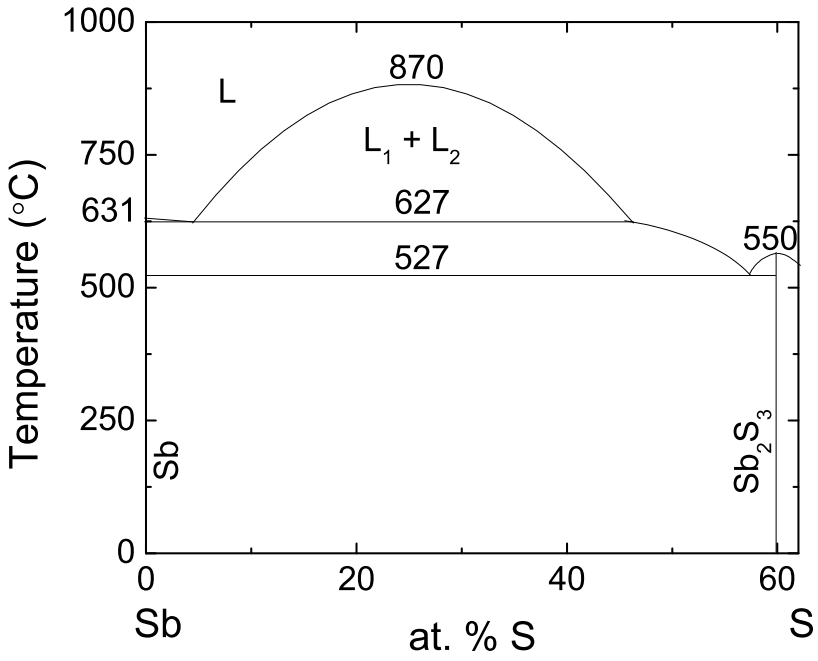

Figure 4.7 The Sb – S binary phase diagram (based on ref. [Massalski, 1990]). [Lin et al., 2012b]

Fe_2GeS_4 (a sulfide variant of the Mg_2SiO_4, olivine, structure) can also be grown in single crystalline form from excess Sb by combining elements in the ratio $Sb_{65}Ge_{14}S_{14}Fe_7$,

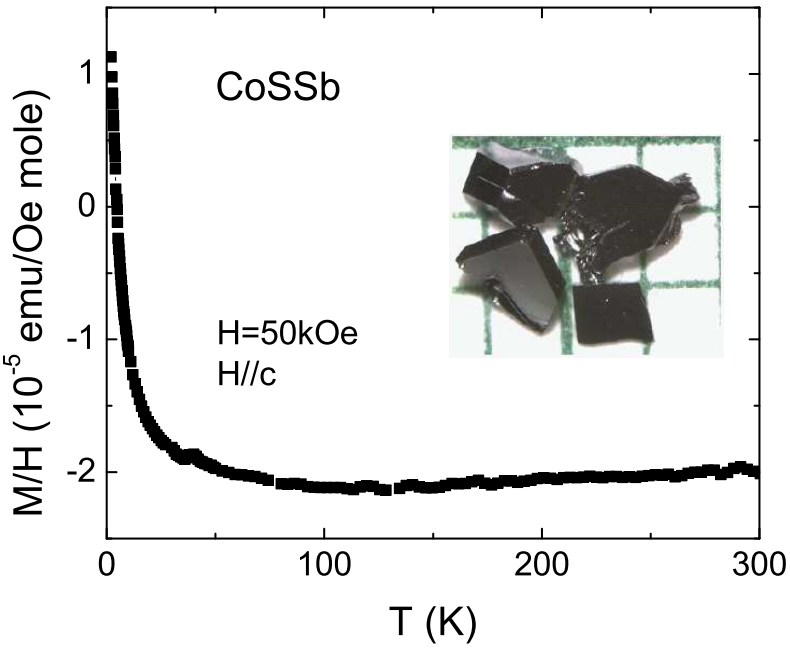

Figure 4.8 Temperature dependent magnetic susceptibility of CoSSb, $\boldsymbol{H} \parallel c$. Inset: picture of single crystalline CoSSb on a millimeter grid. [Lin et al., 2012b]

heating to 900 °C and then cooling to 600 °C over 40 hours. The plate-like single crystals remaining in the growth crucible after decanting are shown in the upper inset to Fig 4.9. Powder x-ray diffraction data refines to an orthorhombic cell with a = 12.477(2) $\AA$, b = 7.205(1) $\AA$, and c = 5.902(1) $\AA$, consistent with the reported unit cell [Junod et al., 1995]. Multiple crystals were chosen for the temperature dependent magnetization measurement of Fe_2GeS_4, as shown in the main body of Fig 4.9 and the higher temperature, inverse susceptibility data for $T > 100$ K are shown in the lower inset. These data are consistent with the reported cascade of magnetic transitions, $T_N \sim 150$ K followed by a lower temperature, first order phase transition to a state with a net ferromagnetic component below $T > 70$ K [Junod et al., 1995].

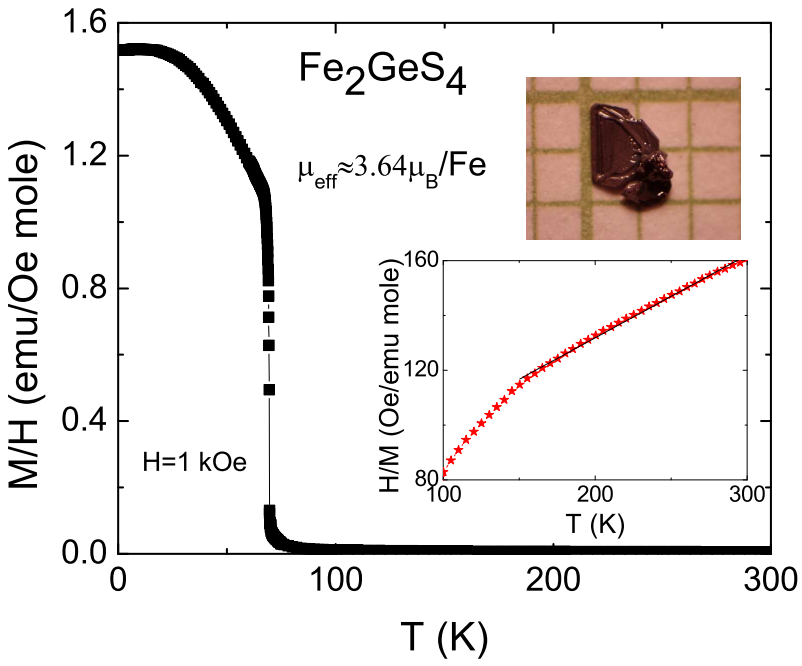

Figure 4.9 Temperature dependent magnetic susceptibility of Fe_2GeS_4. Upper inset: picture of single crystalline Fe_2GeS_4 on a millimeter grid; lower inset: temperature dependent inverse magnetic susceptibility of Fe_2GeS_4. [Lin et al., 2012b]

Two other S-based binary phase diagrams that are promising for use as sulfur bearing liquids are the Pb-S and In-S binaries. For the case of Pb-S (see Fig 4.10a) we have been able to grow single crystals of PbS by cooling $Pb_{90}S_{10}$ from 1000 °C to 600 °C over 15 hours. The crystals (inset to Fig 4.10a) grow as well faceted cubes with twinning along the 111 direction. To date we have not grown a ternary compound of any significant size out of this melt, but there is no reason to doubt its use. The In-S binary phase diagram (Fig 4.10b) also appears to be promising (to some extent resembling a lower temperature variant of the Sb-S binary) and will be explored further in the near future.

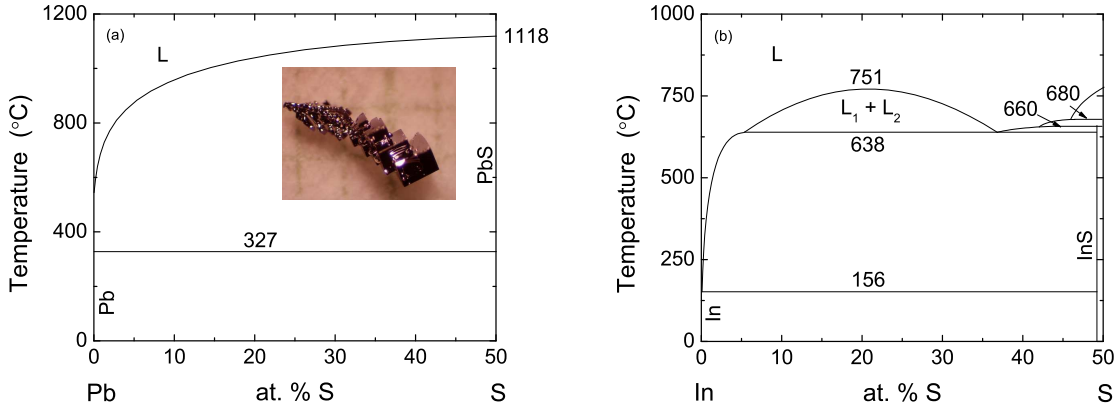

Figure 4.10 (a) The Pb – S binary phase diagram (based on ref. [Massalski, 1990]). Inset: picture of single crystalline PbS on a millimeter grid. (b) The In – S binary phase diagram (based on ref. **?**]). [Lin et al., 2012b]

4.4.2 Sulphur – transition metal binaries

Although S-X (X = Bi, Sn, Sb, Pb, In) binary solutions can be used for the growth of transition metal based compounds, especially ternary compounds that contain X as the third element, more versatile solutions can be found for the growth of Ni, Co, and Pd bearing sulfide compounds; the use of the relatively deep eutectics in the transition metal – sulfur binaries potentially allows for the growth of a wide range of TM – S –

X compounds. Figure 4.11 shows the Pd-rich side of the Pd-S binary phase diagram, specifically the deep eutectic near 28% S. Binary melts can be made from elemental mixtures of powdered Pd and S, combined in alumina crucibles. For sulfur content ranging from 20 to 50 % atomic heating slowly to slightly above 1000 °C is sufficient to reach a liquid state.

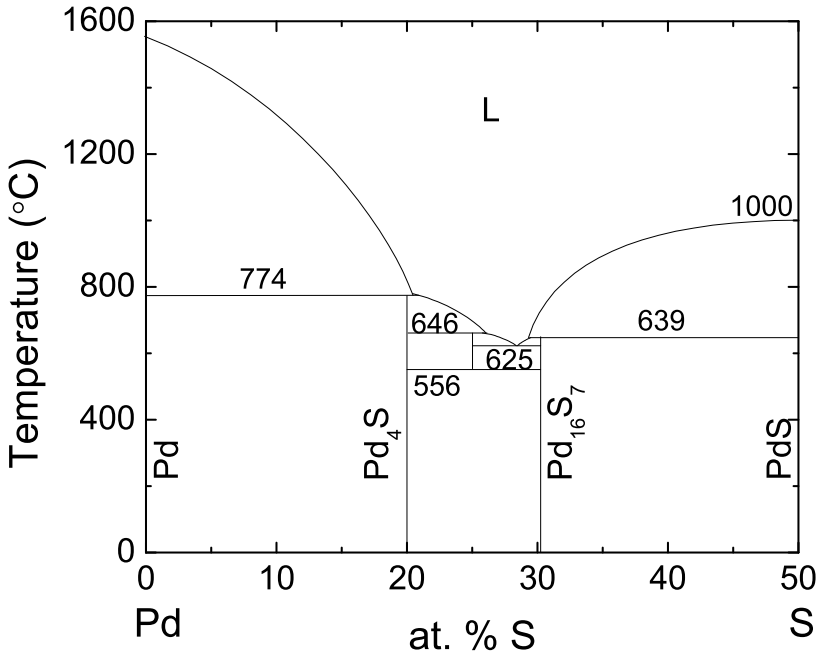

Figure 4.11 The Pd – S binary phase diagram (based on ref. [Massalski, 1990]). [Lin et al., 2012b]

As an example, Pd_4S was grown by cooling a melt of $Pd_{77}S_{23}$ from 780 °C to 660 °C and decanting. Powder x-ray diffraction data refines to a tetragonal unit cell with a = 5.117(1) $\AA$, and c = 5.599(1) $\AA$, consistent with the reported unit cell [Raub et al., 1965]. Figure 4.12 presents the temperature dependent normalized electrical resistivity of Pd_4S. As reported in earlier work [Raub et al., 1965], there is no superconductivity detected down to our base temperature of 1.8 K, but the substantial RRR value, 754

and the large magnetoresistance both indicate that the crystals grow with a very low number of impurities / defects. At 1.8 K, a power law fit shows that $\triangle\rho(H)/\rho(0) \propto H^{1.7}$, this is possibly due to the multi-sheet Fermi surface. At 90 kOe, the magnetoresistance decreases as temperature increases. This is probably a consequence of the magnetoresistance following the Kohler's rule, and is similar to the behaviour of $RAgSb_2$ compounds [Myers et al., 1999].

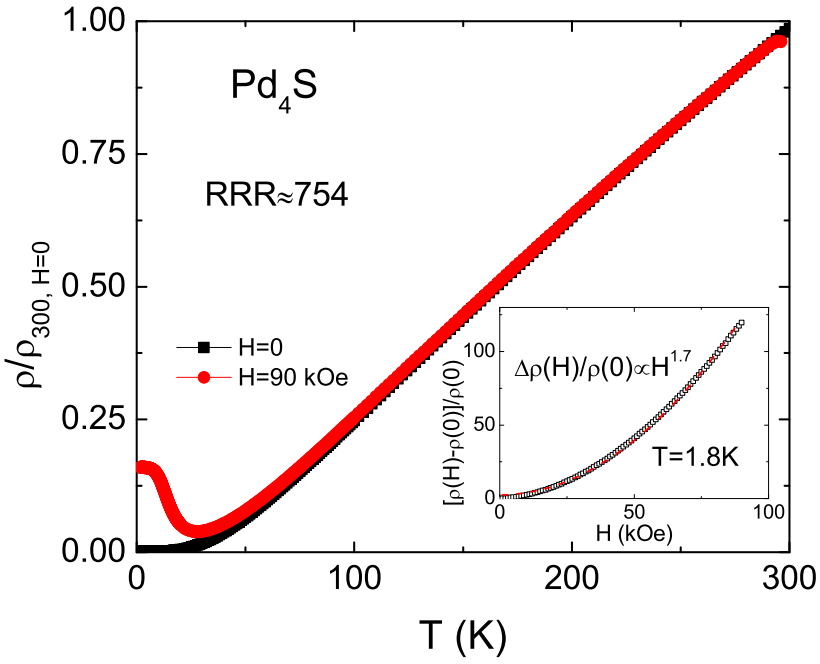

Figure 4.12 Temperature dependent resistivity of Pd_4S in zero field, and in 90 kOe. Inset: magnetoresistance of Pd_4S at $T = 1.8$ K, the red dashed line corresponds to $\triangle\rho(H)/\rho(0) \propto H^{1.7}$. [Lin et al., 2012b]

Ready access to a Pd-S melt offers the possibility of exploring Pd – S – X ternaries. For example, well formed single crystals of the ternary compound, $CePd_3S_4$ were grown were grown out of a melt with an initial stoichiometry of $Ce_5Pd_{58.8}S_{36.2}$ that was slowly cooled from 1000 °C to 700 °C over 65 hours. Powder x-ray diffraction data refines to cubic cell with a = 6.728(1) $\mathring{A}$, consistent with the reported unit cell [Abe et al.,

1999]. Figures 4.13 and 4.14 present the temperature dependent electrical resistivity and low field magnetization of a single crystal of $CePd_3S_4$. Upon cooling below 6.4 K, a ferromagnetic state develops [Abe et al., 1999]. This phase transition is exquisitely clear in the resistivity data as well as in the sudden increase in magnetization. $CePd_3S_4$ is one of a small number of known ferromagnetic, Ce-based, intermetallic compounds; it will be of great interest to study the effects of applied pressures on the low temperature, magnetic state, specifically to search for possible pressure induced, quantum critical points [Colombier et al., 2011].

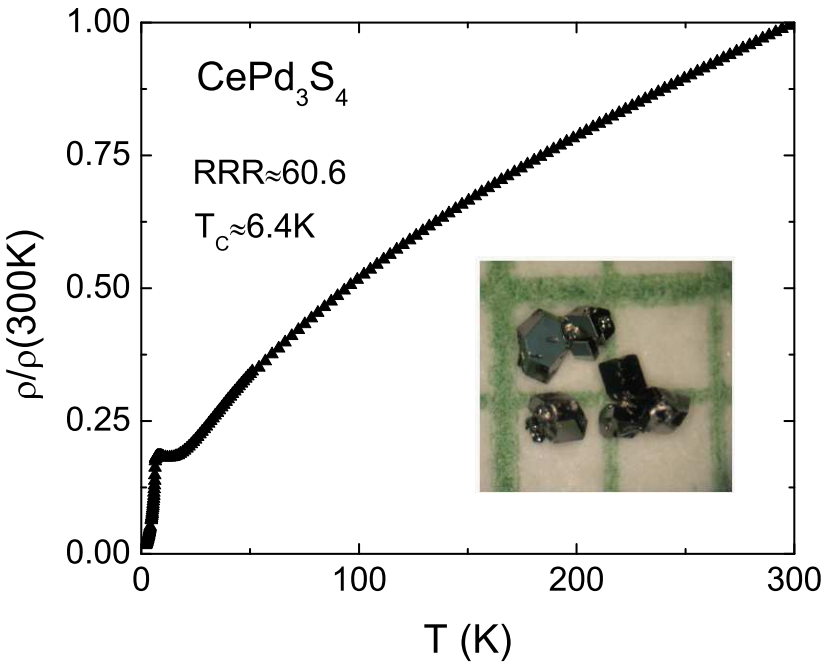

Figure 4.13 Temperature dependent resistivity of $CePd_3S_4$ in zero field. Inset: picture of single crystalline $CePd_3S_4$ on a millimeter grid. [Lin et al., 2012b]

Co-S and Ni-S also have very compelling (and deep) eutectics, as shown in Fig 4.15. For Ni-S we have been able to grow single crystals of elemental Ni by slow cooling of $Ni_{80}S_{20}$ melts from 1100 °C to 725 °C over 50 hours. We have been able to do this

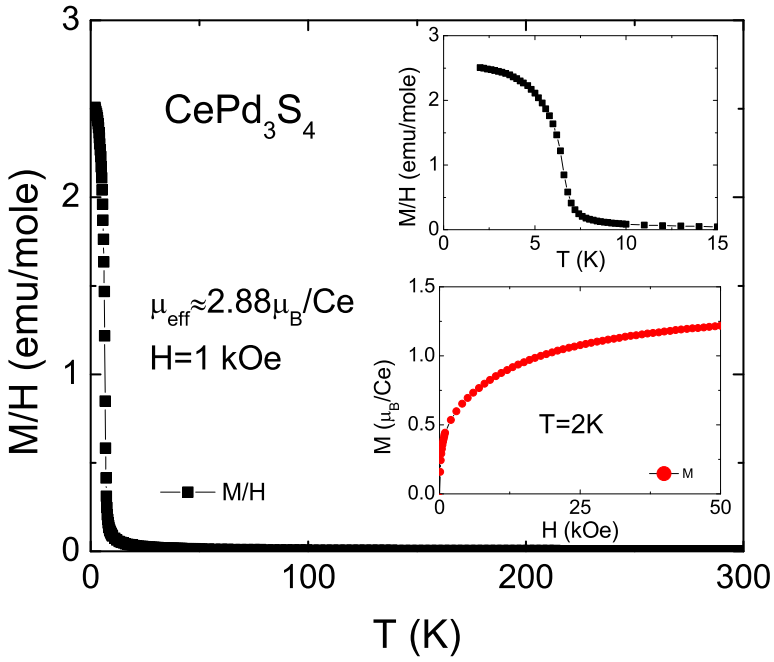

Figure 4.14 Temperature dependent magnetic susceptibility of $CePd_3S_4$. Upper inset: enlarged low-temperature part of magnetic susceptibility; lower inset: magnetization isotherms at $T = 2$ K. [Lin et al., 2012b]

starting with stoichiometric mixtures of either (a) NiS and elemental Ni (powder) or (b) elemental sulfur and elemental Ni. For the case of Co-S, single crystals of elemental Co were grown by cooling a mixture of $Co_{65}S_{35}$ from 1150 °C to 900 °C over 50 hours. In this case, given the very high Curie temperature of elemental Co, we have been able to grow single crystals of a ferromagnetic compound, in the ferromagnetic state. This opens up a range of experiments that allow for the exploration of how applied magnetic field affects the nucleation and growth of highly magnetic compounds.

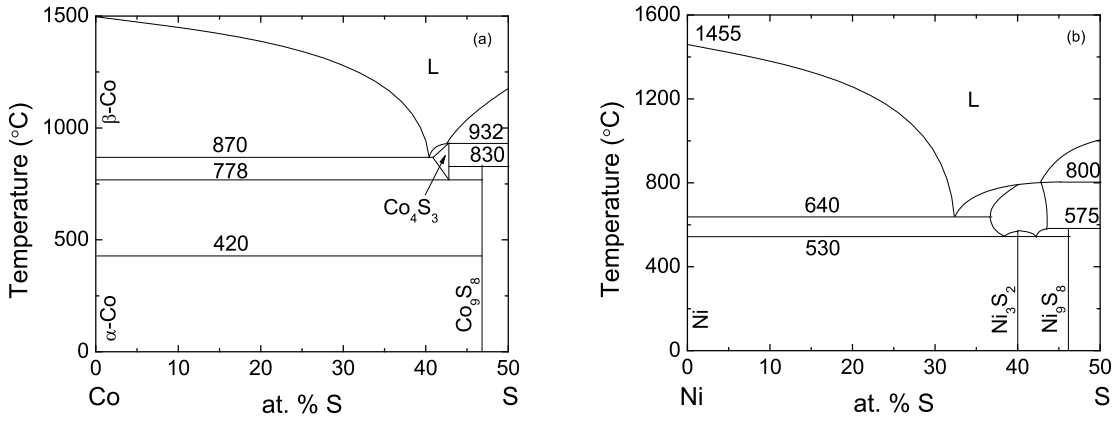

Figure 4.15 (a) The Co – S binary phase diagram (based on ref. [Massalski, 1990]). (b) The Ni – S binary phase diagram (based on ref. [Massalski, 1990]). [Lin et al., 2012b]

The fact that we can create and handle Ni-S and Co-S liquids for temperatures ranging from 1100 °C to 700 °C, with as much as 50% S content, means that Ni – S – X and Co – S – X ternary compounds are as accessible as the Pd – S – X compounds discussed above. Although Pd, Co and Ni represent the majority of the readily accessibly phase space for S – transition metal binaries, they also represent the most promising of the 3d and 4d elements for the discovery of compounds with reduced (or fragile) moment magnetic ordering, the kind of compounds that are thought to be promising parent materials for possible high temperature superconductivity [Canfield, 2011]. In addition,

Co-, Ni-, and Pd-S based compounds represent a large number of the promising mineral based compounds that exhibit metallic or semi-metallic properties, again making them promising for exploration for correlated electron states [Roberts et al., 1990].

4.5 Summary

In this paper we present the results of our initial development of S-based solutions for the exploration of S-based compounds as possible hosts for high temperature superconductivity. We have been able to grow ternary compounds out of Bi-S, Sn-S, Sb-S, and Pd-S and have shown that Pb-S, In-S, Ni-S and Co-S hold comparable potential. We anticipate the use of these solutions will allow for the discovery of new phases as well as ground states.

CHAPTER 5. PHYSICAL PROPERTIES OF SINGLE CRYSTALLINE $BaSn_5$[1]

5.1 Abstract

We present a comprehensive study of the binary intermetallic superconductor, $BaSn_5$. High-quality single crystalline $BaSn_5$ was grown out of Sn flux. Detailed themodynamic and transport measurements were performed to study $BaSn_5$'s normal and superconducting state properties. This material appears to be a strongly coupled, multiband superconductor. $H_{c2}(T)$ is almost isotropic. De Haas-van Alphen oscillations were observed and two effective masses were estimated from the FFT spectra. Hydrostatic pressure causes a decrease in the superconducting transition temperature at the rate of $\approx -0.053 \pm 0.001$ K/kbar.

5.2 Introduction

To search for new superconductors, one of many ways is to look for compounds that share similar features with the already reported superconductors. On the one hand, $BaSn_5$ has a similar band dispersions near the Fermi level (E_F) as A15 type superconductors, such as V_3Si and Nb_3Sn [Fassler et al., 2001]. On the other hand, $BaSn_5$ forms

[1]This chapter is based on the published article: Lin, X., Bud'ko, S. L., and Canfield, P. C., "Physical properties of single crystalline $BaSn_5$", *Philos. Mag.*, 92 (2012): 3006-3014, including the Corrigendum: Lin, X., Jesche, A., Bud'ko, S. L., and Canfield, P. C., "Physical properties of single crystalline $BaSn_5$", *Philos. Mag.*, 92 (2012): 3006

in *P6/mmm* structure, a variant of AlB_2 structure, the prototype of MgB_2 which superconducts at $\sim$ 40 K [Nagamatsu et al., 2001; Kwok et al., 2003; Canfield and Bud'ko, 2005; Wilke et al., 2010].

The first study of $BaSn_5$ can be traced back to 1979 [Moos and Shuppe, 1979], however, only recently has its structure been solved [Fassler et al., 2001]. As one of the alkaline earth stannides group of superconductors (for $SrSn_4$, $SrSn_3$, $BaSn_3$ the superconducting transition temperatures are $\sim$ 4.8 K [Hoffmann and Fassler, 2003; Lin et al., 2011], $\sim$ 5.4 K [Fassler and Hoffmann, 2000] and $\sim$ 2.4 K [Fassler and Kronseder, 1997] respectively), $BaSn_5$'s superconducting transition temperature is reported to be $\sim$ 4.4 K [Fassler et al., 2001]. So far, only its low temperature and low field magnetization has been characterized on polycrystalline samples [Fassler et al., 2001].

In this article we report the growth of single crystalline $BaSn_5$, and the measurement of its thermodynamic and transport properties. Both the superconducting and normal states are characterized. We also present the effect of pressure on the superconducting properties of $BaSn_5$, and the observation of low temperature de Haas-van Alphen oscillations.

5.3 Experimental Details

Single crystals of $BaSn_5$ were grown out of excess Sn by the high-temperature solution technique [Canfield and Fisk, 1992]. Elemental Ba and Sn with an atomic ratio of Ba_8Sn_{92} were placed in a 2 ml alumina crucible. A second catch crucible stuffed with silica wool was placed on the top of the growth crucible. Both crucibles were sealed in a silica ampoule under approximately 1/3 atmosphere of high purity argon gas. To prevent oxidization of the growth materials, the packing and assembly of the ampoule was performed in a glovebox with a nitrogen atmosphere. This ampoule was heated up to 700 °C, then cooled to 425 °C, followed by a slow cool over a period of 40 hours to

270 °C, at which temperature the excess flux was decanted from the crystals. Crystals of $BaSn_5$ grown in this manner form in rod-like shape of a few mm in length and sub-mm in the other two dimensions. Due to the samples' air-sensitivity, crystals were kept in the glovebox, and efforts were made to minimize their exposure during measurement.

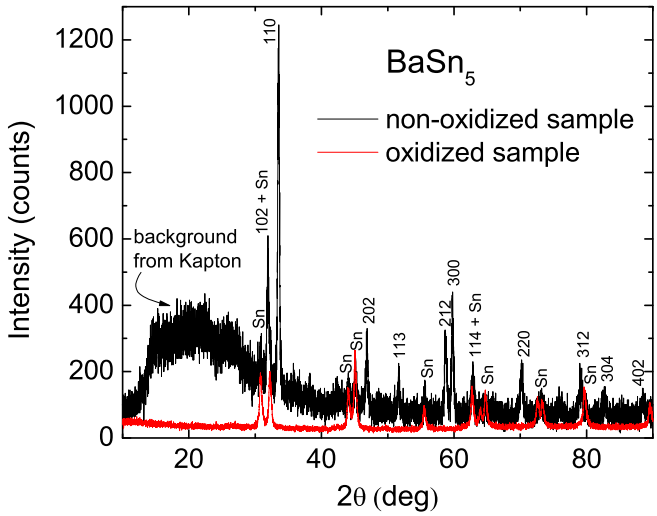

Figure 5.1 Comparison of the x-ray patterns taken on non-oxidized and oxidized powdered $BaSn_5$ single crystals. Peaks that belong to $BaSn_5$ are labeled with their $h\ k\ l$ values. Notes: the only differences between the two runs were (i) removal of Kapton film and (ii) 7 hours exposure to air. [Lin et al., 2012c]

Powder x-ray diffraction data on both non-oxidized and oxidized sample were collected by a Rigaku Miniflex diffractometer with Cu K_α radiation at room temperature. The diffraction pattern of the non-oxidized $BaSn_5$ was taken from the powder of $BaSn_5$ single crystals which was ground in the glovebox. The sample powder was sealed by Kapton film during the measurement to protect it from oxidization. To study the oxidation effect, a second x-ray diffraction was performed on the same powder after removal of Kapton film and a seven-hour exposure to the air. The lattice constants of non-oxidized $BaSn_5$ were statistically determined by measurements of multiple samples with Si (a =

5.4301 $\mathring{A}$) as an internal standard.

Temperature- and magnetic-field dependent dc magnetization data were measured in a Quantum Design MPMS-5 SQUID magnetometer. The ac resistance was measured via a standard four-probe method in a Quantum Design PPMS instrument with the ACT option. Platinum wires were attached to the sample using Dupont 4929 silver paint with the current approximately flowing along the longest dimension (crystal's c-axis). Resistance as a function of temperature was measured at different magnetic fields with field's direction parallel to c-axis and ab-plane respectively. A relaxation technique was applied in the heat capacity measurements in a PPMS instrument. For the measurement of low field dc magnetization under pressure, a commercial, HMD, Be-Cu piston-cylinder pressure cell [QuantumDesign, 2012] was used. The highest pressure reached $\sim$ 10 kbar with Daphne oil 7373 as a pressure medium and superconducting Pb as a low temperature pressure gauge [Eiling and Schilling, 1981].

5.4 Results and discussion

Figure 5.1 presents the comparison of powder x-ray diffraction on both non-oxidized and oxidized sample. The diffraction pattern from the non-oxidized sample confirms that the synthesized crystals are $BaSn_5$ with *P6/mmm* structure. The obtained lattice parameters are a = 5.368(4) $\mathring{A}$, c = 7.097(4) $\mathring{A}$, consistent with the reported data [Fassler et al., 2001]. Together with $BaSn_5$'s diffraction peaks, several peaks from Sn flux residue are also visible in the diffraction pattern. In contrast, after a seven-hour exposure to air, the same specimen lost all its diffraction peaks of $BaSn_5$. As shown in Fig 5.1, only Sn's diffraction peaks survived, with their intensities essentially unchanged. The disappearance of $BaSn_5$ under the powder x-ray diffraction is probably due to the oxidization of $BaSn_5$, resulting in phases that are too small or too disordered to diffract. Similar phenomena was also observed in the powder x-ray diffraction data of non-oxidized and

oxidized single crystalline $SrSn_4$ [Lin et al., 2011].

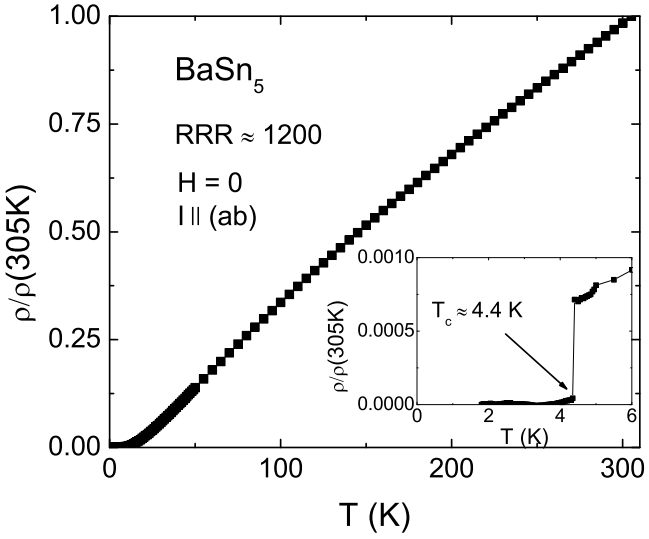

Figure 5.2 The temperature-dependent, normalized resistivity of $BaSn_5$. Inset: low temperature data showing the superconducting transition. [Lin et al., 2012c]

Zero-field, in-plane resistivity of $BaSn_5$ as a function of temperature is presented in Fig 5.2. Due to the sample's irregular shape in cross section and its air-sensitivity, its resistivity is normalized with respect to the room temperature value. To within factor of 25%, the room temperature resistivity reaches approximately 100 $\mu\Omega$ cm. In the higher temperature region, the resistivity manifests a typical metallic behaviour, increasing linearly as the temperature rises. The very substantial residual resistivity ratio (RRR) = ρ(305 K) / ρ(5.0 K) $\sim$ 1200 indicates that the crystals grow with a very low number of impurities/defects (a conclusion further supported by the observation of quantum oscillations, discussed below). The inset to Fig 5.2 shows the low temperature resistivity and a sharp transition to the superconducting state with offset at about 4.4 K, which is consistent with the literature data [Fassler et al., 2001].

The temperature dependent dc magnetic susceptibility, M/H, with the magnetic field

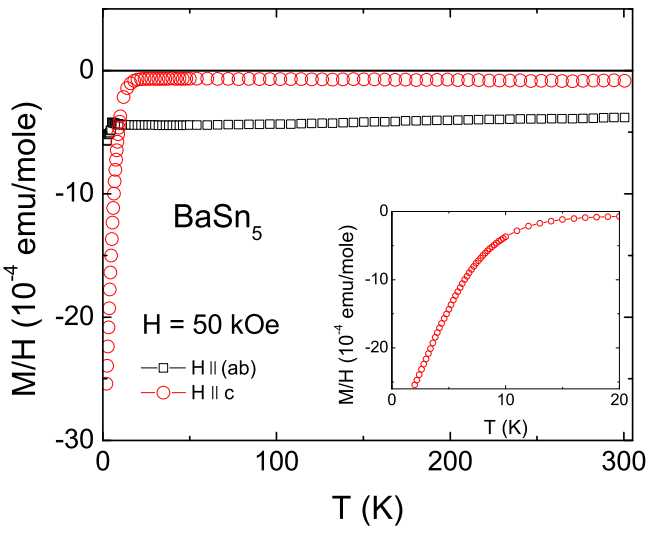

Figure 5.3 Anisotropic temperature-dependent magnetic susceptibility, M/H, of $BaSn_5$. Inset: enlarged low-temperature part of magnetic susceptibility with $H \| c$. [Lin et al., 2012c]

parallel to c-axis and ab-plane is shown in Fig 5.3. For an applied field of 50 kOe, the normal state of $BaSn_5$ exhibits diamagnetic behavior in both directions, and essentially does not change with temperature in the higher temperature region. Small anisotropy can be detected above 20 K, with absolute value of $|(M/H)_{ab}| > |(M/H)_c|$. However, in the low temperature region, a dramatic enhancement of the diamagnetic feature, especially with field parallel to c-axis, is clearly seen in the inset to Fig 5.3. These sudden changes in M/H are most likely brought by de Haas-van Alphen oscillations are shown in the upper inset to Fig 5.4.

To study de Haas-van Alphen oscillations in $BaSn_5$, dc magnetization as a function of applied magnetic field at several different temperatures was measured (Fig. 5.4). However, due to the sample's air-sensitivity and irregular shape in ab-plane, only studies with field parallel to c-axis are included in this work. The oscillations in the magnetization can be observed at multiple temperatures, superimposed on the nearly constant

magnetic background. The upper inset of Fig. 5.4 gives an example of these oscillatory behaviours as a function of inverse field up to 70 kOe at 1.85 K. Linear extrapolation of the $M(1/H)$ data was performed to obtain evenly spaced data. Fast Fourier transform (FFT) was used to convert the oscillations to their Fourier spectra in Fig. 5.4. Four peaks can be resolved from the spectra with frequencies of 1.84 MG(α), 2.01 MG(β), 4.02 MG(γ) and 5.46 MG(δ). Figure 5.4 also represents the evolution of the spectra with respect to temperature. It can be clearly seen that the amplitudes of spectra gradually attenuate and finally fade away at about 15 K. For a certain frequency F, the amplitude of the oscillation in the magnetization M is given by the Lifshitz-Kosevitch (LK) equation [Shoenberg, 1984]:

$$M = -2.602 \times 10^{-6}(\frac{2\pi}{HA''})^{1/2} \times \frac{GFT\exp(-\alpha px/H)}{p^{3/2}\sinh(-\alpha pT/H)} \times \sin[(\frac{2\pi pF}{H}) - 1/2 \pm \frac{\pi}{4}]$$

where $\alpha = 1.47(m/m_0)\times 10^5$ G/K, A'' is the second derivative of the cross sectional area of the Fermi surface with respect to wave vector along the direction of the applied field, G is the reduction factor arising from electron spin, ρ is the number of harmonic of the oscillation, and x is the Dingle temperature. Thus, the temperature dependence of the amplitude (A) of frequency α, β, γ and δ plotted in the lower inset to Fig. 5.4, can be used to determine the effective mass of the orbits via the LK formula, described above. From the slope of $\ln(A/T)$ plotted as a function of temperature, the effective masses were found to be $m_\alpha \approx 0.10\ m_0$, $m_\beta \approx 0.13\ m_0$, $m_\gamma \approx 0.20\ m_0$, and $m_\delta \approx 0.22\ m_0$, where m_0 is the bare electron mass. Since the frequency of the γ orbit is twice that of the β, it is probably that the γ is the second harmonic of the β orbit. However, for further understanding of the oscillations and topology of the Fermi surface, angular dependence of the spectra as well as detailed calculations of band structure and Fermi surfaces of $BaSn_5$ are needed.

The zero-field-cooled (ZFC) susceptibilities measured at a set of different low fields are presented in Fig 5.5 (no corrections for demagnetization factor were employed). At 25

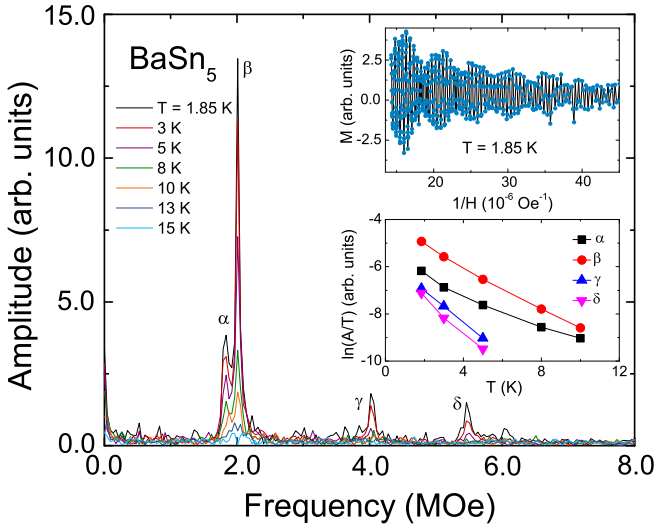

Figure 5.4 Fourier spectra of the oscillations in magnetization of $BaSn_5$ up to 15 K. Upper inset: magnetization as a function of inverse magnetic field of $BaSn_5$ at 1.85 K. Lower inset:Temperature dependence of the amplitudes of the observed oscillations. [Lin et al., 2012a]

Oe, a sharp superconducting transition is clearly seen with the onset of ≈ 4.4 K. To infer an anisotropic upper superconducting critical field for $BaSn_5$, the first data point that deviates from the normal state is chosen as the criterion of superconducting transition. Alternatively, anisotropic $H_{c2}(T)$ can be evaluated from the shifts of resistively measured superconducting transitions in different applied magnetic fields (Fig 5.6). $R = 0$ is chosen as the $T_{R=0}$ criteria in resistivity data. Multiple $M(T)$ and $R(T)$ measurements were carried out on different samples, and the data are consistent with each other. The resulting anisotropic $H_{c2}(T)$ curves are shown in Fig 5.7, in which $H_{c2}(T)$ obtained from the magnetization data agrees with $H_{c2}(T)$ obtained from the resistivity data quite well. Linear extrapolations yielded a upper critical field of ~ 550 Oe at $T = 0$ K from $M(T)$ measurement, and $H_{c2}(T = 0) \approx 950$ Oe from $R(T)$ data. Both measurements clearly show that $BaSn_5$ maintains a rather small upper critical field. Despite of the difference in the H_{c2} values, both $M(T)$ and $R(T)$ support that $BaSn_5$ shows almost isotropic behaviour in its superconducting state as seen in Fig 5.7. It should be noticed that T_c and superconducting critical fields obtained for $BaSn_5$ in this work are different from that for elemental Sn used as flux ($T_c(\mathrm{Sn}) \approx 3.7$ K, and $H_{c2}(\mathrm{Sn}, T = 0) = 305$ Oe), which rules out traces of Sn flux in the crystals as the source of the superconducting behaviour.

The low temperature heat capacity of $BaSn_5$ was measured in both zero and applied magnetic field (Fig 5.8). It is clearly seen that the superconductivity is completely suppressed in 10 kOe without changing its normal state properties. A clear jump at about 4.4 K in the zero-field heat capacity data is associated with the superconducting transition, which gives $\Delta C_\mathrm{p}/T_\mathrm{c} \approx 16.7$ mJ/mol K^2. The lower left inset to Fig 5.8 shows the low temperature (down to 0.4 K), in-field (20 kOe), heat capacity data, the Sommerfeld coefficient for $BaSn_5$ is estimated to be $\gamma \approx 10.8$ mJ/mol K^2, and the Debye temperature $\Theta_\mathrm{D} \approx 182.5$ K. Thus, $\Delta C_\mathrm{p}/\gamma T_\mathrm{c}$ can be estimated to be about 1.55. This value is slightly higher than the canonical 1.43 value expected for isotropic weakly coupled

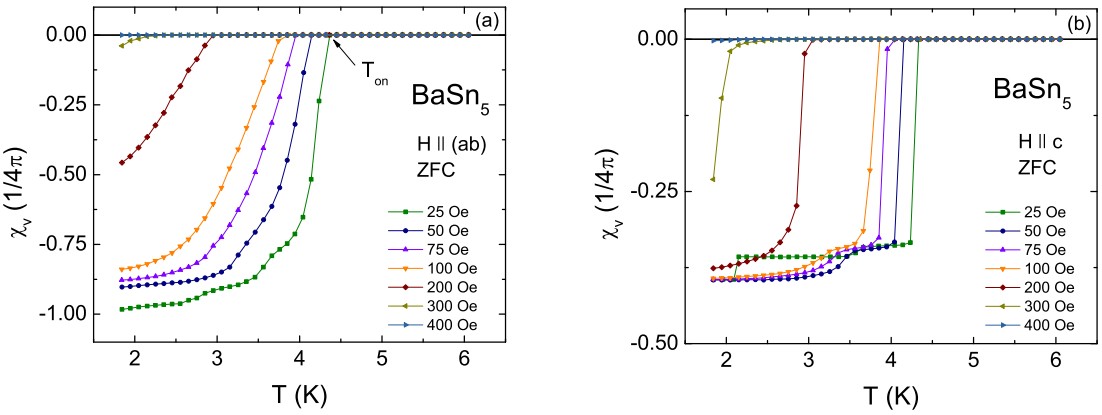

Figure 5.5 ZFC temperature-dependent magnetic susceptibility of $BaSn_5$ measured at 25, 50, 75, 100, 200, 300 and 400 Oe. (a) $H \| ab$ and (b) $H \| c$. Criteria for T_{onset} is shwn for the H= 25 Oe, $H \| ab$ data. [Lin et al., 2012c]

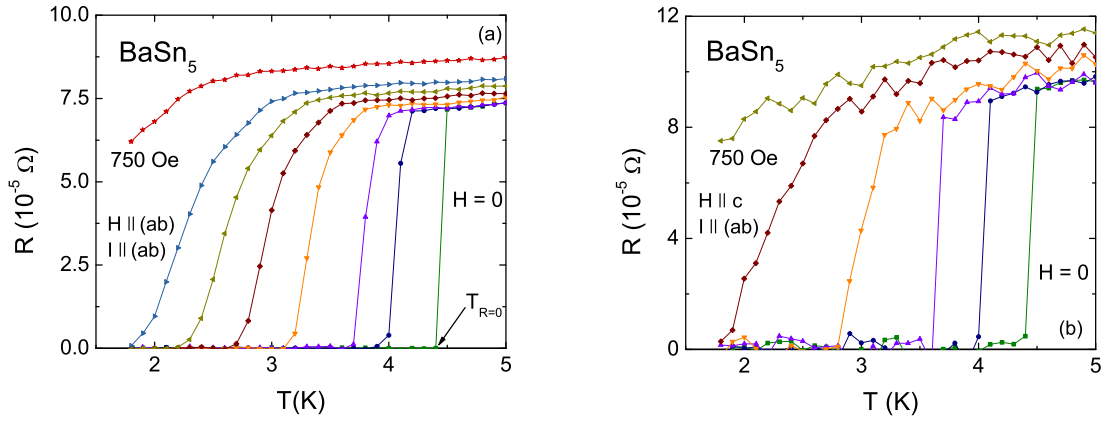

Figure 5.6 (a) Low temperature resistance of $BaSn_5$ measured at 0, 50, 100, 250, 500 and 750 Oe with $H \|$(ab). (b) Low temperature resistance of $BaSn_5$ measured at 0, 50, 100, 200, 300, 400, 500 and 750 Oe with $H \|$c. Criteria for $T_{R=0}$ is shown for the H= 0, $H \|$(ab) data. [Lin et al., 2012c]

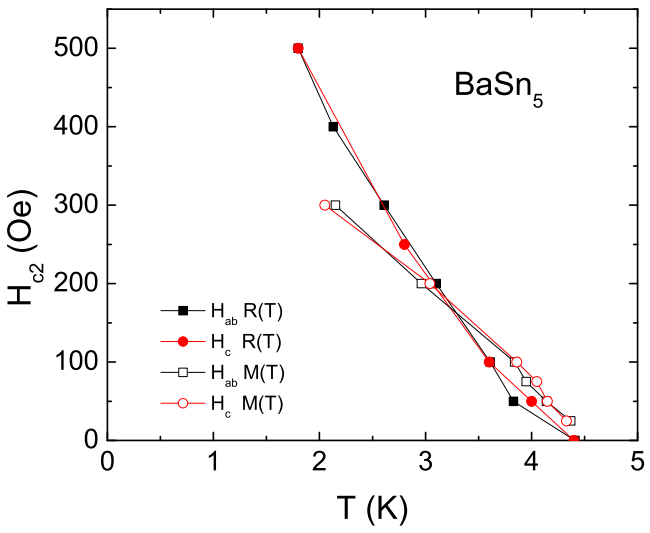

Figure 5.7 The upper critical field of $BaSn_5$ from magnetization and magnetotransport measurements. [Lin et al., 2012c]

BCS superconductor and suggests that $BaSn_5$ might be strongly coupled superconductor [Carbotte, 1990]. Finally, the $C_p(T)$ behaviour in the superconducting state (Fig 5.8, upper right inset) appears to be non-exponential and reasonably well described by $C_p \propto T^{2.8}$ function. If intrinsic, such dependence might point to deviations from isotropic single band superconductivity for this material.

The superconducting transition temperature of $BaSn_5$ linearly decreases under pressure up to ~ 8 kbar (Fig 5.9). The pressure derivative $dT_c/dP \approx -0.053 \pm 0.001$ K/kbar, is rather small, similar in sign and order of magnitude to those measured for a number of elemental and binary superconductors [Brandt and Ginzburg, 1965]. Such pressure dependence is possibly the result of rather weak dependence of the density of states on energy near the Fermi level as well as possibly opposing changes to T_c caused by shift in phonon spectrum by hydrostatic pressure.

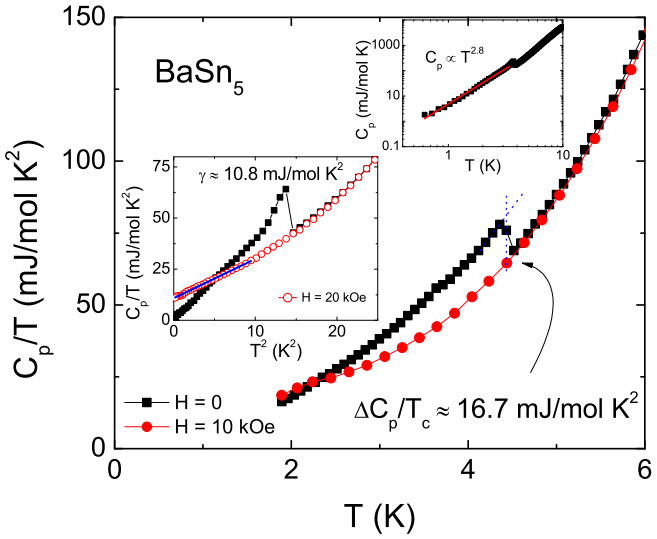

Figure 5.8 Low temperature heat capacity of $BaSn_5$ plotted as $C_p(T)$ versus T in zero and 10 kOe ($H\|$ ab) applied field. Lower left inset: Low temperature heat capacity of $BaSn_5$ plotted as $C_p(T)$ versus T^2 in zero and 20 kOe ($H\|$ ab) applied field, solid line – extrapolation of the low temperature linear region of the 20 kOe data. Upper right inset: zero field $C_p(T)$ data plotted on a log-log scale, the solid line corresponds to $C_p \propto T^{2.8}$. [Lin et al., 2012c]

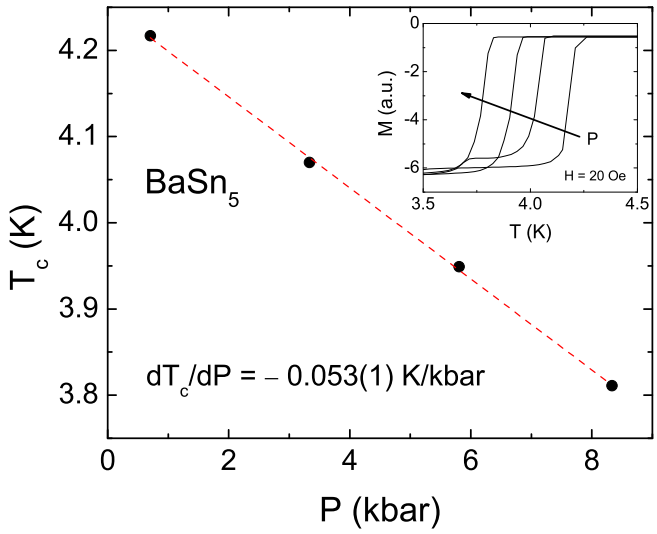

Figure 5.9 Pressure dependence of the superconducting transition temperature of $BaSn_5$. Dashed line – linear fit. Inset: low field magnetization under pressure, the arrow points in the direction of increasing pressure. [Lin et al., 2012c]

5.5 Summary

In this paper we present the synthesis of high quality single crystalline $BaSn_5$, as well as detailed studies on its thermodynamic and transport properties. $BaSn_5$ manifests metallic behavior in its normal state with (RRR) ~ 1200. Its normal-state magnetic susceptibility is diamagnetic and slightly anisotropic. De Haas-van Alphen oscillations were observed in low temperatures and high fields with the applied magnetic fields parallel to c-axis, two effective masses were resolved via FFT. $BaSn_5$ superconducts at ~ 4.4 K with the upper critical field not exceeding 1 kOe. H_{c2} shows almost isotropic behaviour. T_c decreases slowly under hydrostatic pressure up to 10 kbar. The heat capacity data suggest that superconductivity in $BaSn_5$ may be more complex than isotropic BCS.

Since both Haas-van Alphen oscillation and superconducting state are observed for these high-quality $BaSn_5$ single crystals, detailed study on angular dependence of the oscillatory behavior, Fermi topology and the symmetry of the superconducting state could be of interest.

CHAPTER 6. ANISOTROPIC MAGNETIZATION, RESISTIVITY AND HEAT CAPACITY OF SINGLE CRYSTALLINE $R_3Ni_{2-x}Sn_7$ (R = La, Ce, Pr and Nd)[1]

6.1 Abstract

We present a detailed study of $R_3Ni_{2-x}Sn_7$ (R = La, Ce, Pr and Nd) single crystals by measurements of crystal structure, stoichiometry, temperature dependent magnetic susceptibility, magnetization, electrical resistivity, magnetoresistance, and specific heat. This series forms with partial Ni occupancy with x varying from ~ 0.1 for R = La to ~ 0.7 for R = Nd. The electrical resistivity of this series follows metallic behavior at high temperatures. Determination of clear anisotropies as well as antiferromagnetic ordering temperatures for $R_3Ni_{2-x}Sn_7$ (R =Ce, Pr and Nd) have been made. For $Pr_3Ni_{1.56}Sn_7$ and $Nd_3Ni_{1.34}Sn_7$, multiple magnetic transitions take place upon cooling. Metamagnetic transitions in this family (R = Ce, Pr and Nd) were detected for applied magnetic fields below 70 kOe. An $H-T$ phase diagram of $Ce_3Ni_{1.69}Sn_7$ was assembled to shed light on its low field properties and to rule out possible quantum critical effects.

[1]This chapter is a version of the published article: Lin, X., Bud'ko, S. L., Thimmaiah, S. and Canfield, P. C. "Anisotropic magnetization, resistivity and heat capacity of single crystalline $R_3Ni_{2-x}Sn_7$ (R = La, Ce, Pr and Nd)" *J. Magn. Magn. Mater.*, 331 (2013):53

6.2 Introduction

Rare earth (R) compounds have always been of great interest to experimentalists and theorists for their various unusual magnetic, electronic and structural properties [Szytula and Leciejewicz, 1994; Gschneidner and Eyring, 978 ; Bud'ko et al., 1999; Sefat et al., 2008; Mun et al., 2010; Bud'ko and Canfield, 2000]. For the majority of rare-earth elements and compounds, the $4f$ electrons are shielded from the $5s$-, $5p$- and $4d$-shell electrons, and thus do not participate in chemical bonding. However, since the magnetic moments are from the $4f$ electrons, the R-bearing compounds can manifest vastly different magnetic properties. By varying the R elements in a compound, it is possible to tune the magnetism and other physical properties. Known as the lanthanide contraction, the unit cell volume of isostructural R^{3+}-bearing families shrink across the series. This contraction can lead to systematic changes in the lattice constants *a, b, c*, and maybe eventually drive the series out of its structural stability. In addition, the crystalline electric field (CEF) also plays a significant role in determining the temperature-dependent thermodynamic and transport properties of a compound. Associated with the point symmetry of the R ions, the CEF splitting can cause anisotropy, and influence the spin arrangements in the ordered state, often affecting the details of metamagnetic transitions. In terms of the ordering temperature and energy scales, the CEF splitting affects the amount of entropy (associated with the $4f$ electrons) that can be removed. Thus, a comparative study of a series of rare-earth compounds can give an insight into the evolution of the rich and complex physics. Here, we present a study of physical properties of single crystalline samples of the $R_3Ni_{2-x}Sn_7$ (R = La, Ce, Pr and Nd) series.

The early report of $R_3Ni_{2-x}Sn_7$ can be traced back to late 1980s [Skolozdra et al., 1987]. The structure was solved based on polycrystalline samples of $R_3Ni_2Sn_7$ (R = La, Ce, Pr and Nd). Based on neutron diffraction [Schobinger Papamantellos et al., 2001], Ni and Sn sites were reported to have partial occupancies. Although magnetic

susceptibility, electrical resistivity and thermopower of this series were measured between 78-350 K, practically no low-temperature properties were reported for R = La, Pr and Nd.

Later studies were focused on $Ce_3Ni_2Sn_7$ polycrystalline samples [Schobinger Papamantellos et al., 2001; Chevalier and Etourneau, 1999; Chevalier et al., 2001; Matar et al., 2003]. The ground state of Ce-based intermetallic compounds is often governed by the competition between the Ruderman-Kittel-Kasuya-Yosida (RKKY) interaction and the Kondo interaction. Depending on the strength of the hybridization between $4f$ and conduction electrons relative to their coupling strength, the ground state can be either a non-magnetic state dominated by the Kondo interaction or a long-range magneticly ordered state governed by the RKKY interaction. $Ce_3Ni_2Sn_7$ is reported to order antiferromagneticly at $T_N \sim 3.8$ K [Schobinger Papamantellos et al., 2001; Chevalier and Etourneau, 1999]. $Ce_3Ni_2Sn_7$ crystallizes in the orthorhombic structure ($Cmmm$, No. 65) [Skolozdra et al., 1987; Schobinger Papamantellos et al., 2001] and Ce occupies two different crystallographic sites (the Ce1 *2c* site: *mmm* and the Ce2 *4i* site: *m2m*), but studies have shown that only the Ce2 atoms with a trigonal prism arrangement participate in the magnetic ordering [Schobinger Papamantellos et al., 2001]. Moreover, based on measurements on polycrystalline $Ce_3Ni_2Sn_7$, metamagnetic transitions at low temperatures were inferred, indicating a complex spin arrangement [Chevalier et al., 2001]. Since metamagnetism in rare earth compounds is usually very anisotropic, single crystals are required for systematic studies.

In this paper, we present a systematic study of the anisotropic properties of the $R_3Ni_{2-x}Sn_7$ series with R = La, Ce, Pr and Nd. Since this system shows partial occupancy of the Ni site, a detailed structural study and refinement of the site occupancies are also provided in this work. Measurements and analyses of the field and temperature dependence of magnetization, resistivity and specific heat were performed on single crystalline samples. Measurements of the magnetization parallel to the b-axis and the

ac-plane show anisotropic behavior, and the magnetization of some of the compounds manifest metamagnetic transitions.

6.3 Experimental details

Single crystals of $R_3Ni_{2-x}Sn_7$ (R = La, Ce, Pr and Nd) were grown out of excess Sn flux via the high-temperature solution method [Canfield and Fisk, 1992]. High purity elements (>3N), with an initial composition of 9:18:73 (R:Ni:Sn) were used in the synthesis. The constituent elements were placed in an alumina crucible and sealed in a silica tube under a partial pressure of high purity argon gas. This was then heated up to 1100°C and slowly cooled to 800°C, at which temperature the excess solution was decanted using a centrifuge. Single crystals of $R_3Ni_2Sn_7$ grew in plate-like shape with their largest dimensions limited to the size of the crucible (see inset of Fig. 6.1). The crystallographic b-axis is perpendicular to the plane of the plate-like single crystals. Most of the samples had shiny surfaces that were partially covered by secondary phase materials. Since HCl was found to attack the surface material as well as $R_3Ni_{2-x}Sn_7$, and due to Sn's malleable nature, the samples were not etched or polished in the following measurements. Although all samples in this study were grown from the same initial stoichiometry, a significant and variable Ni deficiency ($R_3Ni_{2-x}Sn_7$) develops as R changes from La to Nd.

Powder x-ray diffraction data were collected on a Rigaku MiniFlex diffractometer with Cu Kα radiation at room temperature. The error bars were determined by statistical errors, and standard Si powder was used as the internal reference.

Single crystal x-ray diffraction data were collected by Bruker APEX diffractometer equipped with a CCD detector, using monochromated Mo Kα radiation (λ = 0.71073 Å). Reflections were gathered by taking three sets of 606 frames with 0.3° scans in ω and with an exposure time of 10 s per frame at room temperature. The range of 2θ

extended from $\sim$ 4 to 57°. The reflection intensities were integrated with the *SAINT* program. The measured intensities were corrected for Lorentz and polarization effects and were further corrected for absorption using the *SADABS* program as implemented in the *SAINT* [SMART, 2005] program package. Intensity statistics and space group determination were carried out using *XPREP*, a subprogram in the *SHELXTL* software package. The structural models were obtained from direct methods using *SHELXS*-97 and refined by fullmatrix, leastsquares procedures on F^2 as implemented in the *SHELXTL* [SHELXTLPlus, 2003] package.

Elemental analysis of the samples was performed using wavelength dispersive x-ray spectroscopy (WDS) in the electron probe microanalyzer of a JEOL JXA-8200 Superprobe. For each compound, the WDS data were collected from multiple locations on multiple samples. To determine the bulk concentration, only clear and shiny surface regions were selected for these measurement, i.e. regions with residual Sn flux were avoided.

Measurements of field dependent magnetization and temperature dependent susceptibility were performed in a Quantum Design, Magnetic Property Measurement System (MPMS). The ac resistivity was measured by a standard four-probe method in a Quantum Design, Physical Property Measurement System (PPMS) and with LR700 ac resistance bridge in MPMS. Platinum wires were attached to the sample using either Dupont 4929 silver paint or Epotek H20E silver epoxy with the current flowing in the *ac*-plane. As mentioned above, given the malleable nature of the flux and fragile samples, no polishing was done prior to the resistivity measurement. The room temperature resistivity of this series ranges from 50 - 100 $\mu\Omega$ cm. The absolute values of resistivity are accurate to $\pm$ 50% due to the irregularity of the sample geometry and positions of electrical contacts. For data presentation, the basal plane resistivity is normalized with respect to the room temperature value assuming that current density was uniformly distributed throughout the cross section. The residual resistivity ratio is determined as (RRR) =

Table 6.1 Refined unit cell parameters refined from powder x-ray diffraction for $R_3Ni_{2-x}Sn_7$ (R= La, Ce, Pr and Nd) compounds. [Lin et al., 2013a]

R	a (Å)	b (Å)	c (Å)	V (Å^3)
La	4.599(16)	27.549(24)	4.602(10)	583(3)
Ce	4.564(11)	27.276(76)	4.558(10)	567(4)
Pr	4.547(15)	27.2162(10)	4.546(5)	563(2)
Nd	4.530(12)	27.111(49)	4.529(7)	556(2)

ρ(300 K) / ρ(6.5 K) for $La_3Ni_{1.89}Sn_7$; and (RRR) = ρ(300 K) / ρ(1.8 K, 0.5 kOe) for $R_3Ni_{2-x}Sn_7$ (R = Ce, Pr and Nd). To remove the high frequency noise caused by digital differentiation of closely spaced data points, an FFT filter method provided by Origin 8.5 program was used in calculating the temperature and field derivatives of ρ and M [Origin-8.5,].

A relaxation technique was used in the heat capacity measurements in the PPMS. The specific heat data of $La_3Ni_{1.89}Sn_7$ was used to estimate the non-magnetic contributions to the specific heat of $R_3Ni_{2-x}Sn_7$ (R = Ce, Pr and Nd). Here we assume the differences in non-magnetic specific heat brought by different Ni site deficiencies are negligible. The magnetic contribution to specific heat from the R ions was calculated by the relation of $C_M = C_p$ ($R_3Ni_{2-x}Sn_7$) - C_p ($La_3Ni_{1.89}Sn_7$). A linear extrapolation was used to estimate C_M's behavior down to zero temperature. The magnetic entropy S_M for R = Ce, Pr and Nd members was calculated by integrating C_M/T per mole R with the measured and extrapolated data.

6.4 Results

6.4.1 Crystal stoichiometry and structure

Powder x-ray diffraction patterns were collected on ground single crystals from each compound. Figure 6.1 shows a $La_3Ni_{1.89}Sn_7$ x-ray pattern as an example. The main phase was resolved to be $La_3Ni_{1.89}Sn_7$, and small traces of Sn residue as well as $LaSn_3$

Table 6.2 Unit cell parameters and Ni site occupancies obtained from single crystal x-ray diffraction for $R_3Ni_{2-x}Sn_7$ (R= La, Ce, Pr and Nd). [Lin et al., 2013a]

R	a (Å)	b (Å)	c (Å)	V (Å^3)	2-x (Ni)	Stoichiometry
La	4.6033(6)	27.578(4)	4.6133(6)	585.66(13)	1.89(1)	$La_3Ni_{1.89}Sn_7$
Ce	4.5565(15)	27.300(9)	4.5720(15)	568.7(3)	1.69(1)	$Ce_3Ni_{1.69}Sn_7$
Pr	4.5260(16)	27.173(10)	4.5475(16)	559.3(3)	1.56(1)	$Pr_3Ni_{1.56}Sn_7$
Nd	4.5193(17)	27.091(10)	4.5408(17)	555.9(4)	1.34(1)	$Nd_3Ni_{1.34}Sn_7$

can be detected in the diffraction pattern. Similar results ($R_3Ni_{2-x}Sn_7$ with minority phases of RSn_3 and Sn) were obtained for the other members of the series. The analysis of powder x-ray diffraction data indicates that the lattice parameters a, b and c are monotonically decreasing as the series progresses from La to Nd (presented in Table 6.1).

Since site occupancy was identified as a potential problem [Schobinger Papamantellos et al., 2001], room-temperature single crystal diffraction data were also collected. Table 6.2 summarizes the lattice constants and Ni site occupancies. The refined positional parameters for $R_3Ni_{2-x}Sn_7$ (R=La, Ce, Pr and Nd) series are included in Table 6.3. Proceeding from the larger to the smaller rare-earth elements, all lattice parameters decrease almost linearly: 1.8% for a; 1.8% for b and 1.6% for c (as shown in Fig. 6.2), which is consistent with the results of powder x-ray analysis (Table 6.1) and previously reported data [Skolozdra et al., 1987]. Furthermore, the overall volume decreases by 5.1%. These results are due to the lanthanide contraction that occurs across the 4f series as well as the decreasing Ni occupancy. The ionic radius of trivalent rare-earth was taken from ref. [Shannon, 1976] for 9 coordination number (CN=9).

The stoichiometry of the $R_3Ni_{2-x}Sn_7$ (R = La, Ce, Pr and Nd) samples was also inferred from WDS analyses. The averaged atomic percentages of each element in each compound are normalized to $R_{3.00}$ (Table 6.4). The results show that although the ratio of R:Ni:Sn is close to 3:2:7, significant Ni deficiency develops as the atomic number of

Table 6.3 Atomic coordinates and isotropic displacement parameters for $R_3Ni_{2-x}Sn_7$ (R= La, Ce, Pr and Nd) single crystals. [Lin et al., 2013a]

Atom	Site	Occupancy	x	y	z	Ueq
La1	$2c$	1	0.5	0	0.5	0.09(1)
La2	$4i$	1	0	0.1843(1)	0	0.09(1)
Ni1	$4j$	0.95(1)	0	0.3718(1)	0.5	0.11(1)
Sn1	$2a$	1	0	0	0	0.15(1)
Sn2	$4i$	1	0	0.4102(1)	0	0.12(1)
Sn3	$4j$	1	0	0.0900(1)	0.5	0.12(1)
Sn4	$4j$	1	0	0.2813(1)	0.5	0.12(1)
Ce1	$2c$	1	0.5	0	0.5	0.10(1)
Ce2	$4i$	1	0	0.1846(1)	0	0.11(1)
Ni1	$4j$	0.85(1)	0	0.3718(1)	0.5	0.13(1)
Sn1	$2a$	1	0	0	0	0.11(1)
Sn2	$4i$	1	0	0.4098(1)	0	0.14(1)
Sn3	$4j$	1	0	0.0902(1)	0.5	0.14(1)
Sn4	$4j$	1	0	0.2821(1)	0.5	0.16(1)
Pr1	$2c$	1	0.5	0	0.5	0.09(1)
Pr2	$4i$	1	0	0.1851(1)	0	0.10(1)
Ni1	$4j$	0.78(1)	0	0.3716(1)	0.5	0.13(1)
Sn1	$2a$	1	0	0	0	0.12(1)
Sn2	$4i$	1	0	0.4090(1)	0	0.14(1)
Sn3	$4j$	1	0	0.0912(1)	0.5	0.14(1)
Sn4	$4j$	1	0	0.2823(1)	0.5	0.18(1)
Nd1	$2c$	1	0.5	0	0.5	0.10(1)
Nd2	$4i$	1	0	0.1855(1)	0	0.11(1)
Ni1	$4j$	0.67(1)	0	0.3715(1)	0.5	0.13(1)
Sn1	$2a$	1	0	0	0	0.14(1)
Sn2	$4i$	1	0	0.4084(1)	0	0.15(1)
Sn3	$4j$	1	0	0.0919(1)	0.5	0.16(1)
Sn4	$4j$	1	0	0.2830(1)	0.5	0.21(1)

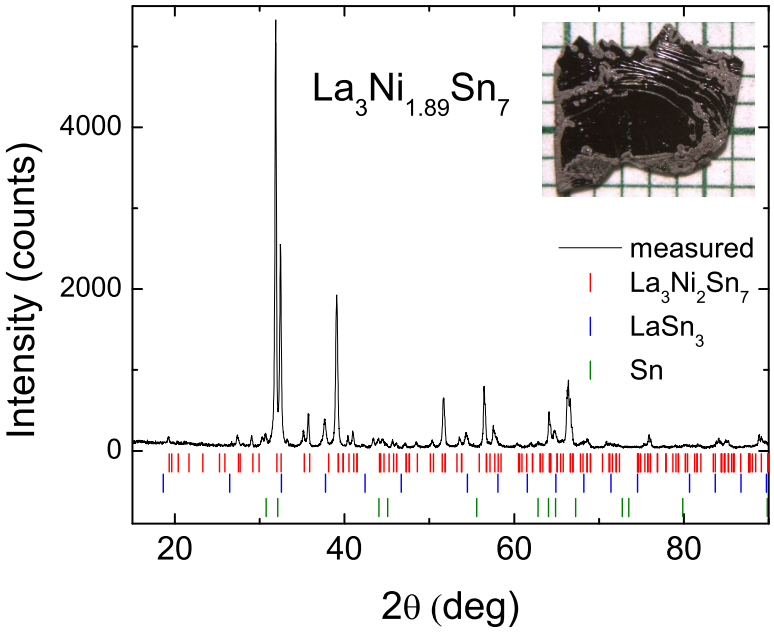

Figure 6.1 Powder x-ray diffraction pattern of $La_3Ni_{1.89}Sn_7$. Inset: picture of single crystalline $La_3Ni_{1.89}Sn_7$ on a millimeter grid. [Lin et al., 2013a]

rare earth elements increases. The stoichiometries inferred from the WDS and single crystal diffraction data are qualitatively similar (Table 6.2 and 6.4). Although there are slight quantitative differences, the clear trend in all increasing Ni deficiency from La to Nd is clear.

Given this series of compounds does not maintain a fixed, stoichiometric composition for all rare-earth samples, the calculation of physical quantities, such as the magnetization and specific heat, the actual stoichiometries from Table 6.2 will be used.

6.4.2 $La_3Ni_{1.89}Sn_7$

The magnetic susceptibility of $La_3Ni_{1.89}Sn_7$ measured in an applied field of 50 kOe (Fig. 6.3(a)), is negative and exhibits an almost temperature independent behaviour from 2 K to 300 K. It also manifests a relatively large anisotropy between the magnetic

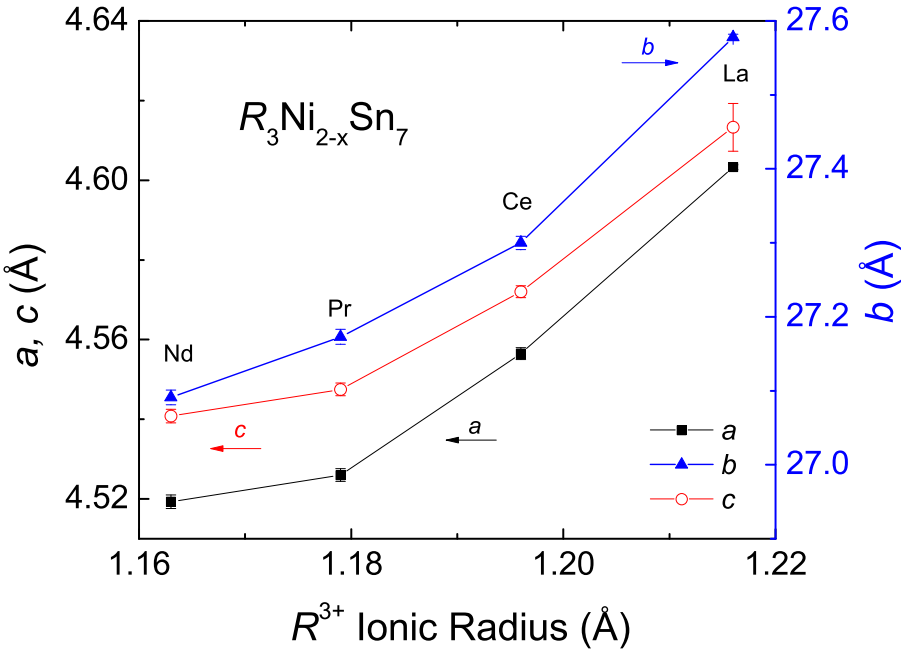

Figure 6.2 The change of unit cell lattice parameters vs. ionic radius of R^{3+} [Shannon, 1976] in $R_3Ni_{2-x}Sn_7$ compounds, refined from single crystal x-ray diffraction data. [Lin et al., 2013a]

Table 6.4 WDS elemental analysis (in atomic %) for $R_3Ni_{2-x}Sn_7$ single crystals. [Lin et al., 2013a]

Compound	R	Ni	Sn	Stoichiometry (WDS)
La	23.67	15.78	57.23	$La_3Ni_{2.00}Sn_{7.25}$
Ce	25.73	14.80	59.47	$Ce_3Ni_{1.72}Sn_{6.93}$
Pr	25.47	13.83	60.70	$Pr_3Ni_{1.63}Sn_{7.15}$
Nd	26.39	12.44	61.16	$Nd_3Ni_{1.41}Sn_{6.95}$

field parallel to the b-axis and the ac-plane, with $|(M/H)_b| > |(M/H)_{ac}|$. Neither the diamagnetism nor anisotropy is uncommon, similar behaviors have been reported for other La-based compounds [Sefat et al., 2008; Myers et al., 1999].

In Fig. 6.3(b), the temperature dependence of the normalized zero-field resistivity ratio of $La_3Ni_{1.89}Sn_7$ displays metallic behaviour with (RRR) $\simeq 3.2$ for current in the ac-plane. To within a factor of 20%, the room temperature resistivity value $\rho(300\ \mathrm{K})$ reaches $\sim 50\ \mu\Omega$ cm. We assume that this small RRR is at least partially due to the deficiencies at the Ni site. At low temperatures, two resistive anomalies are observed near 6.2 K and 3.8 K (inset of fig. 6.3(b)). When measured in an applied magnetic field of 1.0 kOe, the higher-temperature anomaly shifts to lower temperature and the lower one disappears. The ZFC and FC superconducting fractions are also estimated by magnetization measurement at 25 Oe with the field parallel to the ac-plane, as shown in the inset of Fig. 6.3(a). The small values of FC superconducting fractions, $\sim 1.4\%$, and ZFC fraction, as well, $< 15\%$ indicate that superconductivity is filamentary and the anomalies in the resistivity can be attributed to impurities. In fact, it is highly likely that these two anomalies are related to the superconducting transitions of $LaSn_3$ ($T_c \approx$ 6.2 K [Gambino et al., 1968]) and Sn ($T_c \approx 3.7$ K); both phases being seen in the powder diffraction pattern shown in Fig. 6.1.

Figure 6.4 shows the temperature-dependent specific heat C_p for $La_3Ni_{1.89}Sn_7$. C_p increases smoothly up to 50 K showing no resolvable features at low temperatures, confirming the anomalies seen in zero-field resistivity are brought by the impurity phases. The electronic specific heat coefficient (γ) and Debye temperature (Θ_D) were estimated using the relation $C_p/T = \gamma + \beta T^2$ by extrapolating data C_p/T vs. T^2 below 7 K (shown in the inset of Fig. 6.4). The calculated values are $\gamma \approx 10$ mJ/mol-formula-unit K^2 (or less than 1 mJ/mole-atomic K^2), and $\beta \approx 1.5$ mJ/mol-formula-unit K^4, which gives $\Theta_D \approx 250$ K.

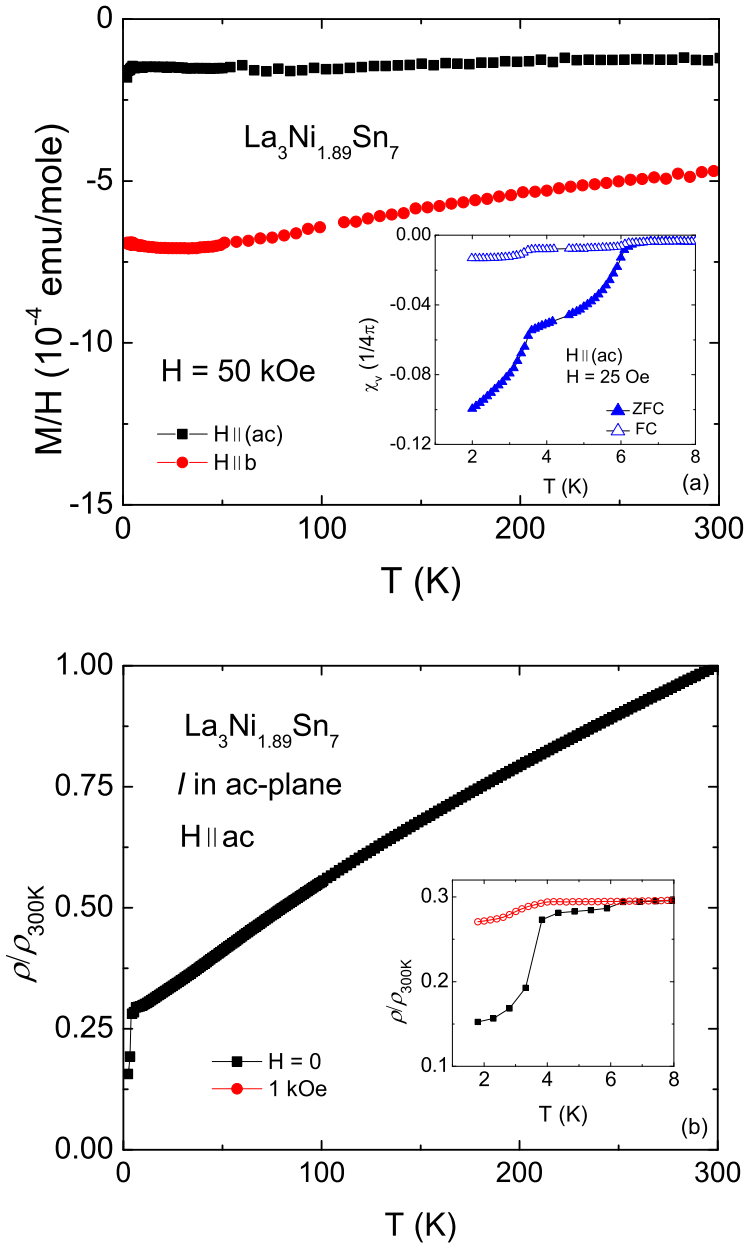

Figure 6.3 (a) Magnetic susceptibility of $La_3Ni_{1.89}Sn_7$ for $H = 50$ kOe, with fields both parallel to b-axis and ac-plane. Inset: ZFC and FC magnetic susceptibility for $H = 25$ Oe. (b) Temperature dependence of the normalized resistivity ratio of $La_3Ni_{1.89}Sn_7$ with $\rho(300\text{ K}) \sim 50\ \mu\Omega$ cm. Inset: enlarged normalized resistivity ratio for $T \leq 8$ K in zero field and 1.0 kOe. [Lin et al., 2013a]

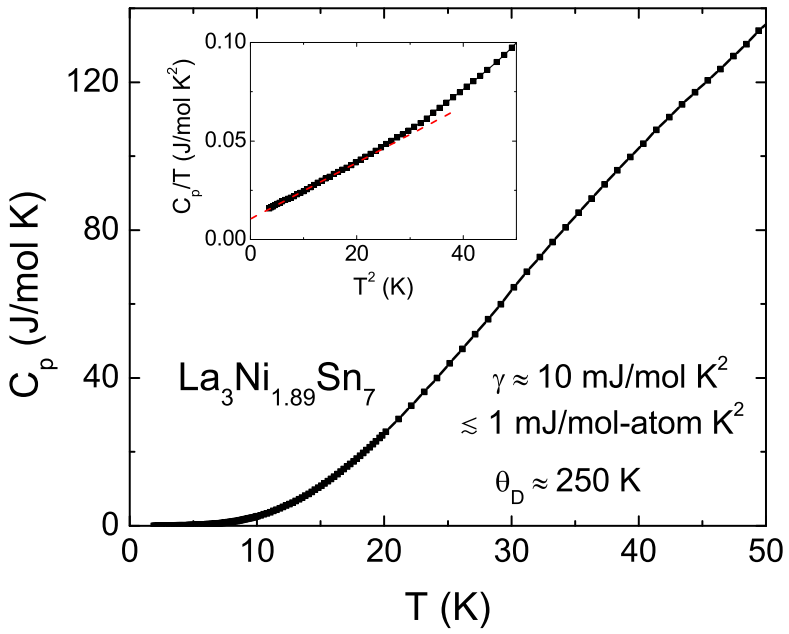

Figure 6.4 Temperature dependence of specific heat of $La_3Ni_{1.89}Sn_7$ in the form of $C_p(T)$ vs. T. Inset: C_p/T vs. T^2; dashed line is guide to the eye.[Lin et al., 2013a]

6.4.3 $Ce_3Ni_{1.69}Sn_7$

The temperature-dependent magnetic susceptibility $\chi(T) = M(T)/H$ and inverse magnetic susceptibility of $Ce_3Ni_{1.69}Sn_7$ were measured with $H = 1$ kOe applied both parallel to the b-axis and the ac-plane, and are plotted in Fig. 6.5(a). The sharp peaks seen at low temperature suggest that this material has an AFM transition, with a larger value of $M(T)/H$ for $\mathbf{H} \parallel ac$-plane for $T < 15$ K. The ordering temperature, consistent with the reported value [Schobinger Papamantellos et al., 2001; Chevalier and Etourneau, 1999], was estimated to be $\sim$ 3.7 K (here and in Table 6.5 the values of the magnetic ordering temperatures obtained from the maximum of the derivatives $\mathrm{d}(\chi T)/\mathrm{d}T$, $\mathrm{d}\rho/\mathrm{d}T$, and/or the specific heat data are quoted). The polycrystalline averaged susceptibility was estimated by $\chi_{ave} = \frac{1}{3}\,(\chi_b + 2\chi_{ac})$. The high-temperature magnetic susceptibility can be fitted with the Curie-Weiss law with θ_b = -43.6 K, θ_{ac} = -75.4 K and θ_{ave} = -57.1 K. The inferred effective moment from the polycrystalline averaged data: $\mu_{eff} = 2.44(1)\ \mu_B$/Ce is slightly smaller than the expected Hund's rule ($J = 5/2$) ground-state value, 2.54 μ_B, but larger than previously reported, 2.33 μ_B/Ce [Chevalier and Etourneau, 1999]. It should be noted that the anisotropy changes its sign upon cooling in the paramagnetic state (as can be seen by comparing Fig. 6.5(a) inset to main body of 6.5(a)).

The temperature-dependence of the normalized electrical resistivity ratio $\rho(T)/\rho(300$ K) for $Ce_3Ni_{1.69}Sn_7$ is shown in Fig. 6.5(b). To within a factor of 50%, the room temperature resistivity $\rho(300\mathrm{K})$ reaches approximately 70 $\mu\Omega$ cm, with (RRR) $\simeq$ 3.0. A broad feature is found at around 60 K, which is probably associated with thermal population of the CEF levels. A dramatic drop in the zero-field resistivity value at $\sim$ 3.7 K can be attributed to the near simultaneous occurrence of the T_c of the minority Sn phase and a bulk AFM transition. The inset of Fig. 6.5(b) shows $\rho(T)/\rho(300$ K) below 8 K measured at zero field, 1 kOe and 70 kOe for field parallel to the ac-plane. The sharp drop in resistivity below 4 K is due, in part, to traces of Sn, but as shown in Fig. 6.5(b) $T_N \sim 3.7$ K as well. The 1 kOe data show the decrease in resistivity is smaller than

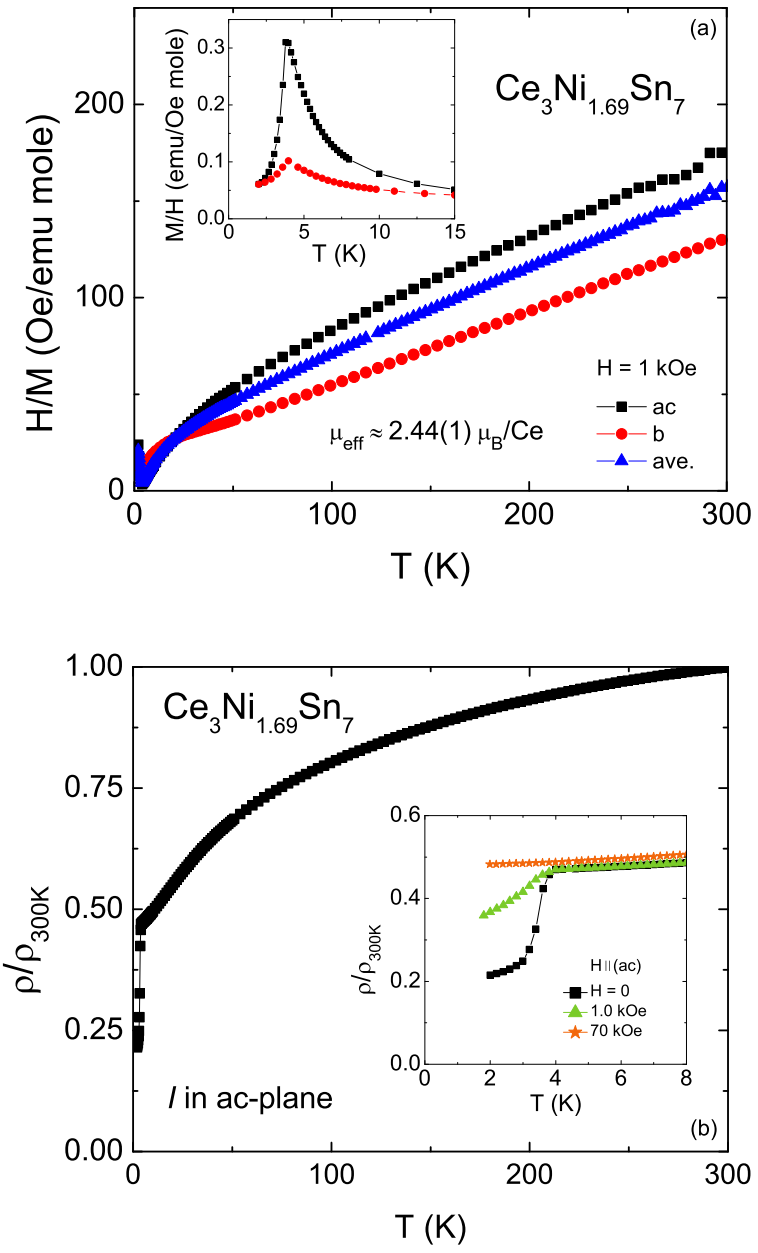

Figure 6.5 (a) Inverse magnetic susceptibility $H/M(T)$ of $Ce_3Ni_{1.69}Sn_7$ for $\mathbf{H} \parallel b$-axis, ac-plane and polycrystalline average. Inset: anisotropic magnetic susceptibility below 15 K. (b) Temperature dependence of the normalized electrical resistivity ratio $\rho(T)/\rho(300\ \mathrm{K})$ of $Ce_3Ni_{1.69}Sn_7$ with $\rho(300\ \mathrm{K}) \sim 50\ \mu\Omega$ cm. Inset: low temperature $\rho(T)/\rho(300\ \mathrm{K})$ measured at $H = 0$, 1 and 70 kOe with $\mathbf{H} \parallel ac$-plane. [Lin et al., 2013a]

in zero field, however, the transition temperature does not change significantly. For the two possible secondary phases in this material, whereas Sn has an upper critical field of 305 Oe at 0 K, no magnetic ordering or superconductivity has been observed for $CeSn_3$ down to low temperatures [Shenoy et al., 1970]. Thus, the sharp drop at 3.7 K for $H = 1$ kOe is primarily caused by the loss of spin disorder scattering. In a higher applied field, 70 kOe, the magnetic ordering has been completely suppressed and no anomaly can be seen (see discussion of metamagnetism below).

The specific heat data manifest a sharp rise with decreasing temperature below 6 K, which peaks at $\sim$ 3.7 K (Fig. 6.6(a)). The AFM ordering temperature can be clearly determined as shown in Fig. 6.6(b), which displays the $\mathrm{d}(\chi T)/\mathrm{d}T$, $\mathrm{d}\rho/\mathrm{d}T$ (to suppress Sn's superconducting feature, data of $H = 0.5$ kOe was used), and $C_M(T)$ curves. Each of these data sets gives $T_\mathrm{N} = 3.7 \pm 0.1$ K.

Due to the AFM ordering and the broad feature associated with the CEF splitting at higher temperatures, γ and Θ_D of $Ce_3Ni_{1.69}Sn_7$ cannot be estimated by the same method used with $La_3Ni_{1.89}Sn_7$. On the other hand, though, the magnetic contribution to specific heat from the Ce ions was calculated by the relation of $C_M = C_p$ ($Ce_3Ni_{1.69}Sn_7$) - C_p ($La_3Ni_{1.89}Sn_7$). C_M data show a broad maximum centered around 45 K, indicating a significant magnetic contribution from the Ce ions above T_N. This broad peak is likely brought by an electric Schottky contribution due to the CEF splitting of the Hund's rule ground state multiplet. The magnetic entropy per mole Ce ion is shown in the inset of Fig. 6.6(a). The S_M reaches about 60% of $R\ln(2)$ at T_N and recovers the full doublet entropy, $R\ln(2)$, by 25 K. This might be caused by the Kondo screening of Ce magnetism, or as suggested by a previous neutron study [Schobinger Papamantellos et al., 2001], not all the Ce ions are participating in the AFM ordering.

The measurements of the low-temperature $M(T)$ with $\mathbf{H} \parallel ac$-plane for various applied fields are plotted in Fig. 6.7. With increasing magnetic field AFM transition systematically shifts to lower temperatures and eventually drops below 2 K for $H >$

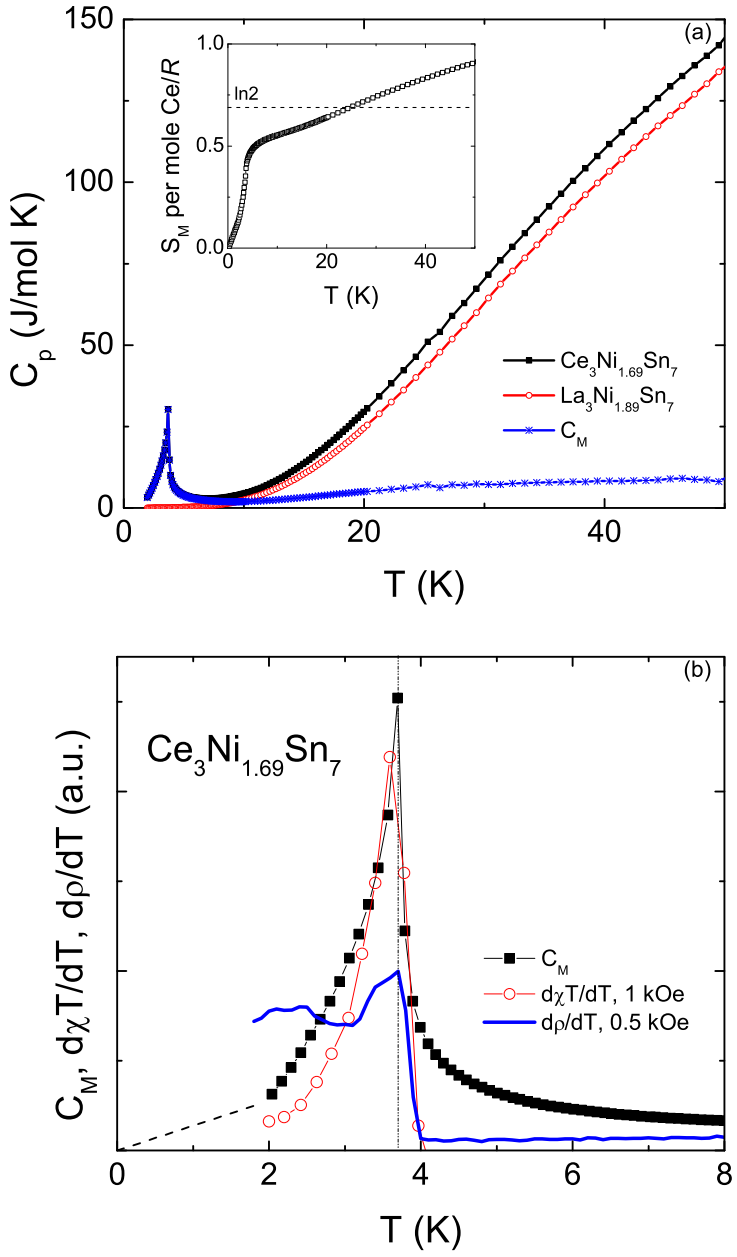

Figure 6.6 (a) Specific heat of $Ce_3Ni_{1.69}Sn_7$ and $La_3Ni_{1.89}Sn_7$ single crystals and the magnetic specific heat of $Ce_3Ni_2Sn_7$. Inset: magnetic entropy per mole Ce ion divided by R. (b) Low-temperature $\mathrm{d}(\chi T)/\mathrm{d}T$ for $H = 1$ kOe, $\mathrm{d}\rho/\mathrm{d}T$ for $H = 0.5$ kOe and $C_M(T)$ for $Ce_3Ni_{1.69}Sn_7$. The dashed line indicates $C_M(T)$ extrapolated to $T = 0$. The antiferromagnetic ordering temperature marked by dotted line shows up as a sharp, well-defined peak in all three data sets. [Lin et al., 2013a]

8 kOe. For $H = 5.5$ kOe and 6.5 kOe, another feature emerges at low temperatures, shown as a cusp at ~ 2 K. However, the origin of this feature and its absence at 6.0 kOe are currently unknown. At higher fields, $H > 8$ kOe, $M(T)$ does not reveal any signature of a phase transition and instead displays a tendency toward saturation at low temperatures.

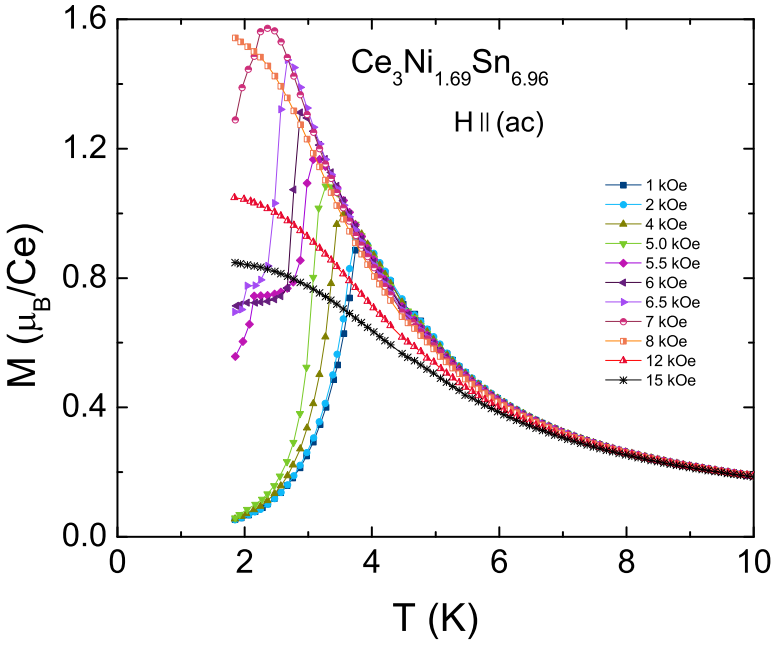

Figure 6.7 $M(T)$ of $Ce_3Ni_{1.69}Sn_7$ for $\mathbf{H} \parallel ac$-plane in selected magnetic fields. [Lin et al., 2013a]

The anisotropic $M(H)$ isotherms of $Ce_3Ni_{1.69}Sn_7$ are plotted in the inset of Fig. 6.8. The observed curves show significant anisotropic behavior at 2 K. For $\mathbf{H} \parallel b$-axis, $M(H)$ linearly increases with field up to 40 kOe, followed by a broad metamagnetic transition, then linearly rises to about 0.36 μ_B per Ce ion near 70 kOe. On the other hand, for $\mathbf{H} \parallel ac$-plane, at least two metamagnetic transitions take place below 10 kOe, which can be clearly seen in the main body of Fig. 6.8 and also indicated in the $dM(H)/dH$ analysis in Fig. 6.9(a). In higher fields, $M(H)$ with $\mathbf{H} \parallel ac$-plane linearly approaches to 0.81 μ_B

per Ce near 70 kOe, which is well below the expected full moment of 2.14 μ_B/Ce.

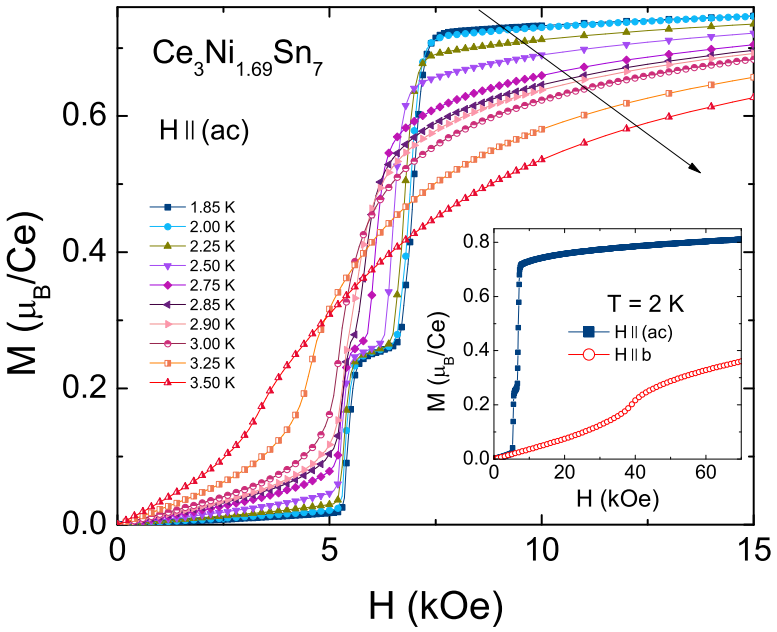

Figure 6.8 Magnetization isotherms of $Ce_3Ni_{1.69}Sn_7$ for $\mathbf{H} \parallel (ac)$ at T = 1.85, 2.00, 2.25, 2.50, 2.50, 2.75, 2.85, 2.90, 3.00, 3.25 and 3.50 K. The arrow indicates the direction of increasing temperature. Inset: anisotropic field-dependent magnetization of $Ce_3Ni_{1.69}Sn_7$ at 2 K. [Lin et al., 2013a]

Figure 6.8 presents the temperature-dependent evolution of the metamagnetic transitions for $\mathbf{H} \parallel ac$-plane. As temperature increased, both metamagnetic transitions were gradually broadened and eventually smeared out at 3.5 K. An examination of the hysteresis associated with metamagnetic transitions is shown in Fig. 6.9(a), $M(H)$ at 1.85 K and $dM(H)/dH$ are plotted for $Ce_3Ni_{1.69}Sn_7$. The two metamagnetic transitions manifest as two distinct steps, and the hysteresis can been clearly resolved in $M(H)$. Correspondingly, the derivatives reveal the metamagnetic transitions at lower and higher field (indicated as 1 and 2 in the subscript, respectively) during the process of increasing and decreasing magnetic fields (indicated as up and down in the superscript, respectively):

$H_1^{\rm down} = 5.25$ kOe, $H_1^{\rm up} = 5.41$ kOe, $H_2^{\rm down} = 6.95$ kOe and $H_2^{\rm up} = 6.96$ kOe (Fig. 6.9(a)). Similarly, the derivatives $dM(H)/dH$ at different temperatures provide the temperature evolution of metamagnetic transitions in Fig. 6.9(b). As temperature increases, the two metamagnetic transition peaks systematically shift to lower fields and broaden. At 3.0 K, the two metamagnetic transitions merge into one and eventually vanishes at ~ 3.5 K.

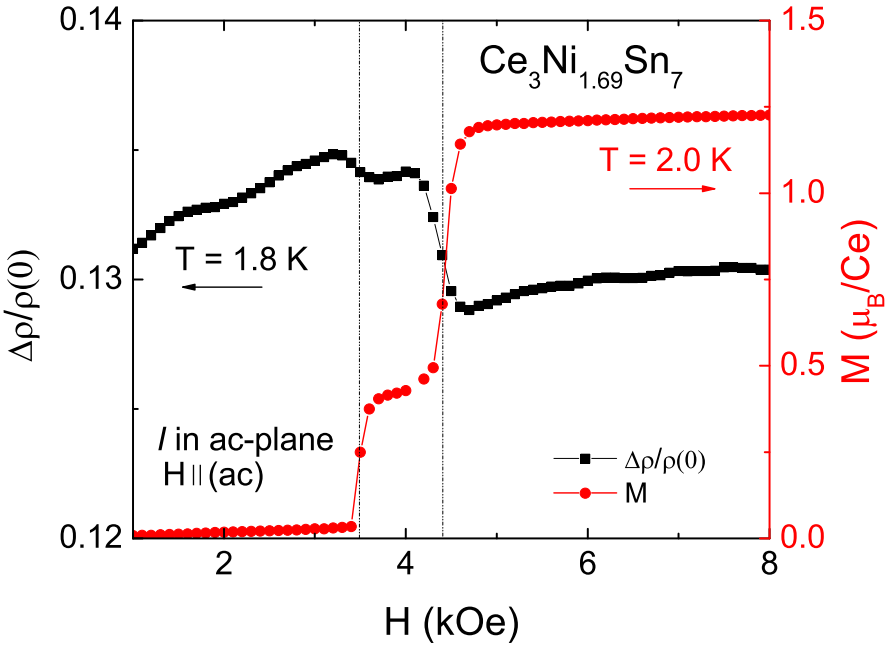

Figure 6.9 (a) Magnetization hysteresis data and $dM(H)/dH$ for $\mathbf{H} \parallel (ac)$ at $T = 1.85$ K. $H_1^{\rm down}$, $H_1^{\rm up}$, $H_2^{\rm down}$ and $H_2^{\rm up}$ indicate lower-field metamagnetic transition measured in decreasing fields, lower-field metamagnetic transition measured in increasing fields, higher-field metamagnetic transition measured in decreasing fields and higher-field metamagnetic transition measured in increasing, respectively. (b) $dM(H)/dH$ for $\mathbf{H} \parallel (ac)$ at $T = 1.85$, 2.00, 2.25, 2.50, 2.50, 2.75, 2.85, 2.90, 3.00, 3.25 and 3.50 K. [Lin et al., 2013a]

In order to correlate features in $\rho(H)$ and $M(H)$, as well as establish in-plane anisotropic response to applied field [Myers et al., 1999; Canfield et al., 1997], the field dependence of mangetoresistance at $T = 1.8$ K and magnetization at $T = 2.0$ K are shown together in Fig. 6.10 from measurements on the same sample in the same in-

plane orientation of **H** ∥ *ac*. Two metamagnetic transitions can be clearly seen and are in good agreement when derived from the magnetoresistance and magnetization curves. The observed metamagnetic transitions fields are lower than previously discussed (see Fig. 6.8), this is possibly due to the in-plane anisotropy [Myers et al., 1999; Canfield et al., 1997].

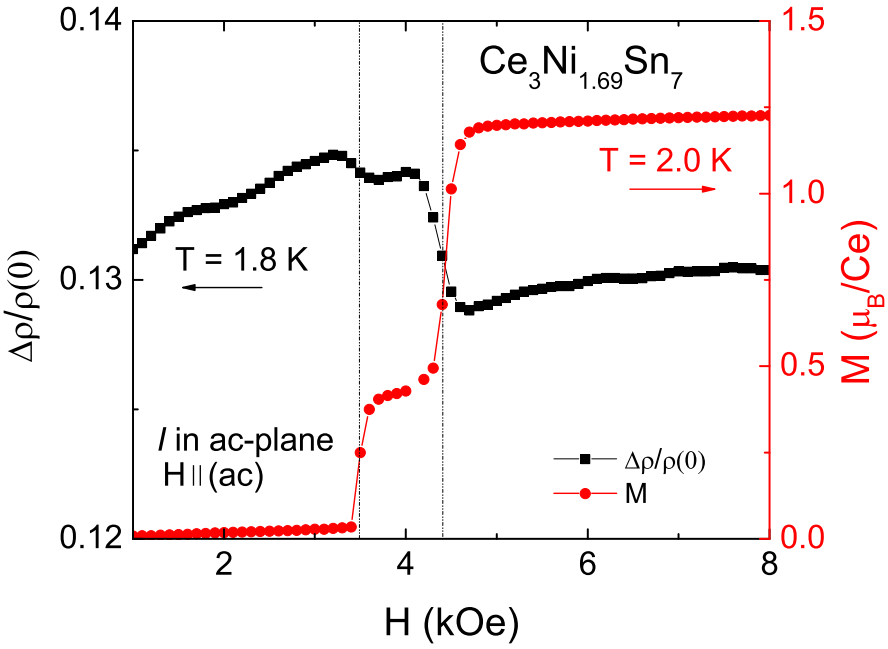

Figure 6.10 Magnetoresistance (left axis) as a function of magnetic field for $T = 1.8$ K and magnetization (right axis) as a function of magnetic field at 2.0 K for **H** ∥ *ac*-plane. Note: both measurements were done on the same sample in the same orientation; dashed lines indicate the magnetic fields where dM/dH peaks. [Lin et al., 2013a]

Based on the above discussion, an $H - T$ phase diagram is constructed (presented in Fig. 6.11), where the metamagnetic transition points are extracted from the temperature dependent magnetic susceptibilities and magnetization isotherms for one, arbitrary field orientation in the *ac*-plane. From the data presented in Figs. 6.7 and 6.8, for $0 < H \lesssim 5$ kOe T_N is gradually suppressed from $T_N \approx 3.7$ K at $H = 0$ to $T_N \approx 3.1$ K at $H = 5$ kOe.

For 5 kOe $\lesssim H \lesssim$ 7.2 kOe a second line in the $H-T$ phase diagram appears. Where as the outer envelop of the $H-T$ diagram continues to show a gradual, but non-linear suppression of $T_{\rm N}$ with **H**, a second, near vertical line appears for $H \sim 5.2$ kOe.

Figure. 6.11, taken together with the implicit in ac-plane anisotropy suggested by comparison to Fig. 6.10, make it clear that $Ce_3Ni_{1.69}Sn_7$ will have a rich $M(T,H,\theta)$ (θ being in plane angle of field with respect to a-axis) phase diagram.

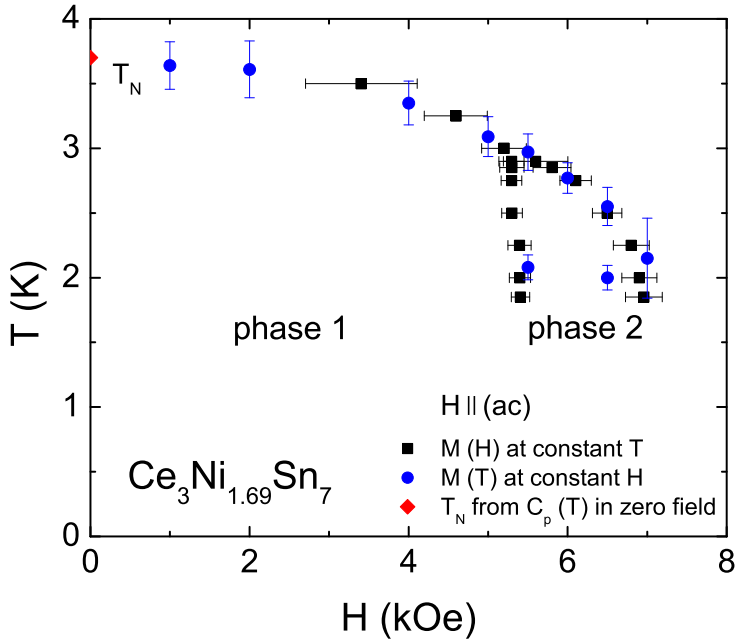

Figure 6.11 $H-T$ phase diagram of $Ce_3Ni_{1.69}Sn_7$ for **H** $\parallel$ (ac), measured on the same sample in the same orientation. The transition points are taken from the derivatives of $M(H)$ at constant temperatures in the process of increasing fields sweep and the derivatives of $M(T)$ at constant fields in the process of increasing temperature. The error bars are taken as the full width at half maximum of the derivatives. [Lin et al., 2013a]

6.4.4 $Pr_3Ni_{1.56}Sn_7$

The anisotropic magnetic properties of $Pr_3Ni_{1.56}Sn_7$ are shown in Fig. 6.12. As revealed by the inverse magnetic susceptibility measured at 1 kOe, the magnetic susceptibility follows the Curie-Weiss law at high temperatures, θ_b = -5.2 K, θ_{ac} = -26.7 K and θ_{ave} = -17.7 K. This anisotropy in the paramagnetic state results in $(M/H)_b > (M/H)_{ac}$ over the whole temperature range measured. The effective moment obtained from the fit of polycrystalline average susceptibility is $\mu_{eff} = 3.58(2)\ \mu_B$ per Pr^{3+} ion (see Table 6.5), identical to the free ion value for Pr^{3+}. In the low temperature region (shown in the left inset of Fig. 6.12), sharp peaks in $\chi(T)$, at $T \sim 4.8$ K, indicate AFM transition. The anisotropic field-dependent magnetization isotherms of $Pr_3Ni_{1.56}Sn_7$ measured at 2 K are shown in the right inset of Fig. 6.12. For both orientations, $M(H)$ linearly increases as the applied field increases, followed by a broad metamagnetic transition occurring at $\sim$ 16 kOe for $\mathbf{H} \parallel b$ and $\sim$ 17.5 kOe for $\mathbf{H} \parallel (ac)$. Since up to 50 kOe $M(H)$ for both orientations does not show saturation and the values of the magnetization at 50 kOe are much lower than expected for Pr^{3+} (3.2 μ_B), it is likely that in higher fields more metamagnetic transitions will occur.

The temperature-dependence of the normalized resistivity ratio for $Pr_3Ni_{1.56}Sn_7$ is shown in Fig. 6.13. To within factor a of 50%, the room temperature resistivity ρ(300 K) reaches approximately 60 $\mu\Omega$ cm, with (RRR) $\simeq$ 1.5. Resistivity decreases with decreasing temperature and shows a broad feature at around 50 K, which can be attributed to the thermal population of CEF levels. The enlarged low-T resistivity in zero field reveals three successive anomalies (see inset of Fig. 6.13), occurring at 3.7 K, 4.7 K and 7.8 K. The sharp transition at 3.7 K is suppressed by $H = 0.5$ kOe making it probable that it is due to a small amount of residual Sn. The 4.7 K feature is seen as a subtle drop in resistivity, but manifests itself as a sharp peak in $d\rho/dT$. This feature coincides with the AFM transition seen in the magnetic susceptibility and is associated with the loss of the spin-disorder scattering. Although difficult to see in the resistivity data, dρ/dT

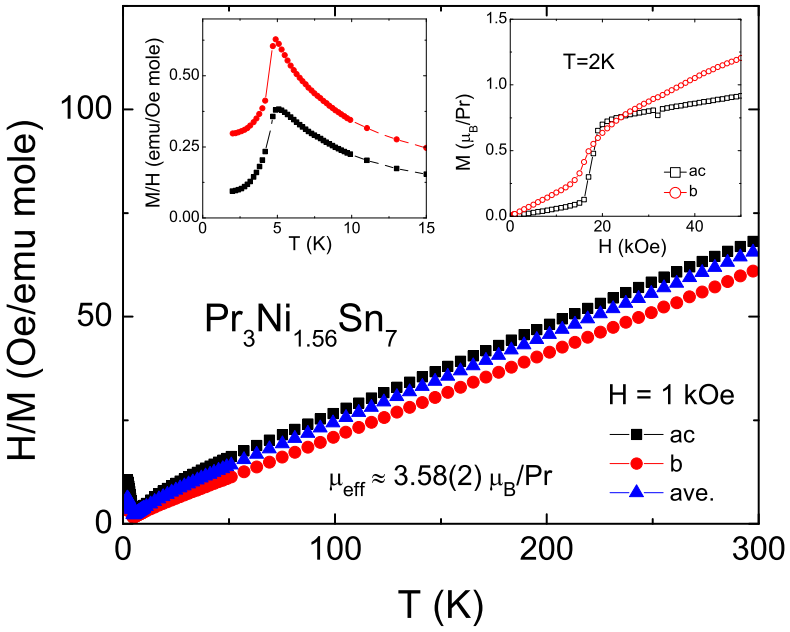

Figure 6.12 Inverse magnetic susceptibility $H/M(T)$ of $Pr_3Ni_{1.56}Sn_7$ for $\mathbf{H} \parallel b$-axis, in ac-plane and polycrystalline average at $H = 1$ kOe. Left inset: enlarged anisotropic magnetic susceptibility below 15 K. Right inset: anisotropic $M(H)$ of $Pr_3Ni_{1.56}Sn_7$ at $T = 2$ K. [Lin et al., 2013a]

shows a clear step-like anomaly at $\simeq$ 6.8 K. At 7.8 K, the resistivity changes its slope, and exhibits a step-like feature in dρ/dT as well.

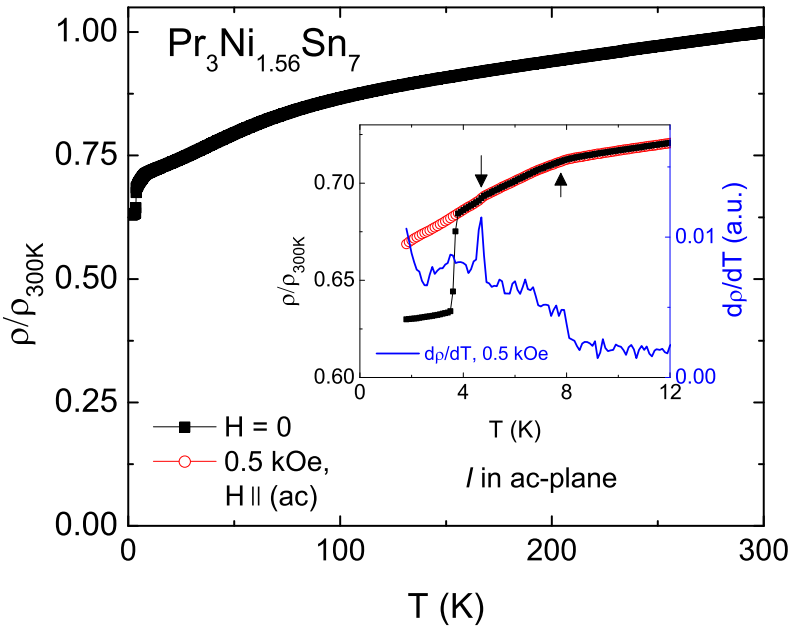

Figure 6.13 Temperature dependence of the normalized electrical resistivity ratio $\rho(T)/\rho(300\ \mathrm{K})$ of $Pr_3Ni_{1.56}Sn_7$ with $\rho(300\ \mathrm{K}) \sim 60\ \mu\Omega$ cm. Inset: low temperature $\rho(T)/\rho(300\ \mathrm{K})$ (left axis) measured at $H = 0$, 0.5 kOe with $\mathbf{H} \parallel (ac)$ and dρ/dT (right axis) at $H = 0.5$ kOe. Arrows indicate the transition temperature 4.7 and 7.8 K, respectively. [Lin et al., 2013a]

Specific heat of $Pr_3Ni_{1.56}Sn_7$ initially decreases with decreasing temperature, and reveals three anomalies, which peak at $\sim$ 7.6 K, 6.6 K and 4.7 K (Fig. 6.14(a)). Enlarged low temperature data of d(χT)/dT, dρ/dT and $C_M(T)$ are shown in Fig. 6.14(b). It is clear that two more anomalies are seen in the derivative d(χT)/dT, which corroborates the specific heat results very well. dρ/dT exhibits a peak at 4.7 K and two step-like features at 6.8 and 7.6 K. Based on the results of thermodynamic and transport measurements, for $Pr_3Ni_{1.56}Sn_7$, the magnetic ordering temperatures are 7.6 K, 6.6 K and 4.7 K. The magnetic contribution to specific heat from Pr^{+3} ions was calculated by the

relation of $C_M = C_p$ ($Pr_3Ni_{1.56}Sn_7$) - C_p ($La_3Ni_{1.89}Sn_7$). The magnetic entropy S_M per mole Pr^{3+} (shown in the inset of Fig. 6.14(a)) is roughly about $R\ln(2)$ at T = 6.8 K, and becomes $R\ln(3)$ by 14.3 K.

The field dependence of the magnetoresistance and magnetization for $Pr_3Ni_{1.56}Sn_7$ are shown in Fig. 6.15(a). To get rid of an off-set associated with superconducting Sn, the magnetoresistance was normalized to ρ(0.5 kOe), i.e. $\triangle\rho/\rho_0 = (\rho(H)$ - ρ(0.5 kOe))/ρ(0.5 kOe). There are two clear metamagnetic transitions visible in the 1.8 K data, one at $\sim$ 17 kOe and a second one near 38 kOe. Although both are clearly seen in the magnetoresistance data, the higher field transition is more clearly seen magnetization via dM/dH plots (Fig. 6.15(b)).

6.4.5 $Nd_3Ni_{1.34}Sn_7$

For $Nd_3Ni_{1.34}Sn_7$, magnetization with the applied magnetic field H = 1 kOe is found to be anisotropic with $(M/H)_bt > (M/H)_{ac}$ (Fig. 6.16). At high temperatures, the magnetic susceptibility follows the Curie-Weiss law, resulting in θ_{ave} = -36.8 K and μ_{eff} = 3.97(6) μ_B per Nd^{3+} ion (see Table 6.5), slightly larger than 3.87 μ_B, the expected value for Nd^{3+} free ion. At low temperatures, $Nd_3Ni_{1.34}Sn_7$ enters antiferromagnetic state at $\sim$ 3.8 K, seen by a subtle cusp in the magnetic susceptibility curve (left inset of Fig. 6.16). Magnetization isotherms of $Nd_3Ni_{1.34}Sn_7$ measured at 2 K are provided in the right inset of Fig. 6.16.

The temperature dependence of the normalized resistivity ratio for $Nd_3Ni_{1.34}Sn_7$ is shown in Fig. 6.17. To within a factor of 50%, the room temperature resistivity ρ (300 K) reaches approximately 100 $\mu\Omega$ cm, with (RRR) $\simeq$ 4.4 in zero magnetic field. A similar broad feature is seen at the higher temperatures and implies the thermal population of CEF levels. The enlarged low-T resistivity ratio measured at several selected magnetic fields is plotted in the left inset of Fig. 6.17. The higher-temperature feature, the break in slope of the resistivity occurring at 4.6 K, does not shift with different magnetic fields.

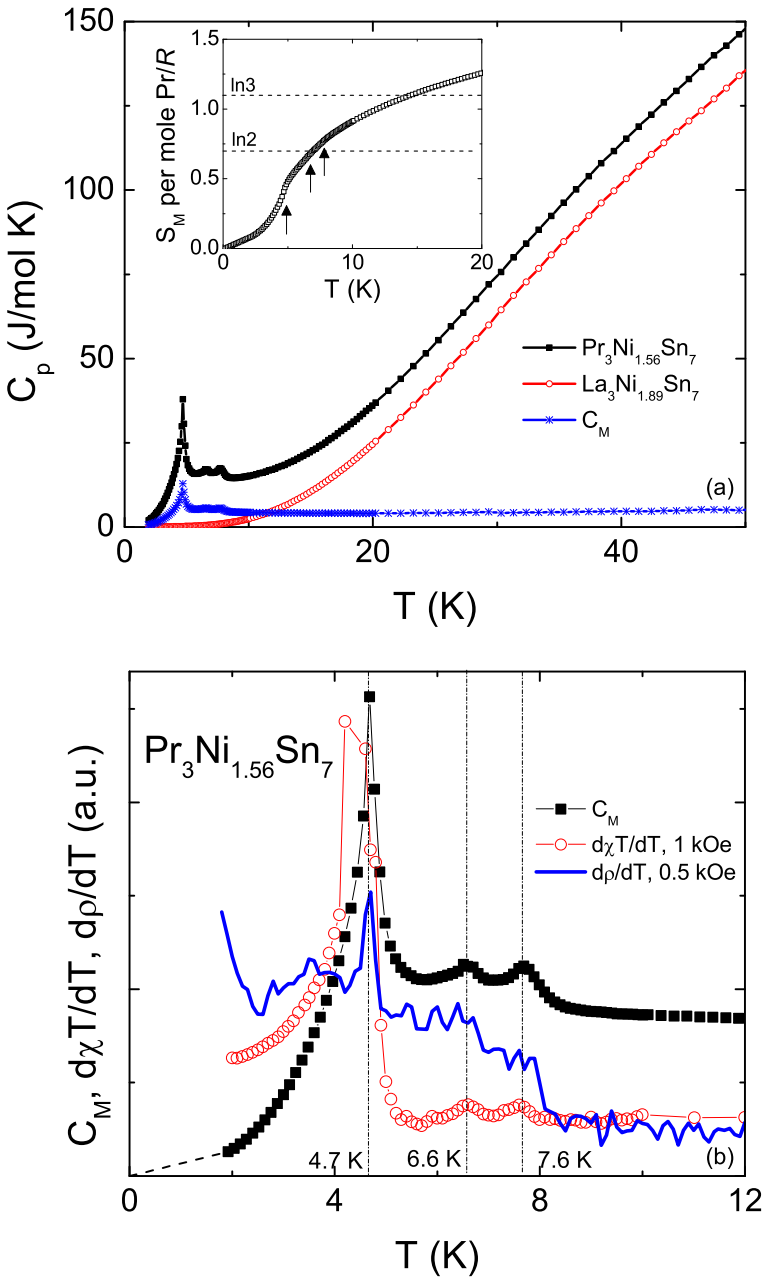

Figure 6.14 (a) Specific heat of $Pr_3Ni_{1.56}Sn_7$ and $La_3Ni_2Sn_7$ single crystals and magnetic specific heat of $Pr_3Ni_{1.56}Sn_7$. Inset: magnetic entropy per Pr^{3+} ion divided by R. The arrows indicate the transition temperatures. (b) Low-temperature $d(\chi T)/dT$ for $H = 1$ kOe, $d\rho/dT$ for H=0.5 kOe and $C_M(T)$ for $Pr_3Ni_{1.56}Sn_7$. The dashed line indicates $C_M(T)$ extrapolated to $T = 0$. The dotted lines mark the transitions in all three plots. [Lin et al., 2013a]

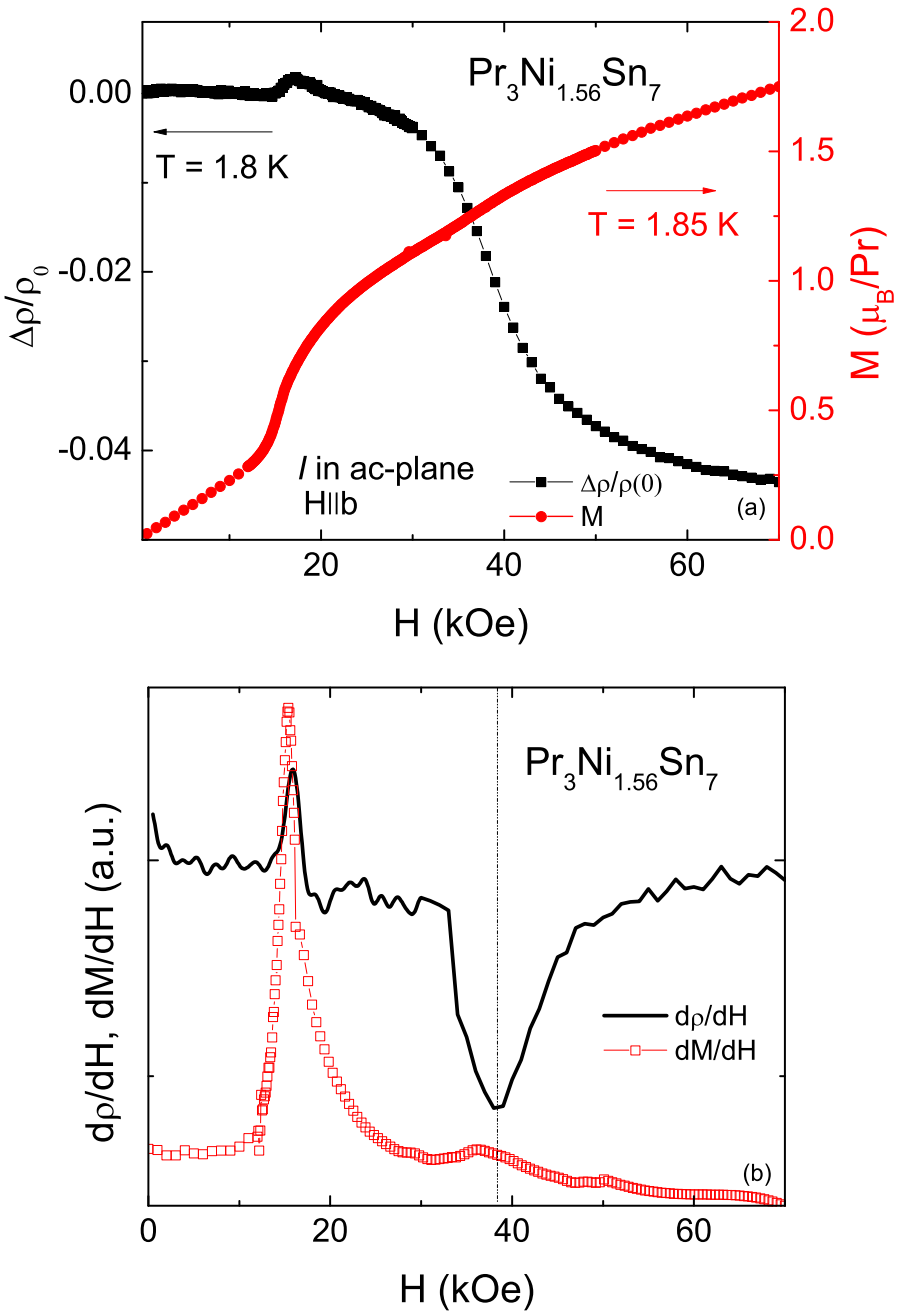

Figure 6.15 (a) Magnetoresistance (left axis) as a function of magnetic field for H at T = 1.8 K and magnetization (right axis) as a function of magnetic field for H at T = 1.85 K for $\mathbf{H} \parallel b$. Note: magnetoresistance was normalized to ρ(0.5 kOe) to remove Sn off-set. (b) $d\rho/dH$ at T = 1.8 K and dM/dH at T = 1.85 K for $\mathbf{H} \parallel b$. Note: both measurements were done on the same sample in the same orientation. [Lin et al., 2013a]

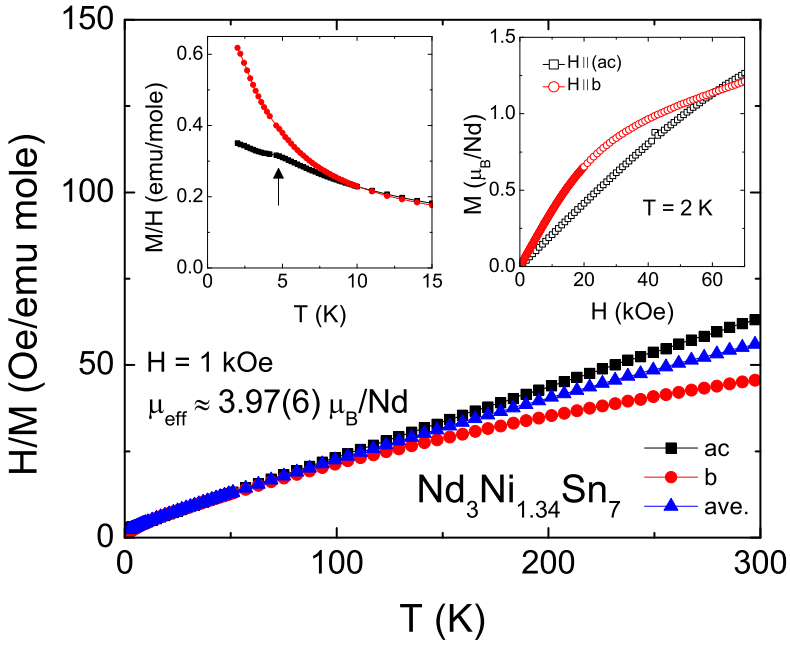

Figure 6.16 Inverse magnetic susceptibility $H/M(T)$ of $Nd_3Ni_{1.34}Sn_7$ for $\mathbf{H} \parallel b$-axis and ac-plane and polycrystalline average at $H = 1$ kOe. Left inset: enlarged anisotropic magnetic susceptibility below 15 K. Right inset: anisotropic $M(H)$ of $Nd_3Ni_{1.34}Sn_7$ at $T = 2$ K. [Lin et al., 2013a]

A second anomaly at ~ 3.8 K in zero field almost disappears when measured with applied fields. This indicates the anomaly is possibly associated with the residual Sn. However, in $d\rho/dT$ (see right inset of Fig. 6.17), the cusp at ~ 3.6 K, does not disappear or shift with applied fields. Thus, it is likely that $Nd_3Ni_{1.34}Sn_7$ has a second, lower-temperature magnetic transition at $T_N \sim 3.6$ K, overlapping with the T_c ($H = 0$) of Sn.

The specific heat data of $Nd_3Ni_{1.34}Sn_7$ are shown in Fig. 6.18 (a). Two anomalies are observed at 3.8 K and 4.3 K. Enlarged low temperature data of $d(\chi T)/dT$, $d\rho/dT$ and $C_M(T)$ are shown in Fig. 6.18(b). The transition at 3.8 K coincides in both magnetic susceptibility and specific heat data, the corresponding transition shifts to 3.6 K in transport measurement. This sharp feature in the specific heat data further indicates

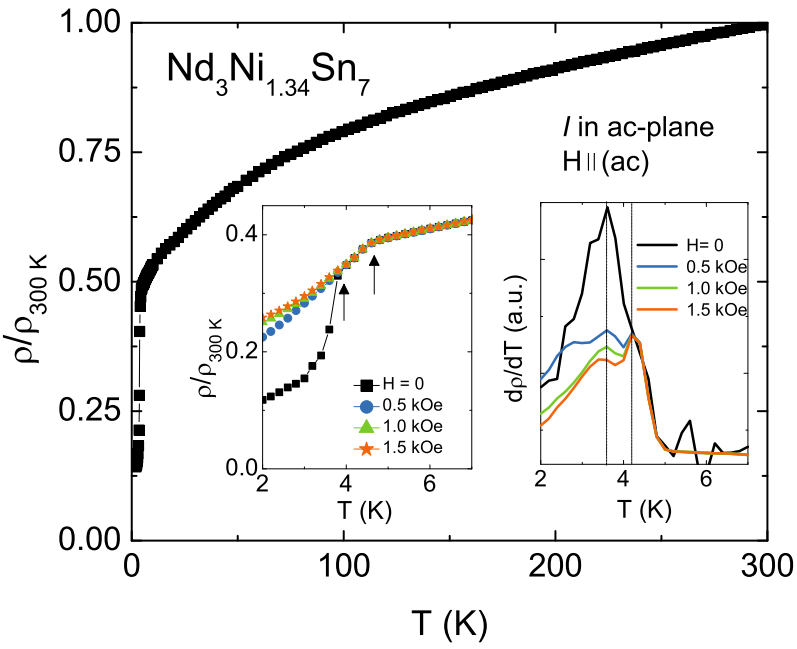

Figure 6.17 Temperature dependence of the normalized electrical resistivity ratio $\rho(T)/\rho(300\ \mathrm{K})$ of $Nd_3Ni_{1.34}Sn_7$ with $\rho(300\ \mathrm{K}) \sim 100\ \mu\Omega$ cm. Left inset: low temperature $\rho(T)/\rho(300\ \mathrm{K})$ (left axis) measured at $H = 0$, 0.5 kOe, 1.0 kOe and 1.5 kOe with $\mathbf{H} \parallel (ac)$. Arrows indicate the anomalies at 3.8 K and 4.6 K. Right Inset: $\mathrm{d}\rho/\mathrm{d}T$ at $H = 0$, 0.5 kOe, 1.0 kOe and 1.5 kOe. [Lin et al., 2013a]

$Nd_3Ni_{1.34}Sn_7$ has a transition at $\sim$ 3.8 K. The higher-temperature (4.3 K) anomaly in the specific heat seems to find its counterpart at $T = 4.2$ K in the transport data. There is a subtle change of change of slope in the similar temperature region seen in $\mathrm{d}(\chi T)/\mathrm{d}T$. The magnetic contribution to specific heat from Nd^{+3} ions was calculated by the relation of $C_M = C_p$ ($Nd_3Ni_{1.34}Sn_7$) - C_p ($La_3Ni_{1.89}Sn_7$). The magnetic entropy S_M per mole Nd^{3+} (shown in the inset of Fig. 6.18(a)) reaches approximately $R\ln(2)$ at $T = 4.3$ K, the full doublet entropy.

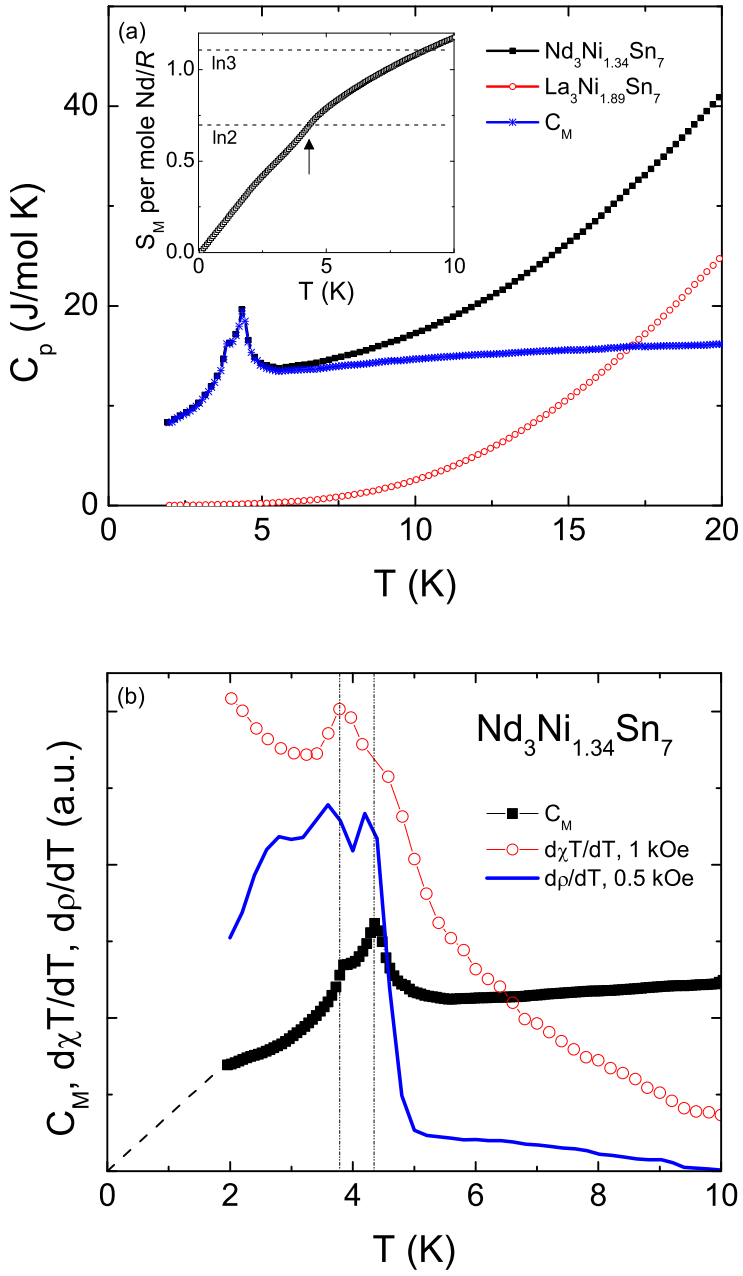

Figure 6.18 (a) Specific heat of $Nd_3Ni_{1.34}Sn_7$ and $La_3Ni_{1.89}Sn_7$ single crystals and magnetic specific heat of $Nd_3Ni_{1.34}Sn_7$. Inset: magnetic entropy per mole Nd^{3+} ion divided by R. The arrow indicates the anomaly at $T = 4.3$ K. (b) Low-temperature $d(\chi T)/dT$ for H=1 kOe, $d\rho/dT$ for H=0.5 kOe and $C_M(T)$. The dashed line indicates $C_M(T)$ extrapolated to T=0. The dotted lines mark the transitions in all three plots. [Lin et al., 2013a]

Table 6.5 Magnetic ordering temperatures, anisotropic Curie temperatures and effective magnetic moment in paramagnetic state for $R_3Ni_{2-x}Sn_7$. [Lin et al., 2013a]

Compound	θ_b (K)	θ_{ac} (K)	θ_{ave} (K)	μ_{eff} (μ_B)	T_M (K)
Ce	-43.6	-75.4	-57.1	2.44	3.7
Pr	-5.2	-26.7	-17.7	3.58	7.6, 6.6, 4.7
Nd	-90.8	-14.6	-36.8	3.97	4.3, 3.8

6.5 Summary and conclusions

Motivated by previous studies of rare-earth compounds [Bud'ko et al., 1999; Sefat et al., 2008; Mun et al., 2010], we have synthesized single crystalline $R_3Ni_{2-x}Sn_7$ (R = La, Ce, Pr and Nd) samples via self-flux Sn. Detailed thermodynamic and transport measurements were performed to study the properties of $R_3Ni_{2-x}Sn_7$ series. The crystals form as plates (inset of Fig. 6.1), and can be identified as having an orthorhombic $La_3Co_2Sn_7$-type structure. We have determined the degree of Ni-site vacancy and see clear evidence of the associated, disorder scattering manifest in the low RRR values. Despite the partial Ni site occupancy there are sharp magnetic transitions and metamagnetic transitions. Although rich and complex $H-T$ phase diagrams are likely, the combination of orthorhombicity and partial Ni site occupancy makes this a less than ideal system for detailed studies.

CHAPTER 7. ANISOTROPIC MAGNETIZATION AND RESISTIVITY OF SINGLE CRYSTALLINE $R\mathrm{Ni}_{1-x}\mathrm{Bi}_{2\pm y}$ (R = La–Nd, Sm, Gd–Dy)[1]

7.1 Abstract

We present a detailed study of $R\mathrm{Ni}_{1-x}\mathrm{Bi}_{2\pm y}$ (R = La–Nd, Sm, Gd–Dy) single crystals by measurements of stoichiometry and temperature dependent magnetic susceptibility, magnetization, and electrical resistivity. This series forms with partial Ni occupancy, $0.72 \leq (1-x) \leq 0.84$, as well as a variable Bi occupancy, $1.76 \leq (2 \pm y) \leq 2.14$. For R = Ce–Nd, Gd–Dy, the $R\mathrm{Ni}_{1-x}\mathrm{Bi}_{2\pm y}$ compounds show local-moment like behavior and order antiferromagnetically at low temperatures. Determination of anisotropies as well as antiferromagnetic ordering temperatures for $R\mathrm{Ni}_{1-x}\mathrm{Bi}_{2\pm y}$ (R = Ce–Nd, Sm, Gd–Dy) have been made. Crystalline samples from this family exhibit minority, second phase superconductivity at low temperatures, which can be associated with Ni-Bi and Bi contamination. No evidence of bulk superconductivity has been observed.

7.2 Introduction

The interesting physical properties of Ce-based intermetallic compounds have been the concern of numerous studies [Steglich, 1985; Myers et al., 1999; Balicas et al., 2005;

[1]This chapter is a version of the published article: Lin, X., Straszheim, W. E., Bud'ko, S. L. and Canfield, P. C. "Anisotropic magnetization and resistivity of single crystalline $R\mathrm{Ni}_{1-x}\mathrm{Bi}_{2\pm y}$ (R = La–Nd, Sm, Gd–Dy)" *J. Alloys Compd.*, 554 (2013):304

Phelan et al., 2012; Bud'ko et al., 1999; Petrovic et al., 2003]. The ground state of Ce-based intermetallic compounds is often governed by the competition between the Ruderman-Kittel-Kasuya-Yosida (RKKY) interaction and the Kondo interaction. Depending on the strength of the hybridization between $4f$ and conduction electrons relative to their coupling strength, the ground state can be either a non-magnetic state dominated by the Kondo interaction or a long-range magnetically ordered state governed by the RKKY interaction. Various exotic phenomena have been observed in these compounds, for example: $CeCu_2Si_2$ was classified as a heavy fermion superconductor [Steglich, 1985], $CeAgSb_2$ [Myers et al., 1999] and $CeAgBi_2$ [Petrovic et al., 2003] were reported to be strongly correlated electron compounds with a magnetically ordered ground state.

It is often enlightening to study not just the Ce-member of a rare earth, intermetallic series, but rather a wide sampling of the whole series. As exhibited in many rare earth series [Myers et al., 1999; Bud'ko et al., 1999; Petrovic et al., 2003; Szytula and Leciejewicz, 1994; Gschneidner and Eyring, 978], the $4f$ electrons are often shielded from the $5s$-, $5p$- and $4d$-shell electrons, and thus do not participate in chemical bonding. On the other hand, the $4f$ electrons have direct influences on the compounds' magnetic properties, since the magnetic moments originate in the partially filled f-shell. As a result, by varying the R elements in a compound, it is possible to tune the magnetism and other physical properties. Moreover, the unit cell volume of isostructural R^{3+}-bearing families shrinks from R = La to R = Lu, which is known as the lanthanide contraction. This contraction leads to systematic changes in the lattice constants a, b, c and unit cell volume V.

Recently $CeNi_{0.8}Bi_2$ has attracted particular attention: a polycrystalline sample was synthesized and reported as a heavy fermion superconductor [Mizoguchi et al., 2011]. Its T_c was found to be $\sim$ 4.2 K. The superconductivity was said to be associated with the light effective mass electrons, whereas the antiferromagnetic (AFM) transition, occurring at $\sim$ 5 K, was related to the strong interactions between the heavy electrons

and Ce $4f$ electrons [Mizoguchi et al., 2011]. The superconductivity was claimed to be introduced by the Ni deficiency, as the "parent" compound $CeNiBi_2$ did not manifest bulk superconductivity [Kodama et al., 2011]. Earlier results on $CeNiBi_2$ suggested it to be a moderately heavy fermion antiferromagnet [Thamizhavel et al., 2003; Jung et al., 2002]. Magnetic susceptibility was measured on single crystalline samples with no diamagnetic signal being observed, and the zero resistivity was attributed "to the thin films of bismuth" [Thamizhavel et al., 2003].

Given that Ni occupancy in the sample is claimed to play a key role in superconductivity, single crystalline samples of $CeNi_{0.8}Bi_2$ are likely to offer further understandings of the superconducting features in this system. Hence, we present a study of physical properties of single crystalline $CeNi_{0.8}Bi_2$ samples.

The early work on the polycrystalline $RNi_{1-x}Bi_{2\pm y}$ samples (R = Ce, Nd, Gd, Tb, Dy and Y) solved the structure and reported the Ni site deficiency [Zeng and Franzen, 1998; Lu et al., 2005]. This series of compounds was found to have a tetragonal $ZrCuSi_2$-type structure (space group $P4/nmm$). Later superconductivity with $T_c \sim 4$ K was reported in this family for R = Y, La, Ce and Nd [Mizoguchi et al., 2011, 2012]. The results were based on the polycrystalline samples containing partial occupancy of the Ni site. Other than for $CeNi_{0.8}Bi_2$, no detailed, anisotropic results were shown for other members in this family.

In this paper, we present a systematic study of the anisotropic properties of the $RNi_{1-x}Bi_{2\pm y}$ series with R = La–Nd, Sm, Gd–Dy. Since this system shows partial occupancy of the Ni site, chemical elemental analysis was performed to determine the stoichiometry of the samples. Analyses of the field and temperature dependence of the magnetization and resistivity were performed on the single crystalline samples. No evidence of bulk superconductivity was observed in this series of compounds. For R = Ce–Nd, Gd–Dy, compounds show local-moment like behavior with an AFM ordering at low temperatures. Measurements of the magnetization parallel to the ab-plane and

the c-axis show anisotropic behavior, and the magnetization of some of the compounds indicate the existence of metamagnetic transitions.

7.3 Experimental details

Single crystals of $R\mathrm{Ni}_{1-x}\mathrm{Bi}_{2\pm y}$ were grown out of excess Bi flux via the high-temperature solution method [Canfield and Fisk, 1992; Canfield, 2010]. Given that this series of compounds is known to have Ni site deficiency, and that the Ni deficiency was considered to be crucial for $\mathrm{CeNi}_{1-x}\mathrm{Bi}_2$ to become superconducting [Mizoguchi et al., 2011], we varied the composition of the starting materials, resulting in crystals with different Ni concentrations. Single crystals of $\mathrm{CeNi}_{1-x}\mathrm{Bi}_2$ with (1-x) varying from 0.64 to 0.85 (as determined from wavelength-dispersive x-ray spectroscopy, see below) were synthesized. Irreproducible and incomplete transitions in resistivity data were seen for (1-x) = 0.64, 0.75, 0.80 and 0.85. They are very likely associated with minority, second phase superconductivity. No qualitative differences were observed for these samples with different (1-x) values. In this work the starting stoichiometry that gives the resulting crystal with the ratio of Ce:Ni:Bi = 1:0.8:2 was selected. This initial stoichiometry was $\mathrm{Ce}_{10.4}\mathrm{Ni}_{14.6}\mathrm{Bi}_{75}$. The same initial stoichiometry was used for R = La, Pr, Nd and Sm. For R = Gd, Tb and Dy, to avoid RBi as an impurity, the stoichiometry was adjusted to $R_{4.5}\mathrm{Ni}_{9.1}\mathrm{Bi}_{86.4}$. For R = Eu and Ho – Lu, there are no reported data on the isostructural compounds. Our attempts to grow these R-members of the series often resulted in poorly-formed R-Bi binaries. Hence, it is likely that this series does not form under the similar growth conditions for R = Eu and Ho – Lu.

High purity (>3N) elements were placed in an alumina crucible and sealed in a fused silica tube under a partial pressure of high purity argon gas. This was then heated up to 1000°C and cooled to 500°C in 65 hours, at which temperature the excess solution was decanted using a centrifuge [Canfield and Fisk, 1992; Canfield, 2010]. Single crystals of

$R\mathrm{Ni}_{1-x}\mathrm{Bi}_{2\pm y}$ grew in plate-like shapes with their sizes varying from $\sim 10\times10\times1.5$ mm^3 for R = La to $\sim 2\times2\times0.6$ mm^3 for R = Dy. The crystallographic c-axis is perpendicular to the plate-like single crystals. Most of the samples had shiny surfaces that were partially covered by secondary phase materials. Due to the samples' air-sensitivity, crystals were kept in an argon glove-box, and efforts were made to minimize their exposure to air during samples' manipulation and measurements. They were neither etched nor polished, and only cleaved samples with fresh surface were used in the resistivity measurements.

Powder x-ray diffraction data were collected on a Rigaku MiniFlex diffractometer with Cu Kα radiation at room temperature. The sample was ground in a glove-box and the powder was protected from atmosphere by Kapton film during the measurement so as to protect it from oxidation. Data collections were performed with the counting time of 2 seconds for every 0.02 degree. The refinement was conducted using the program Rietica [Howard and Hunter, 1998]. The error bars associated with the values of the lattice parameters were determined by statistical errors, and Si powder standard was used as the internal reference.

Elemental analysis of the samples was performed using wavelength-dispersive x-ray spectroscopy (WDS) in a JEOL JXA-8200 electron probe microanalyzer. The measurement was conducted with an accelerating voltage of 20 kV, a probe current of 25 nA and a spot size of 5 μm. The integration time on peak, low background and high background is 10 s, 5 s and 5 s, respectively. Only clear and shiny surface regions were selected for determination of the sample stoichiometry, i.e. regions with residual Bi flux were avoided. For each compound, the WDS data were collected from multiple points on the same sample. Counting statistics suggest there should be 1% or less relative error due to counting.

Measurements of field dependent magnetization and temperature dependent susceptibility were performed in a Quantum Design, Magnetic Property Measurement System (MPMS). The ac resistivity was measured by a standard four-probe method in a Quan-

tum Design, Physical Property Measurement System (PPMS) or with LR700 ac resistance bridge in MPMS. Platinum wires were attached to the sample using Dupont 4929 silver paint with the current flowing in the *ab*-plane. The absolute values of resistivity are accurate to ± 20% due to the irregularity of the sample geometry and accuracy of measurements of electrical contacts' position. The residual resistivity ratio is determined as (RRR) = ρ(300 K) / ρ(5.0 K), so as to avoid any contamination from the minority phase superconductivity.

7.4 Results and analysis

7.4.1 Crystal stoichiometry and structure

The stoichiometry of the $R\mathrm{Ni}_{1-x}\mathrm{Bi}_{2\pm y}$ samples was inferred from WDS analyses. Table 7.1 summarizes the atomic percent of each element determined from the weight percent obtained from the analysis. The precision of the analysis was calculated by $SD/\sqrt{N}$, where SD is the standard deviation of measurements, and N is the number of points taken in analysis. A higher level of oxygen contamination was detected in $\mathrm{DyNi}_{0.74}\mathrm{Bi}_{1.76}$ compound, which results in a lower accuracy of its analysis. The averaged atomic concentrations of each element in each compound were normalized to the rare earth element to have $R_{1.00}$. The result shows that although the ratio of R:Ni:Bi is grossly 1:1:2, a significant Ni deficiency develops across the series, and the Bi concentration varies from slight excess to slight deficiency. Given this series of compounds does not maintain a fixed, stoichiometric composition, for the calculation of physical quantities, the stoichiometries from Table 7.1 were used. It should be noted that if the Bi stoichiometry is simply set to 2.00, the values for effective moments vary significantly as the molar mass changes. For this reason the Bi nonstoichiometry is also shown.

Powder x-ray diffraction patterns were collected on ground single crystals from each compound. Figure 7.1 shows a $\mathrm{CeNi}_{0.80}\mathrm{Bi}_{2.03}$ x-ray pattern as an example. The main

Table 7.1 WDS elemental analysis (in atomic %) for $R\mathrm{Ni}_{1-x}\mathrm{Bi}_{2\pm y}$ single crystals. [Lin et al., 2013b]

Compound	N (number of points analyzed)	R	Ni	Bi	Stoichiometry (WDS)
La	12	25.74 ± 0.14	21.65 ± 0.06	52.61 ± 0.17	$\mathrm{LaNi}_{0.84}\mathrm{Bi}_{2.04}$
Ce	12	26.09 ± 0.11	20.99 ± 0.14	52.92 ± 0.21	$\mathrm{CeNi}_{0.80}\mathrm{Bi}_{2.03}$
Pr	11	26.49 ± 0.08	21.06 ± 0.11	52.45 ± 0.14	$\mathrm{PrNi}_{0.79}\mathrm{Bi}_{1.98}$
Nd	12	25.91 ± 0.11	18.73 ± 0.04	55.36 ± 0.12	$\mathrm{NdNi}_{0.72}\mathrm{Bi}_{2.14}$
Sm	12	25.96 ± 0.10	20.13 ± 0.06	53.91 ± 0.13	$\mathrm{SmNi}_{0.78}\mathrm{Bi}_{2.08}$
Gd	11	27.53 ± 0.11	19.88 ± 0.16	52.58 ± 0.24	$\mathrm{GdNi}_{0.72}\mathrm{Bi}_{1.91}$
Tb	12	27.51 ± 0.06	20.36 ± 0.07	52.13 ± 0.11	$\mathrm{TbNi}_{0.74}\mathrm{Bi}_{1.90}$
Dy	11	28.53 ± 0.21	21.14 ± 0.10	50.33 ± 0.30	$\mathrm{DyNi}_{0.74}\mathrm{Bi}_{1.76}$

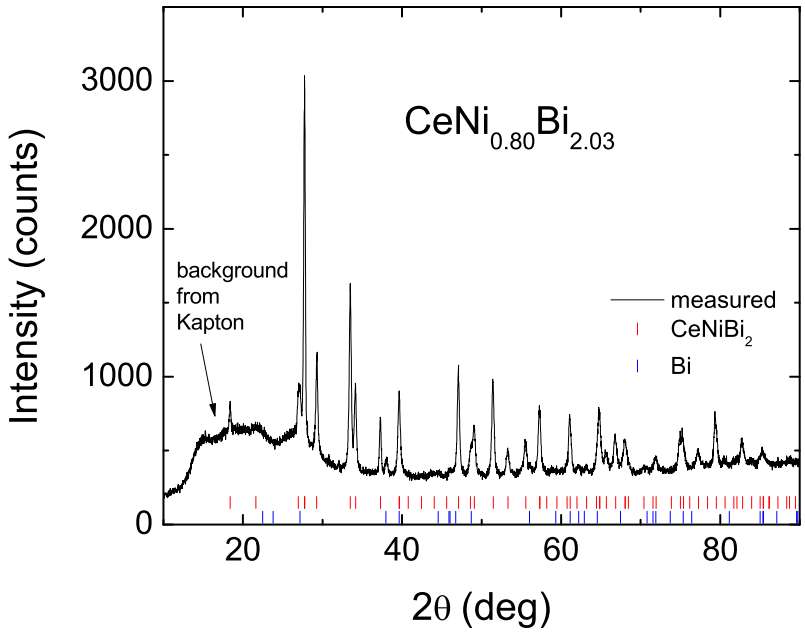

Figure 7.1 Powder x-ray diffraction pattern of $CeNi_{0.80}Bi_{2.03}$. [Lin et al., 2013b]

Table 7.2 Refined unit cell parameters from powder x-ray diffraction for $R\mathrm{Ni}_{1-x}\mathrm{Bi}_{2\pm y}$ compounds. [Lin et al., 2013b]

Compound	a (Å)	c (Å)	V (Å^3)
La	4.56 ± 0.01	9.78 ± 0.02	204.02 ± 0.03
Ce	4.54 ± 0.01	9.64 ± 0.02	199.57 ± 0.03
Pr	4.52 ± 0.01	9.60 ± 0.02	196.68 ± 0.03
Nd	4.52 ± 0.01	9.53 ± 0.02	194.96 ± 0.03
Sm	4.50 ± 0.01	9.42 ± 0.02	191.27 ± 0.03
Gd	4.49 ± 0.01	9.37 ± 0.02	189.20 ± 0.03
Tb	4.48 ± 0.01	9.30 ± 0.02	187.52 ± 0.03
Dy	4.47 ± 0.01	9.29 ± 0.02	185.82 ± 0.03

phase was fitted with $CeNiBi_2$'s diffraction pattern (site occupancy was not analysed), small traces of Bi residue can be detected, whereas no evidence of Ni-Bi binaries was found. Similar results ($R\mathrm{NiBi}_2$ with minority phase of Bi) were obtained for the other members of the series. The analysis of powder x-ray diffraction data indicates that the lattice parameters a and c are monotonically decreasing as the series progresses from La to Dy (presented in Table 7.2). Proceeding from the larger to the smaller rare-earth elements, all lattice parameters decrease almost linearly: 2.1% for a and 5.3% for c (as shown in Fig. 7.2), which is consistent with the previously reported data [Mizoguchi et al., 2011; Zeng and Franzen, 1998; Lu et al., 2005]. In progressing from $\mathrm{LaNi}_{0.84}\mathrm{Bi}_{2.04}$ to $\mathrm{DyNi}_{0.74}\mathrm{Bi}_{1.76}$, the overall volume decreases by 9.8%. These results are likely associated with the lanthanide contraction that occurs across the $4f$ series. In addition, the deficiencies at the Ni site can possibly lead to smaller unit cell volumes as well [Mun et al., 2010].

7.4.2 Resistivity of $\boldsymbol{R\mathrm{Ni}_{1-x}\mathrm{Bi}_{2\pm y}}$

The temperature dependent electrical resistivity for $\mathrm{LaNi}_{0.84}\mathrm{Bi}_{2.04}$ is shown in Fig. 7.3 (a). To within a factor of 20%, the room temperature resistivity value $\rho(300\ \mathrm{K})$ reaches ~ 0.15 mΩ cm. For current in the ab-plane, the resistivity displays metallic behavior

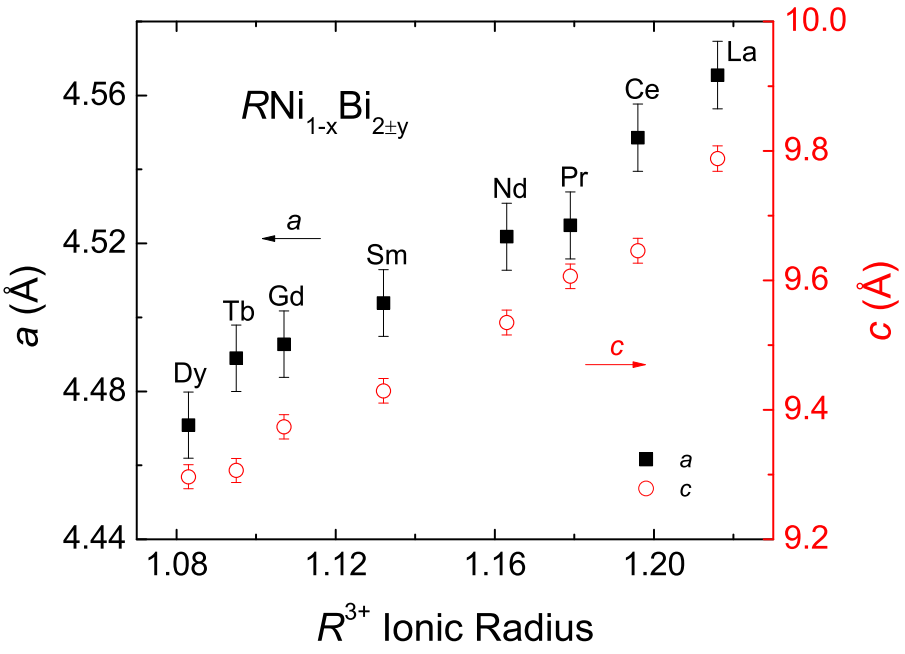

Figure 7.2 The change of unit cell lattice parameters vs. ionic radius of R^{3+} for 9 coordination number (CN=9) [Shannon, 1976] in $R\mathrm{Ni}_{1-x}\mathrm{Bi}_{2\pm y}$ compounds. [Lin et al., 2013b]

with RRR $\approx$ 1.3. We assume that this small RRR value is at least partially due to the deficiencies at the Ni and Bi sites. Although the high temperature ($T > 5$ K) resistivity is quite reproducible, sample to sample, below 5 K the sizes of the two resistive anomalies (observed near 4.2 K and 3.0 K) are very sample dependent (Fig. 7.3 (a) inset). Whereas the resistivity of Sample 2 does not reach zero above $T = 1.8$ K, the higher-temperature anomaly is barely seen for Sample 3. Such incomplete and irreproducible transitions suggest that the superconductivity is extrinsic in both cases and the anomalies in the resistivity can be attributed to minority phases. In fact, it is highly likely that the higher-temperature anomaly is related to the superconducting transition of the Ni-Bi binaries (NiBi with $T_c \approx 4.25$ K and $NiBi_3$ with $T_c \approx 4.06$ K)[Fujimori et al., 2000; Zhu et al., 2012]. The lower-temperature anomaly is probably caused by filamentary, thin film, Bi presented in the sample, which is consistent with the previous work [Thamizhavel et al., 2003]; the T_c of Bi film can vary from 2 K to 5 K depending on its thickness [Strongin et al., 1970]. Moreover, the drop of resistivity at $\sim$ 4.2 K is always much smaller then the drop at $\sim$ 3.0 K. This is possibly due to smaller amount of Ni-Bi binaries than Bi film in the sample, which is consistent with the x-ray diffraction data (where Bi is clearly detected, and no Ni-Bi binary diffraction lines can be resolved). The low temperature resistivity data, measured in different magnetic fields, are plotted in Fig. 7.3 (b). As can be seen, both of the superconducting features are shifting to lower temperatures as the applied field increases.

The temperature dependent electrical resistivity for $CeNi_{0.80}Bi_{2.03}$ is shown in Fig. 7.4 (a). To within a factor of 20%, the room temperature resistivity value ρ(300 K) reaches $\sim$ 0.22 mΩ cm with RRR $\approx$ 1.2. A broad hump at $\sim$ 80 K and a local minimum at $\sim$ 20 K are found. These features are readily associated with the interplay of the thermal population of the crystal electric field (CEF) levels and the Kondo effect, which are often seen in the Ce-based compounds [Myers et al., 1999; Petrovic et al., 2003]. At low temperatures, three successive resistive anomalies are detected near 5.1

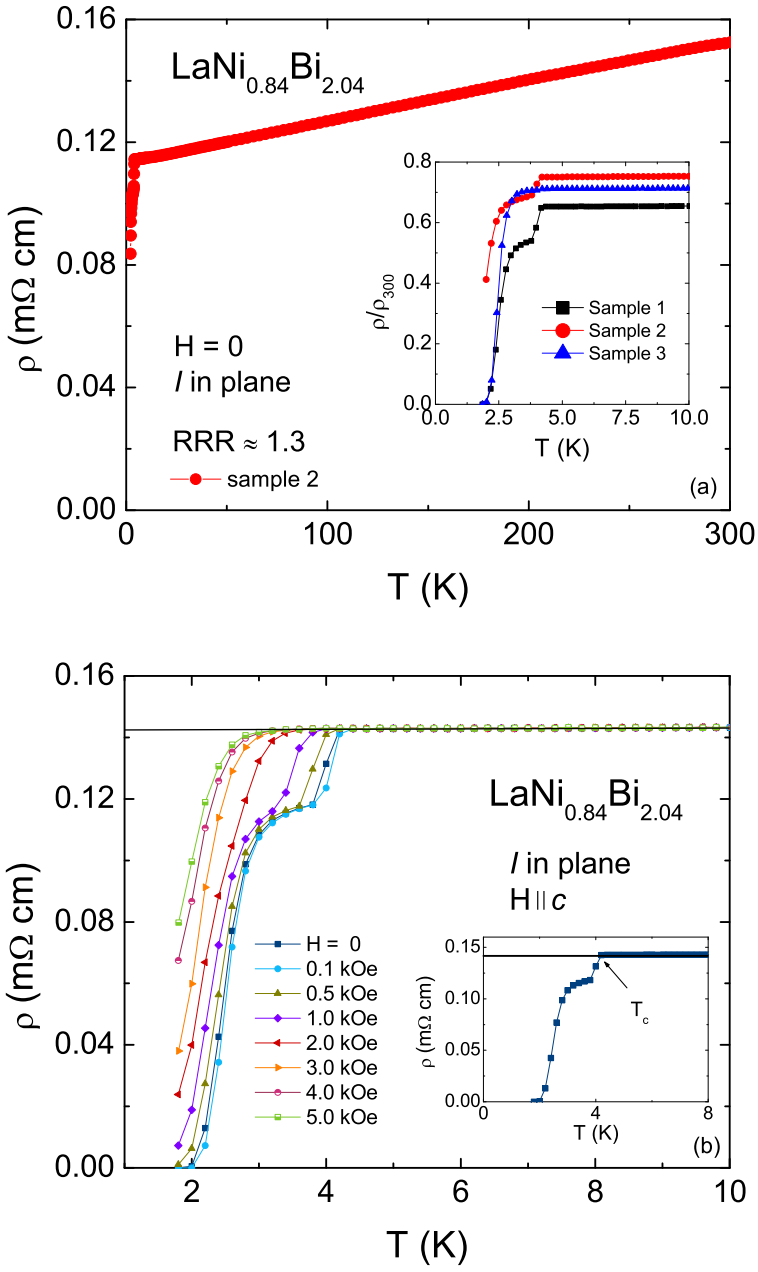

Figure 7.3 (a) Temperature dependence of the electrical resistivity of $LaNi_{0.84}Bi_{2.04}$. Inset: comparison of the enlarged normalized resistivity ratio from three samples for $T \leq 10$ K. (b) Low temperature resistivity of $LaNi_{0.84}Bi_{2.04}$ measured at 0, 0.1, 0.5, 1.0, 2.0, 3.0, 4.0, and 5.0 kOe with $\mathbf{H} \parallel c$. Inset: criteria for the higher-temperature transition T_c is shown for $H = 0$. [Lin et al., 2013b]

K, 4.2 and 2.5 K (see inset of Fig. 7.4 (a)). The criteria for determining the transition temperatures are shown in the inset of Fig. 7.4 (a). The highest transition temperature ($T_1 \approx 5.1$ K) coincides with the AFM transition, which will be shown in the magnetic susceptibility data discussed in the next section. It is likely caused by the loss of the spin-disorder scattering upon entering into the magnetically ordered state. Since the resistivity does not reach zero above 1.8 K, it implies that $CeNi_{0.80}Bi_{2.03}$ does not show bulk superconducting behavior, and the two lower-temperature anomalies are probably associated with minority second phase of Ni-Bi binaries and Bi present in the sample. The low temperature resistivity data measured in different magnetic fields are plotted in Fig. 7.4 (b). As can be seen, whereas the highest transition, T_1, is almost invariant under these fields, whereas both T_2 and T_3 decrease as the applied field increases.

The upper critical fields for the superconductivity associated with the second phase in $LaNi_{0.84}Bi_{2.04}$ and $CeNi_{0.80}Bi_{2.03}$ have been obtained from the magnetotransport data (shown in Fig. 7.5). To estimated the $H_{c2}(T)$ values of the higher-temperature feature of $LaNi_{0.84}Bi_{2.04}$, the first data point deviated from the normal state is chosen as the criterion (shown in the inset of Fig. 7.3 (b)). The criterion for determining T_2 of $CeNi_{0.80}Bi_{2.03}$ is illustrated in the inset of Fig. 7.4 (a). The resulting $H_{c2}(T)$ curves are plotted in Fig. 7.5. As can be seen, the two $H_{c2}(T)$ curves are essentially the same. In addition, they are also quite consistent with the reported $H_{c2}(T)$ phase diagram for $NiBi_3$ [Zhu et al., 2012]. The fact that H_{c2} values in this work are larger is probably due to the difference of the H_{c2} criteria and difference between single crystalline and polycrystalline samples. Hence, it is very likely that the superconducting features are not of bulk properties of $LaNi_{0.84}Bi_{2.04}$ or $CeNi_{0.80}Bi_{2.03}$, but most likely due to Bi and Ni-Bi binary impurities.

The two resistive anomalies (the higher-temperature one occurring $\sim$ 4.2 K and the lower-temperature one varying from 2 to 3 K) are detected in other members of the $RNi_{1-x}Bi_{2\pm y}$ series (R = Pr, Nd, Sm, Gd–Dy) as well. Similar to $LaNi_{0.84}Bi_{2.04}$ and $CeNi_{0.80}Bi_{2.03}$, the superconductivity associated with these two features are partial and

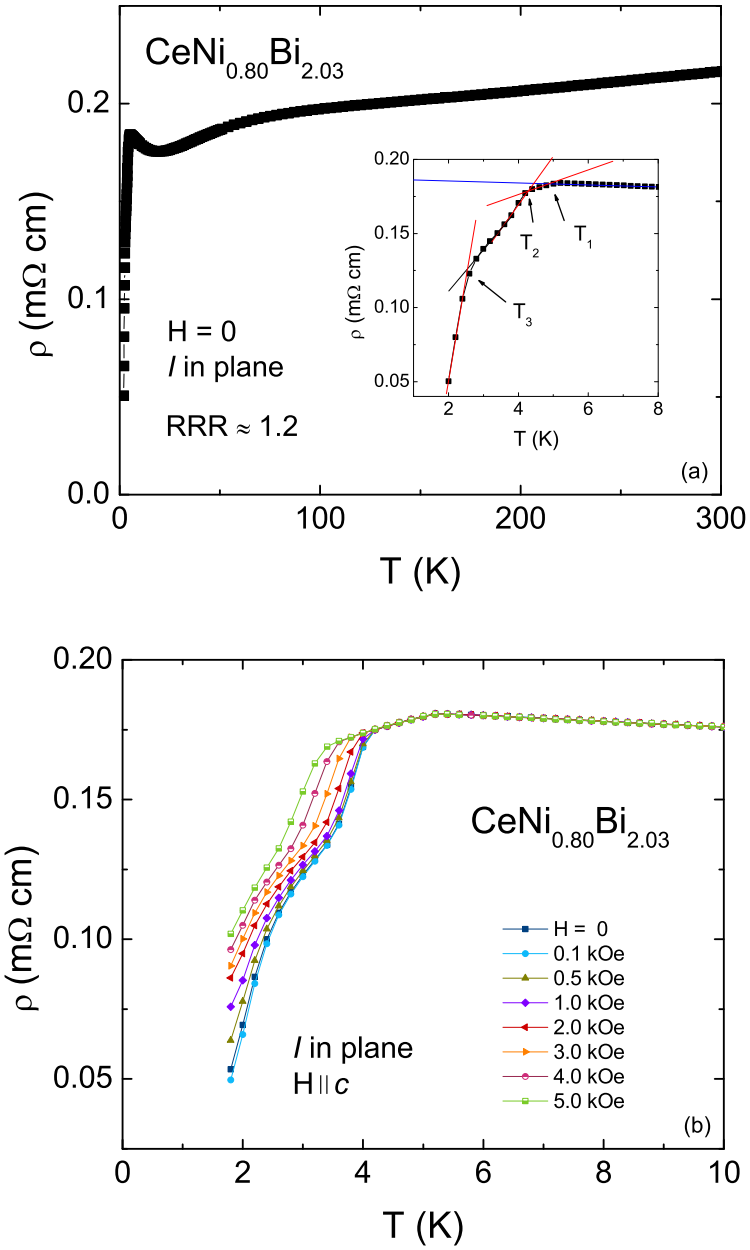

Figure 7.4 (a) Temperature dependence of the electrical resistivity of $CeNi_{0.80}Bi_{2.03}$. Inset: criterion for the transition temperature T_1, T_2 and T_3 are shown for $H = 0$. (b) Low temperature resistivity of $CeNi_{0.80}Bi_{2.03}$ measured at 0, 0.1, 0.5, 1.0, 2.0, 3.0, 4.0, and 5.0 kOe with $\mathbf{H} \parallel c$. [Lin et al., 2013b]

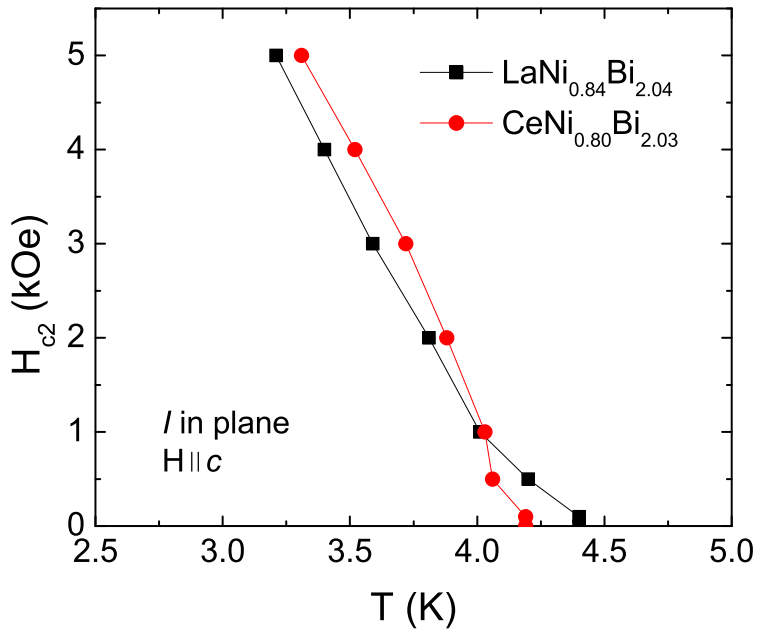

Figure 7.5 $H_{c2}(T)$ plot for the higher-temperature transition of $LaNi_{0.84}Bi_{2.04}$ and T_2 transition of $CeNi_{0.80}Bi_{2.03}$ from the magnetotransport measurements. [Lin et al., 2013b]

very sample dependent. It is most likely that these two anomalies are related to the superconducting transitions of Ni-Bi binaries and films of Bi as well. No evidence of bulk superconductivity has been found in this family from the electrical resistivity data. Unfortunately, the two anomalies often manifest as stronger features than those related to the magnetic transitions, such as in the case of $CeNi_{0.80}Bi_{2.03}$. Hence, the transport data for the rest of the series are not shown in this work.

7.4.3 Magnetic properties of $R\mathbf{Ni}_{1-x}\mathbf{Bi}_{2\pm y}$

The low temperature magnetic susceptibility of $LaNi_{0.84}Bi_{2.04}$ for $T \leq 8$ K is shown in Fig. 7.6 (a). With $H = 50$ Oe parallel to the c-axis, both of the zero-field-cooled (ZFC) and field-cooled (FC) magnetic susceptibilities reveal abrupt drops at around 4.1 K and 2.5 K. This is consistent with the anomalies found in the resistivity data. The small superconducting volume fractions in both ZFC ($< 3\%$) and FC ($< 2\%$) data at 2.0 K further support that $LaNi_{0.84}Bi_{2.04}$ does not manifest bulk superconductivity.

The anisotropic temperature-dependent magnetic susceptibility of $LaNi_{0.84}Bi_{2.04}$ measured from 2 K to 300 K is shown in Fig. 7.6 (b). For $H = 50$ kOe, $LaNi_{0.84}Bi_{2.04}$ shows weak paramagnetism for both orientations. With a larger value for $\mathbf{H} \parallel ab$-plane than $\mathbf{H} \parallel c$-axis, the magnetic susceptibility shows very subtle change as temperature decreases from 300 K. The small up-turn at low temperatures, seen in both orientations, is probably caused by small levels of paramagnetic impurities.

The low temperature magnetic susceptibility of $CeNi_{0.80}Bi_{2.03}$ for $T \leq 10$ K is shown in Fig. 7.7 (a). With $H = 50$ Oe parallel to the c-axis, $CeNi_{0.80}Bi_{2.03}$ shows positive susceptibility in both ZFC and FC measurements. Two sudden breaks, occurring at ~ 5.1 K and 4.0 K can be seen, which are consistent with the anomalies observed in the resistivity data. No anomaly is detected for temperatures between 2.0 and 4.0 K. Exhibiting positive magnetic susceptibility together with the missing feature at low temperatures strongly support that the superconductivity observed in the resistivity data of

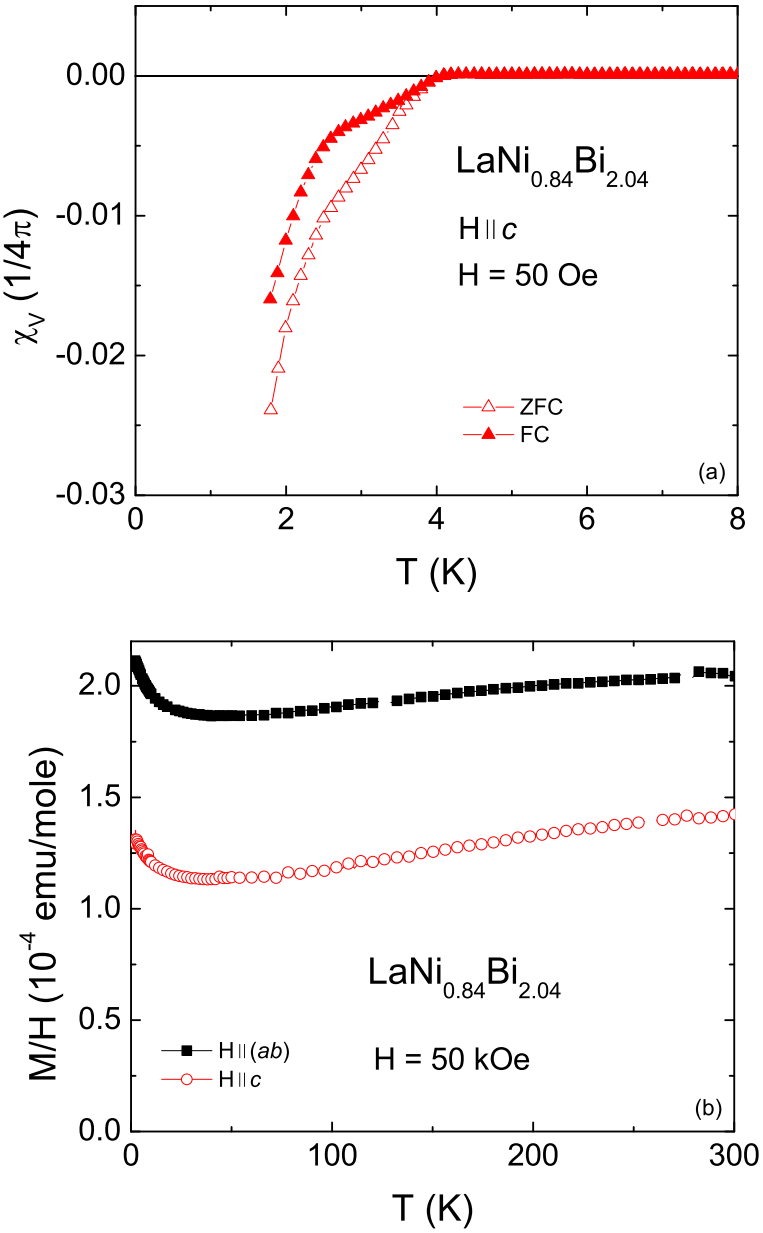

Figure 7.6 (a) The zero-field-cooled and field-cooled magnetic susceptibility of $LaNi_{0.84}Bi_{2.04}$ for $T \leq 8$ K. (b) The anisotropic temperature-dependent magnetic susceptibility of $LaNi_{0.84}Bi_{2.04}$ for $\mathbf{H} \parallel ab$-plane, and c-axis. [Lin et al., 2013b]

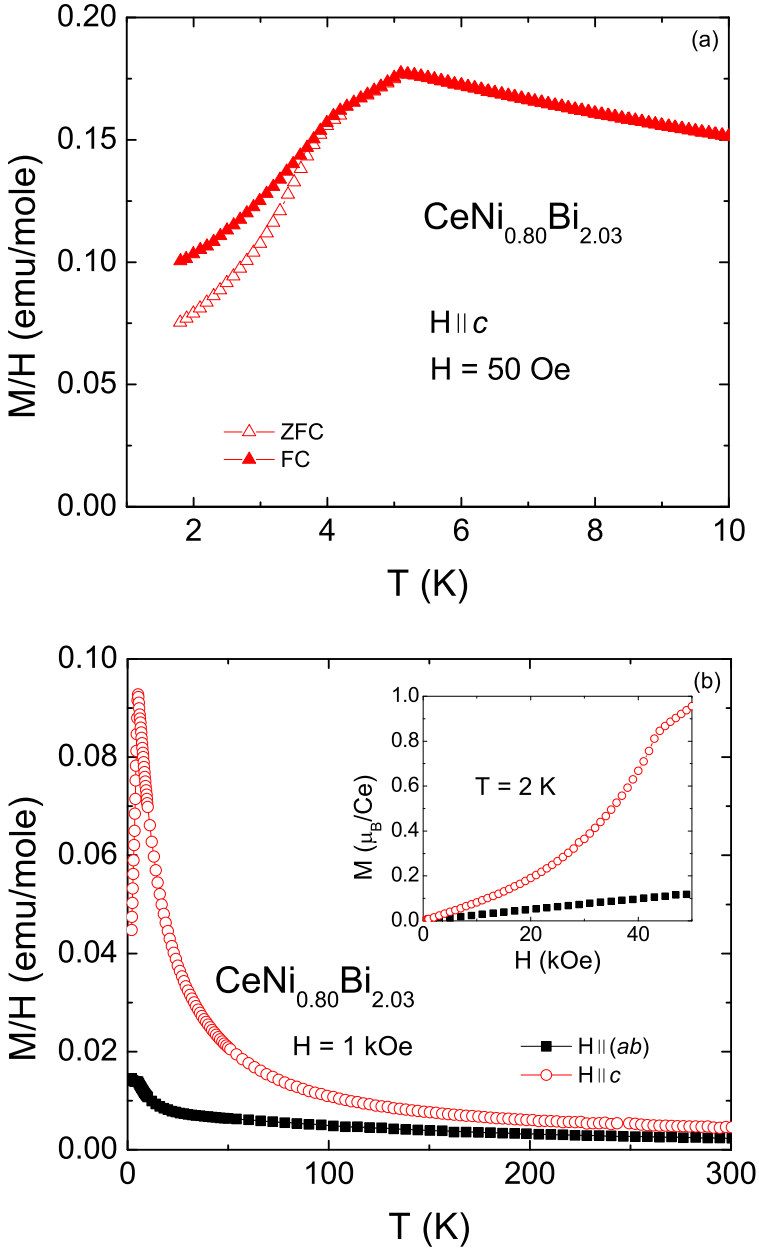

Figure 7.7 (a) The zero-field-cooled and field-cooled magnetic susceptibility of $CeNi_{0.80}Bi_{2.03}$ for $T \leq 10$ K. (b) The anisotropic temperature-dependent magnetic susceptibility of $CeNi_{0.80}Bi_{2.03}$ for $\mathbf{H} = 1$ kOe. Inset: the anisotropic magnetic isotherms of $CeNi_{0.80}Bi_{2.03}$ at $T = 2$ K. [Lin et al., 2013b]

$CeNi_{0.80}Bi_{2.03}$ is related to minority phases.

The anisotropic temperature-dependent magnetic susceptibility of $CeNi_{0.80}Bi_{2.03}$, $\chi(T) = M(T)/H$, measured with $H = 1$ kOe applied both parallel to the ab-plane and the c-axis are plotted in Fig. 7.7(b). χ_c is significantly larger than χ_{ab} over the whole temperature range measured. The sharp peaks seen at low temperature suggest that this material has an AFM transition. The ordering temperature, consistent with the reported value [Thamizhavel et al., 2003; Jung et al., 2002], was estimated to be $\sim$ 4.8 K (here and in Table 7.3 the values of the magnetic ordering temperatures obtained from the maximum of the derivatives $d(\chi T)/dT$ [Fisher, 1962] are quoted). The polycrystalline averaged susceptibility was estimated by $\chi_{ave} = \frac{1}{3}(\chi_c + 2\chi_{ab})$. A modified Curie-Weiss law with inclusion of a temperature-independent term χ_0: $\chi = \chi_0 + \frac{C}{T-\theta}$, was used to fit the magnetic susceptibility in the temperature range from 50 K to 300 K, where C is the Curie constant and θ is the paramagnetic Curie temperature. θ_{ave}, θ_{ab} and θ_c are extracted from the polycrystalline averaged susceptibility, the magnetic susceptibility for $\mathbf{H} \parallel ab$ and $\mathbf{H} \parallel c$, respectively. Considering the presence of impurities, Bi nonstoichiometry and accuracy of measuring sample's mass, the values of the effective moments in this series are accurate to $\pm$3%. For $CeNi_{0.80}Bi_{2.03}$, it gives θ_{ab} = -156 K, θ_c = -6 K and θ_{ave} = -17 K, suggesting the presence of CEF splitting and AFM interaction. The inferred effective moment from the polycrystalline averaged data: $\mu_{eff} = 2.4\ \mu_B$/Ce is consistent with the expected Hund's rule ($J = 5/2$) ground-state value, 2.54 μ_B. The anisotropic field-dependent magnetization isotherms of $CeNi_{0.80}Bi_{2.03}$ measured at 2 K are shown in the inset of Fig.7.7 (b). For both orientations, $M(H)$ increases as the applied field increases. The magnetization is found to be very anisotropic with $M_c > M_{ab}$, and a cusp at $\sim$ 43 kOe for $\mathbf{H} \parallel c$ is most likely associated with a metamagnetic transition.

The anisotropic temperature-dependent magnetic susceptibility data $\chi(T) = M(T)/H$ for R = Pr, Nd, Sm, Gd–Dy measured at 1 kOe are shown in Fig. 7.8 and 7.9. As can be seen in Fig. 7.8 (a), $PrNi_{0.79}Bi_{1.98}$ manifests anisotropy with $\chi_c > \chi_{ab}$ over the whole

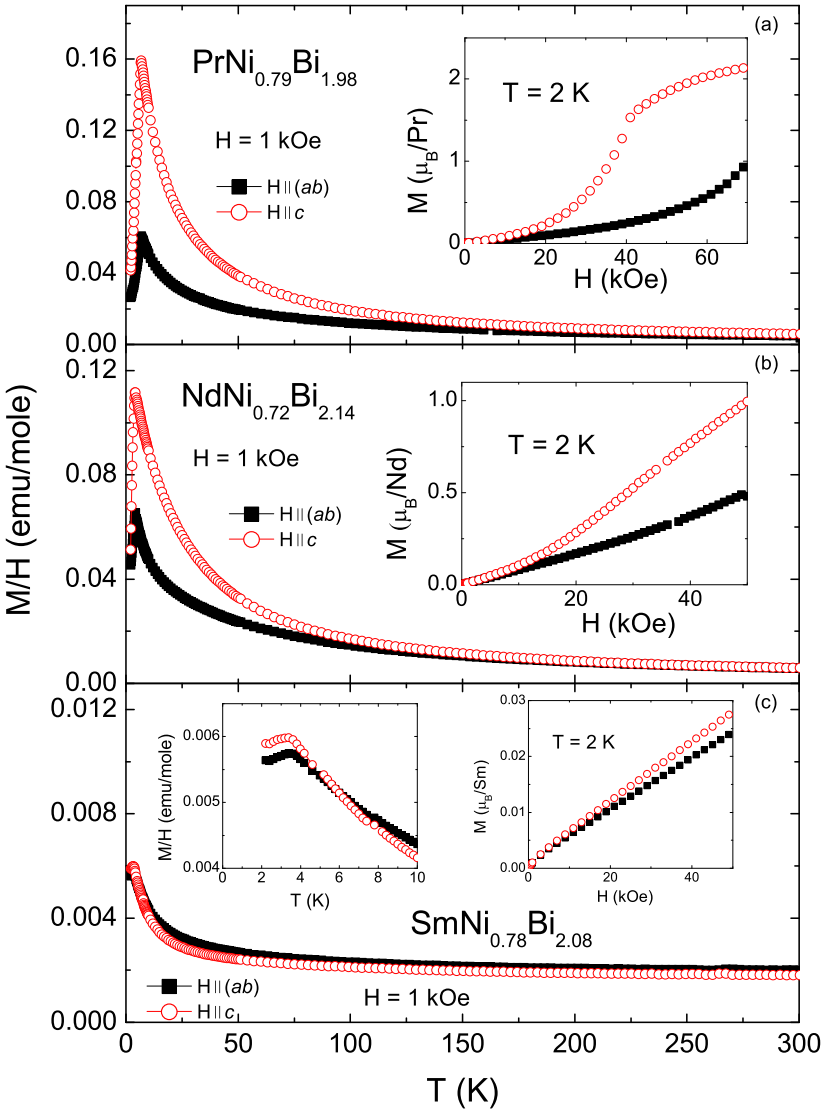

Figure 7.8 (a)The anisotropic temperature-dependent magnetic susceptibility of $PrNi_{0.79}Bi_{1.98}$. Inset: the anisotropic magnetic isotherms of $PrNi_{0.79}Bi_{1.98}$. (b) The anisotropic temperature-dependent magnetic susceptibility of $NdNi_{0.72}Bi_{2.14}$. Inset: the anisotropic magnetic isotherms of $NdNi_{0.72}Bi_{2.14}$. (c) The anisotropic temperature-dependent magnetic susceptibility of $SmNi_{0.78}Bi_{2.08}$. Left inset: enlarged magnetic susceptibility for $T \leq 10$ K. Right inset: the anisotropic magnetic isotherms of $SmNi_{0.78}Bi_{2.08}$. [Lin et al., 2013b]

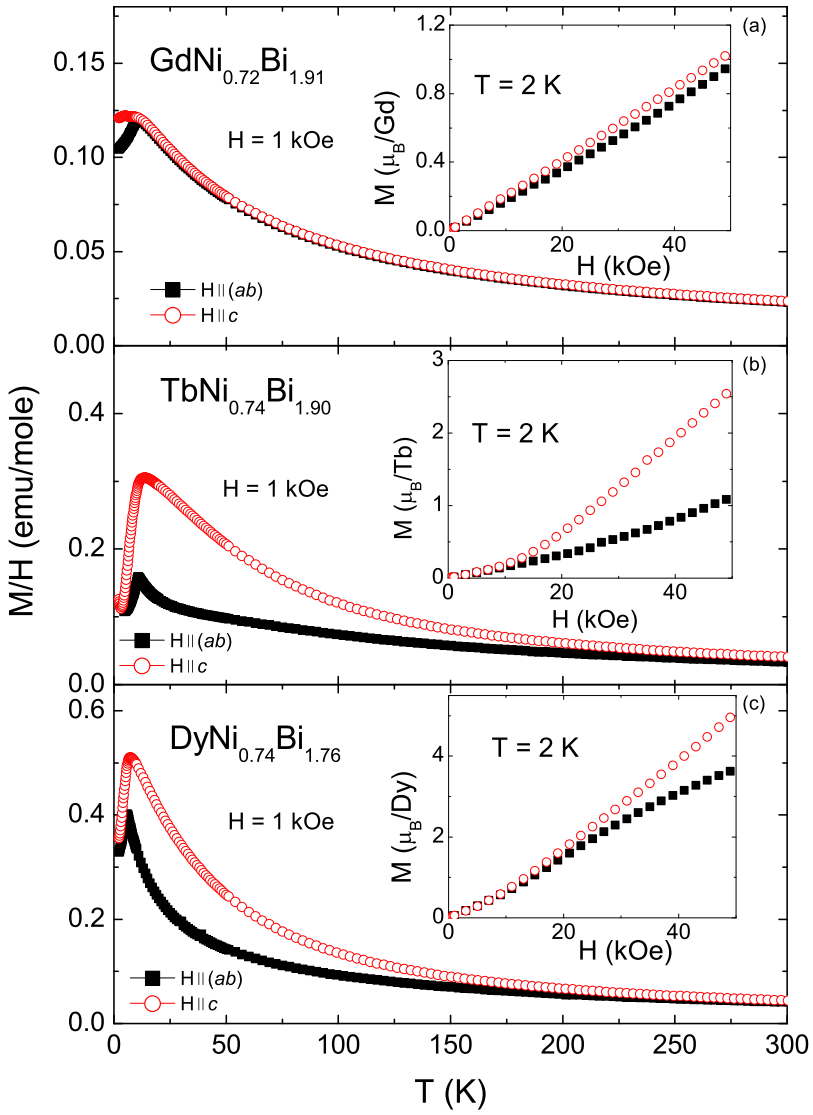

Figure 7.9 (a) The anisotropic temperature-dependent magnetic susceptibility of $GdNi_{0.72}Bi_{1.91}$. Inset: the anisotropic magnetic isotherms of $GdNi_{0.72}Bi_{1.91}$. (b) The anisotropic temperature-dependent magnetic susceptibility of $TbNi_{0.74}Bi_{1.90}$. Inset: the anisotropic magnetic isotherms of $TbNi_{0.74}Bi_{1.90}$. (c) The anisotropic temperature-dependent magnetic susceptibility of $DyNi_{0.74}Bi_{1.76}$. Inset: the anisotropic magnetic isotherms of $DyNi_{0.74}Bi_{1.76}$. [Lin et al., 2013b]

temperature range measured. At low temperatures, sharp peaks are found at $\sim$ 6.4 K, indicating an AFM transition. At high temperatures, its magnetic susceptibility follows the modified Curie-Weiss law, giving θ_{ab} = -18 K, θ_c = -7 K and θ_{ave} = -12 K. The effective moment obtained from the fit of polycrystalline averaged susceptibility is μ_{eff} = 3.6 μ_B per Pr^{3+} (see Table 7.3), almost identical to the free ion value for Pr^{3+}. The anisotropic field-dependent magnetization isotherms of $PrNi_{0.79}Bi_{1.98}$ measured at 2 K are shown in the inset of Fig. 7.8 (a). For both orientations, $M(H)$ increases as the applied field increases up to 70 kOe. For $\mathbf{H} \parallel c$, an anomaly is seen at $\sim$ 41 kOe. For $\mathbf{H} \parallel ab$-plane, an inflection point in $M(H)$ curve is detected at a higher field. Higher magnetic field ($H >$ 70 kOe) is needed for $PrNi_{0.79}Bi_{1.98}$ to be fully saturated.

For $NdNi_{0.72}Bi_{2.14}$, the magnetic susceptibility behaves anisotropically ($\chi_c > \chi_{ab}$) but with reduced anisotropy as compared to $CeNi_{0.80}Bi_{2.03}$ or $PrNi_{0.79}Bi_{1.98}$ (shown in Fig. 7.8 (b)). At low temperatures, a sharp peak is found at $\sim$ 3.8 K, which is likely associated with an AFM transition. At high temperatures, fitting with the modified Curie-Weiss law results in θ_{ab} = -33 K, θ_c = -3 K and θ_{ave} = -16 K. The polycrystalline averaged susceptibility gives μ_{eff} = 3.8 μ_B per Nd^{3+} (see Table 7.3), which is consistent with 3.62 μ_B, the expected value for Nd^{3+} free ion. The anisotropic field-dependent magnetization isotherms of $NdNi_{0.72}Bi_{2.14}$ measured at 2 K are shown in the inset of Fig. 7.8 (b). For both orientations, $M(H)$ increases as the applied field increases up to 70 kOe. A subtle inflection in the $M(H)$ curve can be observed for both orientations, indicating the possible existence of metamagnetic transitions.

The magnetic susceptibility of $SmNi_{0.78}Bi_{2.08}$ exhibits very subtle anisotropic behavior (Fig.7.8 (c)). An anomaly is found at $\sim$ 3.3 K (left inset of Fig.7.8 (c)). When measured with different magnetic fields, the transition temperature shows very little variance. It is probably related to an AFM ordering. Different from $PrNi_{0.79}Bi_{1.98}$ and $NdNi_{0.72}Bi_{2.14}$, the $\chi(T)$ of $SmNi_{0.78}Bi_{2.08}$ does not follow Curie-Weiss law but shows a tendency to saturation at high temperatures. This is commonly seen in the Sm-bearing intermetallic

compounds [Bud'ko et al., 1999; Petrovic et al., 2003]. This behavior may be due to Sm ion's valence fluctuation between 3+ and 2+ and/or Sm ion's excitation to upper Hund's-rule state and the associated Van Vleck paramagnetism. The field-dependent magnetization curves for $SmNi_{0.78}Bi_{2.08}$ show small anisotropy and increase linearly (or close to linearly) with no traces of the field-induced transitions (right inset of Fig.7.8 (c)).

The temperature-dependent magnetic susceptibility of $GdNi_{0.72}Bi_{1.91}$ manifests typical behavior of an antiferromagnet with no CEF effect (Fig. 7.9 (a)). Due to the S-state ($L = 0$, $S = 7/2$) of the Gd^{3+} ion, $\chi(T)$ is virtually isotropic in the paramagnetic state. Below $T_N = 9.8$ K, $\chi_{ab}(T)$ decreases with decreasing temperature and $\chi_c(T)$ stays almost constant. These data suggest that the Gd moment orders in the basal ab-plane. The high-temperature $\chi(T)$ follows the Curie-Weiss law with θ_{ave} = -51 K and $\mu_{eff} = 7.9\ \mu_B$ per Gd^{3+} (see Table 7.3), essentially identical to the expected value for Gd^{3+} free ion. The negative sign of the paramagnetic Curie temperature suggests the presence of the antiferromagnetic correlations. The anisotropic field-dependent magnetization isotherms of $GdNi_{0.72}Bi_{1.91}$ measured at 2 K are shown in the inset of Fig. 7.9 (a). $M(H)$ almost linearly increases as the applied field increases up to 50 kOe with a small anisotropy.

The magnetic susceptibility of $TbNi_{0.74}Bi_{1.90}$ is highly anisotropic (Fig. 7.9 (b)), and manifests the highest ordering temperature among the members of this family with $T_N \simeq 10.2$ K. At high temperatures, $\chi(T)$ follows the modified Curie-Weiss law, giving θ_{ab} = -109 K, θ_c = -19 K and θ_{ave} = -40 K. The effective moment obtained from polycrystalline averaged susceptibility is $\mu_{eff} = 10.0\ \mu_B$ per Tb^{3+} (see Table 7.3), which is consistent with 9.72 μ_B, the expected value for Tb^{3+} free ion. The field-dependent magnetization curve for $TbNi_{0.74}Bi_{1.90}$ behaves anisotropically (inset of Fig.7.9 (b)). An inflection in the $M(H)$ curve for $\mathbf{H} \parallel c$ suggests the possible existence of a metamagnetic transition.

In the case of $DyNi_{0.74}Bi_{1.76}$, the magnetic susceptibility is found to be anisotropic (Fig. 7.9 (c)). At low temperatures, $DyNi_{0.74}Bi_{1.76}$ enters its AFM state at $\sim$ 5.4 K,

Table 7.3 Magnetic ordering temperatures, anisotropic Curie temperatures and effective magnetic moment in paramagnetic state for $R\mathrm{Ni}_{1-x}\mathrm{Bi}_{2\pm y}$. Note: the high temperature data (50 K $\leq T \leq$ 300 K) were selected to fit the modified Curie-Weiss law. [Lin et al., 2013b]

R	θ_{ab} (K)	θ_c (K)	θ_{ave} (K)	μ_{eff} (μ_B)	χ_0 (10^{-4} emu/mole)	T_M (K)
Ce	-156± 2.9	-6 ± 0.1	-17 ± 0.3	2.4	10 ± 0.2	4.8
Pr	-18± 0.5	-7 ± 0.1	-12 ± 0.3	3.6	1 ± 0.6	6.4
Nd	-33± 0.3	-3 ± 0.2	-16 ± 0.1	3.8	2 ± 0.1	3.8
Sm						3.3
Gd	-51± 0.1	-51± 0.1	-51 ± 0.1	7.9	10 ± 0.1	9.8
Tb	-109± 1.8	-19± 0.6	-40 ± 0.5	10	-12 ± 1.5	10.2
Dy	-33± 0.4	-12± 0.4	-24 ± 0.1	10.8	28 ± 0.7	5.4

seen by a cusp in the magnetic susceptibility curve. $\chi(T)$ at high temperatures fits the modified Curie-Weiss law, giving θ_{ab} = -33 K, θ_c = -12 K and θ_{ave} = -24 K. The observed effective moment from the polycrystalline averaged susceptibility is μ_{eff} = 10.7 μ_B per Dy^{3+} (see Table 7.3), consistent with the expected Hund's rule ground-state value, 10.65 μ_B. The field-dependent magnetization curve for $\mathrm{DyNi}_{0.745}\mathrm{Bi}_{1.76}$ shows anisotropic behavior, which is shown in the inset of Fig.7.9 (c).

7.5 Discussion and conclusions

Motivated by the recent claims about $\mathrm{CeNi}_{0.8}\mathrm{Bi}_2$ [Mizoguchi et al., 2011; Kodama et al., 2011; Mizoguchi et al., 2012] and previous studies of rare-earth compounds [Myers et al., 1999; Bud'ko et al., 1999; Petrovic et al., 2003], we have synthesized single crystalline $R\mathrm{Ni}_{1-x}\mathrm{Bi}_{2\pm y}$ (R = La–Nd, Sm, Gd–Dy) samples by using Bi as a flux. Detailed resistivity, magnetic susceptibility and magnetization measurements were performed to study the properties of $R\mathrm{Ni}_{1-x}\mathrm{Bi}_{2\pm y}$. The crystals form as plates, and can be identified as having a $P4/nmm$ structure. We have determined the Ni and Bi concentrations and seen clear evidence of the associated, disorder scattering manifest in the low RRR values.

Superconducting features have been observed in the transport measurements for

$LaNi_{0.84}Bi_{2.04}$ and $CeNi_{0.80}Bi_{2.03}$, as well as the other members in this family. However, the transition temperatures coincide with the T_c of film Bi, NiBi and/or $NiBi_3$, and the features are irreproducible and sample-dependent. Moreover, for $LaNi_{0.84}Bi_{2.04}$, both of the ZFC and FC superconducting volume fractions at 50 Oe are $< 3\%$. The low-field magnetic susceptibility of $CeNi_{0.80}Bi_{2.03}$ is positive. All these strongly suggest that the superconductivity in $RNi_{1-x}Bi_{2\pm y}$ (R = La–Nd, Gd–Dy) is due to minority, second phases.

The high-temperature magnetic susceptibilities of $RNi_{1-x}Bi_{2\pm y}$ (R = Ce–Nd, Gd–Dy) show local-moment like behaviors. For the whole $RNi_{1-x}Bi_{2\pm y}$ family, Ni is non-moment bearing. The values of the effective magnetic moment in the paramagnetic state are close to the theoretical values of the trivalent rare earth ion. μ_{eff}, θ_{ab}, θ_c and θ_{ave} values, obtained by fitting with the modified Curie-Weiss law are summarized in Table 7.3. The local-moment ordering is likely governed by the indirect exchange interactions between the rare earth ions mediated by the conduction electrons (RKKY interaction). The negative sign of the paramagnetic Curie temperatures θ_{ab}, θ_c and θ_{ave} indicates the dominate interactions in this system are antiferromagnetic. Based on the Weiss molecular field theory, both θ_{ave} and the magnetic ordering temperature T_M are expected to be proportional to the de Gennes factor $DG = (g_J - 1)^2 J(J+1)$. Here g_J is the Landé g factor and J is the total spin angular momentum [De Gennes, 1962]. As shown in Fig. 7.10, by removing the CEF effect, the paramagnetic Curie temperature θ_{ave} follows the DG scaling quite well except for R = Ce. This deviation is probably related to the hybridization between $4f$ and the conduction electrons. However, significant deviations from linearity are present for the scaling of the magnetic ordering temperatures T_M. This can occur when a strong CEF constrains the moments to either along the c-axis or within the basal plane [Noakes and Shenoy, 1982]. This may be responsible for the higher value of $TbNi_{0.74}Bi_{1.90}$, as it shows strong anisotropy in Fig. 7.9 (b). The decreasing unit cell volume in this series (lanthanide contraction) may lead to

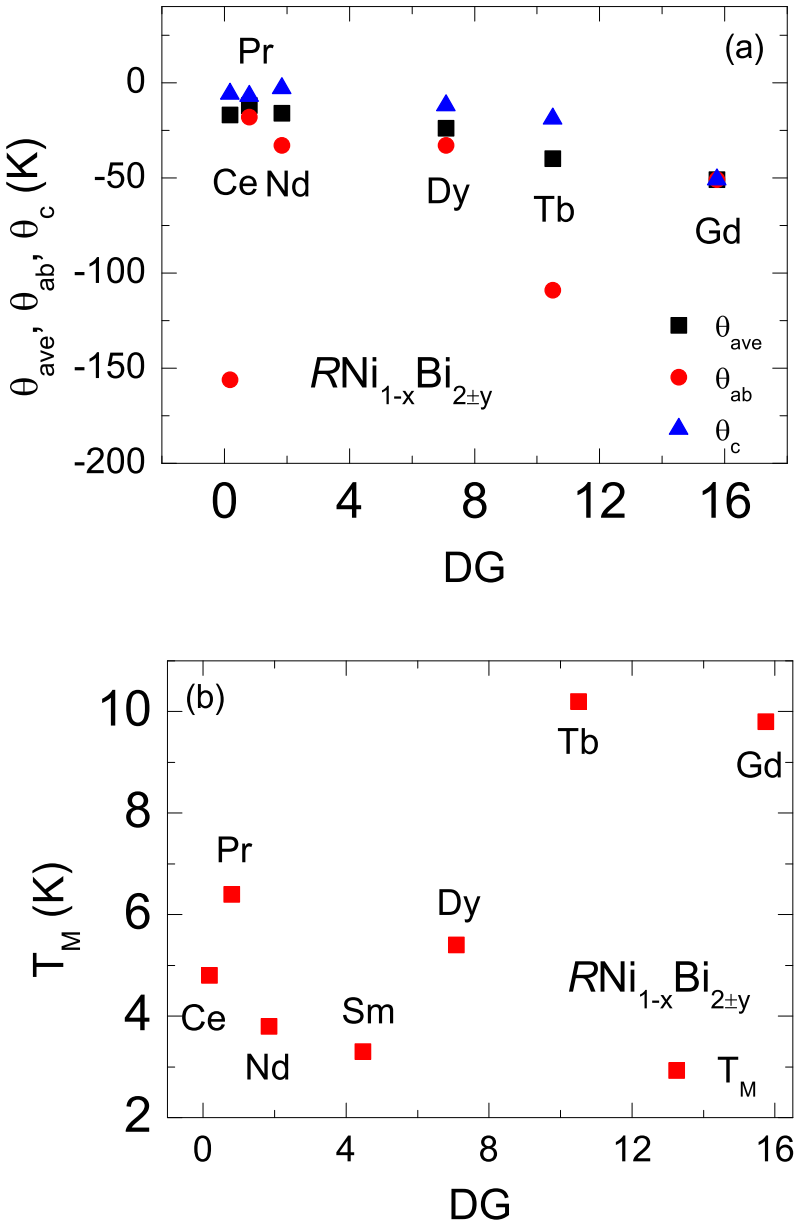

Figure 7.10 Changes of (a) paramagnetic Curie temperature θ_{ave}, θ_{ab}, θ_c and (b) magnetic ordering temperatures with the de Gennes parameter DG. [Lin et al., 2013b]

changes in the conduction electron density and/or the exchange constants (due to shorter atomic distances), and these changes could also be responsible for this deviation from the de Gennes scaling. Similar to their isostructural compounds $R\mathrm{AgSb_2}$ [Myers et al., 1999] and $R\mathrm{AgBi_2}$ [Petrovic et al., 2003], most of the $R\mathrm{Ni}_{1-x}\mathrm{Bi}_{2\pm y}$ members manifest antiferromagnetic ordering at low temperatures. $R\mathrm{Ni}_{1-x}\mathrm{Bi}_{2\pm y}$ shows more anisotropy in their magnetic properties than the $R\mathrm{AgBi_2}$ series, but less than the $R\mathrm{AgSb_2}$ family's. θ_{ave}/T_M values characterizing the level of frustration [Ramirez, 1994] for $R\mathrm{Ni}_{1-x}\mathrm{Bi}_{2\pm y}$ although enhanced, between 1.9 and 5.2, are not significantly different from those found for either the $R\mathrm{AgBi_2}$ or the $R\mathrm{AgSb_2}$ compounds, which means the values are not clearly related to the site disorder.

CHAPTER 8. SUPPRESSION OF FERROMAGNETISM IN THE $LaV_xCr_{1-x}Ge_3$ SYSTEM [1]

8.1 Abstract

We report the synthesis of hexagonal $LaV_xCr_{1-x}Ge_3$ (x = 0 – 0.21, 1.00) single crystals, and present a systematic study of this series by measurements of temperature and field dependent magnetic susceptibility, magnetization, resistivity, and specific heat. Ferromagnetism has been observed for x = 0 – 0.21. The Curie temperature declines monotonically as the V-concentration increases. Single crystalline samples could only be grown for x-values up to 0.21 for which the transition temperature was suppressed down to 36 K. Although we could not fully suppress T_C via V-substitution, for $x = 0.16$, we performed magnetization measurements under pressure. The ferromagnetic state is suppressed under pressure at an initial rate of $dT_C/dp \simeq$ – 11.7 K/GPa and vanishes by 3.3 GPa. The increase of the Rhodes-Wolfarth ratio suggests that the ferromagnetism in this system evolves toward itinerant as the V-concentration increases.

8.2 Introduction

Transition metals and their compounds, can manifest itinerant magnetic behavior, with their magnetic properties originating from delocalized d-electrons [du Tremolet de Lacheisserie, 2005; Uhlarz et al., 2004; Thessieu et al., 1995]. Unlike the localized $4f$-

[1] This chapter is based on the submitted article: Lin, X., Taufour, V., Bud'ko, S. L., and Canfield, P. C., "Suppression of ferromagnetism in the $LaV_xCr_{1-x}Ge_3$ system" *Phys. Rev. B*, 88 (2013):094405

electrons in the lanthanide series or the multiconfigurational $5f$-electrons in some of the actinide elements [Booth et al., 2012; Troc et al., 2012], the d-electrons' orbitals can be significantly altered by the formation of chemical bonds. The d electrons often become part of the conduction band, propagating in the materials, thus, their wavefunctions are very different from those of localized electrons. This gives rise to the relatively large exchange interactions between the d-electrons. Based on the Stoner criterion [Stoner, 1933], at a critical value of the density of states (DOS) and on-site repulsion, d-electrons can spontaneously split into spin-up and spin-down sub-bands, which leads to ferromagnetic ordering. Although the Stoner theory [Stoner, 1933] provides the grounds for understanding the itinerant ferromagnetic state, there are still questions left to be answered about the role of spin fluctuations and the quantum criticality in the itinerant ferromagnetic systems.

Itinerant ferromagnets are of particular interest for studying the mechanism of magnetism and superconductivity near a quantum critical point (QCP). Unlike the classical phase transitions driven by temperature, a quantum phase transition (QPT) at zero temperature is driven by non-thermal parameters [Sachdev, 2001]. A QCP is thought to be a singularity in the ground state, at which point the characteristic energy scale of fluctuations above the ground state vanishes [Sachdev, 2001]. In itinerant ferromagnets, the temperature dependence of the magnetic properties has often been interpreted in terms of spin fluctuations [Lonzarich, 1986, 1988; Hertz, 1976]. With the spin fluctuations, an ordered ground state can change into a non-ordered state by crossing a QCP. Non-Fermi liquid behaviors of the materials associated with a QCP can often be observed, such as the temperature divergences of the physical properties [Stewart, 1984, 2001, 2006; Bud'ko et al., 2004, 2005; Mun et al., 2013]. Moreover, superconductivity has been discovered in the vicinity of a QCP in weakly ferromagnetic systems, such as in the case of UGe_2 [Taufour et al., 2010; Saxena et al., 2000; Huxley et al., 2001] and UCoGe [Huy et al., 2007]. On the boundary of a ferromagnetic state at low temperatures, a strong longitu-

dinal magnetic susceptibility and magnetic interactions may lead to a superconducting state [Saxena et al., 2000; Fay and Appel, 1980; Miyake et al., 1986]. The parallel-spin quasiparticles in the ferromagnetic system should form pairs in odd-parity orbitals, based on the Pauli exclusion principle. Theories suggest that this type of superconductivity should be spin-triplet and magnetically mediated [Saxena et al., 2000; Fay and Appel, 1980; Miyake et al., 1986]. Thus, the suppression of ferromagnetism and the search for a QCP in the itinerant ferromagnetic systems may offer a better understanding of the magnetically mediated superconductivity and non-Fermi liquid behaviors. Chemical doping, pressure and magnetic field are often used to tune the magnetic orderings, and drive the criticality. For example, a QCP emerges in $Zr_{1-x}Nb_xZn_2$ when the doping level reaches $x_c = 0.083$ [Sokolov et al., 2006], and in $CePd_{1-x}Ni_x$ when the doping level is 0.95 [Stewart, 2001]. YbAgGe [Bud'ko et al., 2004], YbPtBi [Mun et al., 2013] and $YbRh_2Si_2$ [Trovarelli et al., 2000] can be driven to field induced QCPs associated with a non-Fermi-liquid behavior in the resistivity. In the case of MnSi [Thessieu et al., 1995] and UGe_2 [Taufour et al., 2010], itinerant-electron magnetism disappears at a first order transition and a QPT appears as pressure is applied.

Both $LaCrGe_3$ and $LaVGe_3$ were reported to form in a hexagonal perovskite type (space group $P6_3/mmc$) structure [Bie et al., 2007; Bie and Mar, 2009]. The structure consists of chains of face-sharing Cr-centered (or V-centered) octahedra extended along the c-direction. The short Cr-Cr (or V-V) distances have been taken as an indication of weak metal-metal bonding [Bie et al., 2007; Bie and Mar, 2009]. It is suggested that by applying the conventional geometric arguments for stabilizing perovskite-related structures, the hexagonal form is favored over the more common cubic form with the Goldschmidt tolerance factor $t > 1$ [Bie and Mar, 2009; Goldschmidt, 1926]. Whereas $LaVGe_3$ is found to be non-magnetic above 2 K [Bie and Mar, 2009]. $LaCrGe_3$ was reported to order ferromagnetically at 78 K [Bie et al., 2007; Cadogan et al., 2013]. Previous work suggests $LaCrGe_3$ is an itinerant ferromagnet, with an estimated effective

moment, 1.4 μ_B/f.u., that is significantly lower than the expected values of Cr^{4+} (2.8 μ_B) or Cr^{3+} (3.8 μ_B) [Bie and Mar, 2009]. Based on the band structure calculated for both compounds, it is claimed that they have very similar DOS features and can probably be explained by the rigid band model [Bie et al., 2007; Bie and Mar, 2009]. For $LaCrGe_3$, the *d*-state of Cr manifests as a sharp peak near the Fermi level in the DOS, consistent with itinerant ferromagnetism as suggested by the Stoner model [Stoner, 1933]. $LaVGe_3$, with fewer electrons, fills the band up to a lower energy level. Thus, the Fermi level of $LaVGe_3$ lies at a local minimum of the DOS, and shows paramagnetic behavior.

To suppress the ferromagnetism in this system, substituting V for Cr in $LaV_xCr_{1-x}Ge_3$ is one of the rational choices, since this is expected to tune the DOS by changing the position of the Fermi level. Studies of polycrystalline samples show that V-substitution does change the magnetic exchange interactions, and the long-range magnetic ordering is suppressed [Bie and Mar, 2009]. Only the temperature dependence of magnetization was measured on the polycrystalline samples, and the precise stoichiometry of this doped system was not analyzed by chemical or physical measurement. The V-concentration dependence of Curie temperature was not reported, and it is not clear at which concentration the ferromagnetism is fully suppressed. Detailed measurements of transport and thermodynamic properties of the doped system are needed, in the hope that they will allow one to follow the evolution of the ferromagnetism and distinguish between itinerant and local moment magnetism.

Besides chemical substitution, an itinerant magnetic system can often be perturbed by applying pressure. Thus, for the $LaV_xCr_{1-x}Ge_3$ series, pressure can also be used to suppress the magnetic state and discover a possible QCP.

In this work, we report the synthesis of single crystalline $LaV_xCr_{1-x}Ge_3$ (x = 0 – 0.21, 1.00) samples, and present a systematic study of their transport and thermodynamic properties. A ferromagnetic transition has been confirmed. Both the effective moment and the saturated moment per Cr decrease systematically as V-concentration

increases with the saturated moment decreasing much more rapidly, indicating that the Cr moment is fragile. The associated increase of the Rhodes-Wolfarth ratio suggests that the ferromagnetism in this system becomes more and more itinerant as x increases. The Curie temperature decreases with V-substitution. The magnetic ordering is suppressed down to 36 K for the highest level of V-substitution obtained ($x = 0.21$), other than the non-magnetic $LaVGe_3$. Given that ferromagnetism is not completely suppressed by our highest level of V-substitution, measurements of magnetization under pressure were performed on the $x = 0.16$ sample. The ferromagnetic state is suppressed by the increasing pressure and vanishes by 3.3 GPa.

8.3 Experimental Details

The relatively deep eutectic in the Cr-Ge binary [Massalski, 1990] provides an opportunity to grow $LaV_xCr_{1-x}Ge_3$ compounds out of high-temperature solutions [Canfield and Fisk, 1992; Canfield, 2010]. Single crystals of $LaV_xCr_{1-x}Ge_3$ were synthesized with a ratio of La:V:Cr:Ge = (13+2x):10x:(13–13x):(74+x) ($0 \leq x \leq 0.6$). High purity ($> 3N$) elements La, V, Cr and Ge were pre-mixed by arc-melting. The ingot was then loaded into a 2 ml alumina crucible and sealed in a fused silica tube under a partial pressure of high purity argon gas. The ampoule containing the growth materials was heated up to 1100 °C over 3 h and held at 1100 °C for another 3 h. The growth was then cooled to 825 °C over 65 h at which temperature the excess liquid was decanted using a centrifuge [Canfield and Fisk, 1992; Canfield, 2010]. For $x = 1.0$, i.e. $LaVGe_3$, excess Ge flux was used with an initial composition of La:V:Ge = 15:10:75, and the decanting temperature was adjusted to 880 °C accordingly. Single crystals of $LaV_xCr_{1-x}Ge_3$ grew as hexagonal rods with typical size of $\sim 0.7 \times 0.7 \times 5$ mm^3 (seen in the inset of Fig. 8.1). A considerable amount of second phase material was grown as the result of secondary solidification, which was identified to be $V_{11}Ge_8$ by powder X-ray diffraction. For growths

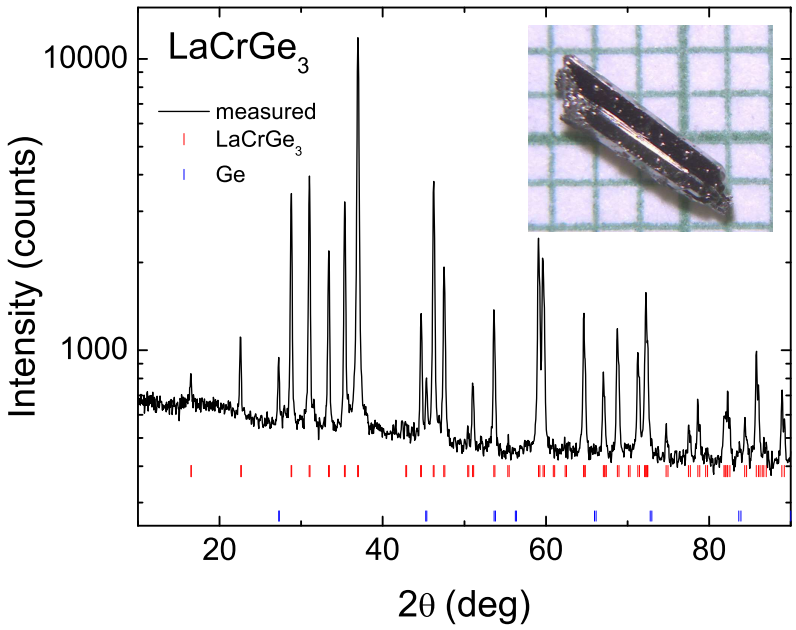

Figure 8.1 Powder X-ray diffraction pattern of $LaCrGe_3$. Inset: Photo of a single crystalline $LaCrGe_3$ sample on a millimeter grid [Lin et al., 2013c].

with initial composition of $0.6 < x < 1.0$, the sizes of crystals dramatically decreased to submillimeters, and could not be visually distinguished from the secondary solidification ($V_{11}Ge_8$). Despite multiple attempts, single crystalline $LaV_xCr_{1-x}Ge_3$ samples with higher x, which are distinguishable from the secondary solidification, could not be grown.

Powder X-ray diffraction data were collected on a Rigaku MiniFlex II diffractometer with Cu Kα radiation at room temperature. Samples with rod-like shape were selected for the measurement. Data collection was performed with a counting time of 2 s for every 0.02 degree. The Le Bail refinement was conducted using the program Rietica [Howard and Hunter, 1998]. Error bars associated with the values of the lattice parameters were determined by statistical errors, and Si powder standard was used as an internal reference.

Elemental analysis of the samples was performed using wavelength-dispersive X-ray

spectroscopy (WDS) in a JEOL JXA-8200 electron probe microanalyzer. Only clear and shiny, as grown surface regions were selected for determination of the sample stoichiometry, i.e. regions with residual Ge flux were avoided. For each compound, the WDS data were collected from multiple points on the same sample.

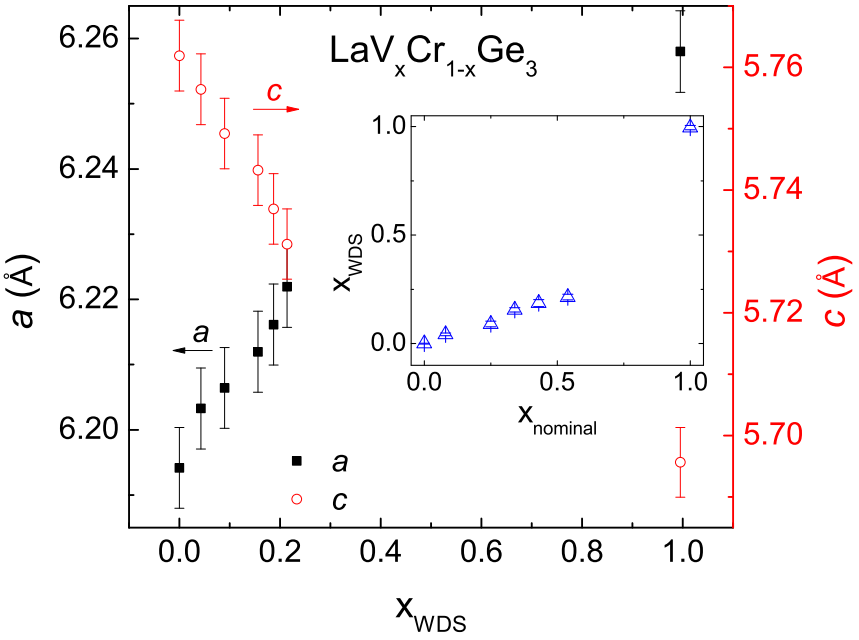

Figure 8.2 The lattice parameters a and c of single crystalline $LaV_xCr_{1-x}Ge_3$ compounds vs. V-concentration x_{WDS} measured by WDS. Inset: x_{WDS} vs. $x_{nominal}$ [Lin et al., 2013c].

The ac resistivity was measured by a standard four-probe method in a Quantum Design, Physical Property Measurement System (PPMS). Platinum wires were attached to the sample using Epo-tek H20E silver epoxy, with the current flowing along the c-axis. The absolute values of resistivity are accurate to $\pm 15\%$ due to the accuracy of measurements of electrical contacts' positions.

Measurements of field and temperature dependent magnetization were performed in a Quantum Design, Magnetic Property Measurement System (MPMS). Magnetization measurements were made by mounting the single crystal samples in a pair of transparent

plastic straws. For the applied field $\mathbf{H} \parallel c$ the crystal was placed between the outer diameter of the inner straw and the inner diameter of the outer straw with both being completely uniform along their lengths. In this field direction there was no addenda associated with the sample mounting. For the applied field $\mathbf{H} \parallel ab$ the crystal was placed between two halves of the split, inner straw with a < 2 cm^2 of transparent plastic film covering the two open ends, providing an effective support for the crystal. The addendum associated with this mounting was less than $\sim 10\%$ of our smallest signal at the highest temperature. The effective moments calculated for $\mathbf{H} \parallel c$, $\mathbf{H} \parallel ab$ and for an effective polycrystalline average ($\chi_{ave} = \frac{1}{3}\ (\chi_c + 2\chi_{ab})$) are all within 0.1 μ_B/Cr of each other, demonstrating basic isotropy of the high-temperature, paramagnetic state of these samples. For this work we will use the results of the polycrystalline average data.

Temperature-dependent specific heat in zero field was measured in a PPMS using the relaxation technique for representative samples. The specific heat of $LaVGe_3$ was used to estimate the non-magnetic contributions to the specific heat of $LaV_xCr_{1-x}Ge_3$. The magnetic contribution to specific heat from the Cr ions was calculated by the relation: $C_M = C_p(LaV_xCr_{1-x}Ge_3) - C_p(LaVGe_3)$.

The temperature dependent, field-cooled magnetization of a single crystal for $x = 0.16$ under pressure was measured in a Quantum Design MPMS-SQUID magnetometer in a magnetic field of 20 Oe, 50 Oe and 1 kOe applied along the c-axis. Pressures of up to 4.9 GPa were achieved with a moissanite anvil cell [Alireza et al., 2007]. The body of the cell is made of Cu-Ti alloy and the gasket is made of Cu-Be. Daphne 7474 was used as a pressure transmitting medium, and the pressure was determined at 77 K by the ruby fluorescence technique.

8.4 Results and Analysis

8.4.1 Crystal Stoichiometry and Structure

The stoichiometry of the $LaV_xCr_{1-x}Ge_3$ samples was inferred by WDS analysis. Table 8.1 summarizes the normalized results showing the atomic percent of each element. The ratio of La:(V+Cr):Ge stays roughly as 1:1:3. The variation is induced by systematic error, and the counting statistics suggests that there should be 2% or less relative error due to counting. As shown in the inset of Fig. 8.2, the ratio of x_{WDS} over x_{nominal} is approximately 0.4, and the small 2σ-values suggest that the samples are homogeneous. In the following, the measured, x_{WDS}, rather than nominal x values will be used to index the stoichiometry of the compounds in this series.

Powder X-ray diffraction patterns were collected on ground single crystals from each compound. Figure 8.1 presents the $LaCrGe_3$ X-ray pattern as an example. The main phase was refined with the known $P6_3/mmc$ (No. 194) structure. Small traces of Ge residue can be detected, whereas no clear evidence of La-Ge, V-Ge, or Cr-Ge binaries was found. Similar results ($P6_3/mmc$ structure with minority phase of Ge) were obtained for the rest of the series. The lattice parameters, obtained by the analysis of the powder X-ray diffraction data, are presented in Fig. 8.2. As is shown, a and c are monotonically changing as the x increases, which is consistent with the reported data [Bie and Mar, 2009]. Crystallographically, transition metal elements in $LaCrGe_3$ and $LaVGe_3$ occupy the same unique site $2a$ [Bie et al., 2007; Bie and Mar, 2009].

8.4.2 Effects of chemical substitution on the physical properties

Figures 8.3(a)–8.3(f) present the anisotropic field-dependent magnetization isotherms for the $LaV_xCr_{1-x}Ge_3$ ($x = 0$ – 0.21) series. The measurements were performed with **H** parallel to the ab-plane and the c-axis at 2 K. For $\mathbf{H} \parallel c$, the magnetization of all compounds saturates very rapidly as the magnetic field increases from $H = 0$, which is

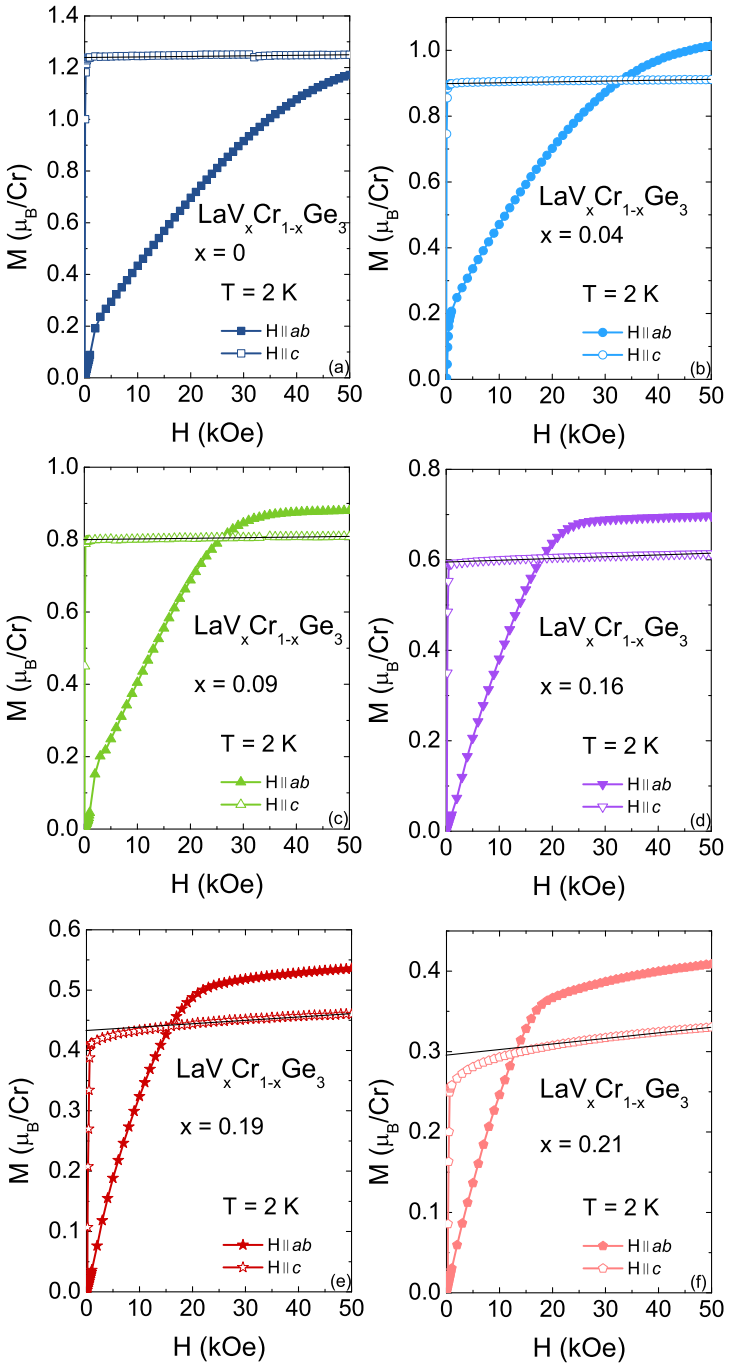

Figure 8.3 Anisotropic field-dependent magnetization data for $LaV_xCr_{1-x}Ge_3$ ($x = 0$ – 0.21) taken at 2 K. Fine solid lines through the high field $\mathbf{H} \parallel c$ data extrapolate back to $H = 0$, μ_S values shown in Table 8.2 [Lin et al., 2013c].

Table 8.1 The WDS data (in atomic %)for $LaV_xCr_{1-x}Ge_3$. N is the number of points measured on one sample, x_{nominal} is the nominal concentration, x_{WDS} is the average x value measured, and 2σ is two times the standard deviation of x_{WDS} from the N values measured [Lin et al., 2013c].

x_{nominal}	N	La	V	Cr	Ge	x_{WDS}	2σ
0.00	13	20.06	0.01	19.80	60.13	0.00	0
0.08	14	20.00	0.83	18.74	60.42	0.04	0.01
0.25	12	19.98	1.76	17.89	60.36	0.09	0.01
0.34	12	20.01	3.06	16.50	60.43	0.16	0.01
0.43	16	20.04	3.69	16.09	60.19	0.19	0.02
0.54	12	20.41	4.29	15.75	59.49	0.21	0.01
1.00	14	19.66	20.46	0.09	59.79	1.00	0.01

a manifestation of a typical ferromagnetic behavior. For $\mathbf{H} \parallel ab$, the magnetization rises more slowly as the applied field increases. As can be seen, in low fields, $M_c \gg M_{ab}$; at $H = H_{\text{Equal}}$, M_c equals M_{ab}; and in high fields, $M_c < M_{ab}$. Also as x increases, H_{Equal} decreases monotonically as shown in Fig. 8.4. We identify the c-axis as the easy axis in low fields, and the x-dependence of H_{Equal} presents a calliper of the diminishing range of the low-field $M_c > M_{ab}$ anisotropy. These data suggest that the $LaV_xCr_{1-x}Ge_3$ compounds may have a complex magnetic structure with a ferromagnetic component along the c-axis. The change of anisotropy is probably caused by field induced spin reorientation, which is consistent with the previous neutron study [Cadogan et al., 2013]. For $\mathbf{H} \parallel c$, the saturated moment μ_{S} per Cr is determined by linear extrapolations of the magnetization from high fields to $H = 0$. For $x = 0$, μ_{S} is found to be about 1.25 μ_{B}/Cr, essentially identical to the reported value 1.22 μ_{B} [Cadogan et al., 2013]. It monotonically decreases as the V concentration increases and drops to 0.30 μ_{B}/Cr for $x = 0.21$. The values of the saturated moment μ_{S} with $\mathbf{H} \parallel c$ are summarized in Table 8.2. Again, the decrease of the saturated moment implies that the $LaV_xCr_{1-x}Ge_3$ series probably is an itinerant ferromagnetic system [Bie et al., 2007].

To estimate the Curie temperature T_{C} from the magnetization measurements, we

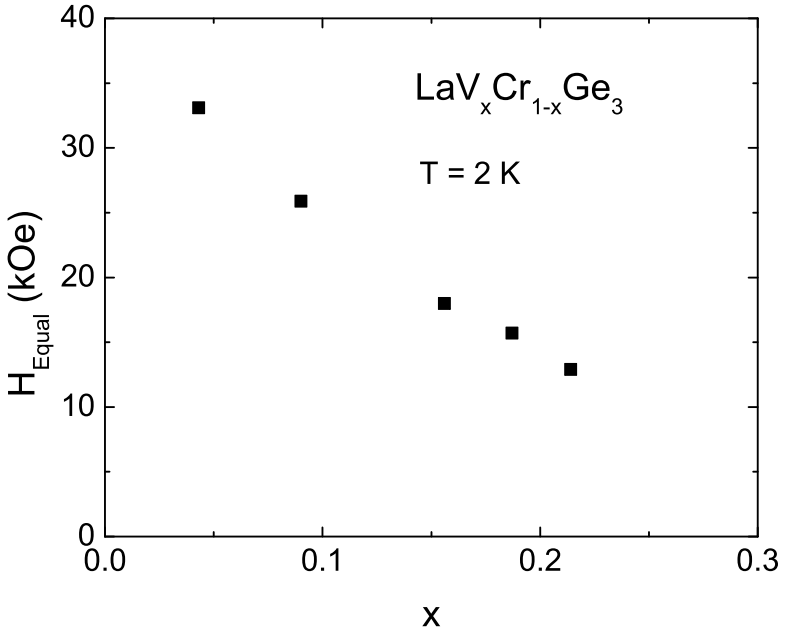

Figure 8.4 H_{Equal} (the field at which $M_c = M_{ab}$) as a function of x for $\mathrm{LaV}_x\mathrm{Cr}_{1-x}\mathrm{Ge}_3$ ($x = 0.04$ – 0.21) taken at 2 K [Lin et al., 2013c].

studied the temperature-dependent, field-cooled (FC) magnetization of the $LaV_xCr_{1-x}Ge_3$ series, with $\mathbf{H} \parallel c$ at 50 Oe, as shown in Fig. 8.5. The magnetization for $LaCrGe_3$ exhibits a sudden increase near 90 K, indicating a transition to a ferromagnetic state. However, at around 68 K, its value starts declining, then saturates at low temperatures, leaving a peak seen in its magnetization. This is probably associated with the changes of the magnetic domains and the demagnetization field upon cooling. A similar feature was not observed for the V-doped compounds. It is possibly due to the pinning effect brought by the V-substitution. For the other members of the series, the susceptibility shows the expected, rapid increase and the tendency to saturation at low temperatures, which indicate the existence of a ferromagnetic state in this series for x up to 0.21. The Curie temperature was estimated by extrapolating the maximum slope in M/H to zero, as shown by the arrow in the inset of Fig. 8.5; the T_C values are listed in Table 8.2. Given that these are very low field $M(T)$ data, these values should not be too different from those inferred from the Arrott plots; see Fig. 8.6. The monotonic change of the Curie temperature demonstrates that the ferromagnetism in the $LaV_xCr_{1-x}Ge_3$ series is systematically suppressed by the V-substitution.

Given that a ferromagnet possesses a spontaneous magnetization below its Curie temperature, even without external magnetic field applied, the determination of the Curie temperature from the temperature-dependent magnetization is not without ambiguity. To better evaluate the Curie temperature, magnetization isotherms in the vicinity of T_C were measured for $x = 0.16$ [Fig.8.6 (a)]. Since the ferromagnetic component is believed to be along the c-axis, the magnetic field was applied along the c-axis. In addition in this orientation we also reduce the uncertainty caused by the demagnetization signal along the long axis of the rod-like sample.

As can be seen in Fig. 8.6 (a), spontaneous magnetization can be easily observed for $M(H)$ measured at 43, 46, 48 and 49 K, indicating that the system possesses a state with a ferromagnetic component at least up to 49 K. To further refine our determination of

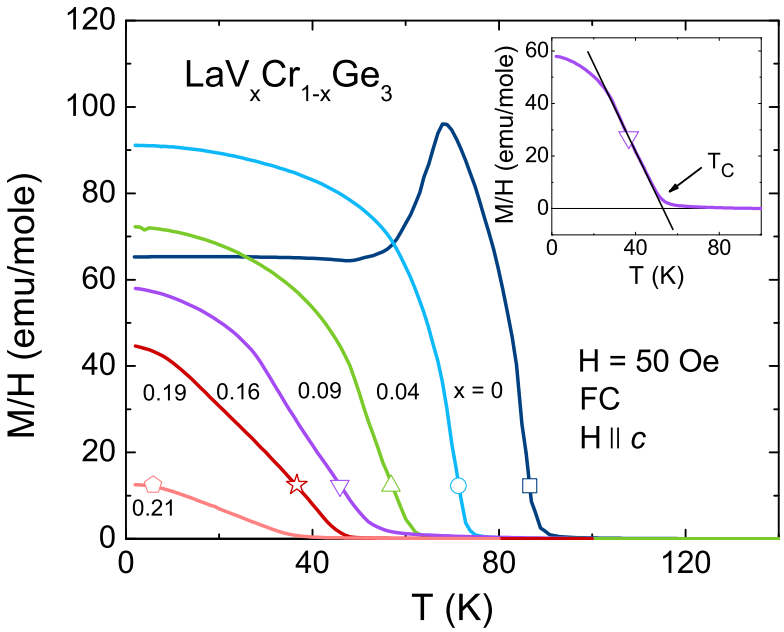

Figure 8.5 Field-cooled (FC) magnetization as a function of temperature for $LaV_xCr_{1-x}Ge_3$ ($x = 0 - 0.21$) at 50 Oe with $\mathbf{H} \parallel c$. Inset: Enlarged temperature dependence of magnetization near phase transition for $x = 0.16$. The arrow shows the criterion used to infer the transition temperature [Lin et al., 2013c].

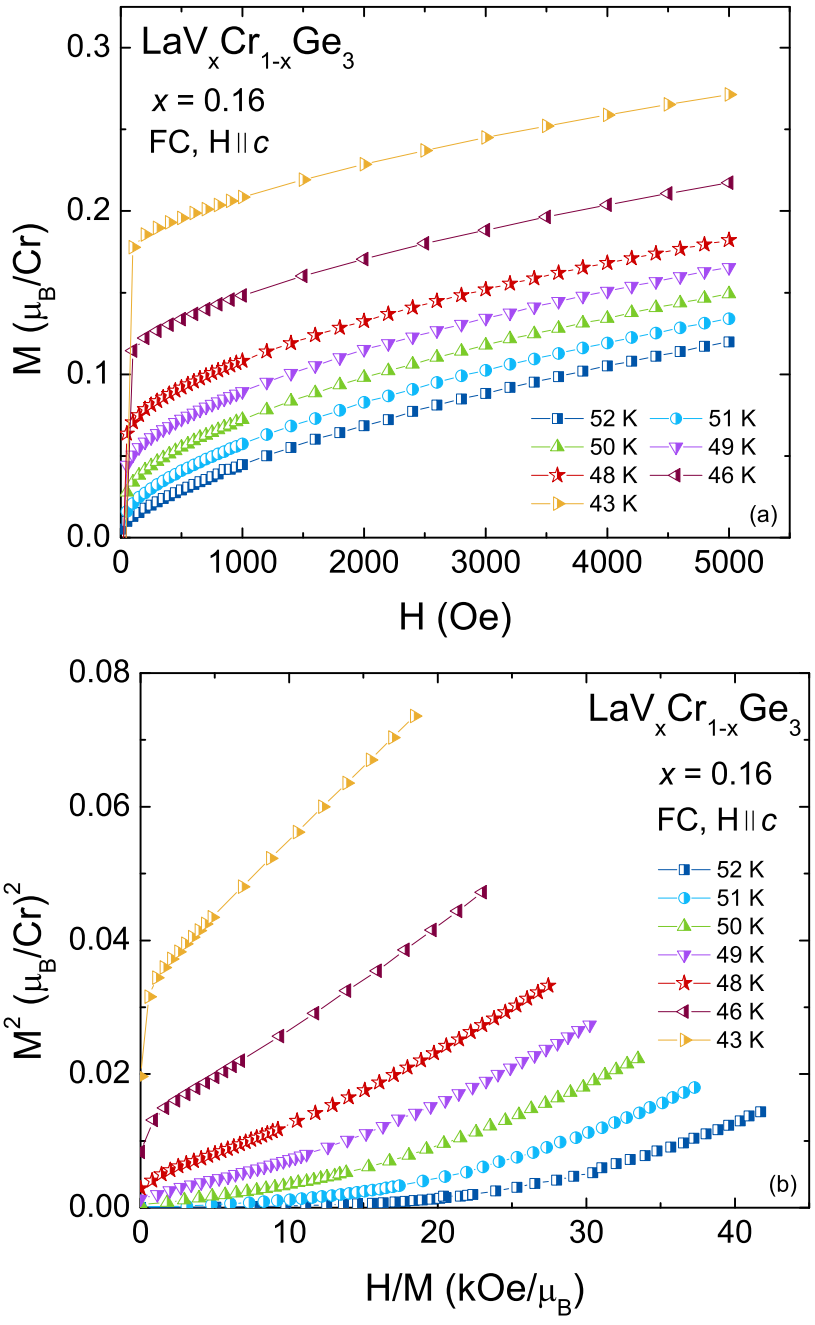

Figure 8.6 (a) Magnetization isotherms for $x = 0.16$ measured at different temperatures. (b) The Arrott plot in the form of M^2 vs H/M for $x = 0.16$, with **H** $\parallel$ c [Lin et al., 2013c].

the Curie temperature, an Arrott plot for $x = 0.16$ is presented in Fig.8.6 (b). According to Arrott [Arrott, 1957], at T_C, the relation between the magnetic field H and the magnetization M can be written in the form of a power law expansion:

$$\frac{M_0 H}{N_A k_B T_C} = a_1(\frac{M}{M_0})^3 + a_2(\frac{M}{M_0})^5 + ...$$

Here a_1 and a_2 are the expansion coefficients, M_0 is the saturated magnetization at zero temperature, and N_A is Avogadro's number. This relation is valid under the condition: $M \ll M_0$, i.e., in the low field region. Therefore, further approximation can be made by only considering the first term in the expansion which leads to the Arrott-Noakes [Arrott and Noakes, 1967] relation: $(H/M) \propto M^2$ at T_C. It suggests that the ferromagnetic ordering temperature T_C can be inferred from the magnetization data by noting the temperature at which the low-field data pass though the origin. As shown in Fig. 8.6 (b), the Curie temperature for $x = 0.16$ is about 50 $\pm$ 1 K, which is very close to the value obtained from the low field magnetization measurement (also seen in Table 8.2). Therefore, the T_C determined from the low field magnetization data appears to be reliable for these materials.

The isothermal curves shown in Fig. 8.6 (b) are found to be deviated from the linearity in the Arrott plot. It should be noted that the theoretical justification on the Arrott plot is based on a simple and clearly defined Landau type second order phase transition [Arrott, 1957]. In the real materials, such deviations can be observed in a disordered system with complex magnetic phenomena, and can be affected by many factors, such as the coupling between the homogeneous matrix and the magnetic clusters, domain wall pinning, or even proximity to field stabilized states, etc [Yeung et al., 1986; Hilscher, 1982; Jia et al., 2008].

The inverse of the polycrystalline averaged susceptibility H/M measured at 1 kOe is shown in Fig. 8.7. The polycrystalline averaged susceptibility was estimated by $\chi_{ave} = \frac{1}{3}(\chi_c + 2\chi_{ab})$. At high temperatures, all of the compounds follow the Curie-Weiss behavior. It should be mentioned that the susceptibility of $LaVGe_3$ is about three orders

Table 8.2 Summarized μ_S ($\mathbf{H} \parallel c$), μ_{eff}, θ and ordering temperatures from magnetization T_C^{mag}, resistivity T_C^{ρ}, specific heat $T_C^{C_P}$, Arrott plot data and residual resistivity ρ_0 for $LaV_xCr_{1-x}Ge_3$ ($x = 0$ – 0.21) [Lin et al., 2013c].

x_{WDS}	μ_S (μ_B/Cr), $\mathbf{H} \parallel c$	μ_{eff} (μ_B/Cr)	θ (K)	T_C^{mag} (K)	T_C^{ρ} (K)	$T_C^{C_P}$ (K)	T_C(Arrott) (K)	ρ_0 ($\mu\Omega$ cm)
0.00	1.25	2.5	91.7	88	84	85		36
0.04	0.91	2.3	84.7	73	68	69		78
0.09	0.81	2.2	64.6	61	54	62		116
0.16	0.59	2.1	45.9	52	37	46	51 ± 1	100
0.19	0.43	2.0	26.2	46				97
0.21	0.30	1.9	6.7	36				66
1.00								8

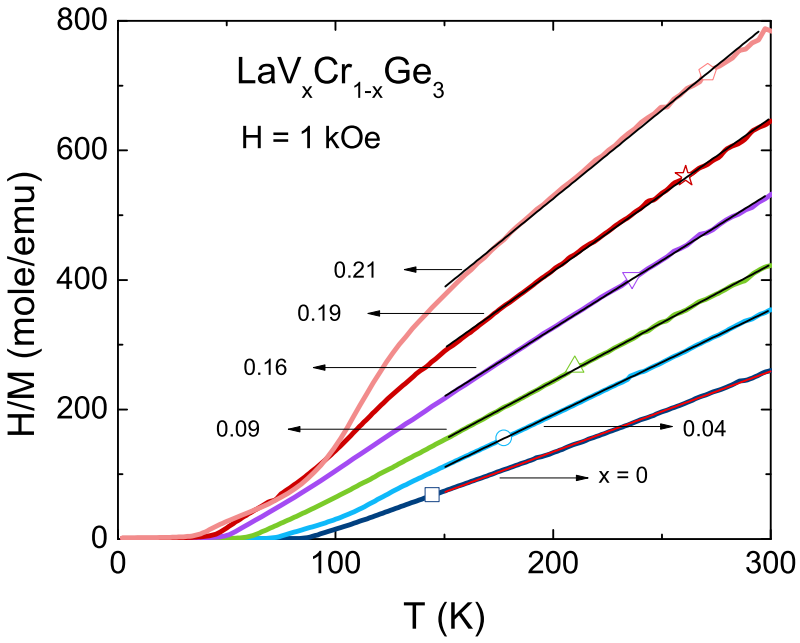

Figure 8.7 The polycrystalline averaged inverse susceptibility H/M as a function of temperature for $LaV_xCr_{1-x}Ge_3$ ($x = 0 - 0.21$) measured at $H = 1$ kOe. The data were fitted with $1/\chi = (T - \theta)/C$ as indicated by the solid lines [Lin et al., 2013c].

of magnitude smaller than those of $LaV_xCr_{1-x}Ge_3$ (x = 0 – 0.21), thus its possible Pauli paramagnetic contribution is negligible. On the other hand, evident deviations from the Curie-Weiss law can be observed below 130 K for x = 0.19 and 0.21. Further investigations are needed to understand the origin of these deviations. The temperature range of 150 to 300 K was selected for fitting the high-temperature magnetic susceptibility with $1/\chi = (T - \theta)/C$, where θ is the Curie-Weiss temperature and C is the Curie constant. The effective moments μ_{eff} and θ are summarized in Table 8.2. Considering the presence of small amount of Ge and $V_{11}Ge_8$ as well as the accuracy of measuring the sample's mass, the values of μ_{eff} in this series are accurate to ±5%. Shown in Fig. 8.7, as x increases, μ_{eff} per Cr decreases systematically, the slope of the H/M curve rises gradually, and the Curie-Weiss temperature decreases from 91.7 K for x = 0 to 6.7 K for x = 0.21 monotonically. The positive θ values indicate that ferromagnetic interactions are dominant in this series. The decrease in θ suggests that the ferromagnetic interaction is suppressed by V doping. Based on all of these results, it is highly likely that the Cr ions in the $LaV_xCr_{1-x}Ge_3$ compounds manifest non-local-moment like behavior. It should be noted that, for x = 0, the μ_{eff} = 2.5 μ_B/Cr, value we found is significantly larger than the reported value (1.4 μ_B) inferred from the data on polycrystalline samples [Bie et al., 2007]. Not only is the Ref. [Bie-JSSC07] value different from our x = 0 value, but it is inconsistent with μ_{eff} evolution across the whole series (Fig. 8.7 and Table. 8.2). It is also inconsistent with the μ_{eff} that we measured on polycrystalline samples: μ_{eff} = 2.5 μ_B/Cr for x = 0.07 and μ_{eff} = 2.3 μ_B/Cr for x = 0.13.

The electrical resistivity as a function of temperature for $LaV_xCr_{1-x}Ge_3$ is presented in Fig. 8.8 (a). At high temperatures, the electrical resistivity drops linearly upon cooling, characteristic of normal metallic behavior. For $LaCrGe_3$, due to the loss of spin disorder scattering, a clear break in resistivity occurs at about 84 K. With the subtraction of the residual resistivity ρ_0 (listed in Table 8.2), the evolution of the ferromagnetic transition with increasing x can be clearly seen in Fig. 8.8 (b). As the V-doping level

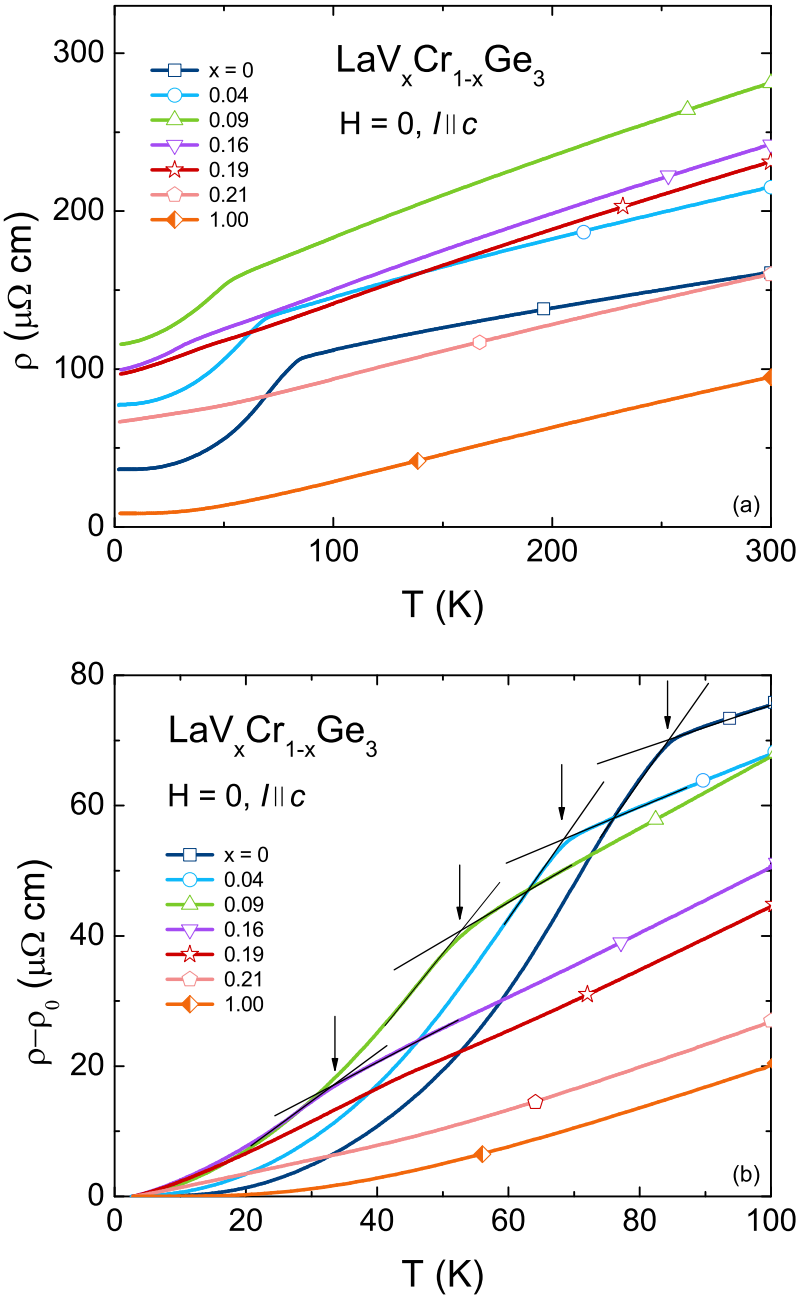

Figure 8.8 (a) The temperature dependent-electrical resistivity for the $LaV_xCr_{1-x}Ge_3$ compounds. (b) Enlarged temperature-dependent ρ -ρ_0 at low temperatures. The transition temperatures are shown by the arrows [Lin et al., 2013c].

increases, the spin disorder scattering associated with the Cr moment ordering becomes broadened . For $x = 0.19$ and 0.21, the feature is too subtle to be clearly detected. Due to the broadening transition feature, determining T_C via $d\rho/dT$ is problematic. Instead, the point at which the slope of $\rho(T)$ changes is used to infer the critical temperature in the resistivity data, as indicated by the arrows in Fig. 8.8 (b). The inferred T_C^{ρ} is summarized in Table 8.2, and it is clear that the Curie temperature decreases monotonically as the V-concentration increases. In addition, ρ_0 seems to show a broad maximum as x increases, which is likely due to more disorder/impurities induced by substitution. The nonmonotonic behavior of ρ_0 is common for substitution series where $x = 0$ and $x = 1$ are well ordered, stoichiometric compounds. The broad maximum located closer to the Cr side is not unexpected given that Cr magnetism (and any scattering associated with it) appears to be dramatically suppressed by V-substitution.

The temperature-dependent specific heat data for the $LaV_xCr_{1-x}Ge_3$ ($x = 0$, 0.04, 0.09, 0.16 and 1.00) series are presented in Fig. 8.9(a) – 8.9(d). The specific heat can be estimated by the relation $C_p(T) = C_e + C_{ph} + C_M$, where C_e is the conduction electron contribution, C_{ph} is the phonon contribution, and C_M is the magnetic contribution. Since $LaVGe_3$ is non-magnetic, $C_e + C_{ph}$ can be approximated by the C_p data of $LaVGe_3$. Thus, the magnetic contribution C_M can be evaluated by the relation: $C_M = C_p(LaV_xCr_{1-x}Ge_3) - C_p(LaVGe_3)$. For a clearer presentation of the transition feature, $C_p(T)$ of all compounds were normalized with respect to the specific heat of $LaVGe_3$, $C_p(LaVGe_3)$, with the highest temperature C_p values set to be equal [as seen in Fig. 8.9(a) – 8.9(d)]. The changes induced by the normalization are less than 3%. An anomaly can be observed in the $C_p(LaV_xCr_{1-x}Ge_3)$ with the comparison of $C_p(LaVGe_3)$. This anomaly, associated with the ferromagnetic transition, can be best seen in the $LaCrGe_3$ sample, at $\sim$ 85 K. As the V-doping level increases, the feature becomes less obvious and systematically shifts to lower temperatures. For $x \geq 0.19$, this feature is no longer detectable. To estimate the ordering temperature, $\triangle C_p/T$ for $x = 0$, 0.04, 0.09, and

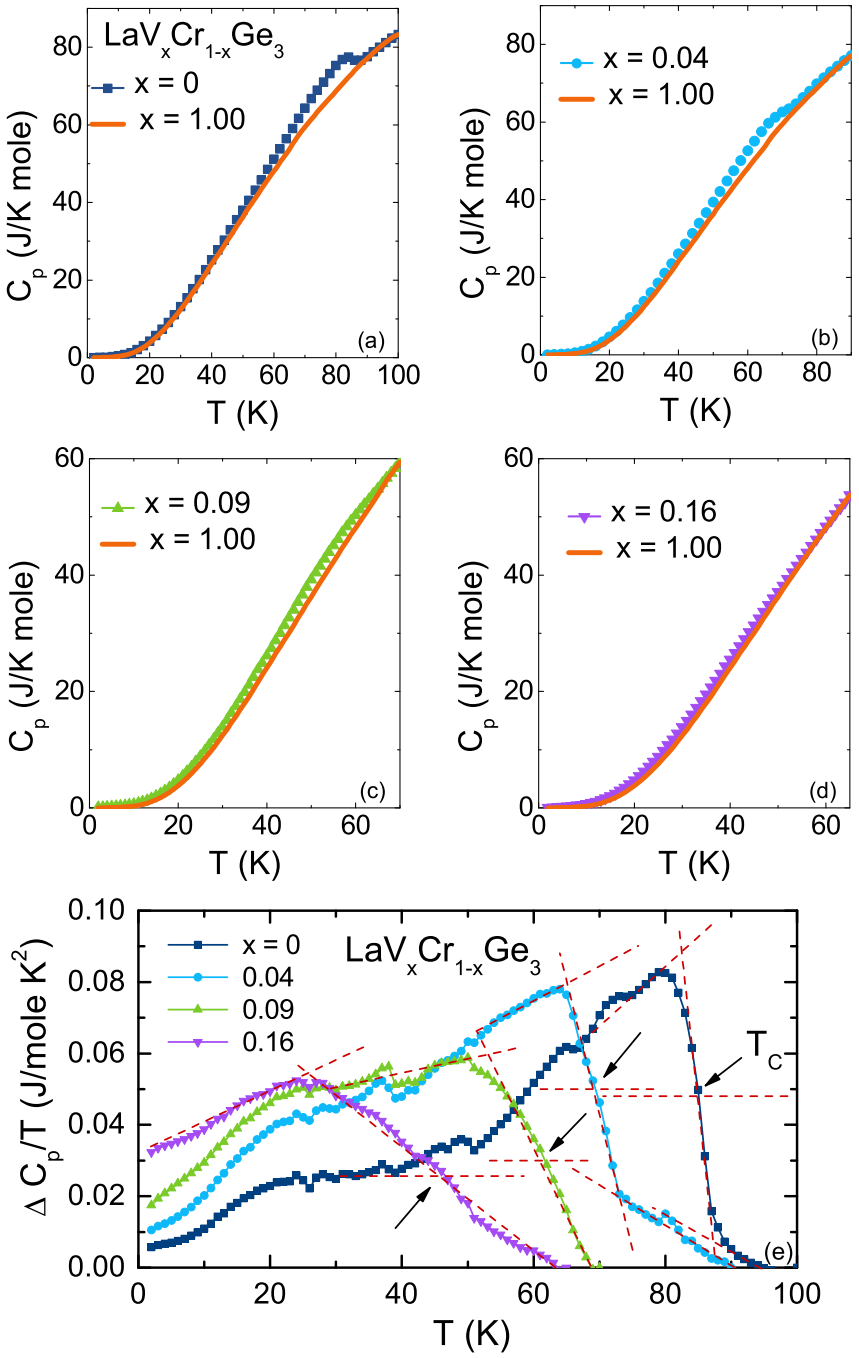

Figure 8.9 Temperature-dependent of specific heat for $LaV_xCr_{1-x}Ge_3$ with (a) $x = 0$ and 1.00, (b) $x = 0.04$ and 1.00, (c) $x = 0.09$ and 1.00, and (d) $x = 0.19$ and 1.00. (e) Magnetic contributions to the specific heat as a function of temperature for $LaV_xCr_{1-x}Ge_3$ ($x = 0 - 0.16$). The arrows show the criteria used to infer the transition temperature [Lin et al., 2013c].

0.16 are plotted in Fig. 8.9 (e). The magnetic phase transition manifests itself as a local maximum. The change of slope seen at $\sim$ 87 K for $x = 0$ and $\sim$ 73 K for $x = 0.04$ may indicate the on-set of the transition. The mid-point on the rise of $\triangle C_p/T$ was chosen as the criteria for $T_{\rm C}^{C_{\rm P}}$, as indicated by the arrows in the plot. These $T_{\rm C}^{C_{\rm P}}$ values are also presented in Table 8.2. Again, we observe that with the increasing amount of V substituted for Cr, the ferromagnetic state in this series is gradually suppressed.

8.4.3 Effects of pressure on the magnetic properties of $LaV_xCr_{1-x}Ge_3$

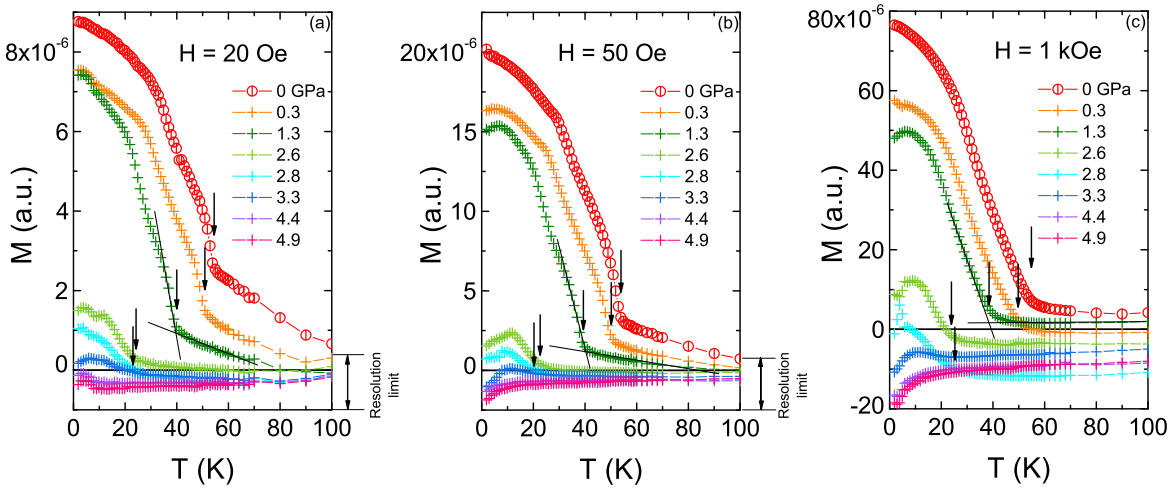

Figure 8.10 Temperature dependence of the field-cooled magnetization for $x = 0.16$ under different pressures with $\mathbf{H} \parallel c$ at (a) 20 Oe, (b) 50 Oe and (c) 1 kOe. Arrows indicate the criteria for the determination of the Curie temperature $T_{\rm C}$ [Lin et al., 2013c].

Given that (i) we could only grow single crystals for $x \leq 0.21$ and (ii) up to $x = 0.16$, the ferromagnetic transition can be confirmed in different measurements, we decided to evaluate the potential for quantum critical behavior by using pressure as a second tuning parameter. Figure 8.10(a) – 8.10(c) show the temperature dependence of the field-cooled magnetization for $x = 0.16$ measured under different pressures. The measurements were performed with $\mathbf{H} \parallel c$ and $H = 20$ Oe, 50 Oe and 1 kOe. The Curie temperature $T_{\rm C}$ is

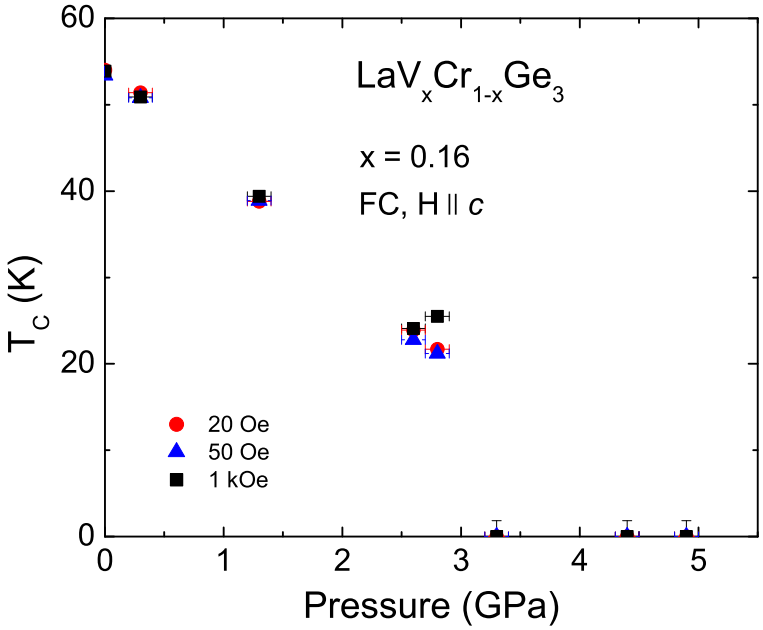

Figure 8.11 Pressure dependence of T_C for $x = 0.16$ measured at 20 Oe, 50 Oe and 1 kOe [Lin et al., 2013c].

revealed by a rather sharp increase of the magnetization. Due to the loss of the signal, there is a serious limitation to the determination of T_C close to the critical pressure. For higher field, $H = 1$ kOe [Fig. 8.10 (c)], measurements and data analysis are limited to the large background of the pressure cell (this is the most likely source of apparent diamagnetic shifts in higher pressure data). By comparing Fig.8.10(a) – 8.10(c), the magnetization under 3.3 GPa is not considered as a ferromagnetic behavior. The pressure dependences of the Curie temperature measured at different fields show consistent behaviors, as plotted in Fig.8.11. The result shows T_C decreases with applied pressure at an initial rate of $dT_C/dp \simeq -11.7$ K/GPa below 2.8 GPa, and no ferromagnetic transition can be detected in our measurements above 3.3 GPa. Similarly, the low temperature magnetization decreases as T_C decreases with applied pressure as shown in Fig. 8.10(a) – 8.10(c). Although the low temperature signal is not necessarily equal to the saturation magnetization, the decrease of the low temperature magnetization following the decrease of T_C is expected for an itinerant ferromagnet [Moriya and Takimoto, 1995] and was experimentally observed in $ZrZn_2$ [Uhlarz et al., 2004; Huber et al., 1975].

8.5 Discussion and Conclusions

The growth of single crystalline $LaV_xCr_{1-x}Ge_3$ ($x = 0 - 0.21, 1.00$) samples has allowed for the detailed study of the anisotropic properties, the determination of the easy axis and the estimate of the effective moment and saturated moment. In addition, careful chemical analysis was performed to determine the precise concentration of this doped system. This offers a clearer understanding of the chemical substitution effect on the suppression of the ferromagnetism in this system, and is also crucial for calculating the saturated and effective moment per Cr ion.

We have been able to suppress the ferromagnetism in the $LaV_xCr_{1-x}Ge_3$ series via chemical substitution. The ordering temperatures inferred from low field magnetization,

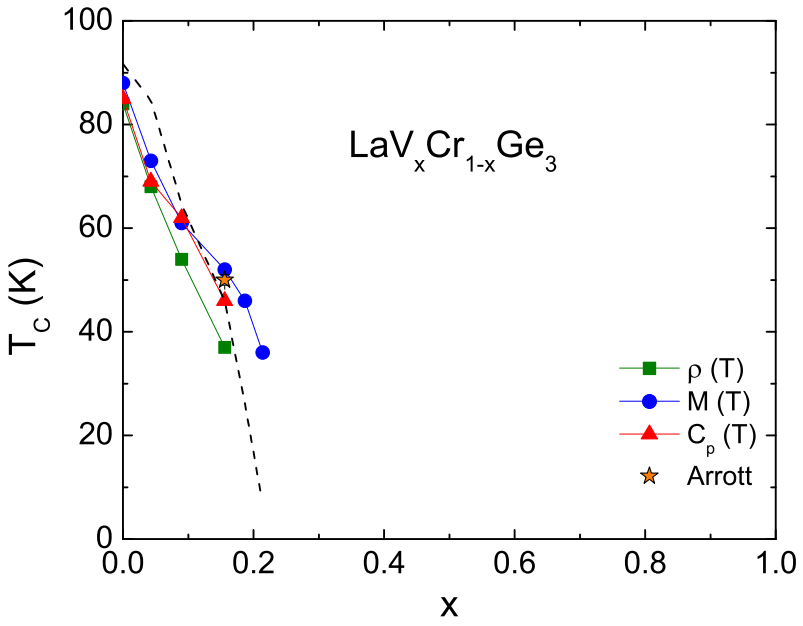

Figure 8.12 x-dependent T_{C} for $\mathrm{LaV}_x\mathrm{Cr}_{1-x}\mathrm{Ge}_3$ determined by $M(T)$, $\rho(T)$ and $C_{\mathrm{p}}(T)$ measurements as well as Arrott plot. For comparison, the dashed line indicates the x dependence of the Curie-Weiss temperature, θ, data that is shown in Fig. 8.13 (a) [Lin et al., 2013c].

resistivity, and specific heat measurements are summarized in Table 8.2. A phase diagram of the x-dependent T_C for $LaV_xCr_{1-x}Ge_3$ was assembled in Fig. 8.12. For $x = 0.19$ and 0.21, magnetic transitions can only be detected in $M(T)$, and not in $\rho(T)$ and $C_p(T)$ measurements. We can see that for the $LaV_xCr_{1-x}Ge_3$ series, the ferromagnetic transition temperature is suppressed almost linearly by V doping: $T_C = 88$ K for $x = 0$, and $T_C = 36$ K for $x = 0.21$. Since single crystalline $LaV_xCr_{1-x}Ge_3$ compounds with $0.21 < x < 1.00$ were not synthesized, the exact concentration x_c at which the ferromagnetism in this series is completely suppressed via V substitution is not determined. Based on the our data, a critical concentration is likely to exist near $x = 0.3$. It is worth noting that this is the substitution range in which a linear extrapolation of the H_{Equal} data shown in Fig. 8.4 reaches zero.

The estimated μ_S and μ_{eff} per Cr as a function of x are plotted in Fig. 8.13 (a). As is shown, both μ_S and μ_{eff} decrease in a clear manner as the V-concentration increases. Consistent with the Stoner model, this suggests that the system possesses a fragile ferromagnetism which can be easily perturbed. The criterion for the ferromagnetic state is given by the relation $UD(\varepsilon_F) \geq 1$, where U and $D(\varepsilon_F)$ are Coulomb repulsion and the DOS at the Fermi level, respectively [Stoner, 1933]. Given the fact that T_C decreases as x increases, it is likely that U and/or $D(\varepsilon_F)$ is changed by V-substitution in the $LaV_xCr_{1-x}Ge_3$ system. With the increasing level of V-doping, the ferromagnetism is continuously suppressed, and will eventually disappear at a critical V-concentration x_c. However, due to the lack of higher V-doped samples, x_c can not be identified precisely in this study. Similarly, in the case of Curie-Weiss temperature, clear suppression in θ by V-doping can be observed, as shown in Fig. 8.13 (a). Again, this implies that the ferromagnetic interaction is weakened by V-substitution. Given the values of μ_S and μ_{eff}, the Rhodes-Wolfarth ratio (RWR) [Rhodes and Wohlfarth, 1963] can be calculated, as seen in Fig. 8.13 (b). According to Rhodes and Wolfarth, RWR = μ_c/μ_S, where μ_c is related to the number of moment carriers, and can be obtained from $\mu_c(\mu_c+1)=\mu_{eff}^2$.

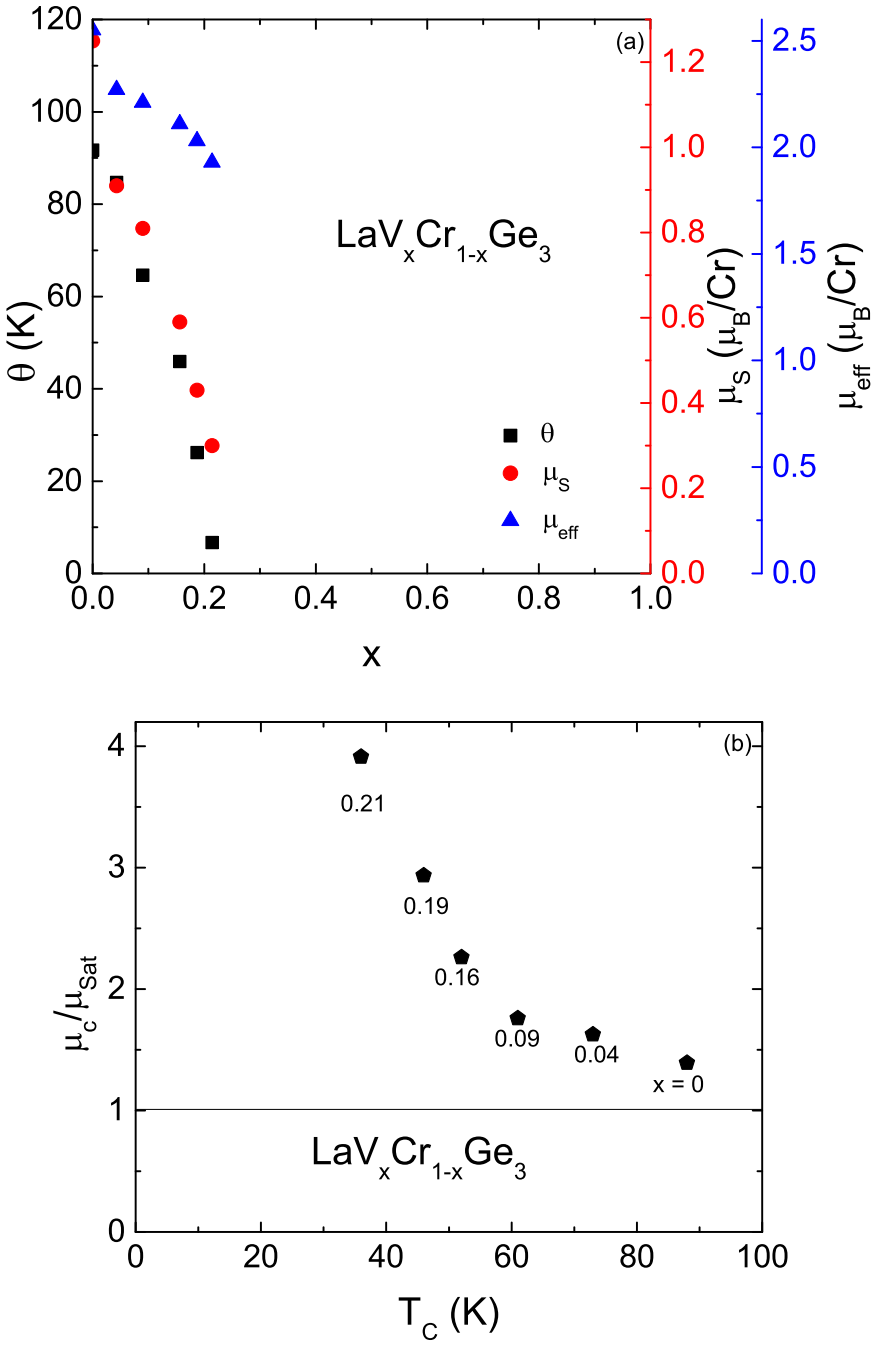

Figure 8.13 (a) The Curie-Weiss temperature θ, saturated moment μ_S along the c-axis and effective moment μ_{eff} per Cr as a function of x for $LaV_xCr_{1-x}Ge_3$. (b) The Rhodes-Wohlfarth ratio μ_c/μ_S as a function of Curie temperature T_C [Lin et al., 2013c].

While RWR = 1 is an indication of localized magnetism, larger RWR values suggest the existence of itinerant ferromagnetism. In our case, for $x = 0$, RWR $\simeq$ 1.4, slightly larger than 1, indicting the possibility of the itinerant ferromagnetism. As x increases, RWR increases accordingly, and reaches $\simeq$ 3.9 for $x = 0.21$, which is much larger than the RWR = 1 criterion. Therefore, it is clear that the ferromagnetism in this series evolves towards itinerant as the V-concentration increase. In addition, as x increases, the change of RWR as a function of T_C exhibits very similar behavior as seen in the original Rhodes-Wohlfarth plot [Rhodes and Wohlfarth, 1963]. It should be noted that the suppression of ferromagnetism does not necessarily lead to a QPT, and a new magnetic state, such as spin glass, may also emerge [du Tremolet de Lacheisserie, 2005; Mydosh, 1993]. However, in the case of the $LaV_xCr_{1-x}Ge_3$ series, given the RWR ratio and the fact that both μ_S and μ_{eff} decrease as the V-concentration increases, it is promising that it may be a potential QCP system [Sokolov et al., 2006; Rhodes and Wohlfarth, 1963].

We further suppressed the ferromagnetism for $x = 0.16$ by pressure up to 4.9 GPa. As seen in Fig. 8.11, the Curie temperature decreases as the applied pressure increases, at an initial rate of $dT_C/dp \simeq -11.7$ K/GPa below 2.8 GPa. The ferromagnetic signal vanishes at $\simeq$ 3.3 GPa, and the ferromagnetism in $x = 0.16$ appears to be completely suppressed. Our data clearly show that this system can be brought to a QPT and, hopefully a QCP. It will be very interesting to study the compounds via transport measurements under pressure and evaluate their critical exponents at p_c. In addition, alternative methods of growing higher x compounds or pressure studies on pure $LaCrGe_3$ will be possible ways to tune the potential QCP system as well.

CHAPTER 9. SUPPRESSION OF FERROMAGNETISM IN THE $La(V_xCr_{1-x})Sb_3$ SYSTEM

9.1 Abstract

To explore the possibility of quantum phase transitions and even quantum criticality in $LaCrSb_3$ based compounds, we performed measurements under pressure as well as a vanadium substitution study. The Curie temperature of $LaCrSb_3$ was found to be invariant under pressure. Although pressure was not able to suppress the ferromagnetism, chemical substitution was used as another parameter to tune the magnetism. We grew $La(V_xCr_{1-x})Sb_3$ ($x = 0$ – 1.0) single crystals, and studied the series by measurements of temperature and field dependent magnetic susceptibility, magnetization, resistivity, and specific heat. Ferromagnetism has been observed for $x \leq 0.22$, and the system manifests a strong anisotropy in its ordered state. The Curie temperature decreases monotonically as the V concentration increases. For $0.42 \leq x \leq 0.73$, the system enters a new magnetic state at low temperatures, and no magnetic ordering above 1.8 K can be observed for $x \geq 0.88$. The effective moment μ_{eff}/Cr varies only slightly as the V concentration increases, from 3.9 μ_{B} for $x = 0$ to 2.9 μ_{B} for $x = 0.88$. Features related to quantum criticality have not been observed in the $La(V_xCr_{1-x})Sb_3$ system.

9.2 Introduction

The study of ferromagnetic materials has long been a focus of research in condensed matter physics. The suppression of an itinerant ferromagnetic transition temperature to

zero is of specific interest, since it may lead to the discovery of a quantum critical point (QCP) [Stewart, 1984, 2001, 2006; Taufour et al., 2010; Saxena et al., 2000; Huxley et al., 2001] which exhibits exotic physical properties, such as non-Fermi liquid behavior and even superconductivity. The Stoner model has been developed to describe a mechanism of an itinerant ferromagnetic system, and is based on the premise that the magnetic properties of the itinerant ferromagnets originate from de-localized electrons [Stoner, 1933]. In particular these de-localized electrons become part of the conduction band and influence the density of state (DOS) at the Fermi level. Based on the Stoner criterion, $UD(\varepsilon_{\mathrm{F}}) > 1$, where U and $D(\varepsilon_{\mathrm{F}})$ are Coulomb repulsion and the DOS at the Fermi level respectively, itinerant ferromagnetism can be suppressed by tuning U and/or $D(\varepsilon_{\mathrm{F}})$. The suppression of itinerant ferromagnetism not only results in the decrease of the ordering temperature, but is also accompanied by decrease of the effective and saturated moments per magnetic species. On the other hand, ferromagnetic ordering can also arise from the interactions of local magnetic moments [du Tremolet de Lacheisserie, 2005; Ashcroft and Mermin, 1976]. As the exchange interaction favors parallel spin alignments, the materials show spontaneous magnetization. Suppressing the ferromagnetism by diluting the local moments, does not reduce the size of effective or saturated moments (per moment bearing ion) and, does not necessarily lead to a QCP [Jia et al., 2007; Szytula and Leciejewicz, 1994]. New magnetic states, such as spin glass, may also emerge in the diluted magnetic system [Mydosh, 1993; Wiener et al., 2000]. Therefore, the suppression of ferromagnetism by substitution may offer an opportunity to approach a QCP, or may result a glassy state, and in doing so, sheds light onto the nature of the ordering mechanism of a specific ferromagnetic system.

$LaCrSb_3$ has been reported to order ferromagnetically below $T_{\mathrm{C}} \sim 125$ – 142 K, with the differences arising from the sample preparation methods [Hartjes et al., 1997; Leonard et al., 1999, 2000; Raju et al., 1998; Jackson et al., 2001]. $LaCrSb_3$ crystallizes in an orthorhombic structure (space group *Pbcm*), where Cr occupies one single crys-

tallographic site 4*c* [Brylak and Jeitschko, 1995]. Extensive investigations into $LaCrSb_3$ have been undertaken, and the compound is found to have a rich magnetic phase diagram [Jackson et al., 2001; Granado et al., 2002; MacFarlane et al., 2006; Crerar et al., 2012; Choi et al., 2007]. $LaCrSb_3$ exhibits unconventional magnetic behavior with a canted ferromagnetism in *bc*-plane. A spin-reorientation transition can be observed in the *bc*-plane at $\sim$ 95 K, and can be suppressed by a small applied magnetic field $\sim$ 250 Oe [Jackson et al., 2001]. Whereas some studies claim $LaCrSb_3$ is an itinerant ferromagnet [Raju et al., 1998; Jackson et al., 2001], the nature of its magnetic moments is still under debate. A neutron scattering study suggests a coexistence of localized and itinerant spins in $LaCrSb_3$ [Granado et al., 2002]. As La is not moment-bearing, the Cr ion plays the primary role in the magnetism of $LaCrSb_3$. Band structure calculations and the X-ray photoelectron spectroscopy studies find that the 3*d* electrons of the Cr exhibit a large DOS peak at/near the Fermi level in the paramagnetic state [Crerar et al., 2012; Choi et al., 2007; Richter et al., 2004], which, based on the Stoner criterion, has a possibility of inducing the ferromagnetic instability.

An itinerant magnetic system can often be perturbed by applying pressure or via chemical substitution. Take MnSi [Thessieu et al., 1995], UGe_2 [Taufour et al., 2010] and $La(V_xCr_{1-x})Ge_3$ [Lin et al., 2013c] as examples; in each, the ferromagnetic state disappears as pressure is applied. Thus, pressure might be able to suppress the ferromagnetic phase and lead to a QCP or quantum phase transition (QPT) in $LaCrSb_3$. Also the DOS can be changed by chemical substitutions for the Cr atoms. $LaVSb_3$, which is an isostructural compound to $LaCrSb_3$, has no magnetic ordering down to 2 K [Brylak and Jeitschko, 1995; Jackson et al., 2001; Sefat et al., 2008]. It is found that the Fermi level in $LaVSb_3$ is shifted away from the highest peak of the DOS [Choi et al., 2007]. Thus, the ferromagnetism in $LaCrSb_3$ may also be suppressed by substituting V for Cr atom.

Previous work on polycrystalline samples showed that V substitution does suppress

the ferromagnetic transitions, and claimed that the mechanism of the ferromagnetic ordering can not be explained by a simple localized magnetic moment model [Dubenko et al., 2001]. Only the temperature dependence of magnetization was measured on the V-doped polycrystalline samples. The nominal V substitution reached only up to 20%, and the precise stoichiometry of this doped system was not analyzed experimentally. It is also not clear at which concentration the ferromagnetism was fully suppressed. In order to better understand the effects of V substitution on the magnetic state of this system, detailed measurements of the transport and thermodynamic properties of systematically substituted single crystals are necessary.

In this work, we report the synthesis of single crystalline $La(V_xCr_{1-x})Sb_3$ (x = 0 – 1.0) samples, and present a systematic study of their transport and thermodynamic properties. In addition, measurements of magnetization under pressure were performed on the $LaCrSb_3$ sample. Whereas the Curie temperature is essentially invariant under pressure, the ferromagnetic ordering is systematically suppressed as the V concentration increases from $x = 0$ to $x = 0.36$. For $0.42 \leq x \leq 0.73$, the system enters into a new magnetic ground state, possibly a complex glassy state. For even higher V-doped compounds, $x \geq 0.88$, the samples stay in the paramagnetic state down to 2 K. The magnetic anisotropy also changes with the V substitution. Although the effective moment per Cr varies slightly as the V concentration increases, possibly suggesting a valence change of Cr ion induced by V substitution, there is no indication of μ_{eff} decreasing toward zero and the Cr moment appears to be robust and fundamentally local-moment like in nature. No experimental features expected in the vicinity of a QCP have been observed by either applied pressure or chemical substitution.

9.3 Experimental Details

Single crystalline $La(V_xCr_{1-x})Sb_3$ samples were synthesized via high-temperature solution method with excess Sb as self-flux [Jackson et al., 2001; Sefat et al., 2008; Canfield and Fisk, 1992; Canfield, 2010]. High purity (> 3N) elements with the starting stoichiometry of La : V : Cr : Sb = 8 : x : 8-x : 84, were placed in a 2 mL alumina crucible and sealed in a fused silica tube under a partial pressure of high purity argon gas. The ampoule containing the growth materials was heated up to 1180 °C over 3 h and held at 1180 °C for another 3 h. The growth was then cooled to 750 °C over $\sim$ 85 h at which temperature the excess liquid was decanted using a centrifuge [Canfield and Fisk, 1992; Canfield, 2010]. Single crystals of $La(V_xCr_{1-x})Sb_3$ grew as rectangular plates, with shiny surfaces that had a few drops of residual Sb-rich flux on them. An example of such a crystal is shown in the inset of fig 9.1. The sizes of crystals increase as the V-concentration increases, varying from $\sim 3.5 \times 1.5 \times 0.7$ mm^3 for $LaCrSb_3$ to being crucible limited, $\sim 8 \times 6 \times 2$ mm^3 for $LaVSb_3$.

Powder X-ray diffraction data were collected at room temperature on a Rigaku Mini-Flex II diffractometer with Cu Kα radiation. Samples with rod-like shape were selected for measurement. Data collection was performed with the counting time of 2 s for every 0.02 degree. The refinement was conducted using the program Rietica [Howard and Hunter, 1998]. Error bars associated with the values of the lattice parameters were determined by statistical errors, and a Si powder standard was used as an internal reference. To identify the crystallographic orientation, real-time back-scattering Laue diffraction measurements were performed with Mo source ($\lambda \sim 0.7093\mathring{A}$). The structural solutions were refined by the Cologne Laue Indexation Program [Schumann, 2011].

Elemental analysis of the samples was performed using wavelength-dispersive X-ray spectroscopy (WDS) in a JEOL JXA-8200 electron probe microanalyzer. Only clear and shiny surface regions were selected for determination of the sample stoichiometry, i.e.

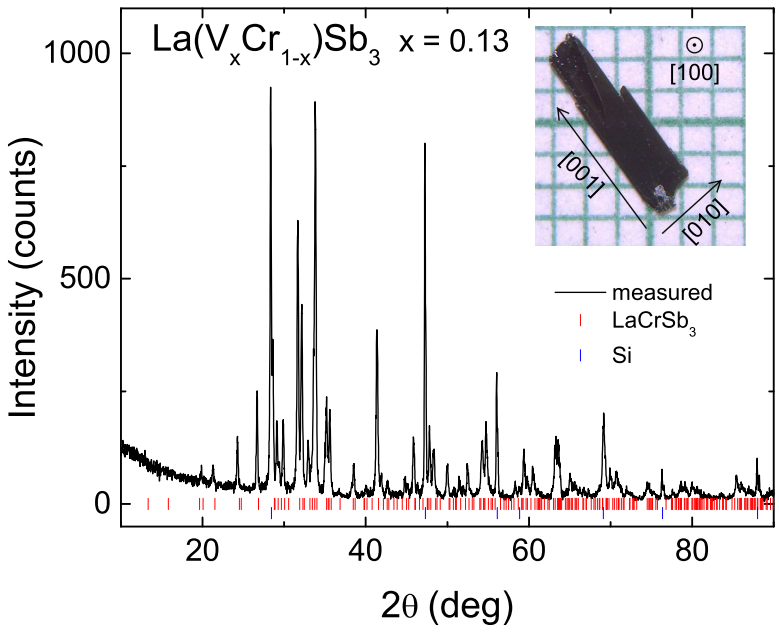

Figure 9.1 Powder X-ray diffraction pattern of $La(V_xCr_{1-x})Sb_3$ ($x = 0.13$). Inset: photo of a single crystalline sample ($x = 0.06$) on a millimeter grid.

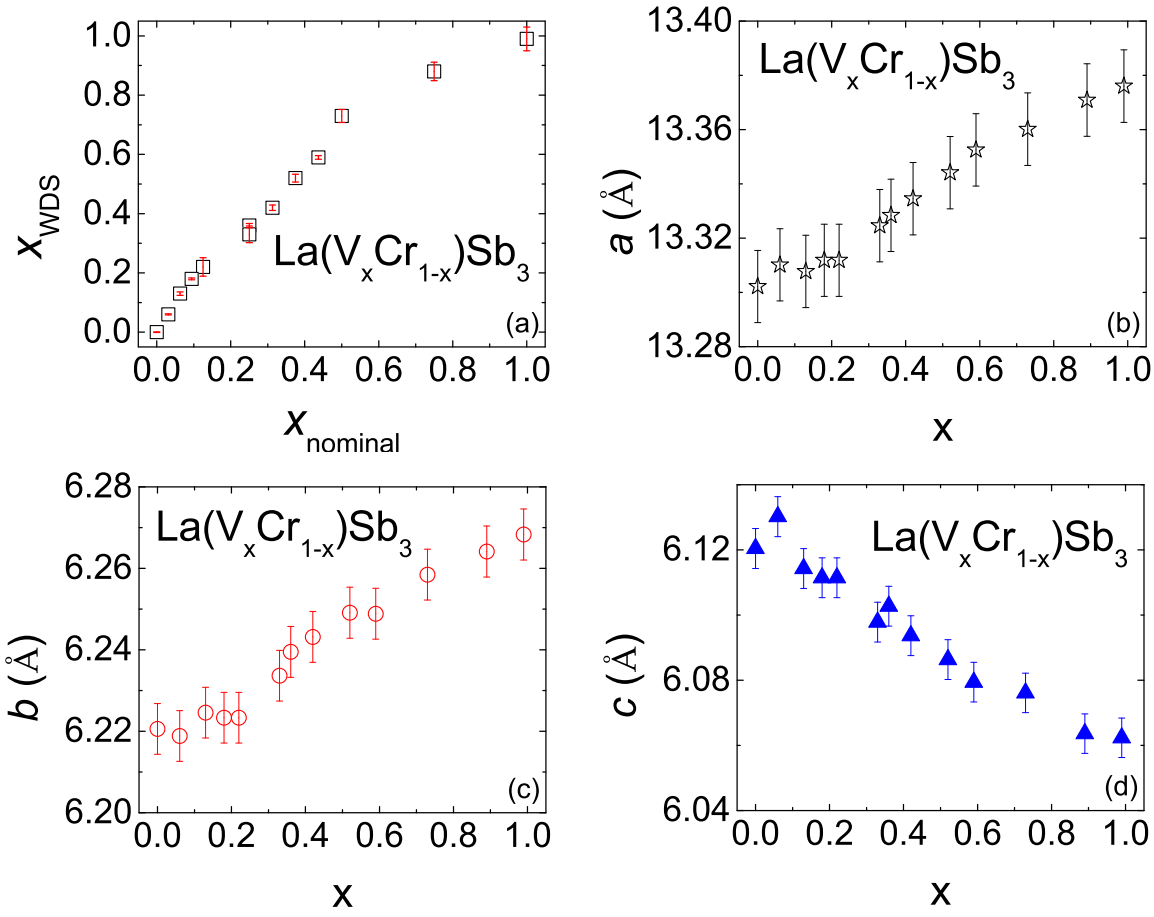

Figure 9.2 (a) x_{WDS} vs. x_{nominal}. The lattice parameters of single crystalline $\mathrm{La(V}_x\mathrm{Cr}_{1-x})\mathrm{Sb}_3$ compounds as a function of the V-concentration are shown in (b) a vs. x, (c) b vs. x, and (d) c vs. x. Note: the measured, x_{WDS} were used to indicate the composition of the compounds in this series.

regions with residual Sb flux droplets were avoided. For each composition, the WDS data were collected from multiple points on the same sample.

Measurements of field and temperature dependent magnetization were performed in a Quantum Design, Magnetic Property Measurement System (MPMS) superconducting quantum interference device (SQUID) magnetometer. The ac resistivity was measured by a standard four-probe method in a Quantum Design, Physical Property Measurement System (PPMS). Samples were polished into long rectangular bars. Platinum wires were attached to the sample using Epo-tek H20E silver epoxy, with the current flowing along the c-axis. The absolute values of resistivity are accurate to $\pm 15\%$ due to the accuracy of measurements of electrical contacts' positions. The residual resistivity ratio is defined as RRR = ρ (300 K)/ρ (2.0 K).

Temperature dependent specific heat data were measured in the PPMS using the relaxation technique in zero field for representative samples. The specific heat of $LaVSb_3$ was used to estimate the non-magnetic contribution to the specific heat of $LaCrSb_3$. The magnetic contribution to specific heat from the Cr ions was calculated by the relation of $C_{\mathrm{M}} = C_{\mathrm{p}}(\mathrm{LaCrSb_3})$-$C_{\mathrm{p}}(\mathrm{LaVSb_3})$.

The temperature dependent field-cooled magnetization of a single crystal under pressure was measured in the MPMS magnetometer in a magnetic field of 100 Oe applied along the c-axis. Pressures of up to 5.3 GPa were achieved with a moissanite anvil cell [Alireza et al., 2007]. The body of the cell is made of Cu-Ti alloy and the gasket is made of Cu-Be. Daphne 7474 was used as a pressure transmitting medium [Murata et al., 2008], and the pressure was determined at 77 K by the ruby fluorescence technique.

Table 9.1 The WDS data for $La(V_xCr_{1-x})Sb_3$. N is the number of points measured on one sample, x_{nominal} is the nominal concentration, x_{WDS} is the average x value measured, and 2σ is two times the standard deviation of the N values measured.

$La(V_xCr_{1-x})Sb_3$													
N	12	12	12	12	12	12	12	12	12	12	12	12	12
x_{nominal}	0	0.03	0.06	0.09	0.13	0.25	0.25	0.31	0.38	0.44	0.50	0.75	1.0
x_{WDS}	0	0.06	0.13	0.18	0.22	0.33	0.36	0.42	0.52	0.59	0.73	0.88	1.0
2σ	0.01	0.01	0.01	0.01	0.06	0.06	0.01	0.02	0.03	0.01	0.04	0.06	0.01

9.4 Results and Analysis

9.4.1 Crystal Stoichiometry and Structure

The stoichiometry of the $La(V_xCr_{1-x})Sb_3$ samples was inferred from WDS measurements. Table 9.1 summarizes the atomic percent of each element determined from the weight percent obtained from the analyses. The error bar is taken as twice the standard deviation σ. As shown in fig. 9.2 (a), the actual V-concentration x_{WDS} follows the initial stoichiometry x_{nominal} systematically, ranging from 0 to 1, and the small 2σ-value suggests that the samples are homogeneous, at least on the length scale probed by the WDS measurements $\sim 1\ \mu$m. In the following, the measured, x_{WDS}, rather than x_{nominal} values will be used to indicate the composition of the compounds in this series.

The crystal structure and orientation were confirmed by back-scattering Laue diffraction. Consistent with the reported data [Brylak and Jeitschko, 1995; Jackson et al., 2001; Sefat et al., 2008], this series of compounds form in an orthorhombic structure, *Pbcm* (No. 57). As shown in the inset of fig. 9.1, the a-axis was verified to be perpendicular to the rectangular plate, and the c-axis is parallel to the longest side, consistent with the reported data [Sefat et al., 2008]. Powder X-ray diffraction patterns were collected on ground single crystals from each compound. Fig. 9.1 gives powder X-ray diffraction pattern for $x = 0.13$ as an example. The main phase can be refined with $LaCrSb_3$'s reflection pattern (*Pbcm* structure), consistent with the Laue diffraction. No clear trace of Sb residue or other secondary solidification can be detected, and similar results (*Pbcm* structure) were obtained for the rest of the series. The lattice parameters obtained by the analysis of the powder X-ray diffraction data are presented in fig. 9.2 (b) – (d). The lattice parameters a, b and c all manifest systematic changes as the x increases, which is consistent with the reported data [Brylak and Jeitschko, 1995; Jackson et al., 2001]. Crystallographically, the transition metal elements in $LaCrSb_3$ and $LaVSb_3$ occupy the same unique site $4c$ [Brylak and Jeitschko, 1995].

9.4.2 Physical properties of $La(V_xCr_{1-x})Sb_3$ ($x = 0$ and 1.0)

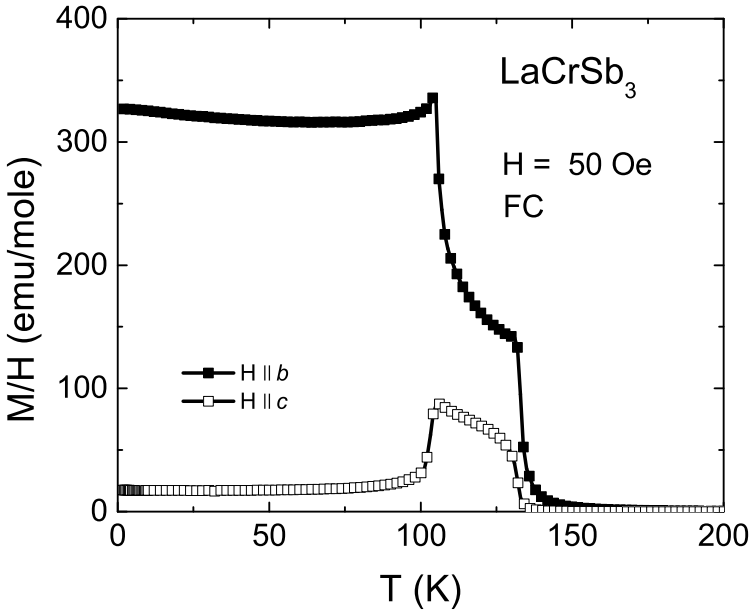

Figure 9.3 Anisotropic field-cooled (FC) magnetization as a function of temperature for $LaCrSb_3$ at 50 Oe.

The anisotropic, temperature-dependent, field-cooled (FC) magnetization of $LaCrSb_3$ is shown in fig. 9.3. The measurements were performed with the applied field parallel to b- and c-axes at 50 Oe. As is shown, the magnetization rises sharply near 130 K for both $\mathbf{H} \parallel b$ and $\mathbf{H} \parallel c$, indicating a transition to a low-temperature ferromagnetic state. A second anomaly can be observed in both directions at around 100 K, which can be associated with spin reorientation, as suggested by previous studies [Jackson et al., 2001; Granado et al., 2002]. Below roughly look, the magnetization data in both directions remain almost constant as temperature is lowered.

The anisotropic magnetic susceptibility of $LaVSb_3$ was measured at 1 kOe, as shown in fig. 9.4. It is clear that the magnetic susceptibility has weakly positive values in all three directions, and $M(T)/H$ is essentially temperature independent. It is evident

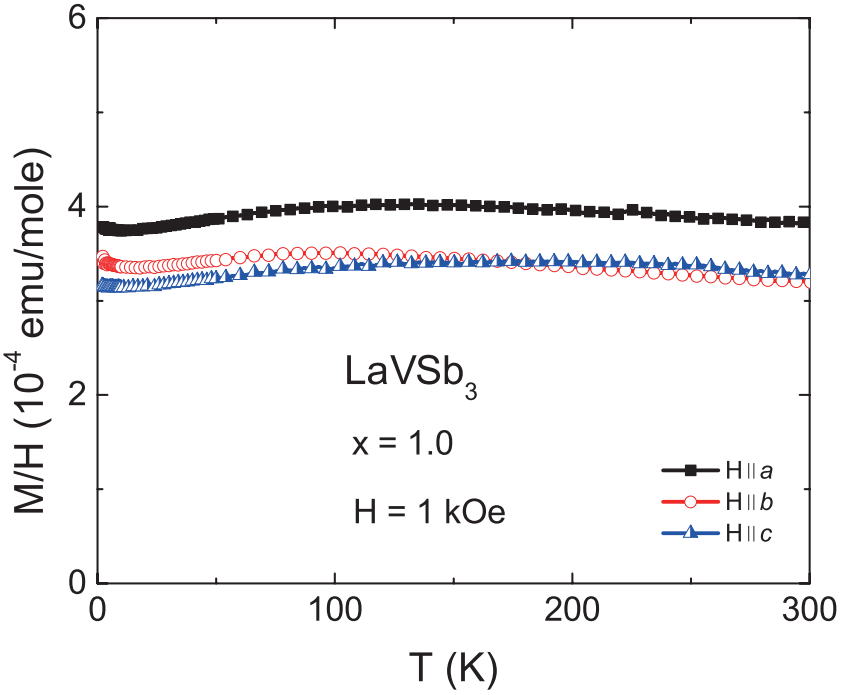

Figure 9.4 Anisotropic magnetic susceptibility as a function of temperature of $LaVSb_3$ measured at 1 kOe.

that $LaVSb_3$ follows Pauli magnetic behavior, and is consistent with the reported data [Jackson et al., 2001; Sefat et al., 2008].

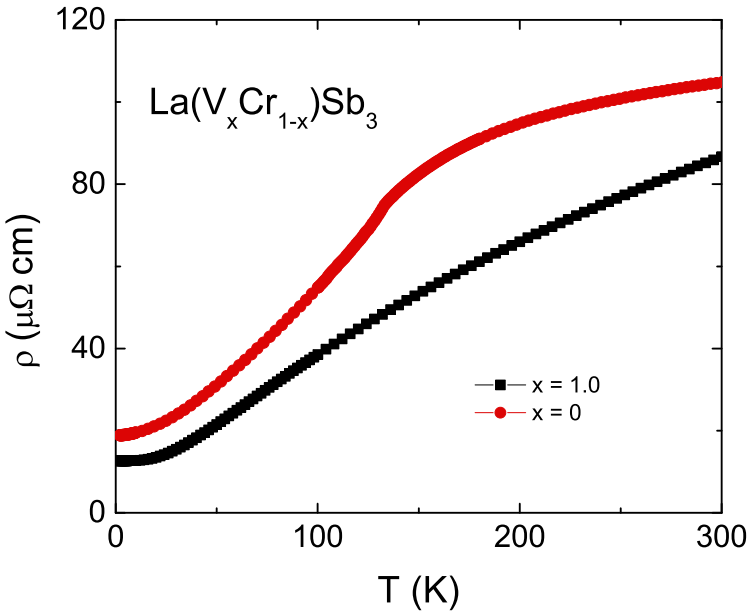

Figure 9.5 The electrical resistivity ρ as a function of temperature for $La(V_xCr_{1-x})Sb_3$ ($x = 0$ and 1.0).

Figure 9.5 presents the electrical resistivity data of $La(V_xCr_{1-x})Sb_3$ ($x = 0$ and 1.0) as a function of temperature. To within 15%, the room temperature resistivity values ρ (300 K) are about 105 $\mu\Omega$ cm for $x = 0$ and 87 $\mu\Omega$ cm for $x = 1.0$. At high temperatures, the electrical resistivity decreases linearly upon cooling, characteristic of normal metallic behavior. For $x = 0$, a dramatic anomaly occurs at about 132 K, which is most likely due to the loss of spin disorder scattering and can be associated with the ferromagnetic transition. For $x = 1.0$, no anomaly was observed for temperatures above 1.8 K.

The temperature-dependent specific heat data for the $La(V_xCr_{1-x})Sb_3$ ($x = 0$ and 1) are presented in fig. 9.6. The specific heat can be estimated by the relation $C_p(T) = C_e + C_{ph} + C_M$, where C_e is the conduction electron contribution, C_{ph} is the phonon con-

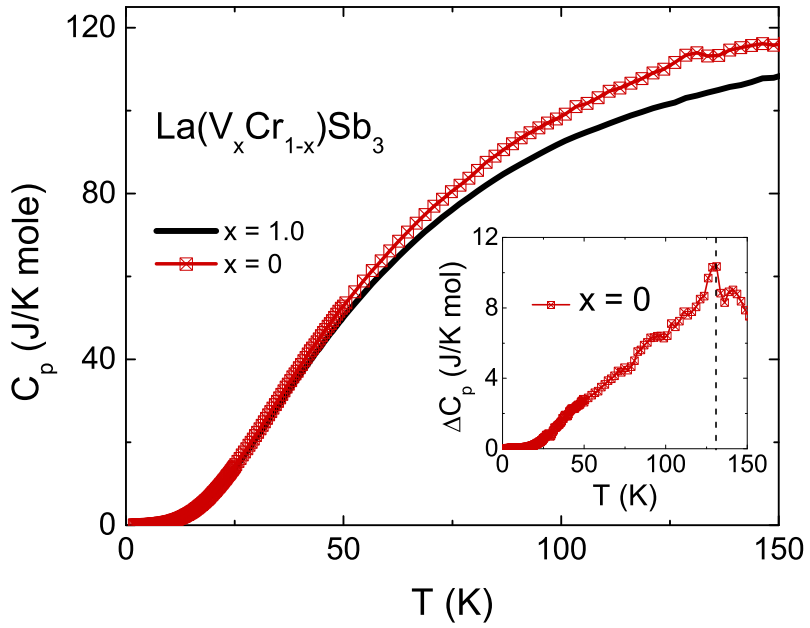

Figure 9.6 Temperature-dependent of specific heat of $La(V_xCr_{1-x})Sb_3$ ($x = 0$ and 1). Inset: magnetic contributions to the specific heat $\triangle C_{\rm p}$ as a function of temperature for $x = 0$. The dashed line indicates the ordering temperature.

tribution, and C_M is the magnetic contribution. $C_e + C_{ph}$ can be roughly approximated by the C_p data of $LaVSb_3$. Thus, the magnetic contribution C_M was, to the specific neat of $LaCrSb_3$, evaluated as $\triangle C_p = C_p(LaCrSb_3)$-$C_p(LaVSb_3)$. A cusp can be seen in $\triangle C_p$, as shown in the inset of fig.9.6. This is the first time that the ferromagnetic transition of $LaCrSb_3$ has been observed in the specific heat data. This anomaly can be associated with the ferromagnetic transition. The ordering temperature T_C obtained from $\triangle C_p$ data for $x = 0$ is about 132 K, as indicated by the dash line in the inset of fig. 9.6.

9.4.3 Effects of pressure on the magnetic properties of of $LaCrSb_3$

In an attempt to suppress the ferromagnetism in $LaCrSb_3$, hydrostatic pressures up to 5.3 GPa were applied. Figure 9.7 (a) shows the temperature dependence of the filed-cooled magnetization of $LaCrSb_3$ under different pressures. At lower pressures, the ferromagnetic transition is revealed by a rather sharp increase of the magnetization. Defined here as a minimum point in $dM(T)/dT$ (as seen in fig. 9.7 (b)), the Curie temperature, T_C, is plotted as a function of applied pressure in fig. 9.7 (c). T_C changes only very slightly with applied pressure with $dT_C/dp \approx 0.1 \pm 0.3$ K/GPa, suggesting that the ferromagnetism is robust with respect to pressure, at least up to 5.3 GPa. At ambient pressure, the spin reorientation is seen as a sharp decrease of the field-cooled magnetization measured along the c-axis (fig. 9.7 (a) and fig. 9.3). A decrease of the magnetization is still observed for pressure of 0.6 and 1 GPa, although the plateau can not be observed. The decrease of magnetization cannot be detected above 3 GPa.

9.4.4 Effects of chemical substitution on the physical properties

Given that accessible pressures appear to have little or no effect on the ferromagnetic transition temperature of $LaCrSb_3$, we decided to study the effects of chemical substitution on the physical properties of the $La(V_xCr_{1-x})Sb_3$ series. The electrical resistivity

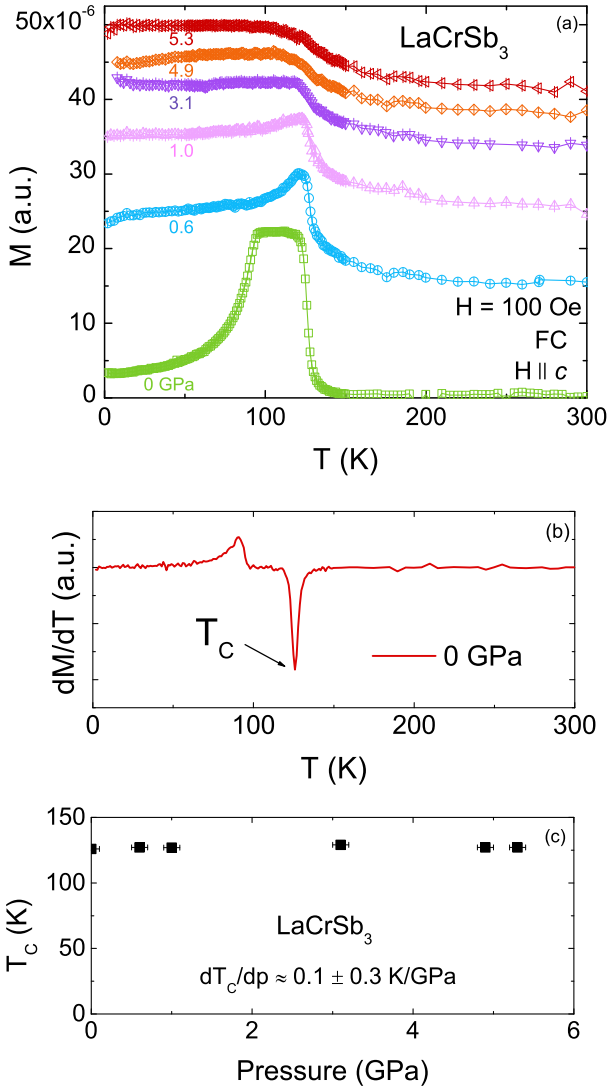

Figure 9.7 (a) Temperature dependence of the FC magnetization for $LaCrSb_3$ under different pressures with $H = 100$ Oe, $\mathbf{H} \parallel c$. Note: The values of the magnetization are shifted for clarity. (b) dM/dT vs. T: the arrow indicates the Curie temperature. (c) Pressure dependence of T_C for $LaCrSb_3$, where T_C is determined by the minimum point in $dM(T)/dT$.

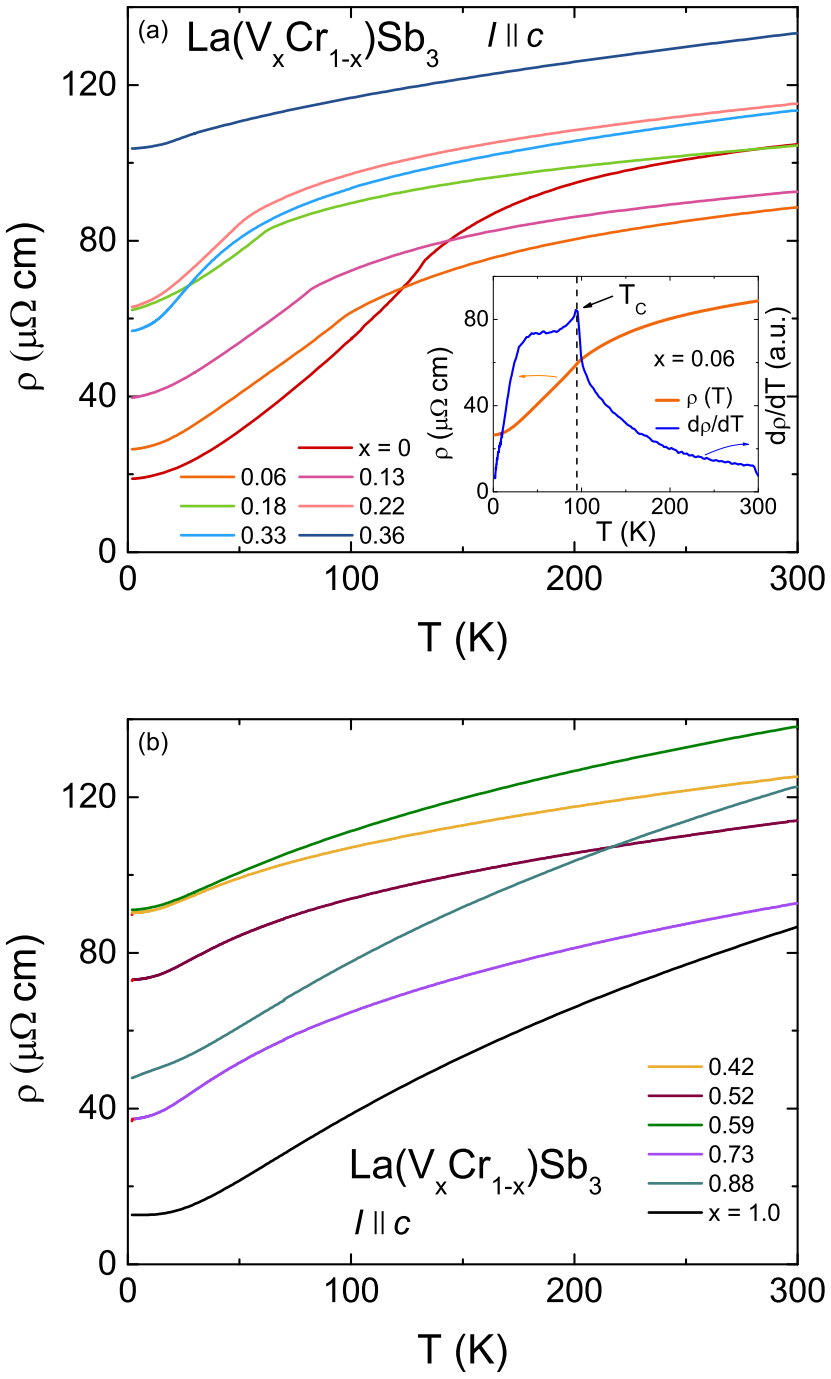

Figure 9.8 The electrical resistivity ρ as a function of temperature for $La(V_xCr_{1-x})Sb_3$. (a) $x = 0 - 0.36$. Inset: $\rho(T)$ and $d\rho/dT$ for $x = 0.06$. The arrow indicates the criterion used to determine the Curie temperature T_C. (b) $x = 0.42 - 1.0$.

data, as a function of temperature for $La(V_xCr_{1-x})Sb_3$ are presented in fig. 9.8 (a) and (b). The room temperature resistivity values ρ (300 K) of all compounds are in the range of 80 – 140 $\mu\Omega$ cm. For low x-value samples, the distinct drop in the resistivity below 150 K is probably associated with the ferromagnetic transition. This anomaly moves to lower temperatures and is broadened as the V concentration increases up to 0.36 (seen in fig. 9.8 (a)). For $x \geq 0.42$, this feature can no longer be clearly observed, as shown in fig. 9.8 (b). The inset of fig. 9.8 (a) provides the criterion used to infer Curie temperature T_C — the peak position in the $d\rho/dT$ indicated by the arrow, and the inferred T_C values are summarized in Table 9.2 (below). With current along c-axis, samples for $x = 1.0$ and 0 have RRR of $\simeq$ 6.8 and 5.6, respectively. The lower RRR values for the intermediate x-value compounds are due to increased site disorder caused by the substitution.

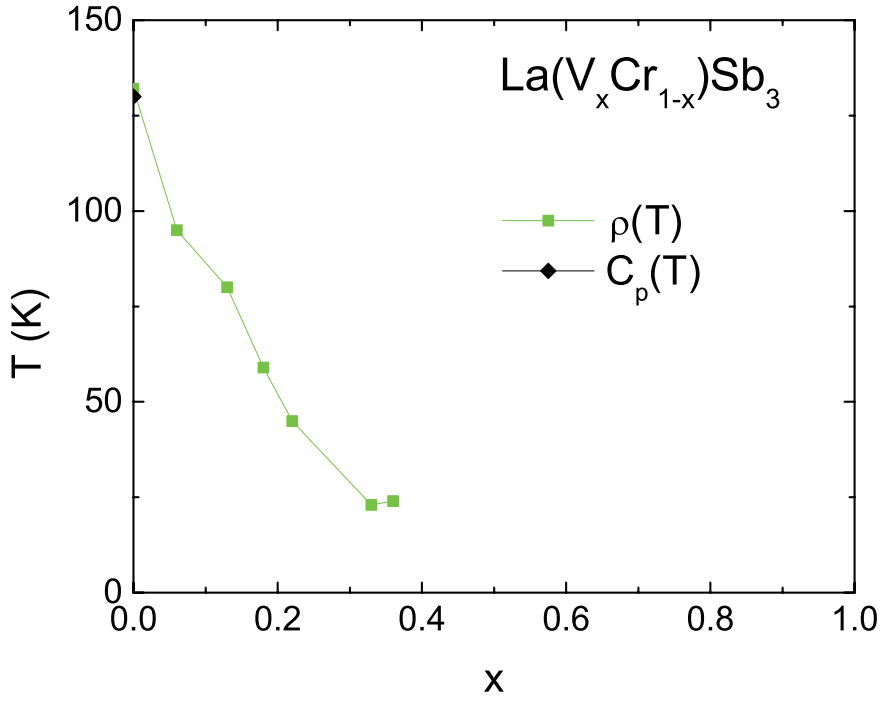

Figure 9.9 x-dependent transition temperatures for $La(V_xCr_{1-x})Sb_3$ determined by $\rho(T)$ and $C_p(T)$ measurements.

Based on the resistivity and specific heat data, a $T - x$ phase diagram was assem-

bled. As shown in fig. 9.9, the Curie temperature decreases systematically as the V concentration increases. For lower V-doped compounds, $x < 0.36$, the system possess a paramagnetic state at high temperatures, and transits into a magnetically ordered state at low temperatures. For higher V-doped compounds, $x \geqslant 0.42$, as no feature can be observed in the resistivity data, the magnetic state in this region is not clear.

To better understand the magnetic state of the V-doped compounds, systematic magnetization measurements were also performed. Figures 9.10 – 9.14 present magnetization isotherms, hysteresis loops, zero-field-cooled (ZFC) and field-cooled (FC) $M(T)$ for selected compounds. Figure 9.10 (a) shows the anisotropic, ZFC, magnetization isotherms for $LaCrSb_3$ measured at $T = 2$ K. The magnetization shows clear ferromagnetic behavior – spontaneous spin alignment in both b and c directions as the applied field increases from zero. At $T = 2$ K, in the ordered state, the magnetization is anisotropic, with $M_b > M_c > M_a$. The value of the magnetization measured at 50 kOe in the b direction is taken as the saturated moment (μ_S). For $x = 0$, μ_S is about 1.61 μ_B per Cr, consistent with the reported value [Jackson et al., 2001; Granado et al., 2002]. Figure 9.10 (b) shows the hysteresis loop of $LaCrSb_3$ measured at 2 K for $\mathbf{H} \parallel b$. The spontaneous spin alignment can be clearly seen, whereas hysteresis can hardly be observed. This probably suggests that $LaCrSb_3$ is a soft ferromagnet. Compared to the V-doped compounds (see below), $LaCrSb_3$ exhibits negligible pinning effect that is associated with the disorder induced by substitution.

Similar magnetization isotherms can be observed for $x = 0.22$, see in fig. 9.11 (a). The b-axis can still be identified as the easy axis and M_a has the lowest value of all three directions, however, the differences in magnetization between different directions becomes slightly less obvious. The saturated moment is 1.37 μ_B/Cr for $\mathbf{H} \parallel b$. The hysteresis loop for $x = 0.22$ is shown in fig. 9.11 (b). Clear hysteresis can be observed, and the coercivity is about 1.63 kOe. At low fields, the magnetization in the virgin curve, instead of showing spontaneous spin alignment, rises slowly with the applied field. This

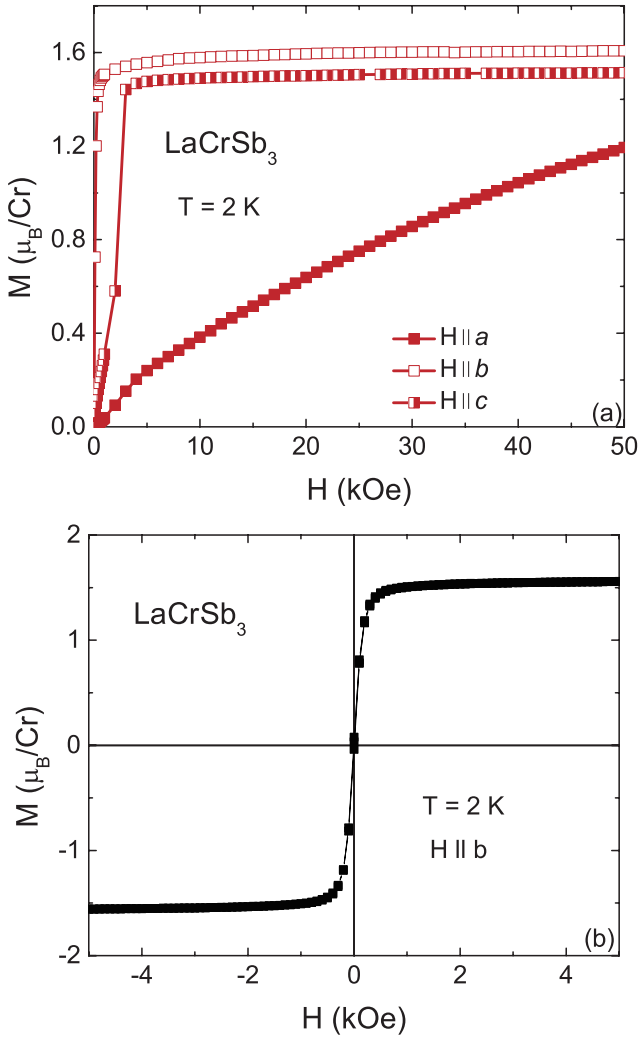

Figure 9.10 (a) Zero-field-cooled (ZFC) anisotropic field-dependent magnetization isotherms taken at 2 K. (b) Hysteresis loop measured at 2 K with $\mathbf{H} \parallel b$ for the $LaCrSb_3$. The applied magnetic field changes from zero to 50 kOe, to -50 kOe, and then up to 50 kOe again.

is probably caused by domain pinning effects. In addition, a discrepancy can be seen in the low-field magnetization for $\mathbf{H} \parallel b$ between fig. 9.11 (a) and fig. 9.11 (b). It is possibly due to the remnant field in a superconducting magnet giving rise to different virgin curve starting points. Based on the behavior of the field-dependent magnetization, it is evident that $La(V_xCr_{1-x})Sb_3$ ($x = 0.22$) possesses a ferromagnetic state at low temperatures. Figure 9.11 (c) shows the ZFC and FC magnetization as a function of temperature. The measurements were performed at 50 and 100 Oe with $\mathbf{H} \parallel b$. As can be seen, the FC M/H increases dramatically upon cooling and continuously rising at low temperatures, indicating the existence of a ferromagnetic state. The complex feature in the ZFC $M(T)/H$ at low temperatures is probably due to domain pinning effects. Hence, with increasing V substitution up till $x = 0.22$, the $La(V_xCr_{1-x})Sb_3$ series maintains a ferromagnetic state at low temperatures.

Starting from $x = 0.33$, two major differences can be found in the magnetization isotherms, as shown in fig. 9.12 (a) and fig. 9.13 (a). First of all, a spontaneous spin alignment can not be observed for any direction of applied field measured. The magnetization for $\mathbf{H} \parallel b$ rises much slower as field increases (compared with the case of $x = 0$), whereas M_a and M_c seem to show rather broad shoulders. With the increased V concentration, even M_b shows a shoulder-like feature, and no saturation can be observed. These data might suggest that the magnetic state for $x \geq 0.33$ in the $La(V_xCr_{1-x})Sb_3$ series is no longer ferromagnetic. The second difference found is the change of anisotropy. Although the b-axis is still the easy axis, M_a is larger than M_c for $x \geq 0.33$. Hysteresis can still be observed for $x = 0.33$ and 0.52, as shown in fig. 9.12 (b) and fig. 9.13 (b). However the coercivity decreases as the V concentration increases. It drops to 1.47 kOe for $x = 0.33$ and 0.58 kOe for $x = 0.52$.

Figures 9.12 (c) and 9.13 (c) also present the ZFC and FC magnetization as a function of temperature measured at 50 and 100 Oe with $\mathbf{H} \parallel b$. Besides the initial increase in both ZFC and FC $M(T)/H$ upon cooling, a local maximum can be observed in both of the

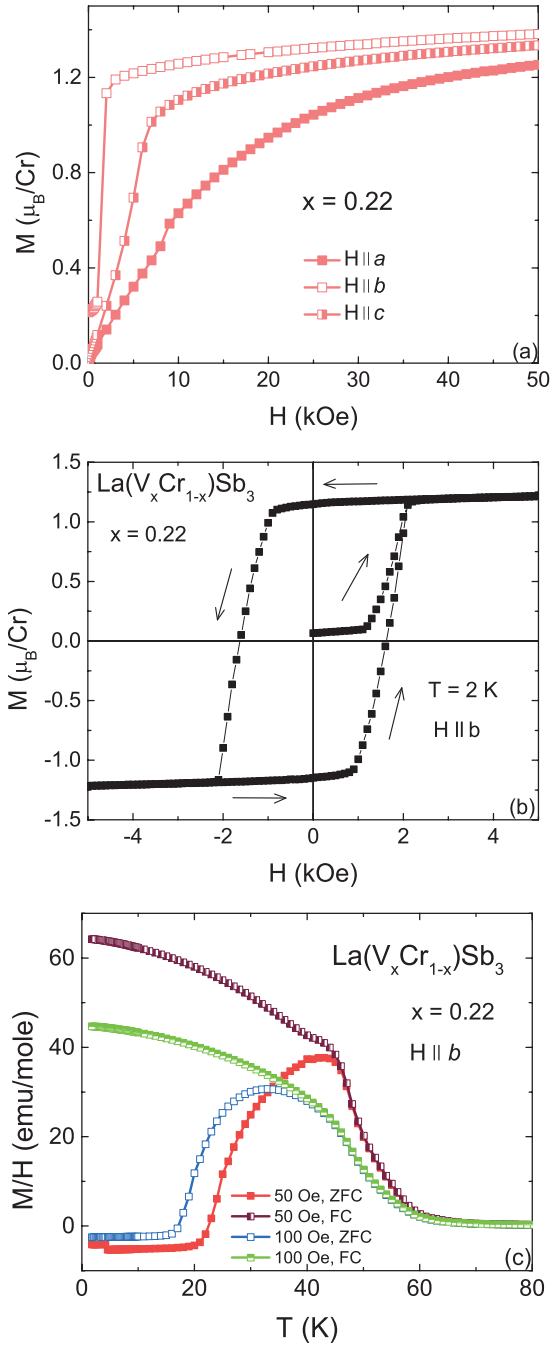

Figure 9.11 (a) Zero-field-cooled (ZFC) anisotropic field-dependent magnetization isotherms taken at 2 K. (b) Hysteresis loop measured at 2 K with $\mathbf{H} \parallel b$. The applied magnetic field changes from zero to 50 kOe, to -50 kOe, and then up to 50 kOe again. The arrows indicate the directions of the field sweeping. (c) Zero-field-cooled (ZFC) and field-cooled (FC) temperature dependence of the magnetic susceptibility taken at 50 and 100 Oe with $\mathbf{H} \parallel b$ for the $La(V_xCr_{1-x})Sb_3$ ($x = 0.22$).

ZFC and FC curves. This feature is more obvious for the higher V-doped compound, $x = 0.52$ (fig. 9.13 (c)). As is shown, the ZFC and FC $M(T)/H$ are split at low temperatures, and the ZFC curves exhibit a dramatic decrease as T decreases. These might imply some degree of frustration which leads to some form of cluster or spin-glass state [Mydosh, 1993]. It is possible that with the continuous suppression of ferromagnetism, the magnetic state in this series evolves into a new magnetic state, which is often observed in the local magnetic moment systems [Mydosh, 1993; Buschow, 1990].

As vanadium content increases, the moment along a-axis continuously gets closer to M_b. As shown in fig. 9.14 (a), M_a and M_b becomes almost identical for $x = 0.73$. At 2 K, the magnetization gradually increases with the increasing field, exhibiting no feature of spontaneous spin alignment. No saturation or hysteresis can be observed for $x = 0.73$ (fig. 9.14 (b)). It is evident that $La(V_xCr_{1-x})Sb_3$ series does not possess a ferromagnetic order above 2.0 K for $x > 0.73$.

Given that the magnetization along b-axis shows typical ferromagnetic behavior for the lower V-doped compounds, and given that the b-axis is the easy axis in almost the whole x range ($0 \leq x \leq 0.73$), in the following, our study of the evolution of the magnetic state in the $La(V_xCr_{1-x})Sb_3$ system is presented with the magnetization data along b-axis. The temperature-dependent FC magnetization curves of the $La(V_xCr_{1-x})Sb_3$ ($x = 0.06 - 0.73$) series, with $\mathbf{H} \parallel b$ at 50 Oe are shown in fig. 9.15 (a) and (b). Magnetization for $x = 0.06 - 0.36$ shows the expected rapid increase of the magnetization as well as the saturation at low temperatures (fig. 9.15 (a)). The Curie temperature decreases as V concentration increases, and the transition shifts to lower temperature, as can be clearly seen in fig. 9.15 (b). With increasing amounts of V substituted for Cr, from $x = 0.42$, the temperature-dependent magnetic susceptibility starts deviating from the ferromagnetic behavior (fig.9.15). As the temperature decreases, the magnetization rises in a much slower manner compared with the lower V-doped compounds, and a local maximum at low temperatures can be observed. It can be inferred that instead of the ferromagnetic

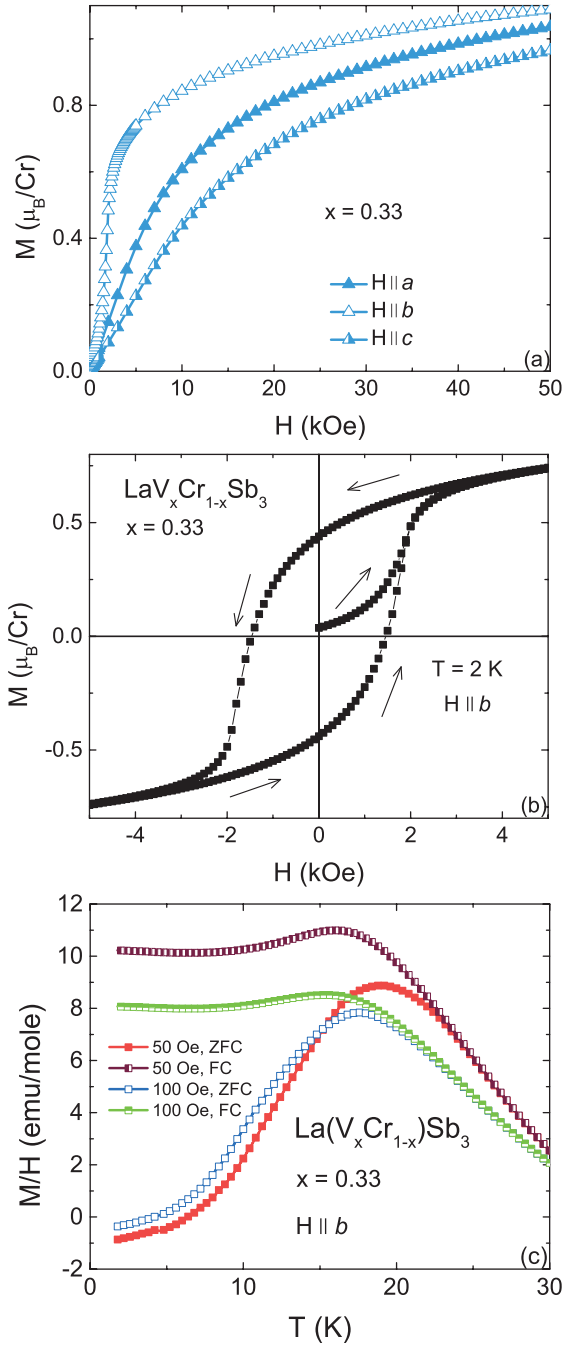

Figure 9.12 ((a) Zero-field-cooled (ZFC) anisotropic field-dependent magnetization isotherms taken at 2 K. (b) Hysteresis loop measured at 2 K with $\mathbf{H} \parallel b$. The applied magnetic field changes from zero to 50 kOe, to -50 kOe, and then up to 50 kOe again. The arrows indicate the directions of the field sweeping. (c) Zero-field-cooled (ZFC) and field-cooled (FC) temperature dependence of the magnetic susceptibility taken at 50 and 100 Oe with $\mathbf{H} \parallel b$ for the $La(V_xCr_{1-x})Sb_3$ ($x = 0.33$).

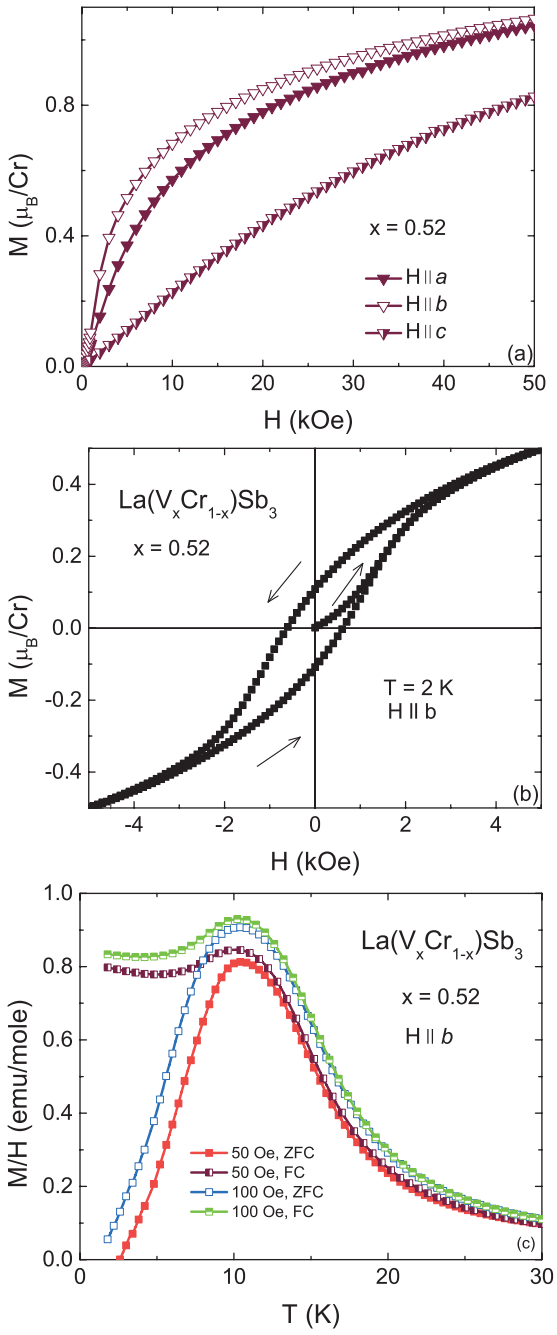

Figure 9.13 (a) Zero-field-cooled (ZFC) anisotropic field-dependent magnetization isotherms taken at 2 K. (b) Hysteresis loop measured at 2 K with $\mathbf{H} \parallel b$. The applied magnetic field changes from zero to 5 kOe, to -5kOe, and then up to 5 kOe again. The arrows indicate the directions of the field sweeping. (c) Zero-field-cooled (ZFC) and field-cooled (FC) temperature dependence of the magnetic susceptibility taken at 50 and 100 Oe with $\mathbf{H} \parallel b$ for the $La(V_xCr_{1-x})Sb_3$ ($x = 0.52$).

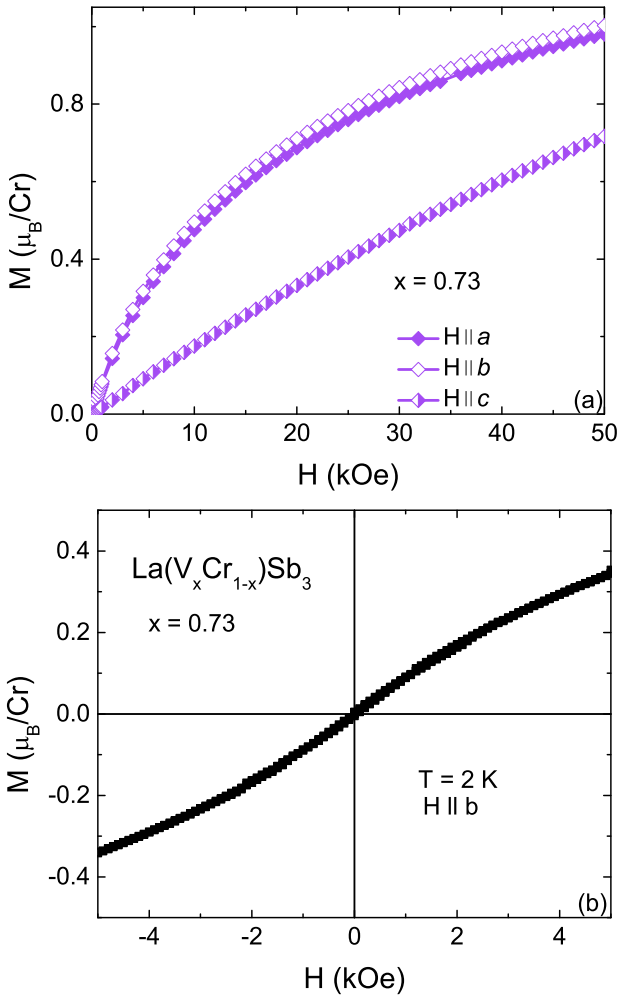

Figure 9.14 (a) Zero-field-cooled (ZFC) anisotropic field-dependent magnetization isotherms taken at 2 K. (b) Hysteresis loop measured at 2 K with $\mathbf{H} \parallel b$ for the $La(V_xCr_{1-x})Sb_3$ ($x = 0.73$). The applied magnetic field changes from zero to 50 kOe, to -50 kOe, and then up to 50 kOe again.

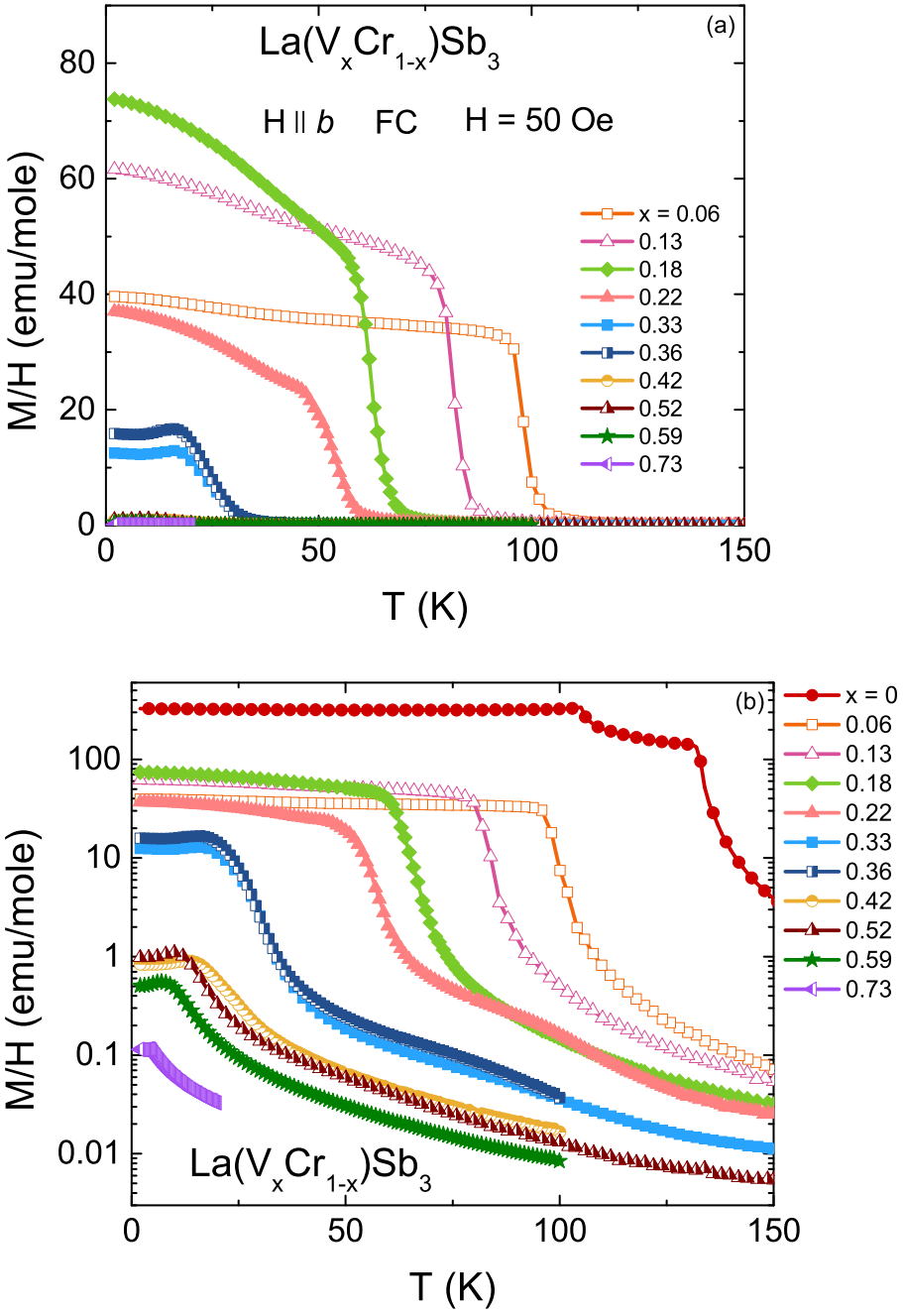

Figure 9.15 (a) FC magnetization as a function of temperature for $La(V_xCr_{1-x})Sb_3$ (x = 0.06 – 0.73) at 50 Oe with $\mathbf{H} \parallel b$. (b) FC magnetization as a function of temperature for x = 0 – 0.73 presented in a semi-log plot.

state, a new magnetic state may emerge for higher V-doped compounds.

The Curie temperature can be estimated by $d(M/H)/dT$ for low values of applied field ($H = 50$ Oe in this case), as indicated by the arrow in fig. 9.16 (a), where the transition temperature T_1 is determined by the sharp anomaly in $d(M/H)/dT$. The obtained T_1-values are listed in Table 9.2. The transition temperature systematically decrease to lower temperatures as the V-concentration increases, from 133 K for $x = 0$ to 24 K for $x = 0.36$ with $\mathbf{H} \parallel b$. On the other hand, for higher V-doped compounds ($x > 0.33$), two features can be observed in $d(M/H)/dT$. Besides the minimum point, the maximum point in $d(M/H)/dT$ is chosen as the criterion to characterize the transition temperature of a potential new magnetic state (shown in fig.9.15 (b)). Again the obtained transition temperatures T_1 and T_2 are listed in Table 9.2.

The polycrystalline average of M/H measured at 1 kOe is shown in fig. 9.17. It is obtained by $\chi_{ave} = \frac{1}{3}(\chi_a + \chi_b + \chi_c)$. A modified Curie-Weiss law with inclusion of a temperature-independent term χ_0: $\chi_{\rm ave} = \chi_0 + C/(T - \theta_{\rm poly})$, was used to fit the magnetic susceptibility, where $\theta_{\rm poly}$ is the Curie-Weiss temperature estimated by the polycrystalline averaged data and C is the Curie constant. Considering the accuracy of measuring sample's mass, the values of the effective moments in this series are accurate to $\pm 10\%$. The fitting parameters χ_0 and the calculated $\mu_{\rm eff}$ and $\theta_{\rm poly}$ are summarized in Table 9.2. For $x = 0$, $\mu_{\rm eff}$ is found to be about 3.9 $\mu_{\rm B}$/Cr, close to the calculated value for Cr^{3+}: 3.8 $\mu_{\rm B}$, and is consistent with the reported value [Jackson et al., 2001]. As shown in Table 9.2, the effective moment gradually decreases as the V concentration increases. However, $\mu_{\rm eff}$ does not approach zero for some critical x value, or even as x gets close to 1, unlike the ferromagnetic system dominated by solely itinerant moments [Rhodes and Wohlfarth, 1963]. Instead, $\mu_{\rm eff}$ falls to 2.9 $\mu_{\rm B}$/Cr for $x = 0.88$, which is close to Cr^{4+}: 2.8 $\mu_{\rm B}$. It is possible that the Cr ion in the $La(V_xCr_{1-x})Sb_3$ compounds has a valence changed in compounds with higher V substitution. In addition, it is found that the Curie-Weiss temperature, $\theta_{\rm poly}$ in this series are all positive, indicating the

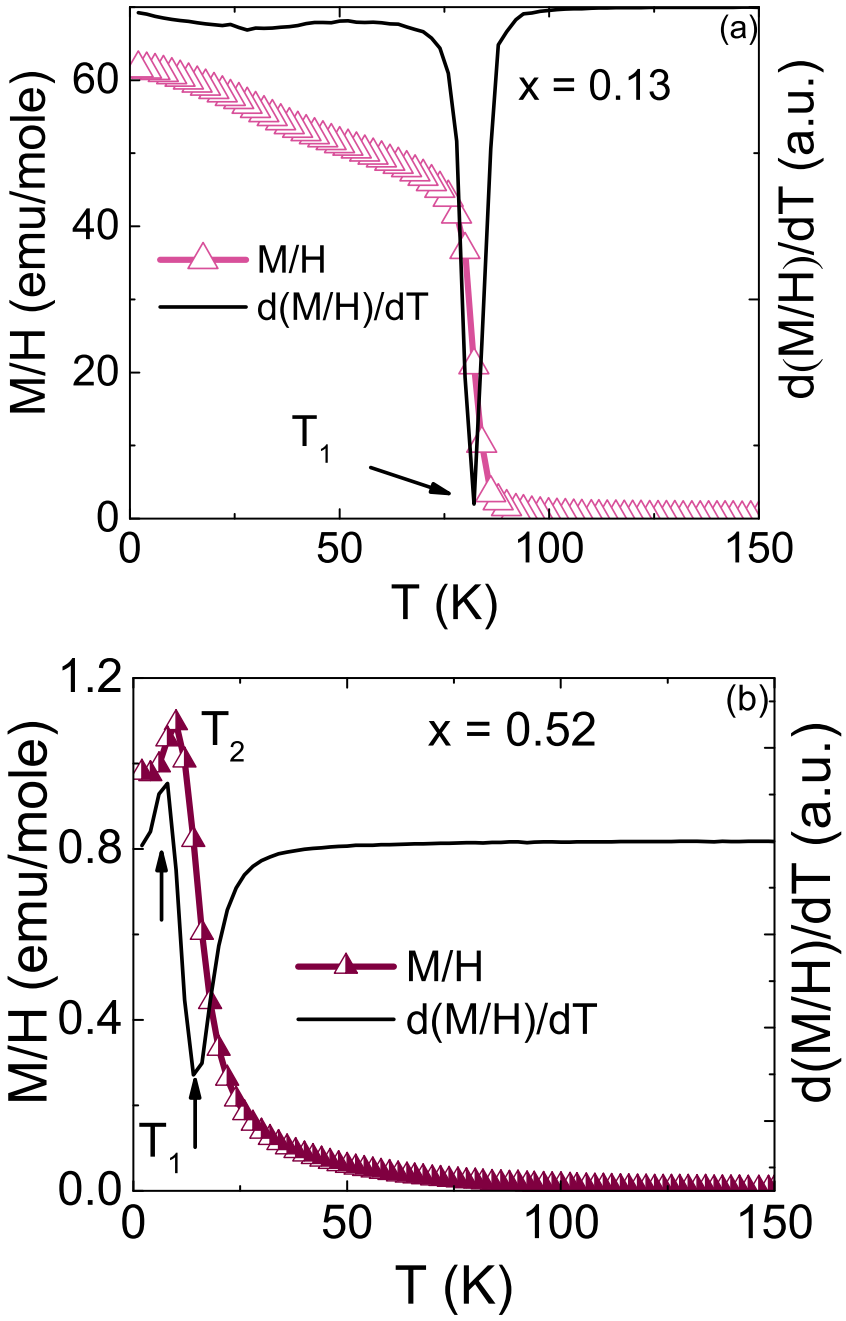

Figure 9.16 (a) The temperature dependence of the magnetization and $d(M/H)/dT$ for $x = 0.13$, and the arrow indicates the criterion used to determine the transition temperature T_1. (b) The temperature dependence of the magnetization and $d(M/H)/dT$ for $x = 0.52$, and the arrow indicates the criteria used to determine the transition temperature T_1 and T_2.

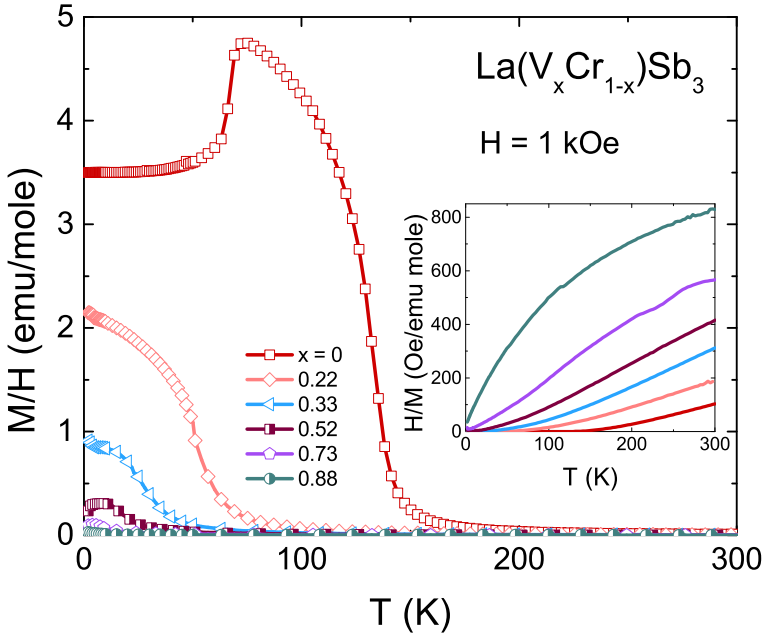

Figure 9.17 Polycrystalline averaged M/H vs. T for $La(V_xCr_{1-x})Sb_3$ (x = 0, 0.22, 0.33, 0.52, 0.73 and 0.88) measured at H = 1 kOe. Inset: inverse magnetic susceptibility as a function of temperature.

ferromagnetic interaction as the dominant interaction in these compounds. Also the fact that $\theta_{\rm poly}$ decreases as x increases implies the ferromagnetic interaction is weakened by the V substitution.

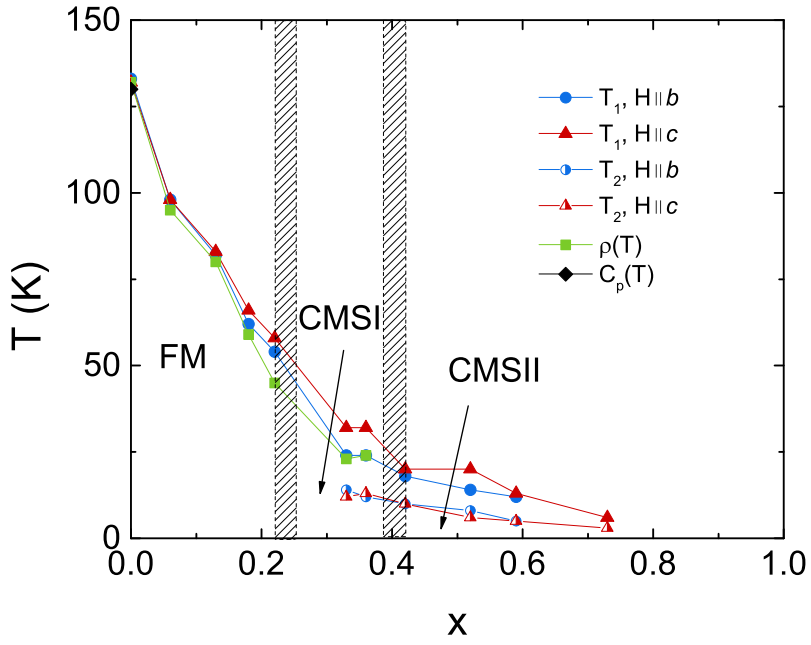

Figure 9.18 x-dependent transition temperatures for $La(V_xCr_{1-x})Sb_3$ determined by anisotropic $M(T)$, $\rho(T)$ and $C_{\rm p}(T)$ measurements. The dashed lines outline three potential regions of the low temperature magnetic behavior: ferromagnetic state (FM), complex magnetic state I (CMSI) and complex magnetic state II (CMSII).

We have been able to suppress the ferromagnetism in the $La(V_xCr_{1-x})Sb_3$ series via chemical substitution. The ordering temperatures inferred from low field magnetization, resistivity and specific heat measurements are summarized in Table 9.2. A phase diagram of x-dependent transition temperature for $La(V_xCr_{1-x})Sb_3$ is assembled in fig. 9.18. For $x \leqslant 0.36$, the transition temperatures that are determined by different measurements and different orientations are fairly consistent. For $x \geqslant 0.42$, only the points inferred from the magnetization data are shown in the phase diagram, since other measurements do not

manifest clear anomalies. As can be seen, for the $La(V_xCr_{1-x})Sb_3$ series, ferromagnetism can be clearly observed for x up to 0.22, and the ferromagnetic transition temperature is suppressed monotonically by the V substitution: $T_C = 133$ K for $x = 0$, and $T_C = 52$ K for $x = 0.22$ (based on the low field $M(T)$ data with $\mathbf{H} \parallel b$). If T_1 is used as a criterion for determining the transition to a low-temperature magnetic state for the whole series, it seems that the magnetic transition temperature gets gradually suppressed by V substitution and drops below our base-temperature of 2.0 K. If T_2 is used as the criterion for higher V-doped samples, then considering the features observed in $M(H)$, $M(T)/H$ and $\rho(T)$ for $x = 0.33$ and 0.36, it seems that $x = 0.33$ – 0.36 is a region for the system to transition from the ferromagnetic state to a new magnetic state. Similar phenomena have also been observed in the $LiHo_xY_{1-x}F_4$ family: for $0.25 \leq x \leq 0.5$, the system is claimed to be in a "ferroglass" regime, where spin glass and ferromagnetic phase coexist [Ancona-Torres et al., 2008; Gingras and Henelius, 2011]. In fig. 9.18 we identify three potential regions of the low temperature magnetic behavior: (1) ferromagnetic state (FM) for $0 \leq x \leq 0.22$, (2) complex magnetic state I (CMSI) for $0.22 \leq x \leq 0.42$, and (3) complex magnetic state II (CMSII) for $x \geq 0.42$. Further investigations are needed to determine the exact concentration at which the transition occurs. In the region of CMSII, given that i) $M(T)$ exhibits a local maximum at low temperature, and ii) field-cooled and zero-field-cooled $M(T)$ deviate from each other, it is possible that this new magnetic ground state is a complex glassy state. As the V concentration reaches even higher, $x \geq 0.88$, no magnetic ordering can be observed and the system shows paramagnetic behavior down to our base temperature of 2.0 K.

Based on our data, the $La(V_xCr_{1-x})Sb_3$ system has a phase diagram consistent with dominantly local moment like behavior of Cr. The progression from well defined magnetic ordering to complex magnetic state, to something that may be glassy state and gradually has a freezing temperature drop toward zero is similar to what has been found for local moment systems such as $(Tb_xY_{1-x})Ni_2Ge_2$ [Wiener et al., 2000]. At no point were

features consistent with a quantum critical point observed.

9.5 Discussion and Conclusions

Our efforts to suppress ferromagnetism in $LaCrSb_3$ started with applications of pressures up to 5.3 GPa. As seen in fig. 9.7, the ferromagnetic ordering temperature, T_C, is essentially insensitive to $p < 5.3$ GPa. On the contrary, the feature of spin reorientation evolves systematically and vanishes as the applied pressure increases.

Given that we could not suppress the ferromagnetism in the $LaCrSb_3$ compound by applying pressure, we evaluated the potential for quantum critical behavior by using chemical substitution as an alternative tuning parameter. The growth of single crystalline $La(V_xCr_{1-x})Sb_3$ samples has allowed for the detailed study of the anisotropic properties, the determination of the easy axis as well as the estimate of the effective moment. In addition, careful chemical analysis was performed to determine the precise concentration of this doped system. This offers a certain understanding of chemical substitution effect on the suppression of the ferromagnetism and the evolution of the magnetic state in this system.

The estimated Curie-Weiss temperature θ_{poly} and the effective moment μ_{eff} per Cr as a function of the V-concentration x are plotted in fig. 9.19. It is clearly seen that θ_{poly} decreases monotonically from about 141 K to almost zero as x increases, implying that the ferromagnetic interaction is suppressed by the V substitution. The effective moment also decreases as x increases, but in a more subtle way. Instead of quickly approaching to zero as seen in the suppression of ferromagnetism in the itinerant ferromagnets [Stewart, 1984, 2001, 2006; Taufour et al., 2010], μ_{eff} per Cr varies slightly as x increases, from 3.9 μ_B for $x = 0$ to 2.9 μ_{eff} for $x = 0.88$. Whereas the former value is close to the theoretical effective moment of Cr^{3+}, the latter one is close to Cr^{4+}. Hence, the decrease of μ_{eff} is more likely as a consequence of the valence change due to the V substitution than

Table 9.2 Summarized effective moment $\mu_{\rm eff}$, saturated moment $\mu_{\rm B}$, polycrystalline averaged Curie-Weiss temperature $\theta_{\rm poly}$, transition temperatures T_1, T_2 estimated from low field M(T) measurements with $\mathbf{H} \parallel b$ and $\mathbf{H} \parallel c$, and Curie temperature $T_{\rm C}$ estimated from $\rho(T)$ and $C_{\rm p}(T)$ measurements for $La(V_xCr_{1-x})Sb_3$ ($x = 0$ – 0.88).

x	$T_{\rm C}$	T_1	T_2	T_1	T_2	$T_{\rm C}$	$\theta_{\rm poly}$	χ_0	$\mu_{\rm eff}$	$\mu_{\rm S}$
(K)	(K)	(K)	(K)	(K)	(K)	(K)	(10^{-4} emu/mole)	(μ_B/Cr)	(μ_B/Cr)	
	$d\rho/dT$	$\mathbf{H} \parallel b$	$\mathbf{H} \parallel b$	$\mathbf{H} \parallel c$	$\mathbf{H} \parallel c$	$C_p(T)$				
0	132	133		132		132	141	-40	3.9	1.61
0.06	95	98		98						
0.13	80	82		83						
0.18	59	62		66						
0.22	45	54		58			90	0	3.7	1.37
0.33	23	24	14	32	12		70	-5	3.2	
0.36	24	24	12	32	13					
0.42		18	10	20	10					
0.52		14	8	20	6		52	1	3.1	
0.59		12	5	13	5					
0.73				6	3		34	6	2.9	
0.88							0.1	8	2.9	

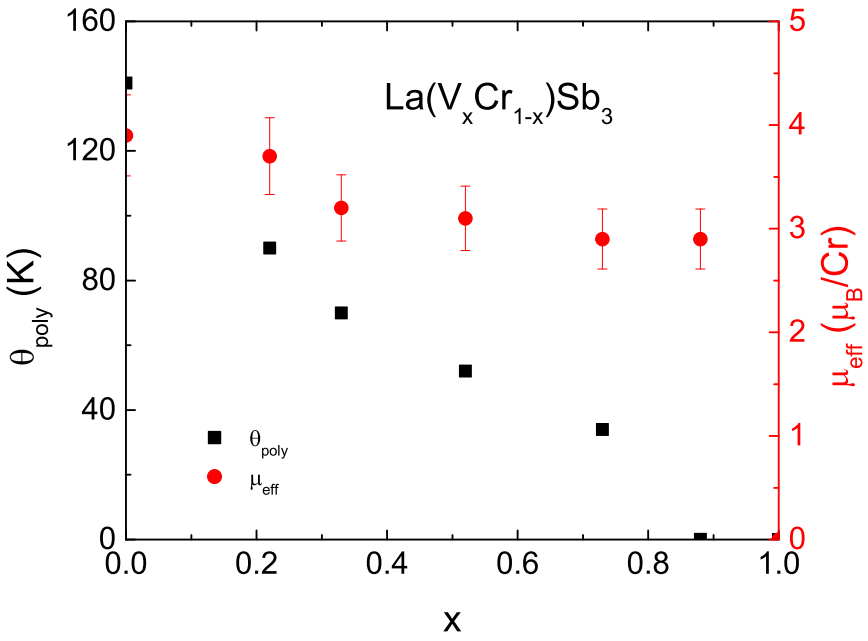

Figure 9.19 The Curie-Weiss temperature θ_{poly} and the effective moment μ_{eff} per Cr as a function of x for $\text{La}(\text{V}_x\text{Cr}_{1-x})\text{Sb}_3$.

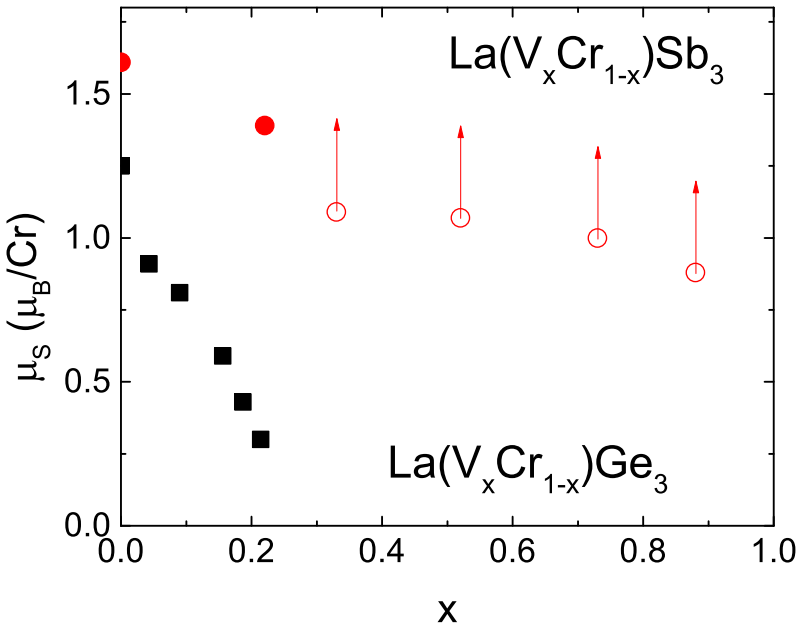

Figure 9.20 The saturated moment μ_S as a function of x for the $La(V_xCr_{1-x})Ge_3$ and $La(V_xCr_{1-x})Sb_3$ series. Note: for $La(V_xCr_{1-x})Sb_3$ compounds with $x > 0.22$, the saturated moment is replaced by the value of magnetization at 50 kOe with field along the b-axis. Data on $La(V_xCr_{1-x})Ge_3$ are from Ref. [Lin et al., 2013c].

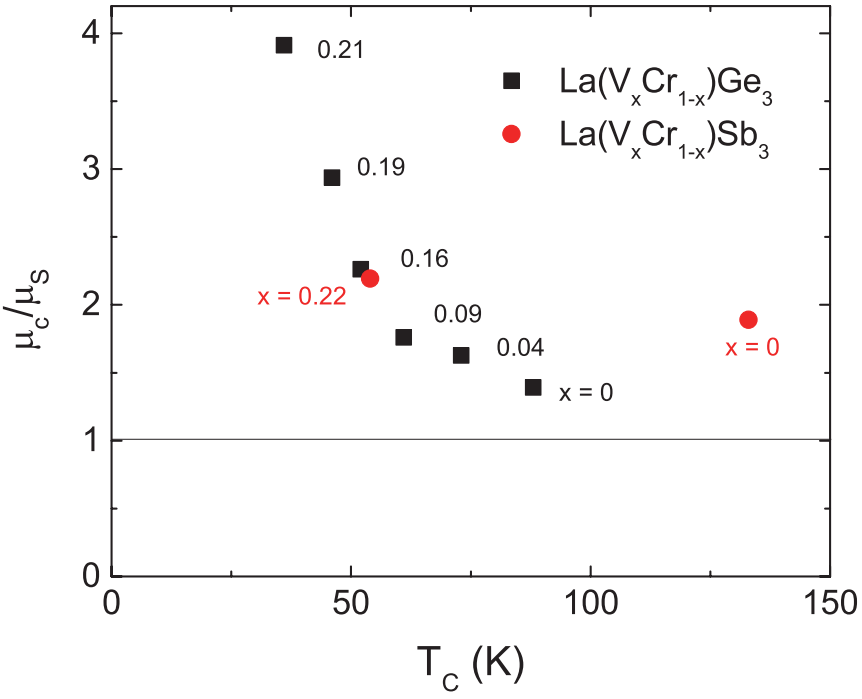

Figure 9.21 The Rhodes-Wohlfarth ratio μ_c/μ_S as a function of Curie temperature T_C for the La(V_xCr_{1-x})Ge_3 and La(V_xCr_{1-x})Sb_3 series. Data on La(V_xCr_{1-x})Ge_3 are from Ref. [Lin et al., 2013c].

manifesting an itinerant-moment behavior.

The saturated moment values for the $La(V_xCr_{1-x})Sb_3$ compounds are presented in fig. 9.20. μ_S shows a slight decrease with the increase of the V concentration, from 1.61 μ_B/Cr for $x = 0$ to 1.37 μ_B/Cr for $x = 0.22$. For higher V-doped compounds ($x > 0.22$), the $La(V_xCr_{1-x})Sb_3$ systems does not have a ferromagnetic state at low temperatures, hence, μ_S is replaced by the value of magnetization at 50 kOe with field along the b-axis. The arrows in fig. 9.20 imply that $M(H = 50$ kOe) is the lower limit of the possible saturated moment of the higher V-doped compounds. It is clear that Cr's moment stays well above zero as the V concentration approaches to 1.

To learn more about Cr's magnetic moment, we can compare the saturated moments of both $La(V_xCr_{1-x})Ge_3$ and $La(V_xCr_{1-x})Sb_3$ series (as shown in fig. 9.20). It can be clearly seen that μ_S of the $La(V_xCr_{1-x})Ge_3$ compounds quickly decreases as the V concentration increase, that is associated with the itinerant magnetism [Lin et al., 2013c]. For the $La(V_xCr_{1-x})Sb_3$ series, μ_S has a slower decreasing rate as the V concentration increases. This possibly implies that the magnetic moment associated with Cr in the $La(V_xCr_{1-x})Sb_3$ compounds is mainly of local character. Based on the values of μ_{eff} and μ_S obtained, one can calculate the Rhodes-Wolfarth ratio (RWR) [Rhodes and Wohlfarth, 1963], seen in fig. 9.21. According to Rhodes and Wolfarth, RWR = μ_c/μ_S, where μ_c is related to the number of moment carriers, and can be obtained from $\mu_c(\mu_c+1)=\mu_{eff}^2$. While RWR = 1 is an indication of localized magnetism, larger RWR values suggest the existence of itinerant ferromagnetism. In our case, RWR equals to $\simeq 1.9$ for $x = 0$ and $\simeq 2.2$ for $x = 0.22$. Although this seems suggesting the ferromagnetism is itinerant, the change of RWR as a function of T_C shows very different behavior compared with the $La(V_xCr_{1-x})Ge_3$ system [Lin et al., 2013c] (fig. 9.21) and the original Rhodes-Wohlfarth plot [Rhodes and Wohlfarth, 1963]. Therefore, unlike $La(V_xCr_{1-x})Ge_3$, $La(V_xCr_{1-x})Sb_3$ is less likely to be dominated solely by itinerant magnetic moments. Probably the magnetism in this family is of predominantly local character.

CHAPTER 10. CONCLUSIONS

As part of my thesis work, potential routes for the discovery of new superconductors have been developed and explored. We developed the use of S-X (X = non-transition metal) as well as S-TM (TM = transition metal) solutions for the growth of S-bearing compounds. We suppressed the ferromagnetism in the $La(V_xCr_{1-x})Ge_3$ and $La(V_xCr_{1-x})Sb_3$ via chemical substitution and the application of pressure. Whereas $La(V_xCr_{1-x})Sb_3$ is found to possess a local-moment-like magnetism, $La(V_xCr_{1-x})Ge_3$ manifests more and more itinerant ferromagnetic behavior as the V-concentration increases. The ferromagnetism in $La(V_xCr_{1-x})Ge_3$ was successfully suppressed by pressure, and a potential QCP was discovered for $x = 0.16$. In addition, we performed detailed characterization on $BaSn_5$ superconductor, giving further understanding of their nature of superconductivity, and on $R_3Ni_{2-x}Sn_7$ and $RNi_{1-x}Bi_{2\pm y}$ series putting to rest spurious claims of superconductivity.

To incorporate sulfur into the high-temperature solution growth, we explored a range of binary sulfur bearing solutions and demonstrated how we have been able to use these as useful starting points for growth of wide range of transition metal – sulfur – X ternary compounds. Bi was found to be one of the most promising candidates as a solvent for S. We were able to safely bring a mixture of $S_{40}Bi_{60}$ up to 1000 °C without any detectable condensation of S outside of the growth crucible and also without any indication of high vapor pressure. With Bi as a flux, single crystalline $Ni_3Bi_2S_2$ has been successfully grown. Similarly, Sn, Sb, Pb and In were also identified as potential solvents for S-based compounds growth. The growths of $Co_3Sn_2S_2$, Fe_2GeS_4, CoSSb and PbS have been

given as examples. In addition, we found the use of the relatively deep eutectics in the transition metal – sulfur binaries potentially allows for the growth of a wide range of TM – S – X compounds. Given that Pd-S binary phase diagram exhibits a deep eutectic near 28% S, a liquid state with a content of 20 – 50% S can be achieved via slow heating to slightly above 1000 °C. By utilizing this liquid state, single crystalline samples of Pd_4S and $CePd_3S_4$ can be grown with high purity. We also found that Ni-S and Co-S hold comparable potential. The use of the relatively deep eutectics gives a remarkably simple method for growth of single crystalline Co with crystallization taking place *below* the Curie temperature.

The re-examination of the known superconductor $BaSn_5$ was enabled by the synthesis of single crystalline samples, and detailed studies of the thermodynamic and transport properties were made. The superconductivity in $BaSn_5$ was found to be more complex than isotropic BCS type. De Haas-van Alphen oscillations were observed in $BaSn_5$, and three effective masses were resolved via FFT. The T_c-value for $BaSn_5$ was suppressed by pressure and this route (to higher T_c) can be considered as a dead-end.

Motivated by previous claims and observations of superconductivity in two specific series of rare-earth compounds, we have synthesized single crystalline $R_3Ni_{2-x}Sn_7$ (R = La, Ce, Pr and Nd) samples via self-flux Sn and $RNi_{1-x}Bi_{2\pm y}$ (R = La–Nd, Gd–Dy) via self-flux Bi. Detailed characterizations were performed to study their properties. However, the superconducting feature in $La_3Ni_{1.89}Sn_7$ was found to be filamentary and the anomalies in the resistivity can be attributed to impurities. It is likely that these features are related to the superconducting transitions of $LaSn_3$ and Sn. Similarly, for $RNi_{1-x}Bi_{2\pm y}$ compounds, the the superconducting features observed in the transport measurements were found to be related to minority, second phase, possibly Bi film, NiBi and/or $NiBi_3$.

The Ni occupancy in the $R_3Ni_{2-x}Sn_7$ (R = La, Ce, Pr and Nd) series varies from ~ 0.1 for R = La to ~ 0.7 for R = Nd. The electrical resistivity of this series follows

metallic behavior at high temperatures. Determination of clear anisotropies as well as antiferromagnetic ordering temperatures for $R_3Ni_{2-x}Sn_7$ (R =Ce, Pr and Nd) have been made. For $Pr_3Ni_{1.56}Sn_7$ and $Nd_3Ni_{1.34}Sn_7$, multiple magnetic transitions take place upon cooling. Metamagnetic transitions in this family (R = Ce, Pr and Nd) were detected for applied magnetic fields below 70 kOe. An $H - T$ phase diagram of $Ce_3Ni_{1.69}Sn_7$ was assembled to shed light on its low field properties and to rule out possible quantum critical effects.

The $RNi_{1-x}Bi_{2\pm y}$ (R = La–Nd, Gd–Dy) series forms with partial Ni occupancy, $0.72 \leq (1 - x) \leq 0.84$, as well as a variable Bi occupancy, $1.76 \leq (2 \pm y) \leq 2.14$. The high-temperature magnetic susceptibilities of $RNi_{1-x}Bi_{2\pm y}$ (R = Ce–Nd, Gd–Dy) show local-moment like behaviors. For the whole $RNi_{1-x}Bi_{2\pm y}$ family, Ni is non-moment bearing. The values of the effective magnetic moment in the paramagnetic state are close to the theoretical values of the trivalent rare earth ion. The local-moment ordering is likely governed by the indirect exchange interactions between the rare earth ions mediated by the conduction electrons (RKKY interaction). The negative sign of the paramagnetic Curie temperatures θ_{ab}, θ_c and θ_{ave} indicates the dominant interactions in this system are antiferromagnetic.

These two series of rare-earth compounds turned out not to be promising systems for the study of superconductivity, as none of the compounds show bulk superconductivity. Similar phenomena have also been observed in the $(R_xCa_{1-x})Fe_2As_2$ (R = La – Nd) and $LaO_{0.5}F_{0.5}BiS_2$ compounds, where it is difficult to distinguish bulk superconductivity from filamentary superconductivity. Careful characterizations and a though literature search are needed to confirm the existence of a new bulk superconductor. The examination of these spurious superconducting phase again showed the importance of high-quality single crystals for the search for new superconductors.

Given that search for QCPs is another potential route for the discovery of new superconductors, we examined two ferromagnetic systems $La(V_xCr_{1-x})Ge_3$ & $La(V_xCr_{1-x})Sb_3$

The growth of single crystalline $La(V_xCr_{1-x})Sb_3$ and $La(V_xCr_{1-x})Ge_3$ samples has allowed for the detailed study of the anisotropic properties, the determination of the easy axis as well as the estimate of the effective moment and saturated moment. In addition, careful chemical analysis was performed to determine the precise concentration of this doped system. This offers a clearer understanding of chemical substitution effect on the suppression of the ferromagnetism and the evolution of the magnetic state in this system.

The suppression of the ferromagnetism in the $La(V_xCr_{1-x})Ge_3$ (x = 0 – 0.21, 1.00) series starts with chemical substitution. The ferromagnetic transition temperature is suppressed almost linearly by V doping: T_C = 88 K for x = 0, and T_C = 36 K for x = 0.21. Consistent with the Stoner model, this suggests the system possesses a fragile ferromagnetism which can be easily perturbed. Also the Curie-Weiss temperature is clear suppressed by V-doping can be observed, implying the ferromagnetic interaction is weakened by V-substitution. However single crystalline $LaV_xCr_{1-x}Ge_3$ compounds with $0.21 < x < 1.00$ were not synthesized, the exact concentration x_c at which the ferromagnetism in this series is completely suppressed via V substitution is not determined. Based on the existing data, a critical concentration is likely to exist near $x = 0.3$. We further suppressed the ferromagnetism for $x = 0.16$ by pressure up to 4.9 GPa. The Curie temperature decreases as the applied pressure increases, at an initial rate of $dT_C/dp \simeq$ – 11.7 K/GPa below 2.8 GPa. The ferromagnetic signal vanishes at $\simeq$ 3.3 GPa, and the ferromagnetism in $x = 0.16$ appears to be completely suppressed. It can be clearly seen that this system can be brought to a QPT and, hopefully a QCP.

The estimated μ_S and μ_{eff} per Cr in the $La(V_xCr_{1-x})Ge_3$ series decrease in a clear manner as the V-concentration increases. In addition, the Rhodes-Wohlfarth ratio (RWR) of $La(V_xCr_{1-x})Ge_3$ ranges from $\simeq$ 1.4 for x = 0 to $\simeq$ 3.9 for x = 0.21, suggesting the ferromagnetism evolves towards itinerant as V-concentration increases. Also the change of RWR as a function of T_C exhibits very similar behavior as seen in the original Rhodes-Wohlfarth plot, again implying that the Cr in the $LaV_xCr_{1-x}Ge_3$ series

holds an itinerant magnetic nature. Given the RWR ratio and the fact that both μ_S and μ_{eff} decrease as the V-concentration increases, it is promising for it being a potential QCP system.

The suppression of the ferromagnetism in the $La(V_xCr_{1-x})Sb_3$ series gives a rather different picture. With the application of pressure up to 5.3 GPa, the ferromagnetic ordering temperature T_C of $LaCrSb_3$ almost does not change. Therefore, chemical substitution was used as a second parameter to evaluate the potential for quantum critical behavior. The ferromagnetism can be observed for x up till 0.36, and the ferromagnetic transition temperature is suppressed monotonically by the V-substitution: $T_C = 133$ K for $x = 0$, and $T_C = 24$ K for $x = 0.36$ (based on the low field $M(T)$ data with $\mathbf{H} \parallel b$). As the level of the V-concentration increases, for $0.42 \leq x \leq 0.73$, the system enters into a new magnetic ground state. As the V-concentration reaches even higher, $x \geq 0.88$, no magnetic ordering can be observed and the system shows paramagnetic behavior. Based on our data, the phase boundary between the ferromagnetic and spin-glass state is at about $x = 0.3$, and the spin-glass state vanishes at around $x = 0.8$. However, in the vicinity of these phase boundaries, no feature of a QCP has been observed.

The effective moment in the $La(V_xCr_{1-x})Sb_3$ series decreases as x increases, but in a very subtle way. Instead of quickly approaching to zero as seen in the suppression of ferromagnetism in the itinerant ferromagnets, μ_{eff} per Cr varies slightly as x increases, from 3.9 μ_B for $x = 0$ to 2.9 μ_{eff} for $x = 0.88$. It probably implies that Cr in the $LaV_xCr_{1-x}Sb_3$ possesses a non-itinerant nature. The saturated moment μ_S for $x = 0$ and 0.22 are found to be 1.60 μ_{eff} and 1.29 μ_{eff}, respectively. Accordingly, the Rhodes-Wohlfarth ratio (RWR) is found to be $\simeq 1.9$ for $x = 0$ and $\simeq 2.2$ for $x = 0.22$. Although this seems suggesting the ferromagnetism is itinerant, the change of RWR as a function of T_C shows very different behavior compared with the the original Rhodes-Wohlfarth plot. Therefore, $La(V_xCr_{1-x})Sb_3$ is more likely to be dominated by local moment magnetism.

In summary, we have been able to grow ternary compounds out of Bi-S, Sn-S, Sb-S,

and Pd-S and have shown that Pb-S, In-S, Ni-S and Co-S melts hold comparable potential. Hopefully, with these solutions, new phases, as well as ground states, can be discovered. We are continuing working on the development of S-based solutions for the exploration of S-based compounds as possible hosts for high temperature superconductivity. Incorporated with the double-flux method, these solutions lead to new ways of growing single crystalline S-based compounds, such as MoS_2.

The suppression of ferromagnetism in the $La(V_xCr_{1-x})Ge_3$ series demonstrates a potential route for the discovery of a QCP and hopefully superconductivity. It will be very interesting to study the compounds via transport measurements under pressure and evaluate their critical exponents at p_c. Alternative methods of growing higher x compounds or pressure studies on pure $LaCrGe_3$ will be possible ways to tune to the potential QCP system as well. Given that the two stoichiometrically similar series $La(V_xCr_{1-x})Ge_3$ and $La(V_xCr_{1-x})Sb_3$ respond differently to chemical substitution and pressure, theoretical calculations will be very helpful in the understanding of these differences as well as the effects of chemical substitution and the application of pressure, which hopefully can provide guidance for the future search for new QCP systems and superconductors.

APPENDIX A. Lists of growths

Listed here are exploratory growths of chalcogen and pnictogen elements-based compounds (mostly S-bearing compounds), and growths of $R_3Ni_{2-x}Sn_7$, $RNi_{1-x}Bi_{2\pm y}$, $SrSn_4$, $BaSn_5$, $La(V_xCr_{1-x})Ge_3$ and $La(V_xCr_{1-x})Sb_3$ compounds. The purpose is to provide useful data and information for the future work. The growths are roughly organized into different groups based on the starting materials, the targeted compounds, or the fluxes/eutectic points that were used. The rules used to group these growths are not mutually exclusive. Each table gives our internal batch growth number, concentration of starting materials and the comments on the growth results.

Tests of Bi and/or Sb used as fluxes

Batch No.	**Initial concentration**	**Comments**
PM989	$S_{.08}(Bi_{.75}Sb_{.25})_{.92}$	Nothing
PM990	$S_{.08}(Bi_{.5}Sb_{.5})_{.92}$	Needle shaped crystals, probably Bi_2S_3, m = 0.1730g, x-ray shows Bi_2S_3 and Bi-Sb-S ternery
SA483	$S_{25}Bi_{75}$	needles stuck in a chunk, m= 1.6284g, spin=4.67g

Exploratory growths of Fe-S based compounds

Batch No.	Initial concentration	Comments
KQ006	$Fe_3S_6(Bi_{.75}Sb_{.25})_{91}$	x-ray separately. Bubble-dot feather-like. Non-magnetic
KQ007	$Fe_3S_6(Bi_{.5}Sb_{.5})_{91}$	more plate. Feather-like, wings. X-ray. Cool down more. Get colder or more materials.
KQ008	$Fe_6S_6(Bi_{.75}Sb_{.25})_{88}$	x-ray: non magnetic. More feather. Less bubbles.
KQ009	$Fe_6S_6(Bi_{.5}Sb_{.5})_{88}$	x-ray. Broken feather and bubbles.
KQ169	$Fe_{.1}S_{.3}Bi_{.45}Sb_{.15}$	ampule brakes–oxidized? a big hard nest
KQ186	FeS_9Sb_{81}	flux comes out of the catch, looks crap. some little irregular and leaf-like stuff
KQ193	FeS_9Sb_{54}	a cluster of irregular dots
KQ207	FeS_9Sb_{54}	hard cylinder-chunk, holes on the surface, looks like moon. Breaking it: shiny plates in it, or shiny dots.
KQ229	$Fe_3S_6(Bi_{.7}Zn_{.3})_{91}$	shiny dust. some Zinc seems not melted.
KQ252	$Fe_3S_6(Bi_{.75}Zn_{.25})_{91}$	shiny cluster, some Zn not melt
KQ253	$Fe_3S_6(Bi_{.5}Sn_{.5})_{91}$	thin shiny rectangular plates and thicker more squared-liked plates.

Continued on next page

Table A.2 – continued from previous page

Batch No.	Initial concentration	Comments
KQ329-A	$(Fe_{.28}Ge_{.15}S_{.57})_{.1}(Bi_{.67}Sb_{.33})_{.9}$	shining, different shapes, feather like, cubic dots stick together, some brown shining color inside, colorful dots on the crucible
KQ329-B	$(Fe_{.28}Ge_{.15}S_{.57})_{.05}(Bi_{.67}Sb_{.33})_{.95}$	shining dots and dendrites
KQ339	$(Ge_2FeS_2)_{.1}Sb_{.9}$	quartz tube breaks during spin, lots of dots and some plates covered by yellow powder like stuff. Maybe some raw materials haven't melted yet? The inside surface of the crucible turned yellow-brown
KQ344	$(Ge_2FeS_2)_{.1}(Bi_{.5}Sb_{.5})_{.9}$	lumps of little dots
KQ345	$(Ge_4FeS_2)_{.1}(Bi_{.5}Sb_{.5})_{.9}$	lumps of dots, shinning rectangular plates, very thin
KQ351	$(Ge_4FeS_2)_{.05}Sb_{.95}$	ampoule broke during spin, a lot of yellow powder (S) inside, delta-small clusters of little dots!
KQ357	$(Ge_4FeS_2)_{.1}Sb_{.9}$	shining plates and clusters of little dots, no yellow stuff. Pulled out at 570C
KQ358	$(Ge_4FeS_2)_{.1}(Bi_{.1}Sb_{.9})_{.9}$	thicker plates and thinner feather like plates, very flat, no yellow stuff. Pulled out at 570C

Continued on next page

Table A.2 – continued from previous page

Batch No.	Initial concentration	Comments
KQ367	$(Ge_2FeS_2)_{.1}Sb_{.9}$	few little plates and clusters of little dots
KQ372	$(Ge_2FeS_2)_{.1}Sb_{.9}$	almost crap, saver little plates attached on the inside surface
KQ373	$(Ge_2FeS_2)_{.05}Sb_{.95}$	crap, inside crucible surface looks pink
KQ556	$FeSbBi_4S_{0.5}$	needles+packages of little brown dots
KQ558	$Cu_{10}Ge_4Fe_{1.9}S_{14}$	no spin
KQ735	$Fe_{10}Sb_{40}S_{50}$	dendrite crystals
SA166	$(Ge_2FeS_2)_3Sn_{94}$	red like plates and polycrystals
SA179	$Fe_5S_5In_{95}$	Fe did not melt

Exploratory growths of Co-S-Bi-Sb based compounds

Batch No.	Initial concentration	Comments
KQ023	$Co_6S_3(Bi_{.75}Sb_{.25})_{91}$	small plates. Dots. Non-magnetic
KQ024	$Co_9S_3(Bi_{.75}Sb_{.25})_{88}$	lumps small plates. Non magnetic.
KQ025	$Co_6S_3(Bi_{.5}Sb_{.5})_{91}$	a big lump. Non magnetic.
KQ026	$Co_9S_3(Bi_{.5}Sb_{.5})_{88}$	bigger crystals. Surrounded by the similar smaller ones and rods. Non magnetic. X-ray needed.

Continued on next page

Table A.3 – continued from previous page

Batch No.	Initial concentration	Comments
KQ035	$Co_3S_6(Bi_{.75}Sb_{.25})_{91}$	broken ampoule. Water goes in. small plates. Two different shapes
KQ036	$Co_3S_9(Bi_{.75}Sb_{.25})_{88}$	huge lumps. Small mirror plate. Non magnetic.
KQ037	$Co_3S_6(Bi_{.5}Sb_{.5})_{91}$	broken ampoule. Water goes in. (seems not affect sample yet)lots of mirrored plates. Non magnetic.
KQ038	$Co_3S_9(Bi_{.5}Sb_{.5})_{88}$	large mirrored plates and needles
KQ062	$(Co_{.1}S_{.9})_{.1}(Bi_{.75}Sb_{.25})_{.9}$	lots of dots. Strong S smell
KQ063	$(Co_{.1}S_{.9})_{.15}(Bi_{.75}Sb_{.25})_{.85}$	irregular shaped dots. Great S smell
KQ087	$(Co_{.4}S_{.6})_{.35}(Bi_{.75}Sb_{.25})_{.65}$	feather or leaves- like. Non magnetic
KQ088	$(Co_{.4}S_{.6})_{.45}(Bi_{.75}Sb_{.25})_{.55}$	a cluster of feather or tree leave like. Not magnetic
KQ094	$(Co_{.25}S_{.65})_{.4}(Bi_{.75}Sb_{.25})_{.6}$	strange transparent glass in the flux side. Tree leaves
KQ095	$(Co_{.1}S_{.9})_{.35}(Bi_{.75}Sb_{.25})_{.65}$	Same as KQ094
KQ105	$((Co_{1-x})_{.4}S_{.6})_{.35}(Bi_{.75}Sb_{.25})_{.65}$	thin rod twisted into a nest. Non-magnetic

More exploratory growths of Co-S-Sb/Sn based compounds

Batch No.	Initial concentration	Comments
KQ912	$Co_9S_6Sn_{94}$	some thicker plates, some thinner ones
KQ914	$Co_6Ni_3S_6Sn_{94}$	plates +needles
KQ915	$Ni_6Co_3S_6Sn_{94}$	big plates + small plates +some needles
KQ916	$Co_5S_6Sn_{94}$	lots of needles+poly-chunk
KQ917	$Co_{12}S_6(Bi_{0.25}Sn_{0.75})_{94}$	more plate($Co_3S_2Sn_2$?)+lots of needles
KQ932	$Co_{11}NiS_6Sn_{94}$	less plates, more needles
KQ933	$Co_{11}NiS_6(Bi_{0.25}Sn_{0.75})_{94}$	chunk of crystals, grows dirty
KQ934	$Co_{12}S_6Sn_{84}In_{10}$	broke during spin, oxidized, huge crystals
KQ948	$Co_{10}Ni_2S_6(Sn_{0.75}Bi_{1.25})_{94}$	plates + needles
KQ949	$Co_9Ni_3S_6(Sn_{0.75}Bi_{0.25})_{94}$	needles
KQ950	$Co_{12}S_6Sn_{84}In_{10}$	plates+rods
KQ951	$Co_{12}S_6Sn_{89}In_5$	few plates, rods
MC083	$(Co_{0.5}Ni_{0.5})_3S_2Sn_2$	
MC104a	$(Ni_{1.5}Co_{1.5}Sn_2S_2)_{0.1}Sn_{0.9}$	little polycrystals not very pretty. m=0.67g
SA002	$Co_9Ni_3S_3Sn_{94}$	
SA003	$Co_{12}S_6Sn_{74}In_{20}$	
SA004	$Co_{12}S_6Sn_{64}In_{30}$	
SA159	$Co_9S_6In_{91}$	rhombohedral
SA160	$Ni_2S_6In_{88}$	plates and rod like stuff crumpled together

Continued on next page

Table A.4 – continued from previous page

Batch No.	Initial concentration	Comments
SA715	$Co_{10}Ni_{10}S_{20}Sb_{60}$	no spin, remelt at 600C
SA716	$Co_{10}Gd_{10}S_{20}Sb_{60}$	no spin, remelt at 600C, remelt m=5.1504g
SA746	$Co_{20}S_{20}Sb_{60}$	no spin put back in furnace spun at 650C crystals m=1.5g
SA797	$Co_{10}Ni_{10}S_{20}Sb_{60}$	some dentritic cubes form large plates. Not magnetic, m=2.4g
SA798	$Co_{15}Fe_5S_{20}Sb_{60}$	many small crystals formed. Some bigger cubes. Not magnetic
SA799	$Co_{15}Gd_5S_{20}Sb_{60}$	large plates/chunks. Some were not melted, not magnetic. Big resistance.m= 2.54g
SA824	$Co_{15}Mn_5S_{20}Sb_{60}$	Clear ampoule strong S smell pen work gone plates something at the bottom not melt not magnetic
SA825	$Co_{15}Cr_5S_{20}Sb_{60}$	Ampoule broke during spin, crystals got oxidized large plates some are more 3D a chunk of stuff of the bottom seems no melt
SA174	$S_4Zn_{50}Sb_{50}$	junk

Exploratory growths of Ni-S-Bi based compounds

Batch No.	Initial concentration	Comments
KQ106	$Ni_{.06}S_{.06}Bi_{.88}$	long thin plates. Non-magnetic
KQ107	$Ni_{.03}S_{.06}Bi_{.91}$	rods+plates+little chunks. Non magnetic
KQ108	$Ni_{.03}S_{.06}Bi_{.88}$	pieces of plates. Non-magnetic
KQ133-1	$Ni_{.06}S_{.06}Bi_{.88}$	nothing
KQ134	$Ni_{.03}S_{.06}Bi_{.91}$	nothing
KQ135	$Ni_{.03}S_{.09}Bi_{.88}$	nothing. 700C is too high.
KQ145	$Ni_{.06}S_{.06}Bi_{.88}$	small pieces of plates tightly crumbled together.
KQ146	$Ni_{.03}S_{.06}Bi_{.91}$	nothing
KQ147	$Ni_{.03}S_{.09}Bi_{.88}$	nothing
KQ156	$Ni_{.05}S_{.25}Bi_{.7}$	a soft nest at the bottom
KQ168	$Ni_{.2}S_{.05}Bi_{.75}$	shiny irregular plates and rods
KQ227	$Co_3S_6(Bi_{.25}Sn_{.25})_{91}$	shiny plates and flat rods, non-magnetic
KQ550	$Ni_9Bi_2S_8$	shining little dots stack in big gray chunk
KQ751	$Ni_9Bi_2S_8$	NiS and $Ni_3Bi_2S_2$
MC084	$(Ni_5Cu_{0.5})_3S_2Bi_2$	
SA056	$Ni_{20}S_{15}Bi_{80}$	big huge plates
SA066	$Ni_{19}Cu_1S_{15}Bi_{80}$	shining plates
SA067	$Ni_{18}Cu_2S_{15}Bi_{80}$	shiny plates

Continued on next page

Table A.5 – continued from previous page

Batch No.	Initial concentration	Comments
SA068	$Ni_{19}Pd_1S_{15}Bi_{80}$	huge amount of shiny plates
SA069	$Ni_{18}Pd_2S_{15}Bi_{80}$	same as SA068, irregular plates
SA070	$Ni_{19}Co_1S_{15}Bi_{80}$	plates on polycrystalline puck
SA071	$Ni_{18}Co_2S_{15}Bi_{80}$	same as SA070, plates on polycrystalline puck
SA084	$Ni_{19}Rh_1S_{15}Bi_{80}$	long rectangular plates + more squared plates + little dentritics
SA085	$Ni_{18}Rh_2S_{15}Bi_{80}$	wired shaped plates, look like triangles, but with bad edges.
SA086	$Ni_{19}Pt_1S_{15}Bi_{80}$	completely different, thicker plates and rods
SA087	$Ni_{18}Pt_2S_{15}Bi_{80}$	poorly formed irregular thin plates.
SA104	$Ni_{16}Cu_4S_{15}Bi_{80}$	smaller, irregular plates
SA105	$Ni_{16}Pd_4S_{15}Bi_{80}$	smaller, irregular plates
SA128	$Pd_{20}S_{15}Bi_{80}$	maybe spin temp is low, a core made of needles and plates
SA135	$Pb_{18}S_{12}Bi_{70}$	Cubes-PbS
SA136	$Ni_7S_7(Pb_{0.8}Bi_{0.2})_{86}$	poly crystals, with cubes and plates
SA139	$Pd_{20}S_{30}Bi_{50}$	
SA157	$Cu_{20}S_{15}Bi_{80}$	
SA158	$Ni_{10}Cu_{10}S_{15}Bi_{80}$	wasn't able to spin immediately. Big pieces

Continued on next page

Table A.5 – continued from previous page

Batch No.	Initial concentration	Comments
SA390	$Cu_{10}Ni_{10}S_{15}Bi_{80}$	NiCu arc-melting after mass= 0.4399, plates dentiitic crystals not magnetic, a few loose large crystals and a few attached to the wall of crucible and getting large

Exploratory growths of Ni-S-X compounds

Batch No.	Initial concentration	Comments
KQ179	$Ni_{0.01}S_{0.02}Sn_{.97}$	pinkish, red transparent plates with shining metallic lines
KQ180	$Ni_{0.01}S_{0.02}In_{.97}$	few things came out, yellow/green/transparent plates and some shining dots, yellow dots on quartz before spin
KQ181	$Ni_{0.01}S_{0.02}Ga_{.97}$	shining irregular plate, some feather and leaf like
KQ552	$CuNi_2S_{1.2}$	a collection of polycrystal like particles
KQ753	$Ni_9Sb_2S_8$	NiS and NiSb and NiSbS
KQ913	$Ni_9S_6Sn_{94}$	some big plates + needles
SA173	$(Ni_9S_8)Sb_{92}$	junk

Continued on next page

Table A.6 – continued from previous page

Batch No.	Initial concentration	Comments
SA427	$(NiS)_{40}In_{60}$	total spin foggy crucible
SA443	$Ni_5S_5Sb_{90}$	total spin
SA453	$(Ni_{.5}S_{.5})_{30}Sb_{70}$	dentrictics

Exploratory growths of RE-S based compounds

Batch No.	Initial concentration	Comments
KQ136	$Lu_{.06}S_{.04}Bi_{.9}$	looked crap. Gray power like cover. Cut- golden brown inside. Cut deeply - solid chunk.
KQ155	$Lu_{.05}S_{.05}Bi_{.9}$	cut Cu into small pieces. Wrapped with non-melted Lu
KQ137	$Sc_{.06}S_{.04}Bi_{.9}$	red-yellows chunk covered with a layer of gray stuff. Looks like melted zinc.
KQ138	$La_{.06}S_{.04}Bi_{.9}$	crucible cracks. Brown on the top quartz chunk and plates covered with mud powder.
KQ223	$(Nd_4NiS_7)_{.01}Sb_{.99}$	colorful cluster of irregular shaped stuff. red, green and sliver.
KQ228	$(Nd_4NiS_7)_{.02}Sb_{.98}$	solid chunk. Breaking it: shiny spots. some part is red gray.

Continued on next page

Table A.7 – continued from previous page

Batch No.	Initial concentration	Comments
KQ645	$La_3CoAlS_7Zn_9Bi_{16}$	CRUCIBLE BROKE INSIDE THE QUARTZ TUBE. DARK LUMPS. RED NEEDLES
KQ646	$La_3NiFeS_7Sb_9Bi_{16}$	crucible cracks inside the quartz tube. Dark lumps.
KQ658	$BaLa_{1.8}Bi_{0.2}CoS_5$	
KQ660	$BaLa_{1.8}Bi_{0.2}NiS_5$	
KQ683	$LaMo_6S_8Ni_{18}Sb_{72}$	Loose polycrystalline chunk with a metal core (Mo?)some small cubes
SA198	$Ni_{10}Yb_{10}S_{15}Bi_{80}$	Plates and solid chunk (Yb?)
SA387	$Bi_{0.26}S_{0.6}Ce_{0.14}$	solid chunk no spin see book No.12 for more temperatures
SA408	$Bi_{.26}S_{.6}Ce_{.14}$	stink polycrystal. Crystal =1.14g
SA442	$La_{10}(Ni_{0.61}S_{0.39})_{90}$	needles, silver and golden chunk magnetic
SA448	$Ce_{10}(Ni_{0.61}S_{0.39})_{90}$	polycrystalline chunk, m=0.9023g, everything has melted

Exploratory growths of BaS-based compounds

Batch No.	Initial concentration	Comments
KQ141	$(BaS)_{.05}S_{.05}Ni_{.05}Bi_{.85}$	yellow powder+shining plates
KQ142	$(BaS)_{.1}S_{.1}Ni_{.1}Bi_{.7}$	yellow powder, gray junk. Some shining pieces of plate buried in
KQ143	$(BaS)_{.05}S_{.045}Ni_{.05}Bi_{.855}$	not melted yellow powder gathered at the bottom + lots of shining irregular plates
KQ144	$(BaS)_{.1}S_{.09}Ni_{.1}Bi_{.71}$	seems not melt. Yellow powder. A big lump, contains tiny pieces of irregular shape plates.
KQ154	$(BaS)_{.05}S_{.05}Ni_{.05}Bi_{.85}$	still have a disk at the bottom with not melted yellow powder. More plates a rods
KQ157	$(BaS)_{.05}S_{.15}Ni_{.15}Bi_{.75}$	one big disk chunk stuck at the bottom some little yellow dot sparkled on it. It seems like most BaS melted. Several thick plates and rods on the top
KQ167	$(BaS)_{.12}Ni_{.47}S_{.41}$	without spin a huge chunk with shiny little dots. Ground into powder, pressed into a pellet
KQ194	$(BaS)_{.12}Ni_{.47}S_{.41}$	part shiny, part gray, when broken, big expanded cylinder with holes in. brown gray coloured stuff covers shiny plates
KQ211	$(BaS)Co_4S_4$	melted chunk, dark black. Breaking it: dark shiny stuff, maybe form some regular shape – hard to tell

Continued on next page

Table A.8 – continued from previous page

Batch No.	Initial concentration	Comments
MC009	$(BaS)_6((Cu_{0.9}Ni_{0.1})_2S)_{10}$	crap
MC010	$(BaS)_6((Cu_{0.9}Fe_{0.1})_2S)_{10}$	crap with some small plates
SA906	$(BaS)_6(Cu_2S)_{10}$	after arc melting, m=1.4216g
SA964	$(BaS)_6(Cu_2S)_{10}$	m = 1.5577g after pellet
SA985	$(BaS)_6((Cu_{0.9}Ni_{0.1})_2S)_{10}$	after pellet m = 1.8863g. Total spin. It seems materials flow out.
SA989	$(BaS)_6((Cu_{0.95}Ni_{0.05})_2S)_{10}$	m = 1.5475g
KQ684	$(BaS)_{0.3}Cr_{0.15}Sn_{1.35}$	solid chunk
KQ685	$BaSCrSn_9$	a chunk of yellow powder with some metallic stuff on the top
KQ634	$BaCrS_2Sb_9$	black chunk inside layer of the crucible gets red
KQ656	$CrSbS_3Bi_{12}$	dark lump (Cr didn't melt)
KQ657	$CrSb_{19}S_3$	metallic chunk

Exploratory growths of Cu-S-X compounds

Batch No.	Initial concentration	Comments
KQ280	$Cu_8S_6Bi_{88}$	a cluster of little dots

Continued on next page

Table A.9 – continued from previous page

Batch No.	Initial concentration	Comments
KQ398	$(CuFeS_2)Sb_{.9}$	several chunks
KQ571	$Cu_{60}Ge_{40}Fe_{17}S_{50}$	no spin
KQ591	$CuNiBi_7S_3$	total spin
KQ605	$Cu_{26}Ge_6Fe_4S_{35}$	solid chunk no spin
KQ614	$CuRh_2S_4Pb_{36}$	marks gone, waxy surface crucible little dots form. Plates
KQ615	$CuRh_2S_4Bi_{18}$	shiny chunks, like cubic phase
KQ625	$CuFeS_2Sb_9$	solid chunks polycrystalline
KQ752	$CuMo_2S_5$	Quartz tube coated by S
SA469	$(CuFe_2S_3)_2Sb_{94}$	non-regular shaped crystals m=0.1712g, spin=4.6355g
SA479	$(CuFe_2S_3)_2Sb_{98}$	irregular shape plates m=0.1834g, spin=4.79g
SA480	$(CuFe_2S_3)_4Sb_{96}$	bubble like stuff m=0.182g, spin=2.27g
SA481	$(CuFe_2S_3)_6Sb_{94}$	bubbles m=0.21g, spin=1.76g
SA535	$Cu(Bi_{0.65}S_{0.35})_9$	formed chunk like a cheese, m=1.054g, flux= 5.05g
SA536	$Cu_2(Bi_{0.65}S_{0.35})_8$	one side of quartz tube gets smoked pencil mark gone, thin tiny needle nest, m=0.467g, flux=5.38
SA540	$Cu_5(Bi_{0.6}S_{0.4})_{95}$	total spin, remelt spin at 500C, m=1.95g

Continued on next page

Table A.9 – continued from previous page

Batch No.	Initial concentration	Comments
SA541	$Cu_{10}(Bi_{0.6}S_{0.4})_{90}$	total spin, remelt spin at 500C, m=2.29g
SA570	$Cu_5(Bi_{0.6}S_{0.4})_{95}$	rods
SA690	$(Cu_{0.75}Ni_{0.25})_5(Bi_{0.6}S_{0.4})_{95}$	rods, not magnetic m=1.87g
SA691	$(Cu_{0.75}Fe_{0.25})_5(Bi_{0.6}S_{0.4})_{95}$	m= 2.1624g
SA710	$(Cu_{0.5}Fe_{0.5})_5(Bi_{0.6}S_{0.4})_{95}$	Bi_5CuS_8 + CuS_2
SA711	$(Cu_{0.75}Pt_{0.25})_5(Bi_{0.6}S_{0.4})_{95}$	smaller rods.
SA712	$(Cu_{0.75}Gd_{0.25})_5(Bi_{0.6}S_{0.4})_{95}$	smaller rods.
SA744	$(Cu_{0.75}Mn_{0.25})_5(Bi_{0.6}S_{0.4})_{95}$	Rods mass = 1.57g
SA745	$(Cu_{0.75}Tb_{0.25})_5(Bi_{0.6}S_{0.4})_{95}$	Rods mass = 1.65g
SA764	$Cu_{40}(Bi_{0.6}S_{0.4})_{60}$	Polycrystalline
SA765	$Cu_{20}(Bi_{0.6}S_{0.4})_{80}$	Total Spin

Exploratory growths of Pb-S-based compounds

Batch No.	Initial concentration	Comments
KQ445	$(Pb_{.2}Cu_{.2}S_{.6})_{12}Bi_{88}$	Needles
KQ446	$(Pb_{.2}Cu_{.2}S_{.6})_{8}Bi_{92}$	Needles
KQ447	$(Pb_{.2}Te_{.4}S_{.4})_{18}Bi_{82}$	
KQ448	$(Pb_{.2}Te_{.4}S_{.4})_{12}Bi_{88}$	

Continued on next page

Table A.10 – continued from previous page

Batch No.	Initial concentration	Comments
KQ464	$Pb_{2.4}Cu_{3.6}S_{7.2}Bi_{88}$	more short needles than other two, $PbCuBiS_3$ and PbS
KQ465	$Pb_{3.6}Cu_{3.6}S_{7.2}Bi_{88}$	$PbCuBiS_3$ and PbS
KQ466	$Pb_{3.6}Cu_{4.8}S_{7.2}Bi_{88}$	PbS and Bi
KQ470	$Ni_{7.5}S_5Pb_{95}$	total spin
KQ475	S_5Pb_{95}	lose markings, shining cubic crystal, transparent "wax" like inside the crucible
KQ476	$S_{10}Pb_{90}$	lost markings
KQ477	$Pt_5S_5Pb_{90}$	lost markings, shining cubic, transparent wax turns brown on the top, may have plate like crystal
KQ478	$Pt_{10.5}S_5Pb_{95}$	shining cubs and plates formed by cubes. Wax and discolouration
KQ479	$Pt_{24}S_5Pb_{95}$	
KQ480	S_5Pb_{95}	shining cubs and wax
KQ486	$Pt_{63.3}S_5Pb_{95}$	almost no spin, marks stays "spin crystal"=5.1166g chunk broken can see rods and plates
KQ487	$Ni_{7.5}S_5Pb_{95}$	marks gone, a layer of crust grown and crystals grown from beneath the crust
KQ489	$S_{10}Pb_{90}$	

Continued on next page

Table A.10 – continued from previous page

Batch No.	Initial concentration	Comments
KQ497	$Ni_7S_7Pb_{86}$	clean crucible, marks gone, 'wax' a chunk, break: a thick layer of crust like powers stuff grown from beneath the layer have many plates or cubes, the crust is pretty soft
KQ498	$Ni_{14}S_7Pb_{86}$	clean crucible, marks gone, 'wax' a chunk, break: a thick layer of crust like powers stuff grown from beneath the layer have many plates or cubes, the crust is pretty soft
KQ499	$Mn_5S_{10}Pb_{90}$	mark stays! A thin layer of rust, shining dots, cubs, plates, and some 'gray ashes'
KQ500	$Cu_5S_{10}Pb_{90}$	hundreds of little dots covered the inside surface of the crucible, grows dirty, little dots mixed with melted stuff, like 'grapes' marks gone,
KQ501	$Pd_{50}S_3Pb_{50}$	mark all gone, not much wax, a little bit of yellow stuff in the catch side, a broken thin crust in the crucible shisning cubs a layer of cubs has grown attached to inside surface of crucible, not much crystal grown out
KQ502	$Ti_5S_{10}Pb_{90}$	marks stay, dark gray crust on the top a little light gray dots

Continued on next page

Table A.10 – continued from previous page

Batch No.	Initial concentration	Comments
KQ503	$V_5S_{10}Pb_{90}$	shining plates grown from beneath the crust, wax, mark stays, cubs, non-melted stuff and little dots, layered cubs
KQ519	$Cu_{10}S_{10}Pb_{90}$	crucibles look like 'wet painted'
KQ567	$Ni_4S_5(Bi_{0.9}Pb_{0.1})_{91}$	shinning long rectangular plates + cubic plates, the ampoule is extremely clean
KQ568	$Ni_4S_5(Bi_{0.75}Pb_{0.25})_{91}$	shining rectangular, cubic, even rod-like plates m=0.377g
KQ581	$Pb_{1/3}Mo_2S_{8/3}Bi_{98}Ge_{98}$	gray staff with little shining clots
KQ848	$Co_5Ge_{10}S_{10}Pb_{90}$	several thin plates, dirty stuff
KQ850	$Fe_6Ge_{12}S_{12}Pb_{88}$	almost nothing
KQ899	$Co_5Ge_{10}S_{10}Pb_{90}$	cubes and poly
KQ900	$Fe_6Ge_{12}S_{12}Pb_{88}$	triangles+cubes+poly
KQ606	$PbMo_6S_8Al_{594}$	polyhedron thick plates m=0.099g
KQ612	$Pb_{90}S_{10}MoGe_{99}$	almost nothing, same small irregular plates

Exploratory growths of Alkali and Alkali earth elements based compounds

Batch No.	Initial concentration	Comments
KQ549	$(K_{1.1}Fe_{3.7}S_{5.2})(Bi_{.5}S_{.5})_{90}$	quartz tube is foggy, quartz wool turned yellow, some little shining plates or dots
KQ723	$Na_{20}Mn_{20}Sb_{60}$	
KQ725	$NaCrS_2Sb_{19}$	black drop-like chunk at the bottom of crucible.
SA193	KNi_2Se_2	Al_2O_3 crucible attacked
SA194	KCo_2Se_2	Al_2O_3 crucible attacked
SA197	KCo_2Se_2	Se+Co solid reactions. Co+Se after first solid state reaction (growth profile shown left).K added: 8hr to 400C, stay 4hr, 10hr to RT. Reground, final temperature profile: 10hr to 750C stay 72hours, 10 hours RT

Exploratory growths of V-S based compounds

Batch No.	Initial concentration	Comments
KQ616	V_3S_{97}	brown liquid sulfur condensed on the top of the ampoule. Dark chunks seems not melt

Continued on next page

Table A.12 – continued from previous page

Batch No.	Initial concentration	Comments
KQ617	VS_4Bi_{36}	shiny needles nest. Some chunks not melt

Exploratory growths of Ag-S based compounds

Batch No.	Initial concentration	Comments
KQ748	Ag_6CuBiS_4	$AgBiS_2$ and Ag? and Bi
KQ749	$AgFeS_2$	FeS_2 and ?
KQ750	$AgFe_8S_8$	Fe_7S_8

Exploratory growths of Mn-S based compounds

Batch No.	Initial concentration	Comments
KQ810	$(FeMnS)_1Sb_9$	no spin
KQ811	$(FeMn_2S)_1Sb_9$	no spin
KQ812	$(FeMnS_2)_1Sb_9$	polycrystals, some MN seems not melt
KQ827	$(Fe_{0.3}Mn_{0.3}Sb_{0.6})(Bi_{0.75}Sb_{0.25})_9$	polycrystals, Mn doesn't melt, covered with polycrystals and green stuff, Sulfur-smell, something magnetic

Continued on next page

Table A.14 – continued from previous page

Batch No.	Initial concentration	Comments
KQ829	$(Fe_{0.6}Mn_{0.6}S_{1.2})(Bi_{0.85}Ge_{15})_9$	some polycrystals, some non-melted stuff covered with a thick metallic layer
KQ838	$(Fe_0.5MnS)(Bi_{0.75}Sb_{0.25})_9$	poly and chunk seems not congruently melt
KQ839	$(Fe_{0.5}MnS)Sb_9$	lots of small needles+ chunk at the bottom
KQ837	$(MnS)_{15}Bi_{85}$	ugly polycrystals
KQ842	$(Ge_2MnS_2)_{0.1}Sb_{0.9}$	polycrystals
KQ843	$(Ge_2Mn_{.5}Fe_{.5}S_2)_{0.1}Sb_{0.9}$	polycrystals
KQ844	$(Fe_{0.29}Mn_{0.71})S$	black snowflakes
KQ849	$Mn_4Ge_6S_8Pb_{92}$	not much left, some polycrystal staff
SA167	$(GeMnS_2)_3Sn_{94}$	rod like plates and solid clunk
KQ583	$(CoMn_1)_5Sn_{95}$	little dots, few rods

Exploratory growths of Mg-B based compounds

Batch No.	Initial concentration	Comments
MC038	$Mg_5(Bi_{0.6}S_{0.4})_{95}$	thick rods than Bi_2S_3

Continued on next page

Table A.15 – continued from previous page

Batch No.	Initial concentration	Comments
MC039	$B_5(Bi_{0.6}S_{0.4})_{95}$	crucibles get really dark.some sulfur condense to the door side. Smell very bad and strong. Bi_2S_3 needles. Brown inside of crucible wall.
MC046	$(Mg_{1/3}B_{2/3})_5(Bi_{0.6}S_{0.4})_{95}$	very bad smell. Ampoule turns dark before spun. The inner wall got smoked. Both crucibles turn yellow-black, the inner wall turns black too, with white spots at the bottom. Bubbles?!... See book No.12, pg 257
MC047	$(Mg_{1/3}B_{2/3})_{10}(Bi_{0.6}S_{0.4})_{90}$	not much stuff left in, some shiny little things are embedded, but no long structure. The bottom of the crucible has some yellow, transparent small plates See book No.12, pg 257
MC056	$(Mg_{1/3}B_{2/3})_5(Bi_{0.6}S_{0.4})_{95}$	very similar to MC047 except lots of rods forming a nest. And some irregular shape stuff on top of the nest.
MC057	$(Mg_{1/3}B_{2/3})_{10}(Bi_{0.6}S_{0.4})_{90}$	very similar to MC047 but no needles formed. An ugly shaped stuff m=0.128g dark and stuffed with shiny plates.
KQ374	$(GeMg_2S_4)_{.05}Sb_{.95}$	chunk, shining surface, dark grey inside

Exploratory growths based on Ni-S eutectic

Batch No.	Initial concentration	Comments
SA293	$Ni_{67}S_{33}$	star-like crystals, m=0.2022g, spn-out mass m=0.8895g, magnetic
SA330	$V_{10}(NiS)_{45}$	Still no spin. Sit at 737C for 3h and spin again. Very small powder-like polycrystal. Magnetic.
SA331	$V_{10}(Ni_3S_2)_{18}$	Spin out mass 1.7260g
SA343	Ni_2S_1	after pressed a pellet with 1.2826g. Spin-out mass 1.0979g. Crystal mass 0.1765g. Adding more NiS, push to the right. Ni_2S_1 left over 1.2744g. NiS= 0.9629g. Total spin. Greenish. See book No.12, pg 127
SA346	$Ni_{63}S_{37}$	dentritic crystal mass 0.0348g. Malleable Ni. Spin out mass 0.9469g
SA351	$Ni_{61}S_{39}$	spin out mass 0.9946g, "crystal" mass 0.0128g (leftover in the crucible). Remelt spin mass 0.9463g (see book No.12 for remelt program, pg 129)
SA354	$V_{3.5}(Ni_{0.61}S_{0.39})_{96.5}$	dark ashed burries thin plates crystals m=0.2380g, magnetic spin out 2.6310g
SA355	$V_7(Ni_{0.61}S_{0.39})_{93}$	shiny polycrystal non-congruently melt, magnetic, crystal was 0.8660g, spin was 1.9540g

Continued on next page

Table A.16 – continued from previous page

Batch No.	Initial concentration	Comments
SA367	$Co_7(Ni_{0.61}S_{0.39})_{93}$	dark blue purple crap and definite crystals
SA373	$Ba_5(Ni_{61}S_{39})_{95}$	dentritic crystals (Ni?), nice cylinder (not melt?)
SA376	NiV_2S_4	then stayed at 800 for 11hrs and 7 days, more notes in book
SA383	$(BaS)_5(Ni_{0.61}S_{0.39})_{95}$	ugly fish-egg like stuff some even transparent (quartz wool fall in?)
SA403	$In_5(Ni_{.61}S_{.39})_{95}$	almost no spin
SA404	$Sn_5(Ni_{.61}S_{.39})_{95}$	almost no spin
SA429	NiV_2S_4	arc-melted, out in furnace annealed, see book No.12 for more notes

Exploratory growths based on Co-S eutectic

Batch No.	Initial concentration	Comments
SA763	$Co_{65}S_{35}$	
SA763-2	$Co_{65}S_{35}$	Crucible turns blue. Form into a puck (blue) magnetic. M = 1.1009g. The book has multiple instances of SA763

Continued on next page

Table A.17 – continued from previous page

Batch No.	Initial concentration	Comments
SA770	$Co_{15}Ni_5S_{20}Sb_{60}$	Beautiful Plates! M = 2.0131. Together with SA716, not congruently melt (m = 2.315g)
SA771	$Co_{65}S_{35}$	No sign of S vapor attack. Crucibles turn blue spin out crystals m = 0.48g. Plus SA763, m = 1.081g
SA785	$Ge_5(Co_{.6}S_{.4})_{95}$	Ampoule turns foggy, white. Growth side crucibles bottom turns into blue. All quartz wool turns into powder material falls into catch crucible. Magnetic, m = 3.126g as a puck
SA786	$Ge_{10}(Co_{.6}S_{.4})_{90}$	Crucibles do not have blue color. Ampoule turns foggy – white. Quartz wool turns to powder no spin, no quartz wool in catch side materials stay in grow side. Not magnetic. M = 3.16g
SA809	$Sb_5(Co_{.6}S_{.4})_{95}$	little foggy, both crucibles turned blue, almost total spin, but the quartz wool stays in the catch, some powder left in growth purple side, some are dentritics m= 0.04 magnetic
SA810	$Sb_{10}(Co_{.6}S_{.4})_{90}$	little foggy, both crucibles turned blue total spin since quartz wool in gone not magnetic
SA818	$Ge_{10}(Co_{.6}S_{.4})_{90}$	quartz tube turns foggy strong S smell crucible has very little blue not magnetic

Continued on next page

Table A.17 – continued from previous page

Batch No.	Initial concentration	Comments
SA828	$Sb_{20}(Co_{.6}S_{.4})_{80}$	severe attack on the quartz tube, a layer of thick crust formed. Quartz tube gets thinner, crucible turned a little blue. Total spin, spin is not magnetic. quartz wool got attacked, but not gone.
SA829	$In_{10}(Co_{.6}S_{.4})_{90}$	total spin. Less foggy, not yellow, lots of attack on wool, crucible (growth side) breaks when hit it. magnetic.
SA830	$Sn_{10}(Co_{.6}S_{.4})_{90}$	very foggy, yellow ampoule, crucible gets blue, quartz wool stays, not gone.
SA850	$Co_{60}S_{40}$	very little foggy on the quartz tube, no smell, both crucibles turns blue crystals turn blue crystal forward, quartz wool stay in the catch top part gets crunchy bottom part seems fine
SA950	$Sn_{10}(Co_{.6}S_{.4})_{90}$	
SA951	$In_{10}(Co_{.6}S_{.4})_{90}$	Several dentrities. Magnetic. Spin at 850 degrees c

Exploratory growths based on Pd-S eutectic

Batch No.	Initial concentration	Comments
MC369	$S_{28}Pd_{72}$	a small pellet, slightly sulfur-smell
MC374	$S_{23}Pd_{78}$	polycrystals, m=2.067g
MC376	PdS	forms a puck, m=3.1722g, some yellow stuff condensed on both top and bottom of the ampoule
MC379	$Ce_5Pd_{58.8}S_{36.2}$	polycrystals, little cubes, m=1.0066g, spin=0.54g, spill-out=2.3918g
MC404	$Ce_{3.75}Pd_{63.58}S_{32.9}$	polycrystals, mostly $CePd_3S_4$, red stuff: Ce_2S_3, rods: $CePd_3S_4$ and lots of 2nd phase stuff.
MC410	$Ce_8Pd_{50}S_{42}$	plycrystls, even smaller, $CePd_3S_4$ is the main phase, $Pd_{16}S_7$ might be the 2nd phase.
MC419	$Ce_3Pd_{52}S_{45}$	almost no spin
MC431	$S_{24.5}Pd_{75.5}$	m=3.72g
MC435	$S_{23.7}Pd_{76.3}$	almost the same as MC431
MC439	$Ce_5Pd_{58.8}S_{36.2}$	pencil mark gone, strong sulfur smell, clear bubles formed. small polycrystals, some red stuff

Continued on next page

Table A.18 – continued from previous page

Batch No.	Initial concentration	Comments
MC440	$Ce_8Pd_{50}S_{42}$	some big crystals, not sure whether it is the right stuff. pencil mark gone, strong sulfur smell, clear bubles formed. small polycrystals, some red stuff
MC441	$S_{23}Pd_{77}$	total spin
MC446	$Ce_{3.75}Pd_{63.58}S_{32.9}$	centrifuge stuck. spin didn't start right away. similar to MC447, colorful thin crust, clear formation of bubbles, dentritics formed in the bottom.
MC447	$Ce_{1.9}Pd_{67.6}S_{30.5}$	purple blue thin crust on top, hollow bottom with dentritics, spin=1.7221g
MC466	$Ba_5Pd_{58.5}S_{36.2}$	polycyrstals (dust), some shiny crystals at the bottom (PdS). The noise is a little bit loud when crack open the ampoule (high pressure?)
MC481	$Pd_{60}S_{40}$	formed into a puck of crystals, bigger, but not in a good shape.

Exploratory growths of Mo-S based compounds

Batch No.	Initial concentration	Comments
KQ582	$Sn_{1/3}Mo_2S_{8/3}Bi_{98}Ge_{98}$	similar with KQ581
KQ662	$Mo_3Ge_{57}Sn_{39}$	numerous little needles
SA887	$Mo_6S_8Ge_{60}Sn_{40}$	pencil marks gone hexagonal soft crystals SSn? Some polycrystal, crystals stuck with flux in the catch side

Exploratory growths of Te-based compounds

Batch No.	Initial concentration	Comments
KQ543	$Co_{10}S_{20}Te_{90}$	S vaporized out of the crucible lots of yellow stuff appeared on top of the ampole before spin, after spin, yellow stuff was mixed with flux. Lots of shining dots in hexagonal shape
KQ557	$Co_{10}S_{20}Te_{90}$	shining cubes, bigger than KQ543, m=0.4962g
KQ580	$Ni_9TeS_8Bi_{36}$	total spin at 670C. Irregular plates m=0.69g at 500C
KQ588	Ni_3SbTe_{17}	total spin
KQ589	$Ni_2SbTe_{11.3}$	total spin

Continued on next page

Table A.20 – continued from previous page

Batch No.	Initial concentration	Comments
KQ659	$BaCrS_2Te_9$	all black, seems sth melt and flow out of crucible, some hex-plates stacked together
KQ661	$(Fe_2SiS_4)_{10}Te_{90}$	stinky. Yellow power left. Lots of shining polycrystals attracted to a magnet.
KQ736	$Fe_{20}Si_{10}Te_{80}$	lots of hex-rods
KQ744	$Fe_{20}Sr_{20}Te_{80}$	long rods and polycrystalline stuff
SA515	$(La_4MnS_7)_{.04}Te_{0.95}$	dark brown smelly crap, La_4S_7 and Te

Exploratory growths of Se-based compounds

Batch No.	Initial concentration	Comments
KQ569	$(Cu_5Sn_5Se_10)Bi_{80}$	a few plates m=0.26g
KQ570	$(Ag_5Sn_5Se_{10})Bi_{80}$	long thin plates m=0.29g
KQ743	Ag_4SeS	can not identify with x-ray
SA417	$LaSe_4Sn_{95}$	SeSn
SA418	$La_2Se_3Sn_{95}$	α SeSn
SA419	$La_3Se_4Sn_{93}$	soft plates and rods some hard stuff seems not melt like plates attached to crucibles crystal m=0.469

Continued on next page

Table A.21 – continued from previous page

Batch No.	Initial concentration	Comments
SA439	$La_2Se_{50}Sn_{48}$	some crystals form on top of the ampoule before spin (Se?) all melt almost no spin seems forming plates
SA444	$La_3Se_{50}Sn_{47}$	aluminium crucible cracks inside the ampoule little spin a big hole in crystal side, less needle and golden color stay
SA527	Pd_8Se_5	polycrystal, m=0.5735g, flux=1.2700g
SA563	KCo_2Se_2	after heating m=0.898g add K=0.125g then out back into furnace see notebook for more notes

Exploratory growths of P-based compounds

Batch No.	Initial concentration	Comments
KQ584	$(Co_{0.5}CuP)_{10}Sn_{90}$	lump. Little shining cubes. Magnetic
KQ585	$(CoPS)_5Sn_{95}$	rods. Plates+lumps. Non-magn
KQ613	$Nb_5P_5S_4Sn_{50}Sb_{95}$	some chunks seem not melted. Shining cubes and shining plates. Ampoule' s bottom gets a little biowa a glass-like ring form on the connection part of the two crucible

Continued on next page

Table A.22 – continued from previous page

Batch No.	Initial concentration	Comments
KQ619	$Ge_{57}Mo_3Sn_{39}P_1$	plates+cubes form clusters
KQ620	$Ge_{57}Mo_3Sn_{29}P_1$	small plates form clusters
KQ626	$NbPSTe_{19}Sn_8$	quartz tube turns yellow and brown. Little shiny dots, a silver chunks gold-brown color spotted inside.
KQ632	$Mo_3PGe_{57}Sn_{39}$	5ml. Lots of flax dots, few plates
KQ635	NbPS	thin shiny plates
KQ643	$Mo_3PGe_{57}Sn_{39}$	
KQ654	$Mn_{0.9}Ba_{0.1}PS_3$	green transparent plates
KQ655	$Fe_{0.9}Ba_{0.1}PS_3$	shiny black plates
KQ664	$FeP_{0.9}Si_{0.1}S_3$	lots of dark shining hex-plates+ a lump
KQ668	CoPS	a dark sticky lump
KQ678	$(NaPMn)_{10}Sn_{90}$	shining plates, dark red stuff, lumps
KQ695	$(MoP)_3Fe_7Sn_{28}$	total spin. Everything dissolved
KQ696	$(Mo_3P)_6Fe_4Sn_{76}$	needle-like crystals
KQ722	$MoPFe_3Sn_{57}$	needle crystals - very thin crystals in flux
KQ746	$FeP_{0.5}Si_{0.5}S_3$	black thin plates, something not transported
KQ747	$Fe_{0.9}Co_{0.1}PS_3$	much smaller plates, something was not transported

Continued on next page

Table A.22 – continued from previous page

Batch No.	Initial concentration	Comments
SA752	$Sr_{1.3}Ni_2P_{2.3}Sn_{16}$	crystals attached tot the crucible can't measure mass, square plates and long rectangle plates
SA753	$Tb_{1.3}Ni_2P_{2.3}Sn_{16}$	crap. m=0.8432g, something seemed to not melt
SA754	$Sr_{1.2}Fe_2P_2Sn_{20}$	no crystals, crap, m=0.1900g
SA847	$Sr_{7.5}Pt_{72.5}P_{20}$	used SA823 $Pt_{80}P_{20}$ see book No.12 for more notes
SA926	$(SrPPt_3)_7Sn_9$	few plates, but all seem oxidized
SA927	$(SiPPt_3)_7Sn_{93}$	It seems the materials spill out from the crucible, leaving some needle like stuff in the crucible
SA928	$Sr_{10}Pt_{65}P_{25}$	pre-react Pt-P. m=4.1143g
SA936	$(SrPPt_3)_4Sn_{96}$	a chunk, some polycrystalline stuff
SA937	$(SrPPt_3)_7Sn_{93}$	layers of polycrystalline stuff

Exploratory growths of As-based compounds

Batch No.	Initial concentration	Comments
SA662	$Pt_{72}As_{28}$	when break, two pellets formed, loose powder beneath. remelt at 700C, the same. remelt again at 1150C, m=3.7697g
SA682	$Sr_8(Pt_{0.72}As_{0.28})_{92}$	total spin, reseal=3.4558g, 0.3g spin, 3.5g puck

Growths of $SrSn_4$ and $BaSn_5$

Batch No.	Initial concentration	Comments
SA658	$Sr_{3.5}Sn_{96.5}$	good spin, one nice plate m=0.2g, few small plates and goo
SA679	$Sr_{3.5}Sn_{96.5}$	m=0.588g
MC165	$Sr_{3.5}Sn_{96.5}$	
SA693	Ba_8Sn_{92}	quartz, wool, polycrystal, rods, total mass=2.26g

Growths of $R_3Ni_{2-x}Ni_7$

Batch No.	Initial concentration	Comments
SA447	$Ce_{10}Ni_{20}Sn_{80}$	
SA457	$Ce_{10}Ni_{20}Sn_{80}$	shining big plates m=0.6264g, the spin stuck in the crucible cant measure mass
SA462	$Nd_{10}Ni_{20}Sn_{80}$	plates not very clean m=0.3578g spin=3.3596g
SA463	$Sm_{10}Ni_{20}Sn_{80}$	almost total spin
SA466	$Ce_{12}Ni_8Sn_{80}$	lots of cubic crystals m=2.4361g cannot get the spin out
SA474	$Ce_{10}Ni_{10}Sn_{80}$	cubic crystals, m=1.859g
SA475	$Ce_{10}Ni_{15}Sn_{80}$	cubes with plates some are shiny, some are dark grey, m=2.47g
SA476	$Ce_{10}Ni_{25}Sn_{80}$	remelt m=2.88g spin at 750C not much change m=2.7307g
SA477	$Ce_{10}Ni_{20}Sn_{80}$	same as SA478 spin temp is low, cubes and plates stuck in flux, remelt m=2.1739g, spin at 750C bigger better crystals, but still dirty m=1.9254g
SA478	$Sm_{10}Ni_{20}Sn_{80}$	the edge of crucible turns pink, the spin temp is low, plates, rods, cubes, stuck in the flux m=2.17, remelt m=2.1775 spin at 750C still not much spin, crystal m=1.8351g

Continued on next page

Table A.25 – continued from previous page

Batch No.	Initial concentration	Comments
SA494	$Ce_{10}Ni_{25}Sn_{80}$	ugly plates, some attached to the crucible m=0.92g
SA495	$Sm_{10}Ni_{20}Sn_{80}$	ugly crystal like m=0.3156g
SA496	$Pr_{10}Ni_{20}Sn_{80}$	
SA497	$La_{10}Ni_{20}Sn_{80}$	
SA501	$La_{10}Ni_{20}Sn_{80}$	flux floated out from crucible, during spin quartz, tube top, breaks after spin crack sound, big plates facet dirty and oxidized m=0.6066
SA502	$Pr_{10}Ni_{20}Sn_{80}$	small plates ugly stuff chunks m=0.6g
SA522	$Eu_{10}Ni_{25}Sn_{65}$	Eu oxidized before put into growth purple, several yellow dots on the quartz tube, seems attacked, alumina crucible attacked, the inner wall turns yellow and brown, outside has yellow brown outside has yellow spots
SA523	$Gd_{10}Ni_{25}Sn_{65}$	quartz tube looks fine, thick rods m=0.6406g
SA542	$Eu_{10}Ni_{25}Sn_{80}$	thin sharp needles m=0.365g
SA543	$Gd_{10}Ni_{25}Sn_{81}$	inside crucible gets yellow and brown leaf like stuff
SA549	$Ce_{10}Ni_{25}Sn_{65}$	plate stuck into flux m=1.658g

Continued on next page

Table A.25 – continued from previous page

Batch No.	Initial concentration	Comments
SA505	$Sm_{10}Ni_{25}Sn_{65}$	a few dirty plates formed m=0.2992g flux breaks the quartz ampoule
SA565	$Ce_{10}Ni_{30}Sn_{60}$	total spin
SA572	$Ce_{10}Ni_{30}Sn_{60}$	crystal flow to the thin side, mixed with flux chunk, small plates, $Ce_3Ni_2Sn_7$?
SA578	$Gd_{10}Ni_{20}Sn_{80}$	plate, m=0.1668g
SA579	$Tb_{10}Ni_{20}Sn_{80}$	thin needles, m=0.114g
SA592	$La_{10}Ni_{20}Sn_{80}$	
SA593	$Pr_{10}Ni_{20}Sn_{80}$	
SA594	$Sm_{10}Ni_{25}Sn_{65}$	
SA758	$Dy_{10}Ni_{20}Sn_{80}$	long needles attached to the crucibles, do not measure mass
SA759	$Ho_{10}Ni_{20}Sn_{80}$	tiny rods, mass 0.5g
SA807	$Sm_{10}Ni_{25}Sn_{65}$	rods formed plates. m=0.4593g.
SA808	$Tb_{10}Ni_{20}Sn_{90}$	thin rods and some crap. m=0.2474g

Growths of $R\mathbf{Ni}_{1-x}\mathbf{Bi}_{2\pm y}$

Batch No.	**Initial concentration**	**Comments**
MC033	$Ce_{14}Ni_{14}Bi_{72}$	big shiny plates, m=2.57g, growth crucible cracked
MC034	$Ce_{14}Ni_{10}Bi_{72}$	big shiny plates, m=2.17g
MC035	$Ce_{14}Ni_{7}Bi_{72}$	even bigger plates, m=2.44g
MC080	$Ce_{10}Ni_{14}Bi_{72}$	bottom crucible cracked, big plates, m=1.377g
MC081	$Ce_{7}Ni_{14}Bi_{72}$	big plates, m=1.298g
MC233	$Nd_{7}Ni_{7}Bi_{86}$	big shiny plates
MC234	$Gd_{7}Ni_{7}Bi_{86}$	almost total spin, some 3d stuff left
MC235	$Yb_{14}Ni_{14}Bi_{72}$	almost total spin, several thin irregular plates left.
MC261	$Gd_{14}Ni_{14}Bi_{72}$	thermite reaction, crucible has a hole, materials came out.
MC262	$Ho_{14}Ni_{14}Bi_{72}$	tiny plates
MC263	$Tb_{14}Ni_{14}Bi_{72}$	crucible cracks, but nothing got out. Tiny crystals
MC264	$Yb_{20}Ni_{20}Bi_{60}$	big nice plates
MC272	$Gd_{14}Ni_{7}Bi_{72}$	
MC273	$Gd_{14}Ni_{14}Bi_{72}$	
MC274	$Gd_{4.5}Ni_{9.1}Bi_{86.4}$	small plates

Continued on next page

Table A.26 – continued from previous page

Batch No.	Initial concentration	Comments
MC325	$Tb_{4.5}Ni_{9.1}Bi_{86.4}$	small plates
MC326	$Dy_{4.5}Ni_{9.1}Bi_{86.4}$	small plates
MC332	$Ho_{4.5}Ni_{9.1}Bi_{86.4}$	nothing
MC333	$Er_{4.5}Ni_{9.1}Bi_{86.4}$	nothing
MC349	$HoNiBi_{72}$	failed
MC405	$Yb_{4.5}Ni_{9.1}Bi_{86.4}$	
MC416	$YbNiBi_{72}$	arc melting
MC454	$La_{10}Ni_{14}Bi_{72}$	big plates
MC455	$Pr_{10}Ni_{14}Bi_{72}$	big plates
MC462	$Eu_{10}Ni_{14}Bi_{72}$	crucible cracks, very small polycrystalline stuff.
MC465	$Eu_{4.5}Ni_{9.1}Bi_{86.8}$	total spin

Growths of $La(V_xCr_{1-x})Ge_3$

Batch No.	Initial concentration	Comments
MC519	$La_{13}V_9Ge_{78}$	much worse than MC520, even thinner and shorter rods, polycrystals

Continued on next page

Table A.27 – continued from previous page

Batch No.	Initial concentration	Comments
MC520	$La_{15}V_{10}Ge_{75}$	some long rods, most are short rods, clusters, polycrystals
MC524	$La_{17}V_{11}Ge_{72}$	P.A.M. = 4.4908g, loss about 0.05 %, heavily inter-grown plates, thin needles and dentritics and polycrystals.
MC525	$La_{14}V_{14}Ge_{72}$	polycrystals in the shape of arc-melted puck, as if not melt. But there is spin.
MC534	$La_{15}V_{10}Ge_{75}$	almost total spin, a small lump stuck in the spin side stuffed with rods, plates and polycrystals
MC535	$La_{15}(V_{.9}Cr_{.1})_{10}Ge_{76}$	polycrystal chunk and lots of very thin crystals
MC536	$La_{15}(V_{.8}Cr_{.2})_{10}Ge_{75}$	polycrystals, chunk of lots of very thin needles
MC543	$La_{15}V_{10}Ge_{75}$	flux flew out of crucible while spun, ampoule cracked
MC544	$La_{15}V_{10}Ge_{75}$	a chunk left in the catch side, rods and polycrystal chunk, looks like MC534, the chunk is crumbled with serveral pieces, as if the materials never completely melted.
MC552	$La_{15}V_{10}Ge_{75}$	after spin, growth = 0.588g
MC559	$La_{15}Cr_{10}Ge_{75}$	a nest of dirty rods with small shiny dots

Continued on next page

Table A.27 – continued from previous page

Batch No.	Initial concentration	Comments
MC560	$Cr_{13}La_{13}Ge_{74}$	a larger nest of dirty rods with little trigonals inside.
MC572	$Cr_{13}La_{13}Ge_{74}$	P.A.M. = 3.7302g, loss 0.2%
MC579	$La_{13}(V_{.9}Cr_{.1})_{13}Ge_{74}$	loss 0.1%
MC580	$La_{13}(V_{.8}Cr_{.2})_{13}Ge_{74}$	loss 0.1%
MC604	$(LaCrGe_3)_2Sb_{90}$	total spin
MC605	$(LaCrGe_3)_3Sb_{85}$	long rectangles glued together
MC611	$(LaCrGe_3)_2Bi_{90}$	almost total spin, plates, trigonals, something didn't melt.
MC612	$(LaCrGe_3)_3Bi_{85}$	plates and trigonals, looks like something did not melt
MC613	$La_{11}Cr_{11}Ge_{89}$	reseal at 850C, total spin, go lower.P.A.M = 4.0345g, loss 0.2%
MC614	$La_{13}Cr_{15}Ge_{85}$	P.A.M. = 4.9112g, loss 0.3%
MC618	$La_{15}Cr_{15}Ge_{85}$	rods and plycrystals
MC619	$La_8Cr_{15}Ge_{85}$	triangles and plates
MC646	$La_{13}V_{1.8}Cr_{10.4}Ge_{74.8}$	P.A.M. = 3.3464g, rods, looks similar to MC634, but thinner
MC647	$La_{13}V_{4.5}Cr_{6.5}Ge_{76}$	P.A.M. = 3.3895g, rods and plycrystals
MC658	$La_{13.6}V_3Cr_{9.1}Ge_{74.3}$	P.A.M. = 3.4437g, strange thin rods

Continued on next page

Table A.27 – continued from previous page

Batch No.	Initial concentration	Comments
MC659	$La_{13.8}V_3Cr_{7.8}Ge_{74.4}$	P.A.M. = 3.4272g, rods grown out of polycrystal chunk
MC660	$La_{14}V_5Cr_{6.5}Ge_{74.6}$	P.A.M. = 3.4488g, rods grown out of polycrystal chunk
MC661	$La_{14.2}V_6Cr_{5.2}Ge_{74.6}$	P.A.M. = 3.4156g, rods grown out of polycrystal chunk
MC674	$La_{14.6}V_7Cr_{3.9}Ge_{74.7}$	P.A.M. = 3.4128g, thin rods and plycrystals
MC675	$La_{14.8}V_8Cr_{2.6}Ge_{74.8}$	P.A.M. = 3.3557g, thin rods and plycrystals
MC676	$La_{14.8}V_9Cr_{1.3}Ge_{74.9}$	few rods, mostly polycrystals
MC681	$La_{13}(V_{.7}Cr_{.3})_{13}Ge_{74}$	P.A.M. = 3.3074g
MC682	$La_{13}(V_{.8}Cr_{.2})_{13}Ge_{74}$	P.A.M. = 3.4447g
MC683	$La_{13}(V_{.9}Cr_{.1})_{13}Ge_{74}$	P.A.M. = 3.4049g
MC684	$La_{13}V_{13}Ge_{74}$	P.A.M. = 3.3634g
MC702	$La_{15}V_{10}Ge_{75}$	polycrystals
MC703	$La_{14.4}V_7Cr_{3.9}Ge_{74.7}$	rods and plycrystals
MC719	$La_{14.3}V_{6.5}Cr_{4.5}Ge_{74.7}$	P.A.M. = 3.4864g, polycrystals, seems not completely melt
MC720	$La_{14.3}V_{7.5}Cr_{3.2}Ge_{74.7}$	P.A.M. = 3.3829g, polycrystals, seems not completely melt
MC754	$LaV_{0.9}Cr_{0.1}Ge_3$	P.A.M. = 0.9402g, loss 0.2%
MC755	$LaV_{0.8}Cr_{0.2}Ge_3$	P.A.M. = 0.9151g, loss 1.0%

Continued on next page

Table A.27 – continued from previous page

Batch No.	Initial concentration	Comments
MC756	$LaV_{0.7}Cr_{0.3}Ge_3$	P.A.M. = 0.9184g, loss 0.2%
MC757	$LaV_{0.6}Cr_{0.4}Ge_3$	P.A.M. = 0. 9662g, loss 0.7%
MC758	$LaV_{0.5}Cr_{0.5}Ge_3$	P.A.M. = 0.9407g, loss 0.6%
MC760	$La_4V_4Ge_{92}$	almost total spin, several long rods, and a nest of small rods
MC765	$La_{14.7}V_7Cr_{3.9}Ge_{74.7}$	Arc-melt $V_7Cr_{3.9}$, Cr=0.5938g, V=1.0439g. P.A.M. = 1.6053g, 0.2%, rods and polycrystals
MC766	$La_6V_3Cr_3Ge_{92}$	ampoule cracks, did not spin well, most stuff did not go to the spin, but outside made quartz cracked. several big rods, heavily oxidized.
MC779	$La_6(V_7Cr_{3.9})_{0.5}Ge_{92}$	lots of thin rods
MC780	$La_6V_3Cr_3Ge_{92}$	2 big rods, turn to be $V_{11}Ge_8$
MC781	$(La_{.2}Cr_{.2}Ge_{.6})_5Sn_{95}$	total spin
MC782	$(La_{.2}V_{.2}Ge_{.6})_5Sn_{95}$	total spin
MC787	$LaVGe_3$	no cracks on crucible. Sample material all melt. Pellet = 1.1426g
MC788	$LaCrGe_3$	Crucible cracked inside puck looks homogeneous. Pellet = 1.0651g

Continued on next page

Table A.27 – continued from previous page

Batch No.	Initial concentration	Comments
MC789	$La_{10.9}V_7Cr_{3.9}Ge_{32.7}$	Crucible cracked (reacted) inside puck looks homogeneous. Pellet = 1.1097g
MC795	$LaV_{.3}Cr_{.7}Ge_3$	
MC796	$LaV_{.4}Cr_{.6}Ge_3$	
MC837	$LaV_{.4}Cr_{.8}Ge_3$	P.A.M. = 0.9373g
MC838	$LaV_{.3}Cr_{.7}Ge_3$	P.A.M. = 0.9562g
MC844	$LaV_{.1}Cr_{.9}Ge_3$	P.A.M. = 0.9489g
MC893	$LaV_{.55}Cr_{.45}Ge_3$	P.A.M. = 1.1836g

Growths of $La(V_xCr_{1-x})Sb_3$

Batch No.	Initial concentration	Comments
MC545	$La_{10}Cr_{20}Sb_{70}$	a chunk of plates left in catch side. very thin and small plates compared to $LaVSb_3$.
MC586	$La_8Cr_8Sb_{84}$	several big thick plates and rods
MC587	$La_8V_4Cr_4Sb_{84}$	one big plate with several small ones. The big one looks like several wide plates glued together
MC588	$La_8V_6Cr_2Sb_{84}$	one big, thick, plate. With several rods
MC589	$La_8V_2Cr_6Sb_{84}$	total spin

Continued on next page

Table A.28 – continued from previous page

Batch No.	Initial concentration	Comments
MC594b	$La_{20}Cr_{15}Sb_{65}$	chunks of crystals (plates) stuck inside crucibles, the spin temperature seems not high enough.
MC595	$La_{15}Cr_{25}Sb_{60}$	La attacks crucible, leaked out, nothing left.
MC596	$La_8V_2Cr_6Sb_{84}$	flat plates, long rectangles, needles
MC597	$La_8V_3Cr_5Sb_{84}$	stronger and wider and thicker plates, some fell into catch side.
MC598	$La_8V_1Cr_7Sb_{84}$	long plates, some are narrower, some are wider, some malleable plates, maybe different phase.
MC797	$La_8V_{3.5}Cr_{4.5}Sb_{84}$	thick rectangle plates
MC798	$La_8V_{2.5}Cr_{5.5}Sb_{84}$	thick rectangle plates
MC799	$La_8V_{.75}Cr_{7.25}Sb_{84}$	thick rectangle plates, malleable thin bigger plates
MC800	$La_8V_{.5}Cr_{7.5}Sb_{84}$	thick rectangle plates
MC801	$La_8V_{.25}Cr_{7.75}Sb_{84}$	thick rectangle plates
MC802	$La_8Cr_8Sb_{84}$	thick rectangle plates, rod-like-rectangle-plates
MC865	$La_8V_1Cr_7Sb_{84}$	thick rectangle plates
MC866	$La_8V_2Cr_6Sb_{84}$	thick rectangle plates

BIBLIOGRAPHY

Abe, K., Kitagawa, J., Takeda, N., and Ishikawa, M. (1999). Evidence for strong quadrupolar pair interactions in rare-earth palladium bronzes RPd_3S_4. *Phys. Rev. Lett.*, 83(25):5366–5369.

Abrikosov, A. (1957). On the Magnetic Properties of Superconductors of the Second Group. *Zh. Eksp. Teor. Fiz.*, 32:1442.

Alireza, P. L., Barakat, S., Cumberlidge, A. M., Lonzarich, G., Nakamura, F., and Maeno, Y. (2007). Developments on Susceptibility and Magnetization Measurements under High Hydrostatic Pressure. *J. Phys. Soc. Jpn.*, 76:216.

Ancona-Torres, C., Silevitch, D. M., Aeppli, G., and Rosenbaum, T. F. (2008). Quantum and Classical Glass Transitions in $LiHo_xY_{1-x}F_4$. *Phys. Rev. Lett.*, 101:057201.

Arrott, A. (1957). Criterion for Ferromagnetism from Observations of Magnetic Isotherms. *Phys. Rev.*, 108:1394–1396.

Arrott, A. and Noakes, J. E. (1967). Approximate Equation of State For Nickel Near its Critical Temperature. *Phys. Rev. Lett.*, 19:786–789.

Ashcroft, N. and Mermin, N. (1976). *Solid state physics*. Saunders College, Philadelphia.

Balicas, L., Nakatsuji, S., Lee, H., Schlottmann, P., Murphy, T. P., and Fisk, Z. (2005). Magnetic field-tuned quantum critical point in $CeAuSb_2$. *Phys. Rev. B*, 72:064422.

Baranov, A. I., Olenev, A. V., and Popovkin, B. A. (2001). Crystal and electronic structure of $Ni_3Bi_2S_2$ (parkerite). *Russ. Chem. Bull.*, 50(3):353–358.

Bardeen, J., Cooper, L. N., and Schrieffer, J. R. (1957). Theory of Superconductivity. *Phys. Rev.*, 108:1175–1204.

Bie, H. and Mar, A. (2009). Structure and magnetic properties of hexagonal perovskite-type rare-earth vanadium germanides $REVGe_3$ (RE = La-Nd). *J. Mater. Chem.*, 19(34):6225–6230.

Bie, H., Moore, D., Piercey, D. G., Tkachuk, A. V., Zelinska, O. Y., and Mar, A. (2007). Ternary rare-earth titanium antimonides: Phase equilibria in the RE-Ti-Sb (RE = La, Er) systems and crystal structures of $RE_2Ti_7Sb_{12}$ (RE = La, Ce, Pr, Nd) and $RETi_3(Sn_xSb_{1-x})_4$ (RE = Nd, S). *J. Solid State Chem.*, 180(8):2216–2224.

Booth, C. H., Jiang, Y., Wang, D. L., Mitchell, J. N., Tobash, P. H., Bauer, E. D., Wall, M. A., Allen, P. G., Sokaras, D., Nordlund, D., Weng, T.-C., Torrez, M. A., and Sarrao, J. L. (2012). Multiconfigurational nature of 5f orbitals in uranium and plutonium intermetallics. *Proc. Natl. Acad. Sci. U. S. A.*, 109(26):10205–10209.

Brandt, N. B. and Ginzburg, N. I. (1965). Effect of high pressure on the superconducting properties of metals. *Usp. Fiz. Nauk*, 85:485.

Brice, J. C. (1973). *The growth of crystals from liquids.* Elsevier.

Brice, J. C. (1986). *Crystal growth processes.* Halsted Press.

Brylak, M. and Jeitschko, W. (1995). Ternary Antimonides $LnTSb_3$ with Ln=La – Nd, Sm and T=V, Cr. *Z. Naturforsch. B (Chem. Sci)*, 50:899.

Bud'ko, S. L. and Canfield, P. C. (2000). Rotational tuning of H_{c2} anomalies in $ErNi_2B_2C$: Angular-dependent superzone gap formation and its effect on the superconducting ground state. *Phys. Rev. B.*, 61(22):14932–14935.

Bud'ko, S. L., Canfield, P. C., Mielke, C. H., and Lacerda, A. H. (1998). Anisotropic magnetic properties of light rare-earth diantimonides. *Phys. Rev. B*, 57(21):13624–13638.

Bud'ko, S. L., Islam, Z., Wiener, T. A., Fisher, I. R., Lacerda, A. H., and Canfield, P. C. (1999). Anisotropy and metamagnetism in the RNi_2Ge_2 (R = Y, La – Nd, Sm – Lu) series. *J. Magn. Magn. Mater.*, 205(1):53–78.

Bud'ko, S. L., Morosan, E., and Canfield, P. C. (2004). Magnetic field induced non-Fermi-liquid behavior in YbAgGe single crystals. *Phys. Rev. B*, 69:014415.

Bud'ko, S. L., Morosan, E., and Canfield, P. C. (2005). Anisotropic Hall effect in single-crystal heavy-fermion YbAgGe. *Phys. Rev. B.*, 71(5):054408.

Buschow, K. H. J.and Wohlfarth, E. P., editor (1990). *Ferromagnetic Materials A handbook on the properties of magnetically ordered substances*, volume 5. Elsevier, New York.

Cadogan, J. M., Lemoine, P., Slater, B. R., Mar, A., and Avdeev, M. (2013). Neutron diffraction study of the hexagonal perovskite-type compound $LaCrGe_3$. *Solid State Phenom.*, 194:71–74.

Canfield, P. C. (2010). *Solution growth of intermetallic single crystals: a beginner's guide*, volume 2 of *Book Series on Complex Metallic Alloys*, chapter 2, pages 93–111. World Scientific.

Canfield, P. C. (2011). Still alluring and hard to predict at 100. *Nature Mater.*, 10(4):259–261.

Canfield, P. C. and Bud'ko, S. L. (2005). Materials Science: Low-Temperature Superconductivity is Warming Up. *Sci. Am.*, 292:80.

Canfield, P. C., Budko, S. L., Cho, B. K., Lacerda, A., Farrell, D., Johnston-Halperin, E., Kalatsky, V. A., and Pokrovsky, V. L. (1997). Angular dependence of metamagnetic transitions in $HoNi_2B_2C$. *Phys. Rev. B.*, 55(2):970–976.

Canfield, P. C., Caudle, M. L., Ho, C.-S., Kreyssig, A., Nandi, S., Kim, M. G., Lin, X., Kracher, A., Dennis, K. W., McCallum, R. W., and Goldman, A. I. (2010). Solution growth of a binary icosahedral quasicrystal of $Sc_{12}Zn_{88}$. *Phys. Rev. B*, 81:020201.

Canfield, P. C. and Fisher, I. R. (2001). High-temperature solution growth of intermetallic single crystals and quasicrystals. *J. Cryst. Growth*, 225(2-4):155–161.

Canfield, P. C. and Fisk, Z. (1992). Growth of single crystals from metallic fluxes. *Philos. Mag. B*, 65(6):1117–1123.

Carbotte, J. P. (1990). Properties of boson-exchange superconductors. *Rev. Mod. Phys.*, 62:1027–1157.

Carlini, R., Artini, C., Borzone, G., Masini, R., Zanicchi, G., and Costa, G. A. (2011). Synthesis and characterisation of the compound CoSbS. *J. Therm. Anal. Calorim.*, 103(1):23–27.

Chevalier, B., Durivault, L., Fernandez, J. R., Sal, J. C. G., Barandiaran, J. M., and Etourneau, J. (2001). Magnetoresistance behaviour of the ternary stannides $CeNi_{0.86}Sn_2$ and $Ce_3Ni_2Sn_7$. *J. Alloys Compd.*, 323:435–439.

Chevalier, B. and Etourneau, J. (1999). Antiferromagnetic properties of the intermetallics $Ce_3Ni_2X_7$ (X = Ge or Sn). *J. Mater. Chem.*, 9(8):1789–1792.

Choi, H. C., Shim, J. H., Kwon, S. K., and Min, B. I. (2007). Electronic structures and magnetic properties of layered compound $RCrSb_3$ (R = La, Yb). *J. Appl. Phys.*, 101:09G513.

Colombier, E., Knebel, G., Salce, B., Mun, E. D., Lin, X., Bud'ko, S. L., and Canfield, P. C. (2011). Phase diagram of $CeVSb_3$ under pressure and its dependence on pressure conditions. *Phys. Rev. B*, 84:064442.

Cooper, L. N. (1956). Bound Electron Pairs in a Degenerate Fermi Gas. *Phys. Rev.*, 104:1189–1190.

Crerar, S. J., Mar, A., and Grosvenor, A. P. (2012). Electronic structure of rare-earth chromium antimonides $RECrSb_3$ (RE = La – Nd, Sm, Gd – Dy, Yb) by X-ray photoelectron spectroscopy. *J. Solid State Chem.*, 196(0):79–86.

De Gennes, P. G. (1962). Interactions indirectes entre couches 4f dans les métaux de terres rares. *J. Phys. Radium.*, 23:510.

du Tremolet de Lacheisserie, E. (2005). *Magnetism: Fundamentals*. Springer, Boston.

Dubenko, I. S., Hill, P., and Ali, N. (2001). Magnetic properties of $LaCr_{1-x}M_xSb_3$ (M = V, Mn, Fe, Cu, and Al). *J. Appl. Phys.*, 89:7326.

Eiling, A. and Schilling, J. S. (1981). Pressure and temperature dependence of electrical resistivity of Pb and Sn from 1 – 300k and 0 – 10 GPa – use as continuous resistive pressure monitor accurate over wide temperature range; superconductivity under pressure in Pb, Sn and In. *J. Phys. F: Metal Phys.*, 11:623.

Elliott, R. J. (1972). *Magnetic properties of rare earth metals*. Plenum Press, London, New York.

Fassler, T. F. and Hoffmann, S. (2000). $SrSn_3$ – eine supraleitende Legierung mit freien Elektronenpaaren. *Z. Anorg. Allg. Chem.*, 626:106.

Fassler, T. F., Hoffmann, S., and Kronseder, C. (2001). Novel Tin Structure Motives in Superconducting $BaSn_5$ – The Role of Lone Pairs in Intermetallic Compounds [1]. *Z. Anorg. Allg. Chem.*, 627:2486.

Fassler, T. F. and Kronseder, C. (1997). $BaSn_3$: A Superconductor at the Border of Zintl Phases and Intermetallic Compounds. Real-Space Analysis of Band Structures. *Angew. Chem. Int. Edn Engl.*, 36:2683.

Fay, D. and Appel, J. (1980). Coexistence of p-state superconductivity and itinerant ferromagnetism. *Phys. Rev. B*, 22:3173–3182.

Finnemore, D. K. (1992). *A Child's Guide to BCS*. Nova Science Publishers, New York.

Fisher, I. R., Wiener, T. A., Bud'ko, S. L., Canfield, P. C., Chan, J. Y., and Kauzlarich, S. M. (1999). Thermodynamic and transport properties of single-crystal $Yb_{14}MnSb_{11}$. *Phys. Rev. B*, 59(21):13829–13834.

Fisher, M. E. (1962). Relation between the specific heat and susceptibility of an antiferromagnet. *Philos. Mag.*, 7:1731.

Fisk, Z. and Remeika, J. P. (1989). *Handbook on the Physics and Chemistry of Rare Earths*, volume 12. Amsterdam.

Fröhlich, H. (1954). On the Theory of Superconductivity: The One-Dimensional Case. *Proc. Roy. Soc. A*, 223(1154):296–305.

Fujimori, Y., Kan, S., Shinozaki, B., and Kawaguti, T. (2000). Superconducting and Normal State Properties of $NiBi_3$. *J. Phys. Soc. Jpn.*, 69(9):3017–3026.

Gambino, R. J., Stemple, N. R., and Toxen, A. M. (1968). Superconductivity of lanthanum in intermetallic compounds with Cu_3Au structure. *J. Phys. Chem. Solids*, 29(2):295.

Gingras, M. J. P. and Henelius, P. (2011). Collective Phenomena in the $LiHo_xY_{1-x}F_4$ Quantum Ising Magnet: Recent Progress and Open Questions. *J PHYS: Conference Series*, 320(1):012001.

Ginzburg, V. and Landau, L. (1950). To the Theory of Superonductivity. *Zh. Eksp. Teor. Fiz.*, 20:1064.

Goldman, A. I., Kong, T., Kreyssig, A., Jesche, A., Ramazanoglu, M., Dennis, K. W., Budko, S. L., and Canfield, P. C. (2013). A family of binary magnetic icosahedral quasicrystals based on rare earths and cadmium. *Nat. Phys.*, 12:714718.

Goldschmidt, V. M. (1926). *Die Naturwissenschaften*, 21:477.

Gottfried, K. (1966). *Quantum Mechanics: Fundamentals*, volume 1. W. A. Benjamin, Menlo Park, California.

Granado, E., Martinho, H., Sercheli, M. S., Pagliuso, P. G., Jackson, D. D., Torelli, M., Lynn, J. W., Rettori, C., Fisk, Z., and Oseroff, S. B. (2002). Unconventional Metallic Magnetism in $LaCrSb_3$. *Phys. Rev. Lett.*, 89:107204.

Gschneidner, K. A. and Eyring, L., editors (1978-). *Handbook on the Physics and Chemistry of Rare Earths series*. Elsevier, Amsterdam.

Hartjes, K., Jeitschko, W., and Brylak, M. (1997). Magnetic properties of the rare-earth transition metal antimonides $LnVSb_3$ and $LnCrSb_3$ (ln = la – d, sm). *J. Magn. Magn. Mater.*, 173(1):109–116.

Henry, R., Steger, J., Nahigian, H., and Wold, A. (1975). High-pressure synthesis and properties of coxy compounds (X = P, As, Sb, Y = S, Se). *Inorg. Chem.*, 14(12):2915–2917.

Hertz, J. A. (1976). Quantum critical phenomena. *Phys. Rev. B*, 14:1165–1184.

Hiess, A., Boucherle, J. X., Givord, F., and Canfield, P. C. (1995). Magnetic-susceptibility and magnetization measurements of an $YbAl_3$ single-crystal for ground-state investigation. *J. Alloys Compd.*, 224(1):33–35.

Hilscher, G. (1982). Onset of magnetism in concentrated ternary alloys I. *J. Magn. Magn. Mater.*, 25(3):229–250.

Hoffmann, S. and Fassler, T. F. (2003). $SrSn_4$: A Superconducting Stannide with Localized and Delocalized Bond Character. *Inorganic Chemistry*, 42(26):8748–8754.

Hosono, H. (2008). Layered Iron Pnictide Superconductors: Discovery and Current Status. *J. Phys. Soc. Jpn.*, 77SC(Supplement C):1–8.

Howard, C. J. and Hunter, B. A. (1998). A Computer Program for Rietveld Analysis of X-Ray and Neutron Powder Diffraction Patterns. NSW, Australia: Lucas Heights Research Laboratories.

Huber, J. G., Maple, M. B., Wohlleben, D., and Knapp, G. S. (1975). Magnetic properties of $ZrZn_2$ under pressure. *Solid State Comm.*, 16(2):211–216.

Huxley, A., Sheikin, I., Ressouche, E., Kernavanois, N., Braithwaite, D., Calemczuk, R., and Flouquet, J. (2001). UGe_2: A ferromagnetic spin-triplet superconductor. *Phys. Rev. B*, 63:144519.

Huy, N. T., Gasparini, A. de Nijs, D. E., Huang, Y., Klaasse, J. C. P., Gortenmulder, T., de Visser, A., Hamann, A., Görlach, T., and Löhneysen, H. V. (2007). Superconductivity on the Border of Weak Itinerant Ferromagnetism in UCoGe. *Phys. Rev. Lett.*, 99:067006.

Jackson, D. D., Torelli, M., and Fisk, Z. (2001). Anisotropy in magnetic and transport properties of $LaTSb_3$ (T = Cr, V). *Phys. Rev. B*, 65:014421.

Jia, S., Bud'ko, S. L., Samolyuk, G. D., and Canfield, P. C. (2007). Nearly ferromagnetic Fermi-liquid behaviour in YFe_2Zn_{20} and high-temperature ferromagnetism of $GdFe_2Zn_{20}$. *Nat. Phys.*, 3(5):334–338.

Jia, S., Ni, N., Samolyuk, G. D., Safa-Sefat, A., Dennis, K., Ko, H., Miller, G. J., Bud'ko, S. L., and Canfield, P. C. (2008). Variation of the magnetic ordering in GdT_2Zn_{20} (T = Fe, Ru, Os, Co, Rh and Ir) and its correlation with the electronic structure of isostructural YT_2Zn_{20}. *Phys. Rev. B*, 77:104408.

Jung, M. H., Lacerda, A. H., and Takabatake, T. (2002). Magnetic and transport properties of the antiferromagnetic Kondo-lattice compound $CeNiBi_2$. *Phys. Rev. B*, 65:132405.

Junod, A., Wand, K. Q., Triscone, G., and Lamarche, G. (1995). Specific-heat, magnetic-properties and critical-behavior of Mn_2SiS_4 and Fe_2GeS_4. *J. M*, 146(1-2):21–29.

Kittel, C. (2005). *Introduction to Solid State Physics*. John Wiley & Sons, 8th edition.

Kodama, K., Wakimoto, S., Igawa, N., Shamoto, S., Mizoguchi, H., and Hosono, H. (2011). Crystal and magnetic structures of the superconductor $CeNi_{0.8}Bi_2$. *Phys. Rev. B*, 83:214512.

Kwok, W., Crabtree, G., Bud'ko, S. L., and Canfield, P. C. (2003). Superconductivity in MgB_2: Electrons, Phonons and Vortices. *(eds.), Physica C*, 385.

Leonard, M., Saha, S., and Ali, N. (1999). Magnetic properties of $RTSb_3$. *J. Appl. Phys.*, 85:4759.

Leonard, M. L., Dubenko, I. S., and Ali, N. (2000). Investigation of the ferromagnetism in $RCrSb_3$ (R = La, Ce, Pr, Nd). *J. Alloys Compd.*, 303-04(0):265–269.

Lin, X. Jesche, A., Bud'ko, S. L., and Canfield, P. C. (2012a). Corrigendum: Physical properties of single crystalline $BaSn_5$. *Philos. Mag.*, 92:3006.

Lin, X., Bud'ko, S. L., and Canfield, P. C. (2012b). Development of viable solutions for the synthesis of sulfur bearing single crystals. *Phil. Mag.*, 92:2436.

Lin, X., Bud'ko, S. L., and Canfield, P. C. (2012c). Physical properties of single crystalline $BaSn_5$. *Phil. Mag.*, 92:3006.

Lin, X., Bud'ko, S. L., Samolyuk, G. D., Torikachvili, M. S., and Canfield, P. C. (2011). Physical properties of $SrSn_4$ single crystals. *J. Phys.: Condens. Matter*, 23:455703.

Lin, X., Bud'ko, S. L., Thimmaiah, S., and Canfield, P. C. (2013a). Anisotropic magnetization, resistivity and heat capacity of single crystalline $R_3Ni_{2-x}Sn_7$ (R = La, Ce, Pr and Nd). *J. Magn. Magn. Mater.*, 331:53–61.

Lin, X., Straszheim, W. E., Bud'ko, S. L., and Canfield, P. C. (2013b). Anisotropic magnetization and resistivity of single crystalline $RNi_{1-x}Bi_{2y}$ (R = La, Ce-Nd, Sm, Gd-Dy). *J. Alloys Compd.*, 554:304.

Lin, X., Taufour, V., Bud'ko, S. L., and Canfield, P. C. (2013c). Suppression of ferromagnetism in the $LaV_xCr_{1-x}Ge_3$ system. *Phys. Rev. B*, 88:094405.

Lonzarich, G. G. (1986). The magnetic equation of state and heat-capacity in weak itinerant ferromagnets. *J. Magn. Magn. Mater.*, 54-7(2):612–616.

Lonzarich, G. G. (1988). Magnetic oscillations and the quasiparticle bands of heavy electron-systems. *J. Magn. Magn. Mater.*, 76-7:1–10.

Lu, Y., Liang, Y., Yang, X., Chen, H., and Zhao, J. (2005). *Chin. J. Struct. Chem.*, 24:769.

MacFarlane, W. A., Chow, K., Salman, Z., Tkachuk, A., and Mar, A. (2006). A μ SR study of the unusual magnetism of $LaCrSb_3$. *Physica B: Condensed Matter*, 374-375(0):71–74.

Massalski, T. B. (1990). *Binary Alloy Phase Diagrams*. ASM International, New York, 2nd edition.

Matar, S. F., Chevalier, B., Isnard, O., and Etourneau, J. (2003). Electronic band structure calculations on the antiferromagnetic ternary compounds $Ce_3Ni_2X_7$ (X = Ge and Sn) and $CeNiGe_3$. *J. Mater. Chem.*, 13(4):916–920.

Meissner, W. and Ochsenfeld, R. (1933). Ein neuer Effekt bei Eintritt der Supraleitfhigkeit. *Naturwissenschaften*, 21:787–788.

Millis, A. J. (1993). Effect of a nonzero temperature on quantum critical points in itinerant fermion systems. *Phys. Rev. B*, 48:7183–7196.

Miyake, K., Schmitt-Rink, S., and Varma, C. M. (1986). Spin-fluctuation-mediated even-parity pairing in heavy-fermion superconductors. *Phys. Rev. B*, 34:6554–6556.

Mizoguchi, H., Kamiya, T., and Hosono, H. (2012). Superconducting compounds with metallic square net. *Solid State Comm.*, 152(8):666–670.

Mizoguchi, H., Matsuishi, S., Hirano, M., Tachibana, M., Takayama-Muromachi, E., Kawaji, H., and Hosono, H. (2011). Coexistence of Light and Heavy Carriers Associated with Superconductivity and Antiferromagnetism in $CeNi_{0.8}Bi_2$ with a Bi Square Net. *Phys. Rev. Lett.*, 106:057002.

Moos, E. and Shuppe, G. N. (1979). *Izv. AN SSSR, Ser. Fizicheskaya*, 43:1843.

Moriya, T. and Takimoto, T. (1995). Anomalous Properties around Magnetic Instability in Heavy Electron Systems. *J. Phys. Soc. Jpn.*, 64(3):960–969.

Mun, E. D., Bud'ko, S. L., Ko, H., Miller, G. J., and Canfield, P. C. (2010). Physical properties and anisotropies of the $RNiGe_3$ series (R = Y, Ce – Nd, Sm, Gd – Lu). *J. Magn. Magn. Mater.*, 322(21):3527–3543.

Mun, E. D., Bud'ko, S. L., Martin, C., Kim, H., Tanatar, M. A., Park, J.-H., Murphy, T., Schmiedeshoff, G. M., Dilley, N., Prozorov, R., and Canfield, P. C. (2013). Magnetic-

field-tuned quantum criticality of the heavy-fermion system YbPtBi. *Phys. Rev. B*, 87:075120.

Murata, K., Yokogawa, K., Yoshino, H., Klotz, S., Munsch, P., Irizawa, A., Nishiyama, M., Iizuka, K., Nanba, T., Okada, T. Yoshitaka Shiraga, ., and Aoyama4, S. (2008). Pressure transmitting medium Daphne 7474 solidifying at 3.7 GPa at room temperature. *Rev. Sci. Instrum.*, 79(8):085101.

Mydosh, J. A. (1993). *Spin Glasses: An Experimental Introduction.* Taylor & Francis, London.

Myers, K. D., Bud'ko, S. L., Fisher, I. R., Islam, Z., Kleinke, H., Lacerda, A. H., and Canfield, P. C. (1999). Systematic study of anisotropic transport and magnetic properties of $RAgSb_2$ (R = Y, La – Nd, Sm, Gd – Tm). *J. Magn. Magn. Mater.*, 205(1):27–52.

Nagamatsu, J., Nakagawa, N., Muranaka, T., Zenitani, Y., and Akimitsu, J. (2001). Superconductivity at 39 K in magnesium diboride. *Nature*, 410:63–64.

Natarajan, S., Rao, G. V. S., Baskaran, R., and Radharishnan, T. S. (1988). Synthesis and electrical-properties of Shandite-Parkerite phase, $A_2M_3CH_2$. *J. Less-Common Met.*, 138(2):215–224.

Ni, N., Bud'ko, S. L., Kreyssig, A., Nandi, S., Rustan, G. E., Goldman, A. I., Gupta, S., Corbett, J. D., Kracher, A., and Canfield, P. C. (2008a). Anisotropic thermodynamic and transport properties of single-crystalline $(Ba_{1-x}K_x)Fe_2As_2$ (x = 0 and 0.45). *Phys. Rev. B.*, 78:014507.

Ni, N., Nandi, S., Kreyssig, A., Goldman, A. I., Mun, E. D., Bud'ko, S. L., and Canfield, P. C. (2008b). First-order structural phase transition in $CaFe_2As_2$. *Phys. Rev. B*, 78:014523.

Ni, N., Tillman, M. E., Yan, J.-Q., Kracher, A., Hannahs, S. T., Bud'ko, S. L., and Canfield, P. C. (2008c). Effects of Co substitution on thermodynamic and transport properties and anisotropic H_{c2} in $Ba(Fe_{1-x}Co_x)_2As_2$ single crystals. *Phys. Rev. B*, 78:214515.

Noakes, D. K. and Shenoy, G. K. (1982). The effect of a crystalline electric field on the magnetic transition temperatures of rare-earth rhodium borides. *Phys. Lett. A*, 91(1):35–36.

Onnes, H. K. (1911). The resistance of pure mercury at helium temperatures. *Commun. Phys. Lab. Univ. Leiden*, 12.

Onsager, L. (1952). Interpretation of the de Haas-van Alphen effect. *Phil. Mag.*, 43:1006.

Origin-8.5. Originlab. Northampton, MA.

Pamplin, B. R. (1975). *Crystal growth*. Oxford.

Petrovic, C., Bud'ko, S. L., Strand, J. D., and Canfield, P. C. (2003). Anisotropic properties of rare earth silver dibismites. *J. Magn. Magn. Mater.*, 261(1):210–221.

Phelan, W. A., Nguyen, G. V., DiTusa, J. F., and Chan, J. Y. (2012). Synthesis, magnetic, transport, and thermodynamic investigation of CeCo(Sb, Sn)$_3$. *J. Alloys Compd.*, 523(0):176–181.

QuantumDesign (2012). Quantum Design – High Pressure Cell Kit for the MPMS. [Online; accessed 23-January-2012].

Raju, N. P., Greedan, J. E., Ferguson, M. J., and Mar, A. (1998). $LaCrSb_3$: A New Itinerant Electron Ferromagnet with a Layered Structure. *Chem. Mater.*, 10(11):3630–3635.

Ramirez, A. P. (1994). Strongly Geometrically Frustrated Magnets. *Annu. Rev. Mater. Sci.*, 24:453.

Raub, C. J., Compton, V. B., Geballe, T. H., Matthias, B. T., Maita, J. P., and Hull, G. W. (1965). Occurence of superconductivity in sulfieds tellurides of Pt-group metals. *J. Phys. Chem. Solids*, 26(12):2051.

Rhodes, P. and Wohlfarth, E. P. (1963). The Effective Curie-Weiss Constant of Ferromagnetic Metals and Alloys. *Proc. R. Soc. Lond. A.*, 273:247.

Richter, M., Rusz, J., Rosner, H., Koepernik, K., Opahle, I., Nitzsche, U., and Eschrig, H. (2004). Unconventional metallic magnetism in $LaCrSb_3$. *J. Magn. Magn. Mater.*, 272(0):E251 – E252.

Roberts, W. L., Campbell, T. J., and Rapp, G. R. (1990). *Encyclopedia of Minerals*. Van Nostrand Reinhold, New York.

Rotter, M., Hieke, C., and Johrendt, D. (2010). Different response of the crystal structure to isoelectronic doping in $BaFe_2(As_{1-x}P_x)_2$ and $(Ba_{1-x}Sr_x)Fe_2As_2$. *Phys. Rev. B*, 82:014513.

Rotter, M., Tegel, M., and Johrendt, D. (2008). Superconductivity at 38 K in the iron arsenide $(Ba_{1-x}K_x)Fe_2As_2$. *Phys. Rev. Lett.*, 101:107006.

Sacchetti, A., Degiorgi, L., Giamarchi, T., Ru, N., and Fisher, I. R. (2006). Chemical pressure and hidden one-dimensional behavior in rare-earth tri-telluride charge-density wave compounds. *Phys. Rev. B.*, 74(12):125115.

Sachdev, S. (2001). *Quantum Phase Transitions*. Cambridge University Press.

Sakamoto, T., Wakeshima, M., and Hinatsu, Y. (2006). Superconductivity in ternary chalcogenides $Bi_2Ni_3X_2$ (X = S, Se). *J. Phys.: Condens. Matter*, 18(17):4417–4426.

Saxena, S. S., Agarwal, P., Ahilan, K., Grosche, F. M., Hasselwimmer, R. K. W., Steiner, M. J., Pugh, E., Walker, I. R., Julian, S. R., Monthoux, P., Lonzarich, G. G., Huxley, A., Sheikin, I. Braithwaite, D., and Flouquet, J. (2000). Superconductivity on the border of itinerant-electron ferromagnetism in UGe_2. *Nature*, 406:587.

Schobinger Papamantellos, P., Andre, G., Rodriguez-Carvajal, J., Buschow, K. H. J., and Durivault, L. (2001). Magnetic ordering of $CeNi_{0.78}Sn_2$ and $Ce_3Ni_2Sn_7$ compounds by neutron diffraction. *J. Alloys Compd.*, 325(1-2):29–36.

Schumann, O. J. (2011). The Cologne Laue Indexation Program. Gnu general public license.

Seeger, M., Kronmtiller, H., and Blythe, H. (1995). The magnetic phase transition in $ZrZn_2$. *J. Magn. Magn. Mater.*, 139:312–322.

Sefat, A. S., Bud'ko, S. L., and Canfield, P. (2008). Magnetization, resistivity and heat capacity of the anisotropic $RCrSb_3$ crystals (R = La – Nd, Sm, Gd – Dy). *J. Magn. Magn. Mater.*, 320(3):120–141.

Shannon, R. D. (1976). Revised effective ionic-radii and systematic sutudies of interatomic distances in halides and chalcogenides. *Acta Cryst. A*, 32(SEP1):751–767.

SHELXTLPlus (2003). Bruker AXS, Inc. Madison, WI, USA.

Shenoy, G. K., Dunlap, B. D., Kalvius, G. M., Toxen, A. M., and Gambino, R. J. (1970). Magnetic and structural properties of some rare-earth-Sn_3 compound. *J. Appl. Phys.*, 41(3):1317.

Shoenberg, D. (1984). *Magnetic Oscillations In Metals*. Cambridge University Press, Cambridge, England.

Skolozdra, R. V., Yasnitskaya, I. V., and Akselrud, L. G. (1987). Properties of new rem stannides of the $La_3Co_2Sn_7$ structure. *Ukr. Fiz. Zh.*, 32(5):729–732.

SMART (1997-2005). Bruker AXS, Inc. Madison, WI, USA.

Sokolov, D. A., Aronson, M. C., Gannon, W., and Fisk, Z. (2006). Critical Phenomena and the Quantum Critical Point of Ferromagnetic $Zr_{1-x}Nb_xZn_2$. *Phys. Rev. Lett.*, 96:116404.

Steglich, F. (1985). *Theory of Heavy Fermion Systems and Valence Fluctuations*, volume 62. Springer Series in Solid State Sciences.

Stewart, G. R. (1984). Heavy-fermion systems. *Rev. Mod. Phys.*, 56:755–787.

Stewart, G. R. (2001). Non-Fermi-liquid behavior in d- and f-electron metals. *Rev. Mod. Phys.*, 73:797–855.

Stewart, G. R. (2006). Addendum: Non-Fermi-liquid behavior in d- and f-electron metals. *Rev. Mod. Phys.*, 78:743–753.

Stoner, E. C. (1933). Atomic moments in ferromagnetic metals and alloys with non-ferromagnetic elements. *Phil. Mag.*, 15(101):1018–1034.

Strongin, M., Thompson, R. S., Kammerer, O. F., and Crow, J. E. (1970). Destruction of Superconductivity in Disordered Near-Monolayer Films. *Phys. Rev. B*, 1:1078–1091.

Szytula, A. and Leciejewicz, J., editors (1994). *Handbook of Crystal Structures and Magnetic Properties of Rare Earth Intermetallics*. CRC Press.

Taufour, V., Aoki, D., Knebel, G., and Flouquet, J. (2010). Tricritical Point and Wing Structure in the Itinerant Ferromagnet UGe_2. *Phys. Rev. Lett.*, 105:217201.

Thaler, A., Hodovanets, H., Torikachvili, M. S., Ran, S., Kracher, A., Straszheim, W., Yan, J. Q., Mun, E., and Canfield, P. C. (2011). Physical and magnetic properties of $BaFe_{1-x}Mn_x)_2As_2$ single crystals. *Phys. Rev. B*, 84:144528.

Thamizhavel, A., Galatanu, A., Yamamoto, E., Okubo, T., Yamada, M., Tabata, K., Kobayashi, T. C., Nakamura, N., Sugiyama, K., Kindo, K., Takeuchi, T., Settai, R., and Onuki, Y. (2003). Low Temperature Magnetic Properties of $CeTBi_2$ (T: Ni, Cu and Ag) Single Crystals. *J. Phys. Soc. Jpn.*, 72(10):2632–2639.

Thessieu, C., Flouquet, J., Lapertot, G., Stepanov, A. N., and Jaccard, D. (1995). Magnetism and spin fluctuations in a weak itinerant ferromagnet: MnSi. *Solid State Comm.*, 95(10):707–712.

Tinkham, M. (2004). *Introduction to Superconductivity*. Dover Publications.

Troc, R., Gajek, Z., and Pikul, A. (2012). Dualism of the 5f electrons of the ferromagnetic superconductor UGe_2 as seen in magnetic, transport, and specific-heat data. *Phys. Rev. B.*, 86(22):224403.

Trovarelli, O., Geibel, C., Mederle, S., Langhammer, C., Grosche, F. M., Gegenwart, P., Lang, M., Sparn, G., and Steglich, F. (2000). $YbRh_2Si_2$: Pronounced Non-Fermi-Liquid Effects above a Low-Lying Magnetic Phase Transition. *Phys. Rev. Lett.*, 85:626.

Uhlarz, M., Pfleiderer, C., and Hayden, S. M. (2004). Quantum phase transitions in the itinerant ferromagnet $ZrZn_2$. *Phys. Rev. Lett.*, 93(25):256404.

Vojta, M. (2003). Quantum phase transitions. *Rep. Prog. Phys.*, 66(12):2069.

Weihrich, R. and Anusca, I. (2006). Half Antiperovskites. III. Crystallographic and Electronic Structure Effects in $Sn_{2x}In_xCo_3S_2$. *Z. Anorg. Allg. Chem.*, 632:1532.

Wernick, J. H. (1972). Magnetic behavior of the monosilicides of the 3d-transition elements. *Mater. Res. Bull.*, 7:1431 –1441.

Wiener, T. A. and Canfield, P. C. (2000). Magnetic phase diagram of flux-grown single crystals of CeSb. *J. Alloys Compd.*, 303-304(0):505–508.

Wiener, T. A., Fisher, I. R., Bud'ko, S. L., Kracher, A., and Canfield, P. C. (2000). Design of a metallic Ising spin glass in the $y_{1-x}tb_xni_2ge_2$ system. *Phys. Rev. B*, 62:15056–15066.

Wilke, R. H. T., Bud'ko, S. L., Canfield, P. C., and Finnemore, D. K. (2010). *High Temperature Superconductors*, chapter Superconductivity in MgB_2. WILEY-VCH Verlag GmbH & Co. KGaA, Weinheim.

Yan, J.-Q., Kreyssig, A., Nandi, S., Ni, N., Bud'ko, S. L., Kracher, A., McQueeney, R. J., McCallum, R. W., Lograsso, T. A., Goldman, A. I., and Canfield, P. C. (2008). Structural transition and anisotropic properties of single-crystalline $SrFe_2As_2$. *Phys. Rev. B*, 78:024516.

Yeung, I., Roshko, R. M., and Williams, G. (1986). Arrott-plot criterion for ferromagnetism in disordered systems. *Phys. Rev. B*, 34:3456–3457.

Zabel, M., Wandinger, S., and Range, K. J. (1979). Ternary metallic Chalcogenides $M_3M'_2X_2$ (M = Ni, Co, Pd, Rh), (M' = In, Tl, Sn, Pb, Bi), (X = S, Se) with Shandite and Parkerite structure. *Z. Naturforsch. B*, 149(1-2):157.

Zeng, L. and Franzen, H. F. (1998). Crystal structure of a new compound Bi_2NdNi. *J. Alloys Compd.*, 266:155–157.

Zhu, X., Lei, H., Petrovic, C., and Zhang, Y. (2012). Surface-induced magnetic fluctuations in a single-crystal $NiBi_3$ superconductor. *Phys. Rev. B*, 86:024527.